MULTISCALE ANALYSIS OF LOW-TEMPERATURE THERMOCHEMICAL ENERGY STORAGE WITH COMPOSITE MATERIALS

by

Robin Nicolas Fisher

A thesis submitted to the University of Birmingham for the degree of
DOCTOR OF PHILOSOPHY

Birmingham Centre for Energy Storage
School of Chemical Engineering
College of Engineering and Physical Sciences
University of Birmingham
July 2022

Supervisor: Adriano Sciacovelli
Co-supervisor: Yulong Ding

Abstract

Residential space heating accounts for ~60% of private domestic energy use, and for approximately 10%-15% of global greenhouse gas emissions. Increasing the penetration of renewable energies for power provision, and in particular solar power, is essential for future energy systems. Discrepancy between the high space heating demand during winter and high solar energy availability during summer leads to the need for efficient long-term thermal energy storage solutions. Storing heat by means of reversible endothermic chemical reactions is a promising strategy, since energy is maintained without losses and at higher energy storage densities than other typical methods, such as sensible or latent thermal energy storage. Energy can be stored thermochemically through reversible water adsorption into inorganic salts, and discharged later at the low to medium temperatures required for domestic space heating.

Thermochemical energy storage's current level of maturity is between fundamental research and practical applications. Composite thermochemical materials with two or more components are being developed by the scientific community. These components include at least one active material which provides thermochemical energy storage capacity, and at least one supporting matrix. Dispersion of the active material into a matrix modifies the thermochemical equilibrium, improves heat and mass transfer, and in some instances contributes to the energy storage capacity. While the behaviour of pure active materials is reasonably well understood, their behaviour when dispersed into a matrix requires further investigation. The mechanisms behind the heat discharge phase are particularly unclear and are further complicated by the number of available host matrixes. Furthermore, technical hurdles, such as material instability, high storage volume and low discharge power, have emerged from the development of larger scale thermochemical energy storage systems, leading to poor economic performance. These issues tend to occur when operating thermochemical storage systems with pure active materials, whereas use of composites is usually confined to sample-scale experiments. At this stage, it is unclear what the performance of large-scale systems would be if operated with composite thermochemical materials, and whether the technical hurdles at reactor and system scales may be addressed this way. In this thesis, thermochemical energy storage is analysed in a cross-scale manner to help bridge the gap between material, reactor, and system scales. The overarching aim is to improve the understanding of the behaviour over time of thermochemical composite materials during heat charge/discharge and evaluate how this behaviour affects performance of thermochemical energy storage systems.

After a general introduction and a review of the TCS literature relevant for this thesis, results and contributions are presented. First of all, an analysis is carried out of the heat discharge kinetics of thermochemical materials in both pure form and dispersed into a matrix. The purpose of this analysis is to identify the rate-limiting processes of the reaction and propose suitable kinetic models to improve precision in thermochemical energy storage simulations. It was found that while the hydration of pure K_2CO_3 is severely kinetically hindered and difficult to model using conventional solid-state kinetic models, integration into a vermiculite host matrix provided improvements and was accurately

predicted by nucleation models at 25°C and phase-boundary control model at 40°C. $MgCl_2$ hydration shifted from an intraparticle diffusion to an interparticle diffusion kinetic control when dispersed into vermiculite, with a 5 to 10-fold reaction rate increase. Thus, the effect of salt impregnation, specifically in vermiculite, was precisely quantified in terms of rate-controlling mechanism and reaction rate. These results can feasibly be extrapolated to other salt and matrix combinations which demonstrate similar thermal energy storage capabilities. Secondly, the performance of a thermochemical energy storage reactor, integrated into a dwelling equipped with solar thermal, is carried out through numerical simulation. It became apparent that open TCS in European domestic context requires additional humidification to reach high enough temperature lifts. The choice of kinetic models (identified in the previous chapter) and reaction rates was found to affect performance during simulations by up to 5%. When modelling for different thermochemical storage materials, $MgCl_2$-based composites showed a promising balance between power output, energy storage density and overall system cost. Finally, the techno-economic viability of a thermochemical energy storage system coupled to power-to-heat technologies is assessed. Reviewing electrified reactor technologies showed that microwave and radiofrequency heating could be more efficient (~75% to 80% versus over 80%) than conventional heating, however depth of penetration of electromagnetic waves could be a significant technical hurdle. This part of the thesis also aims to evaluate performance at the system scale, with the additional objective of quantifying the potential of combining solar photovoltaics with thermochemical energy storage. It was found that with TCS capital costs below 20 €/kWh which is conventionally the technological objective by the TCS community, domestic thermal energy storage with levelized costs between 400 and 500 €/MWh are achievable.

Acknowledgements

The work presented in this PhD thesis is the result of over four years of effort at the Birmingham Centre for Energy Storage (BCES). I would like to acknowledge the people who have directly or indirectly contributed to the stage I am at now.

First and foremost, I would like to thank Adriano Sciacovelli, my PhD supervisor. Adriano has provided me with guidance, support, and a framework within which to focus my research and progress my PhD thesis. His understanding of the scientific challenges and his passion for research and knowledge motivated me. His willingness to push the boundaries and aspiration to bring the best out of his students were a great driver for my work. I would like to thank him for helping me push myself to be the best I can be and aim for excellence. I would also like to thank him for the continued trust in me by encouraging me to take up a post-doctoral position in the BCES group. I would also like to thank Professor Yulong Ding, the head of the BCES group and my secondary supervisor, without whom the PhD opportunity, and now the post-doctoral position I was given would not have happened. I would like to thank my two PhD comrades, Andrea and Gabriele, with whom I share a bond in pursuing the PhD degree under Adriano's supervision. I wish them well in achieving their goals.

Many people at the university have directly or indirectly supported me. I would like to thank Anabel, Helena, Gan, Gilmore, Marco, Aris, Mark, Jie and many others. While it was several years ago, I would like to thank Sara and Ilaria who welcomed me when I first arrived. I also wish the best to all the Italian visitors from the Politecnico of Turin who came to complete their Masters: Serena, Luca, Marisa and Adina. I have had the opportunity to meet some very interesting and skilled visiting researchers who provided me with unique insight and were a great source of inspiration, on top of being great conversationalists for all the non-scientific topics as well. Luca and Guido, I thank you. I would like to acknowledge the three Master students I had the opportunity to assist, Gavan, Ciara and Jonas. It was a pleasure to help them achieve their goals and move on in their respective careers. I would also like to acknowledge the researchers who have worked with Adriano and therefore with me; Giovanni, Ruihuan. I would like to acknowledge in particular Shivangi and Pouriya, who are or were my colleagues, and I can now call them among my friends.

Back in France, I would like to acknowledge my friends who are a constant source of support and joy: Alaric, Alex, Gregoire, Simon, Thibaut, Quentin, Hugo, Leo, Alexis, and others who I apologise for not naming. I thank my cousins, Jeremy, Gail, Zack, Jamie, Katie, Aimee, and Paul, Taryn, Taylor, and Reece, for having their doors open to me, and taking me to some great football matches. I would like to also thank Gabrielle, whom I met at the University; though our paths have now separated, her support throughout much of my thesis study was invaluable and I am grateful to her.

From the first day back in 2018 to the last, I would like to thank my parents, Gillian and Graham, for the tireless support, patience and encouragement that have led me here. Without them, this PhD project would never have come to fruition.

Table of Contents

Nomenclature

List of abbreviations

Abbreviation	Description
AC	Alternating Current
DC	Direct Current
DHW	Domestic Hot Water
DSC	Differential Scanning Calorimetry
DVS	Dynamic Vapour Sorption
EFI	Electric Field Intensity
ESC	Energy Storage Capacity
EU	European Union
FPC	Flat Plate Collector
HRU	Heat Recovery Unit
HTF	Heat Transfer Fluid
HX	Heat Exchanger
I	Intensity
KPI	Key Performance Indicators
LCOE	Levelised Cost of Energy
LMTD	Log Mean Temperature Difference
LTES	Latent Thermal Energy Storage
MW	Microwaves
NTU	Number of Transfer Units
P2H	Power-to-Heat
PV	Photovoltaic
RES	Renewable Energy Storage
RF	Radiofrequency
SCC	Specific Capacity Cost
SIM	Salt-in-Matrix
STES	Sensible Thermal Energy Storage
TCM	Thermochemical Material
TCS	Thermochemical Energy Storage
TES	Thermal Energy Storage
TG	Thermogravimetric
TRL	Technological Readiness Level

List of symbols

Symbol	Definition	Unit
A	Area	m^2
A_f / A	Arrhenius factor	1/s
AICc	Akaike criterion	-
A_p	Aperture area	m2
c	Concentration	mol/m^3
C	Heat capacity rate	W/K
comp	Salt content in composite	%
Cp	Heat capacity	J/kg/K
D	Diameter	m
E_a / E	Activate energy	J/mol
E_d	Energy density	GJ/m^3
f	Kinetic model	-
g	Integral kinetic function	-
h	Heat transfer coefficient	$W/m^2/K$
I_t	Total solar irradiance	W/m^2
k	Kinetic rate constant	1/s
L	Length	m
m	Mass	kg
M	Molar mass	kg/mol
n	Stochiometric coefficient	-
N	Number of data points	-
p	Partial pressure	Pa
P	Power	W
Q_m	Mass flow rate	kg/s
Q_v	Volumetric flow rate	m^3/s
R	Perfect gas constant	J/mol/K
r	Radius	M
R^2	Coefficient of determination	-
RH	Relative Humidity	%
S	Solar radiation	W
T	Temperature	K
t	Time	S
U	Heat transfer coefficient	$W/K/m^2$
UA	Overall heat loss coefficient	W/K
V	Volume	m^3
w	Absolute Humidity	kg/kg
wt.-%	Weight percentage	%
z	Expansion factor	-
ΔG	Free Gibbs energy	J/mol
ΔH	Reaction enthalpy	J/mol
ΔS	Reaction entropy	J/mol/K

List of Greek symbols

Symbol	Definition	Unit
λ	Thermal conductivity	W/m/K
α	Reaction advancement	-
β	Relative mass uptake	%
γ	Heating rate	K/min
δ	Barrier thickness	m
Δ	Difference	-
ε	Porosity	-
η	Efficiency	%
κ	Stochiometric coefficient	-
ρ	Density	kg/m^3
τ α	Transmittance-absorptance	-

List of subscripts

Symbol	Definition
a or amb	Ambient
air	Air
c	Cover
cin	Kinetic
eq	Equilibrium
exp	Experimental
f	Final
fan	Fan
H_2O	Water
in	Inlet
inv	Inverter
m	Matrix
m	Mean
min	Minimum
num	Numerical
o	Initial
p	Plate
pm	Mean absorber plate
R	Reacted
s	Solid
UR	Unreacted
v	Vapour
w	Water

Chapter I. General Introduction

1 Energy context and wider need for thermal energy storage

Significant change is required in the way society deals with energy needs to face the current environmental crisis. Energy systems requires an overhaul to meet the increasing worldwide energy demand due to an increasing population, increased quality of life expectations, and to meet the current carbon emission reduction targets needed and avoid the more catastrophic global warming scenarios [1]. In order to move away from a fossil fuel-based energy system, an obvious and realistic course of action is the integration of renewable energies sources (RES).

In the EU, RES reached a share of 14.4% of the total gross inland consumption, for an energy production share of 36.5% (**Figure 1**). While the share of RES in the EU's energy production mix is the highest amongst all fuel types, a higher share of RES in the gross consumption is required to reach the emissions target and combat climate change. The recent European Climate Law proposed, as an updated target, to achieve a share of 40% renewables by 2030 in the gross final energy consumption of the European Union [2].

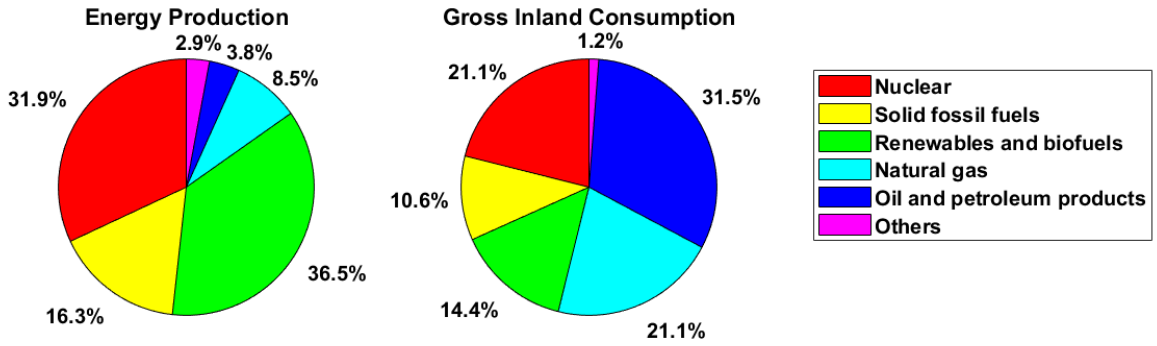

Figure 1 (left) EU Energy production in 2019, by fuel, (right) EU Gross inland energy consumption in 2020, by fuel [3].

One of the main hurdles to the penetration of RES is the mismatch between availability of renewable energy and energy demand at a given time. Indeed, both renewable energy generation and thermal energy demand for space heating are subject to intermittency at different time scales (**Figure 2**) and are often mismatched. RES are intermittent both on daily and seasonal time scales. Thermal energy storage (TES) is a potential solution to this mismatch, as energy available at a period of low demand can be stored, and used later when demand overtakes availability [4]. The consistent implementation of TES could also have further ramifications such as increased energy security, load shifting, decentralisation of energy sources, and improving economic viability of technologies relying on renewable energy sources [2].

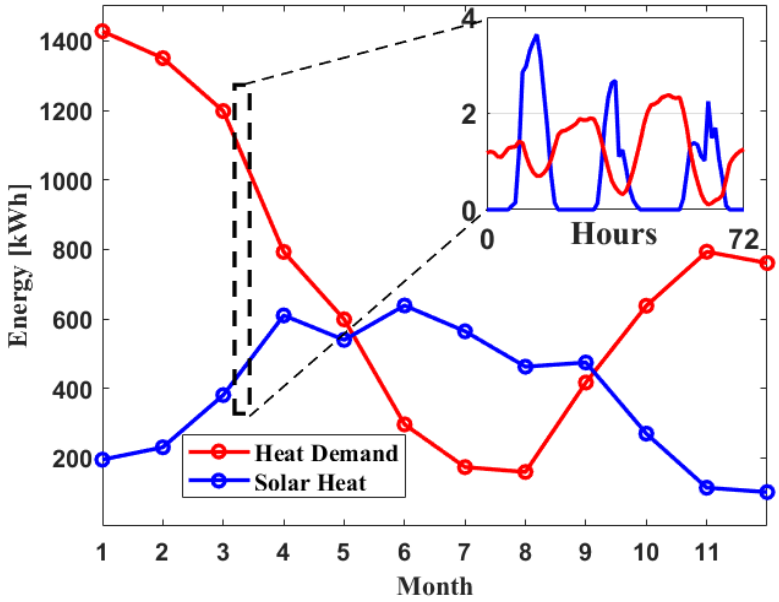

Figure 2 (main) seasonal intermittency of average monthly heat demand and available solar energy, (zoomed insert) daily intermittency of non-averaged heat demand and solar energy during April. Available solar energy and ambient temperatures obtained from renewables.ninja [5] **for Birmingham in 2017. Heat demand calculated for a dwelling in Birmingham with heat loss coefficient UA = 4 W/m^2/K and a baseline indoor temperature T = 16.5°C.**

2 Classification of thermal energy storage

Heat can be stored through one of three methods:

- Sensible thermal energy storage (STES), where heat is stored by raising the temperature of a solid or liquid substance. At low temperature, water is often used. While sensible TES is at the highest technological readiness level (TRL = 8-9 i.e. commercial solutions are developed and large scale integration still needs effort [6,7]) and the cheapest and simplest heat storage method, it displays the lowest energy storage density. Heat losses occur as the STES material gradually cools to the ambient temperature, particularly for individual domestic sensible heat storages. Stored heat must therefore be used within a timeframe of 24 hours. Larger, community-scale STES suffers from reduced heat losses compared to individual-scale domestic STES.
- Latent thermal energy storage (LTES) relies on heat being stored by melting a solid or liquid substance at constant temperature. Heat is recovered by cooling the so-called phase change material (PCM) which solidifies. LTES is at a TRL of 5 to 7 where prototypes are being deployed at various scales without necessarily achieving economic viability [6,7].
- Thermochemical energy storage (TCS) relies on reversible chemical reactions to store heat as chemical bonds in a thermochemically active material. Many reversible endo-exothermic reactions can theoretically be used as thermochemical storage materials (TCMs). TCS is at

the lowest readiness level of the three TES technologies (TRL = 4 where early prototypes are being developed) [6,7].

'Sorption' is a type of thermochemical reaction where a substance in vapour/gas phase (sorbate) is captured in a condensed state by a solid (sorbent). The exact meaning and use of 'thermochemical' and 'sorption' reactions differ between authors which complicates the classification of the different types of reactions applied to TCS. Several distinctions are required in order to fully appreciate the landscape of chemical reactions used for TCS:

- Chemical storage and sorption storage. According to the IUPAC Compendium of chemical terminology [8], sorption is the '*process by which a substance (sorbate) is sorbed (adsorbed or desorbed) on or in another substance (sorbent)*'. However, several reversible exo/endothermic reactions, in which no sorption mechanism is involved, may be used for TCS.
- Absorption and adsorption. Absorption refers to sorption reactions where the sorbate is retained within the chemical structure of the sorbent, whereas during adsorption the sorbate is retained at the surface of the sorbent.
- Physical sorption and chemical sorption. In the case of adsorption, these processes are also referred to as chemisorption and physisorption. According to IUPAC [8], chemisorption is '*adsorption in which the forces involved are valence forces of the same kind as those operating in the formulation of chemical compounds*'. The resulting chemical binding is of an order magnitude of approximately 1 to 10 eV. Thus, the main difference is the nature of the bond tying the sorbent to the sorbate. Physical sorbents are generally microporous solids such as alumina, zeolites, silica gel, and activated carbon, and the main physical forces involved are mainly van der Waals bonds and electrostatic interactions, of an order of magnitude approximately 10 to 100 meV. While very similar in many aspects which can sometimes make distinction difficult, chemical sorption results in a typically much stronger bond and is more difficult to reverse than physical adsorption [9].

The various terms and distinctions, and how the reaction of interest in this work fits within this classification, are summarised in **Figure 3**. Chemical sorption can be seen as overlapping over both sorption and thermochemical reactions [10]. Alternatively, thermochemical storage reactions can be seen as being either with or without sorption [11]. Hydration of composites can be considered as overlapping between chemical adsorption (due to the salt) and physical adsorption (due to the matrix). However, some authors also appear to classify the hydration/dehydration of inorganic salts as reaction-based TCS, distinctively from sorption-based TCS [12]; conventional classification of these reactions remains a grey area despite efforts in the TCS scientific community.

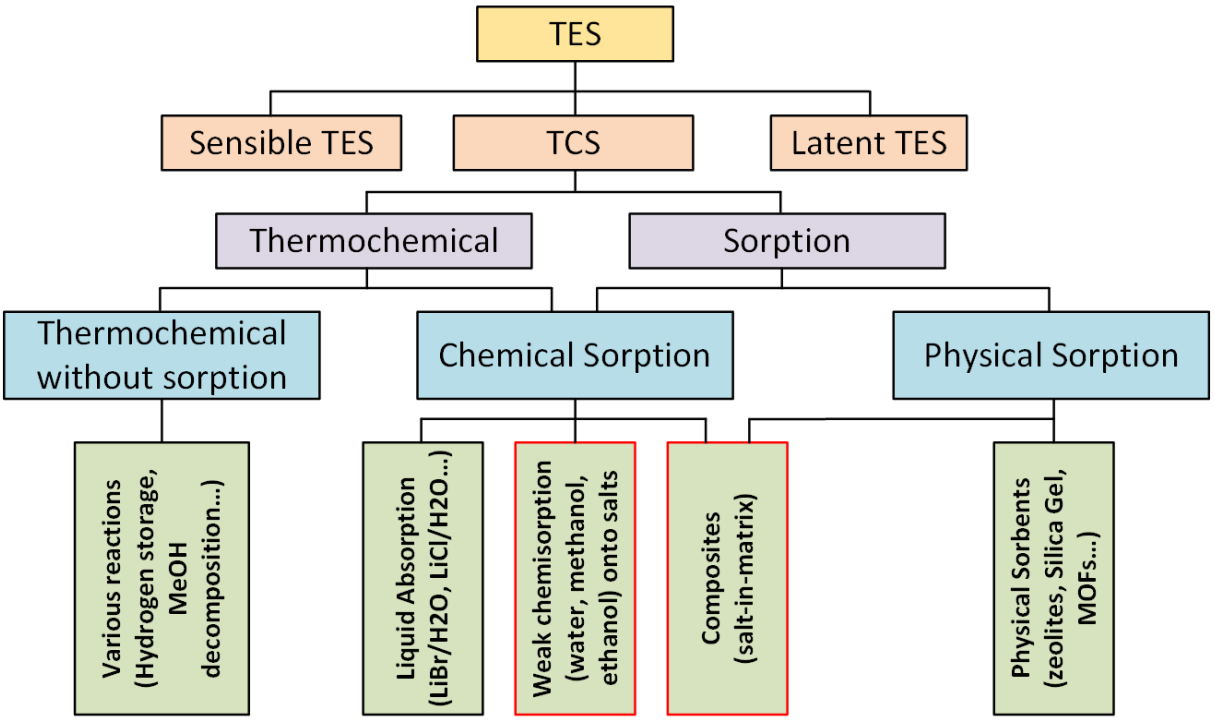

Figure 3 Classification of TES and TCS. The two types of reaction of interest in this thesis are highlighted in red.

3 Sorption thermal energy storage and its challenges

Chemical adsorption reactions of inorganic salts with water (chemical adsorption) and of salt-in-matrix (SIM) composites with water (hybrid chemical adsorption and physical adsorption) are the subject of this thesis. Such reactions occur at temperatures of approximately 50°C-120°C. This temperature range combined with the potential to store heat indefinitely with minimal heat losses [13–15] make salt-based TCS suitable for capturing low-temperature heat from solar thermal collectors and releasing heat for domestic space heating.

$$A \cdot (\mathrm{m}+\mathrm{n})B + \Delta H_r \rightleftarrows A \cdot m\mathrm{B} + \mathrm{n}B_{(g)} \qquad (1)$$

At least two materials are required to carry out sorption TCS: a solid adsorbent A and a gaseous adsorbate B, as shown in **equation (1)**. During heat charge, heat is provided to the material and adsorbent A and adsorbate B are separated during the endothermic reaction. A and B are stored separately, and thermal energy is stored without losses as chemical bonds while they are kept separate. To discharge heat, A and B are brought together and react exothermically. The open sorption TCS principle is illustrated in **Figure 4**.

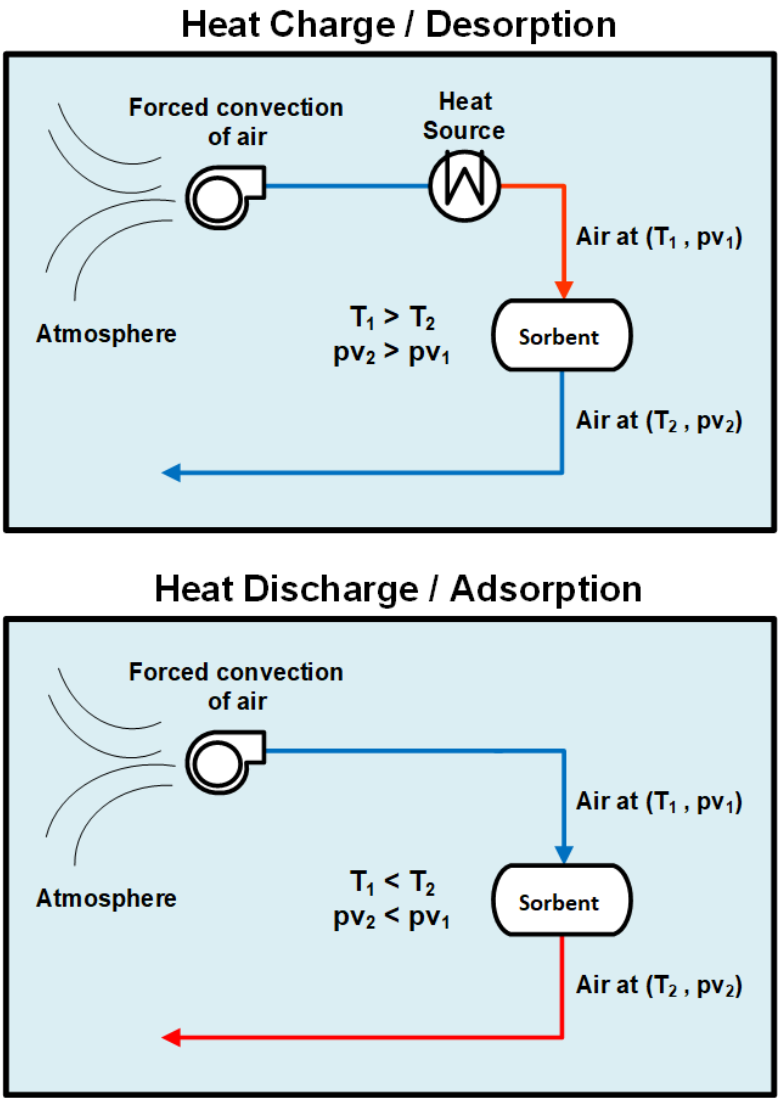

Figure 4 Open sorption TCS principle. Red arrows denote hot air, blue arrows denote cool air. T denotes air temperature and pv air vapour pressure.

Salt-based sorption TCS offers several advantages compared to other TES methods:

- In general, TCS exhibits higher energy storage density (150 kWh/m^3 to 300 kWh/m^3) compared to STES (10 kWh/m^3 to 30 kWh/m^3) and LTES (50 kWh/m^3 to 160 kWh/m^3), with virtually lossless storage over long time-periods allowing for a decentralised and decarbonised thermal energy source, ideal for solar-based space heating systems.
- Specifically inorganic salt-based TCS displays many promising material candidates showing a wide variety of properties which allows for selection depending on the applications, with some of these materials being abundant and relatively cheap, such as magnesium-based salts [16].

  Inorganic salt based TCS requires relatively low temperature level heat to perform the endothermic reaction (i.e. heat storage), sometimes as low as 50°C. The exothermic reaction

is performed using humid air which does not impose any significant technical hurdles compared to systems with different working fluid such as ammonia.

Sorption TCS remains at a low TRL however due to technical challenges that hinder its development. Present research in the literature surrounding TCS at the time of this thesis is generally focused on either of the three following scales: material, reactor, and system scales. Certain technical challenges are specific to one of these scales, while others occur when switching from one scale to another.

- Obtaining high energy storage density materials with good thermo-physical properties for TCS has been considered a bottleneck to the advancement of this field in several reviews. As a result, new materials are being developed and demonstrated at the milligram scale. However, in current reactor prototypes and reactor models, (de)hydration is mostly carried out using less advanced materials such as:
    - pure salts which have been demonstrated, in part by the scientific community and in this work, as impractical for use when not integrated within a supporting matrix, or,
    - physical adsorbents such as zeolite or silica gel which require higher temperatures for dehydration (over 160°C) than generally available from solar thermal (below 150°C).
- The disparity between material-scale performance and reactor/system scale performance is currently major bottleneck. The ideal energy storage density of investigated TCMs (in the range ~ 200 kWh/m^3 to 300 kWh/m^3) is often stated, however, when integrated into a device, the energy storage density drops significantly (below 150 kWh/m^3). This is mainly due to lower reaction performance at a larger scale, and the volume occupied by process units such as humidification / evaporators, heat exchangers and fans. The lower performance is particularly noticeable in terms of delivered power during discharge compared to the theoretical power output based on the chosen TCM and affects the economic viability of such systems.
- The fundamental understanding behind the reaction kinetics of water sorption into salts requires further investigation. It is unclear how similar the reaction kinetics are during the hydration of different inorganic salts. The impact of integrating salts into a host matrix on the reactions kinetics is also unclear, and further complicated by the large number of possible salt/matrix pairs.

4 Aims, objectives and methodologies

The overarching aim is therefore to carry out a multi-scale analysis of the transient behaviour of low-temperature thermochemical energy storage based on salt-in-matrix adsorption of water to further its penetration into modern energy systems. By carrying over experimental results obtained at the material scale to larger scale systems through modelling, this thesis aims to bridge the gap between material and reactor/system scale for low-temperature TCS. At material scale, this research aims to investigate the limiting mechanisms during salt and salt-in-matrix hydration processes, and as a result how to best model the reaction kinetics of hydration. The work then investigates how these limiting mechanisms can be accounted for in larger scale TCS systems, and whether this improved accuracy

has an impact on the performance of such systems. With the context and research objectives, the following research questions were formulated:

- Q1: What are typical materials used for low-temperature TCS? What kinetic models exist to capture their dynamic reaction behaviour at material and reactor scale?
- Q2: What is the impact of salt impregnation on the kinetic behaviour of salt hydration? How is the choice of kinetic model affected by the impregnation of the salt into a host matrix?
- Q3: What impact does the selected thermochemical material (TCM) and the reaction kinetics have on the performance of sorption-based low-temperature TCS processes?
- Q4: Can domestic solar photovoltaics or other electrical energy sources be feasibly coupled to a low-temperature TCS system? Is combining solar photovoltaics and power-to-heat technologies with TCS technically and economically viable?

A review of existing TCS literature is first carried out (Q1). The hydration of carefully selected salts, and of these same salts dispersed into a host matrix, was performed using dynamic vapour sorption. Reaction kinetics were evaluated, to infer rate-limiting mechanisms, and modelled using solid-state kinetics (Q2). A reduced 1D model for a TCS reactor was developed and integrated into a system model to evaluate the performance of a domestic TCS system coupled to the solar thermal. Kinetic models obtained previously were used to model the reaction kinetics, and their impact on overall performance, along with material selection and operating conditions, were investigated (Q3). The same reactor model was then coupled to a system using solar photovoltaics and various power-to-heat technologies to evaluate the techno-economic viability of such systems using key performance indicators (Q4).

5 Novelties

There have been a growing number of studies on sorption TCS in the recent years. The work presented in this thesis differs from these published studies for the following reasons:

- The kinetics of hydration of inorganic salts are evaluated using a solid-state kinetic framework, providing accurate kinetic models which are directly usable in TCS system simulations.
- The differences between pure salt and salt-in-matrix hydration kinetics were quantified using solid-state kinetics.
- The impact of the selected kinetic model and the selected material on the performance of a domestic TCS system coupled to solar thermal was explored and quantified, with the additional novelty of considering realistic, non-ideal weather conditions.
- The potential of combining solar photovoltaics with low-temperature TCS in domestic applications was explored.

6 Outline

The outline of the different chapters of the thesis and how they seek to address the proposed research questions is as follows:

Chapter I: the present chapter.

Chapter II aims to answer the first research question Q1. A review of the salts and salt/matrix composites that have been formulated/characterised for low-temperature TCS is carried out. In parallel, a review of the existing kinetic models that have been proposed for the reviewed materials is also presented. In addition to the materials review, a review of TCS reactors and system prototypes proposed in the literature using either salt or SIM hydration is presented. In parallel, a review of the models used to simulate the dynamic behaviour of these TCS reactors is carried out, with a particular focus on the methodology used for kinetic reaction modelling.

Chapter III investigates the second research question Q2. A solid-state kinetic analysis of the hydration of two promising inorganic salts, and of two composite materials based on the impregnation of these two salts in a vermiculite host matrix, is carried out. The hydration of these materials is performed in a dynamic vapour sorption (DVS) apparatus. Based on analysis of thermogravimetric data, and numerical fitting of relevant solid-state kinetic models, the limiting mechanisms during these chemical reactions are explored, including how the presence of a host matrix impacts the rate-limiting process.

Chapter IV addresses the third research question Q3. A system consisting of a TCS reactor used to store heat retrieved from a flat plat solar collector for domestic space heating in a family house is considered. A simplified reduced model of a TCS reactor is proposed and imbedded into a TCS process model. Performance of the system is quantified for various salt-in-matrix composites selected from the most promising inorganic salts for low temperature TCS. Furthermore, the impact of selection of reactor kinetic model on system performance is evaluated using key performance indicators. In addition to the analysis of the performance with regards to the weather and operating conditions, existing kinetic models for salt hydration from the literature and developed in this work are integrated to the system model and their impact on overall performance prediction is evaluated.

Chapter V is targeted towards addressing the final research question Q4. Differently from **Chapter IV**, Chapter V focuses on the performance of the TCS system during both hydration and dehydration. Furthermore, in this chapter the techno-economic potential for TCS coupled to power-to-heat (P2H) technologies is investigated, which would enable the use of renewable power generation for several applications, with the focus here being on domestic space heating provided by solar energy. A similar numerical model as the one developed in **Chapter IV** is coupled to power-to-heat to evaluate the techno-economic potential when providing for residential space heating. Yearly weather and PV power generation data are used as inputs to the simulation. Evaluation criteria such as normalised TCS volume, simple payback time and levelised cost of electricity are used.

Chapter VI offers a summary of the main results obtained from the preceding chapters, the main conclusions to be drawn, and recommendations for future courses of action to advance scientific knowledge surrounding the kinetic behaviour of salt and SIM hydration for low temperature TCS.

Chapter II. Review of Dynamic Aspects of Low-Temperature Salt-Based TCS

1 Introduction

This chapter reviews the current TCS literature relevant to the work presented in this thesis. The review is focused on:

- A systematic classification of hydration/dehydration reactions of low-temperature inorganic salts and composite materials based on inorganic salts.
- Relevant studies on the fundamental understanding of these reactions applied to low to medium temperature TCS and the quantitative description of their kinetic dynamic behaviour, at material (i.e., milligram), and reactor scales (i.e. kilogram to ton).

The overarching aim of this chapter is to answer the research question Q1 formulated in **Chapter I** (Q1: What are typical materials used for low-temperature TCS? What kinetic models exist to capture their dynamic reaction behaviour at material and reactor scale?). The chapter is organised as follows: the chemical and thermodynamic fundamentals of inorganic salt/hydration are discussed (**Section 2.1**), followed by an overview of the relevant reactions for low-temperature space heating (**Section 2.2**) and of composite TCM (**Section 2.3**). In **Section 3** an overview is given of the fundamentals of gas-solid reaction kinetics and of the existing kinetic models for material scale hydration of pure salt and salt-in-matrix composites. **Section 4** gives an overview of existing open TCS reactor prototypes, and reviews the kinetic models used in reactor scale simulation.

2 Inorganic salt sorption

2.1 Chemical and thermodynamic fundamentals

As discussed briefly in **Chapter I**, the chemical adsorption and desorption reactions of inorganic salts with water is a means to thermochemically store (during dehydration) and release (during hydration) heat. **Equation (2)** shows the generic form of inorganic salt hydration/dehydration reactions.

$$Salt \cdot (\mathrm{m}+\mathrm{n})H_2O + \Delta H \rightleftarrows Salt \cdot mH_2\mathrm{O} + \mathrm{n}H_2O_{(g)} \qquad (2)$$

Where m is the stoichiometric coefficient of the lower hydrate (state of the salt with energy stored), n is the stoichiometric coefficient of the reaction i.e. the number of added moles of water per mole of lower hydrate. The hydration and dehydration reactions of inorganic salts with water are characterised by their Gibbs free energy change of reaction, calculated with **equation (3)**:

$$\Delta G = \Delta H - T\Delta S \qquad (3)$$

Application of the Gibbs phase rule to inorganic salt hydration/dehydration [17], i.e. the equilibrium between the lower hydrate, upper hydrate and water vapour, yields **equation (4)** and **equation (5)**:

$$F = C - \varphi + P \tag{4}$$

Where F is the system variance, C is the number of components minus the number of reactions (2, hydrated salt, anhydrate, and water vapour, minus one reaction), φ the number of phases (3, the water vapour phase and 2 solid phases), and P the number of intensive variables (2, temperature and vapour pressure).

$$F = 2 - 3 + 2 = 1 \tag{5}$$

Thus, these thermochemical reactions are monovariant systems, where variation in either reaction temperature or water vapour pressure results in a variation of the other to maintain equilibrium. The equilibrium conditions of reversible inorganic salt hydration and dehydration processes are defined by a Clausius-Clapeyron relationship [18,19] shown in **equation (6)**:

$$\ln\left(\frac{P_{eq}}{P^o}\right) = -\frac{\Delta H}{RT_{eq}} + \frac{\Delta S}{R} \tag{6}$$

Where $P^o = 10^5 Pa$ is the standard pressure reference pressure. Thus, at a given temperature T, if the water vapour pressure around the material exceeds the equilibrium vapour pressure ($P > P_{eq}$), the reaction is favoured thermodynamically towards hydration. On the other hand, if the equilibrium vapour pressure is superior to the water vapour pressure ($P < P_{eq}$), then the dehydrated state is more stable, and dehydration is favoured thermodynamically. Enthalpy and entropy of reaction, ΔH and ΔS, are functions of the enthalpy and entropy of formation of the reactants and products. As is often the case of non-ideal thermochemical systems [20], varying levels of thermal hysteresis can be observed for inorganic salt hydration, which can range from negligible (less than 5°C difference) [21,22] to significant (~50°C) [20,23].

According to the current literature, hydration can take place via two potential pathways [24];

- a direct solid/solid phase transition, where the unhydrated crystal lattice of the salt reorganises itself to incorporate water molecules.
- a two-step process consisting first in the dissolution of the crystalline phase followed by recrystallisation of the lattice with incorporated water molecules from a supersaturated salt solution.

The hydration pathway depends mainly on the temperature / humidity conditions of the reaction. If above the deliquescence humidity, hydration takes place via the two-stage pathway. Below deliquescence humidity, hydration takes place via a direct solid-solid transition. The two hydration pathways are shown schematically in **Figure 5**. Dehydration is performed by providing heat to the

inorganic salt in its hydrated state, which will cause the solid water molecules to desorb from the crystalline lattice of the salt back into a vapour state.

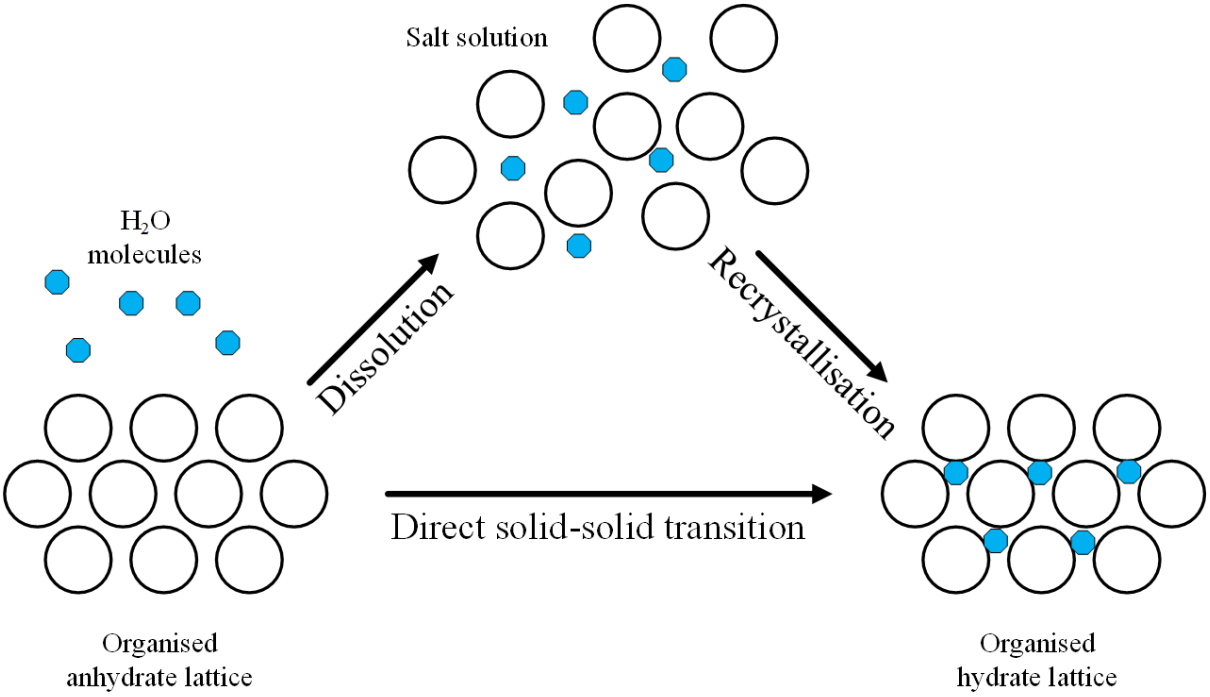

Figure 5 Inorganic salt hydration can take place either via direct solid-solid transition or via a two-step process where the salt dissolves into salt solution before recrystallisation into a new organised hydrated crystal configuration. The two step process was first presented in [25]**.**

2.2 Most promising inorganic salt hydration reactions

Salts are neutral ionic compounds formed by the chemical association of a cation and an anion. Inorganic salts are a specific type of salt that do not contain any carbon-hydrogen bonds. Typical cations forming inorganic salts are, but not exclusively, ionic alkaline earth metals (magnesium, calcium, and strontium in particular) and certain alkali metals (potassium, lithium, and sodium in particular). Typical anions associating with the above cations are the ions of halogens (chloride and bromine in particular) and certain more complex ions such as sulphates (SO_4^{2-}), carbonates (CO_3^{2-}), and others.

Many of the possible cation/anion combinations result in stable inorganic salt compounds. A 2014 review by N'Tsoukpoe et al. screened 125 different salts and attempted to identify the best candidates for TCS through a series of discriminatory filters based on energy storage density, upper temperature limit of the charging step, material safety and price [26]. They concluded that the hydration of $LaCl_3$ and $SrBr_2$ were the most promising reactions. In a later 2017 study, Donkers et al. compiled a database of potential inorganic salts and their sorption reactions, which resulted in 262 different salts being screened along with 563 different hydration/dehydration reactions [19]. In addition to the criteria

from N'Tsoukpoe's review, salt discrimination was refined with the addition of volume variation of the salt, temperature level of the heat release, salt melting point, deliquescence, cyclability and reaction kinetics.

Table 1 shows the most promising and most investigated salt/water reactions for TCS (at the time of this thesis), along with the physical and thermochemical properties of the salts in both hydrated and dehydrated states. The hydration/dehydration reactions of $CaCl_2$, K_2CO_3, $MgCl_2$, $MgSO_4$ and $SrBr_2$ should be specifically highlighted in the context of this review. These reactions all have energy storage densities above 300 kWh/m^3, are non-toxic materials, and their hydration/dehydration reactions occur in the relevant temperature range for domestic heating systems, and 4 out of 5 are inexpensive.

- **Calcium chloride $CaCl_2$** was one of the earliest studied salts in the context of TCS, and the first salt dispersed into a matrix for this application, by Aristov [27]. $CaCl_2$ is characterised by a 520 kWh/m^3 energy storage density, low cost, but poor stability as deliquescence often occurs during hydration due to a low hydration equilibrium vapour pressure. Furthermore, as a chloride, the upper limit of temperature for dehydration is around 140°C to 160°C, where gaseous thermal decomposition can occur.
- **Potassium carbonate K_2CO_3** was first singled out for TCS by Donkers et al. [19]. Studies have demonstrated its stability and cyclability which could offset its relatively low energy storage density (~360 kWh/m^3) [28]. A common issue with reversible reactions is that reactants degrade with repeated reaction cycles; however in the case K_2CO_3 evidence has been presented that reaction performance may improve with multiple cycles due to induced cracking of salt particles with hydration/dehydration cycles which favours the transport of water molecules [29].
- As a chloride, **magnesium chloride $MgCl_2$** thermally decomposes around 150°C, and has a very low equilibrium vapour pressure which leads to deliquescence. $MgCl_2$ is known to hydrate quickly even in not particularly humid indoor ambient conditions. The low vapour pressure equilibrium yields the advantage of generating a high temperature lift during hydration; thus $MgCl_2$ should be considered when temperature lift / power output during heat discharge is an important criterion. Furthermore, $MgCl_2$ is relatively inexpensive and highly available [16].
- **Magnesium sulphate $MgSO_4$** shows the highest theoretical energy density (620 kWh/m^3) and lowest cost among all five reactions. The high energy storage density is tied to its water adsorption up to the heptahydrate. $MgSO_4$ is characterised by a large number of intermediary reaction steps which complicates the prediction of the adsorption level for given hydration/dehydration conditions. Furthermore, the desorption of the final water molecule (from $MgSO_4.H_2O$ to $MgSO_4$) occurs at temperatures above 200°C, beyond achievable dehydration temperatures in the context of low-temperature TCS. The main issues with $MgSO_4$ are slow hydration kinetics, even at small scales, which prevent its utilisation for TCS due to low delivered power [30,31].
- **Strontium bromide $SrBr_2$** shows all of the desirable thermochemical properties for an inorganic salt, in particular in terms of kinetics, energy storage densities and temperature level. However, strontium is classified as a critical raw material by the EU commission, as it

is in high demand for the production of fuel cells, drones and robotics [32]. This supply fragility is reflected in the very high cost of $SrBr_2$ compared to the other salts, which likely prevents a TCS system based on this salt to be economically viable.

Table 1 Thermochemical and physical properties of some relevant inorganic salt/water reactions for TCS applications. Unless specified, value retrieved from NBS Table of thermodynamic properties [44].

Reaction		Lower hydrate		Higher hydrate		Reaction			
Parameter	n	ɟ	Cp	ɟ	Cp	ɷH	ɷS	E_d	Cost
Units		[kg/m^3]	[J/kg/K]	[kg/m^3]	[J/kg/K]	[J/mol]	[J/mol/K]	[kWh/m^3]	[ú /]k
$SrBr_2.H_2O + 5H_2O = SrBr_2.6H_2O$	5	2396	455	2386 [33]	966	58162	144	542	26.03
$MgSO_4.H_2O + 6H_2O = MgSO_4.7H_2O$	6	2570 [34]	802 [34]	1680 [34]	1047	55950	148	636	0.16
$CaCl_2.2H_2O + 4H_2O = CaCl_2.6H_2O$	4	1850	1170	1710	1340	59432	155	516	0.21
$MgCl_2.2H_2O + 4H_2O = MgCl_2.6H_2O$	4	1860 [19]	1213	1569	1444	63007	142	541	0.41
$K_2CO_3 + 1.5H_2O = K_2CO_3.1.5H_2O$	1.5	2430	828	2430	828	63635	157	390	0.34

2.3 Salt-in-matrix composites

While inorganic salt hydrates show theoretical potential as suitable materials for TCS, their hydration and dehydration generally face a number of practical problems. As discussed in **Section 2.1**, during the course of hydration (respectively dehydration), the crystalline structure of the inorganic salt rearranges itself in order to accommodate (respectively release) the mobile water molecules. Shrinkage, expansion, and other mechanical-type stresses follow this crystalline lattice rearrangement. These phenomena can lead to irreversible damage to the salt, hindering over time the material's water uptake ability and therefore energy storage capacity [35]. In the case of hydration, if excessive humidity is used in relation to the salt's equilibrium conditions, full dissolution of the salt into a liquid phase may occur, known as deliquescence. Deliquescence also impacts energy storage capacity, hydration/dehydration cyclability and reaction rates.

It has been found that integrating inorganic salts into a so-called host matrix can be a viable solution to stability issues [36–38]. A common method for formulating such composite materials is impregnation, where the matrix is first dried to remove all adsorbed water, before being immersed into a solution of the chosen inorganic salt in order for salt molecules to infiltrate its pore network. Final filtration and drying steps remove the liquid water from the matrix and precipitate the salt into the matrix pores and onto its surface. Two distinct variants for this method exist: dry and wet impregnation. Dry impregnation is carried out when the volume of salt solution is equal to the pore volume of the matrix, whereas during wet impregnation the volume of salt solution exceeds the pore volume of the matrix [39]. Properties of the final material depend mainly on the pore volume density of the selected matrix, the average pore diameter in the matrix, the solubility of the inorganic salt and the concentration of the salt solution. The process of wet impregnation has been carried out in the work and presented in this thesis, and will later be discussed in **Chapter III**.

Several different materials have been identified as suitable hosts for salt hydrates. Physical sorbents such as zeolite or silica gel beads [40,41] may be used as hosts. These matrices have their own water sorption capacity and contribute to the final material's overall energy storage density. Other host matrices are inert, such as vermiculite or expanded graphite, and do not take part in the sorption reaction; their higher stability and other benefits come at the cost of a lower energy storage density. The working principle of the reversible sorption process in salt-in-matrix composites is shown in **Figure 6**.

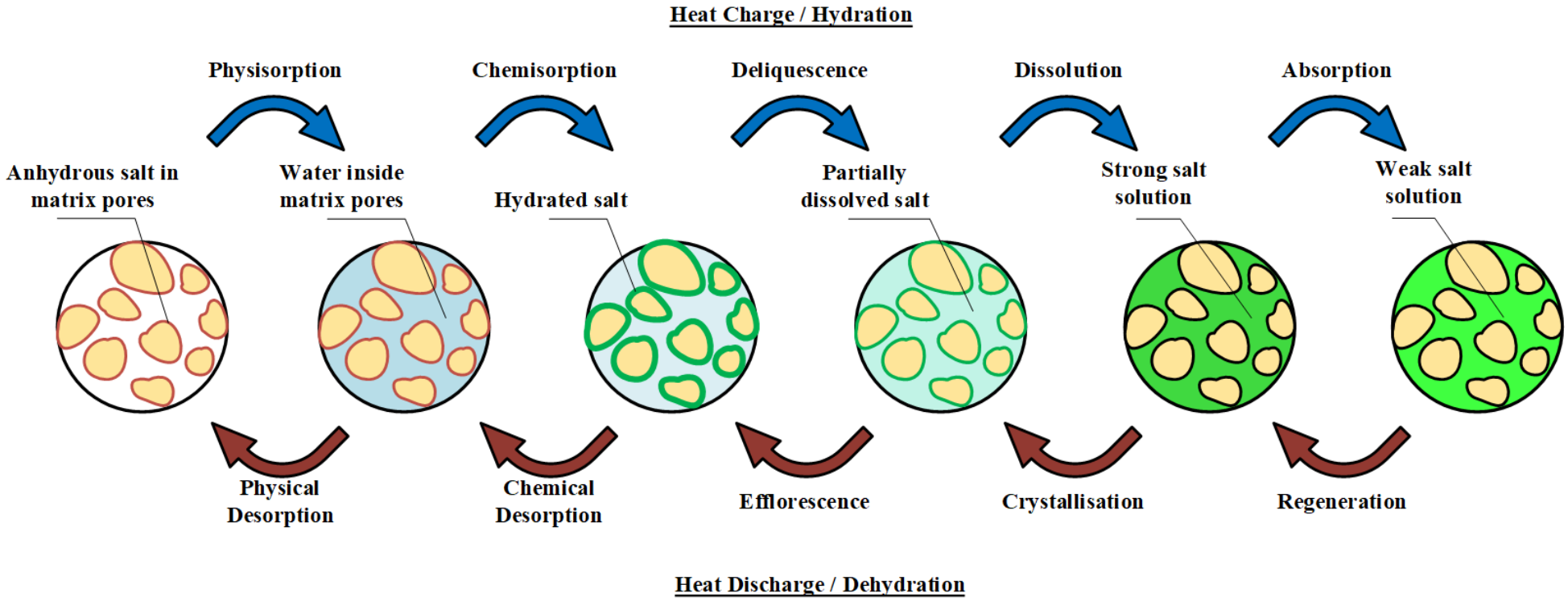

Figure 6 Multistep reversible sorption process in salt-in-matrix composites. The multistep sorption process was first outlined for composites in [29].

Inert matrixes

Inert matrixes refer to matrixes which do not directly contribute to the energy storage capacity of the complete composite. Ideal candidates should be highly porous, in order to house the maximum amount of active TCM, cheap, thermally conductive and with low volumetric density. Successful integration of salt into a host matrix is generally characterised by reduced adsorption capacity loss after multiple sorption cycles, increased reaction speeds even when accounting for reduced amounts of active material, improved thermal conductivity, and prevention of deliquescence. **Vermiculite** is an attractive option due to very low cost and high porosity (pore volume of approximately 3 cm^3/g) which allows for the formulation of high salt content composites whilst benefiting from the mechanical properties of the host matrix [42,43]. Depending on the impregnated salt, salt mass contents in the range of 50 wt.% - 70 wt.% are generally achieved for salt/vermiculite SIMs. The success of the salt impregnation process is typically verified through measurement of the reduction of pore volume before and after salt inclusion (**Table 2**).

Table 2 Physical properties of vermiculite-based composites

Salt	Salt Content	Vermiculite pore volume	SIM pore volume	Max. Adsorption Capacity	Energy Storage Density	Ref.
	%	cm^3/g	cm^3/g	g/g	kWh/m^3	
$MgCl_2$	6.54	-	-	0.12	-	[44]
	23.08	-	-	0.225	-	
	27.18	-	-	0.225	-	
	38.14	-	-	0.3	-	
	49.24	-	-	0.41	-	
LiCl	52.00	2.6	1.2	-	-	[45]
LiCl	59.00	2.7	0.8	-	-	[43]
LiCl	11.89	4.76	2.3179	0.5	40.46	[46]
	23.74		2.2099	0.99	104.51	
	34.30		1.9646	1.41	171.61	
K_2CO_3	69.00	3.02	0.9	0.8	~ 200	[47]
$SrBr_2$	30.19	4.76	-	0.32	38.38	[48]
	48.61		-	0.45	68.29	
	58.94		-	0.51	86.83	
	63.02		-	0.53	105.36	
$CaCl_2$	57.30	1.8	1.55	-	-	[49]

The dispersion of salt into vermiculite improves the heat and mass transfer during hydration and dehydration reactions compared to the pure salt. Successive hydration/dehydration cycles of vermiculite-based SIMs without reduction of the material's water adsorption capacity have been demonstrated, such as for a LiCl/vermiculite composite which showed no change to its water sorption capacity after 14 cycles [45], whereas the stability of a K_2CO_3/vermiculite composite was maintained over 74 cycles [47]. In more recent studies, the hydration process of salt in vermiculite has been

shown to take place in three steps: physical sorption of the water into the vermiculite, chemical sorption of the water into the salt crystals (the main reaction step for heat release), and a gas-liquid phase adsorption as a salt solution forms in the material (this latter step is a part of deliquescence). Gas-liquid absorption occurs due to capillary forces retaining liquid water and a resulting salt solution within the vermiculite pores. Gas-liquid absorption could boost energy storage capacity by approximately 190 - 250 kWh/m^3 in the case of K_2CO_3/vermiculite [47]. While several authors have discussed the liquid retention in vermiculite pores at the material scale, this effect has yet to be leveraged in a TCS device.

Expanded graphite (EG) is known for its high thermal conductivity and is a strong candidate when high thermal transfer is needed: typically salt hydrates have low thermal conductivities, such as $SrBr_2$ with λ_{SrBr2} = 0.38 W/m/K at 50°C, whereas a 40 wt.-% $SrBr_2$ / expanded graphite SIM was found to have a thermal conductivity 5 times higher of 2.3 W/m/K [50]. Salts impregnated into EG also demonstrate improved cyclability: NH_4T-Zn dispersed into EG showed a 7.6% energy storage density loss after 20 hydration/dehydration cycles, an improvement to the 24.5% energy storage density loss of the pure salt after 20 cycles [51]. Other inert matrixes for SIM fabrication are shown in **Table 3**. Other types of matrices include polymers, either as capsules [52] or as a matrix [53], foams [54] and a multitude of other types which are actively being suggested by the TCS community.

Table 3 Physical properties of other inert matrix-based composites.

Salt	Salt Content	Matrix	Matrix pore volume	SIM pore volume	Energy Storage Capacity	Energy Storage Density	Cyclability	Ref
	%		cm^3/g	cm^3/g	kJ/kg	kWh/m^3	%/cycles	
$MgSO_4$	30	Diatomite	0.048	0.025	475		7% / 20 cycles	[55]
	60			0.012	672.8		9% / 20 cycles	
LiCl		Anodic Aluminium Oxide			242.2			[56]
$LiNO_3$					251.6			
$MgCl_2$					231.6			
$CaCl_2$					220.8			
$MgSO_4$		Zirconia Ceramic				177	0% / 10 cycles	[57]
						417	0% / 10 cycles	
$MgSO_4$		Graphene			1194.3		9.65% / 60 cycles	[58]
$MgCl_2$					890.1		14.26% / 60 cycles	
$MgSO_4$ + $MgCl_2$					1065.9		9.16% / 60 cycles	

Reactive matrixes

The main drawback to integrating salts into host matrices is the reduction in energy storage density of the final material compared to a pure adsorbent due to the inert volume. A potential workaround is the use of reactive matrixes, i.e., materials with their own water sorption capacity and that could also serve as a host for inorganic salt deposition due to their pore structure. Reactive matrixes are not the main topic of interest in this thesis, however a brief overview of reactive matrix / salt SIMs in the TCS literature is given here. Zeolites, silica gels and metal-organic frameworks (MOFs) are the three most often considered candidates for this class of host matrix.

Table 4 Pore volume of adsorptive host matrixes compared to vermiculite.

Matrix	Pore Volume cm^3/g	Adsorption capacity	Ref
Vermiculite	2.5 - 4	Inert	[43,45,47]
Activated Alumina	0.4	Adsorptive	[59]
Zeolite	0.3 - 0.4	Adsorptive	[60]
Silica Gel	0.8 - 1.1	Adsorptive	[61–63]
MOF	0.5 - 2	Adsorptive	[64,65]
Siliceous shale	0.309	Adsorptive	[66]

While salt-in-matrix composites using inert supports are often described as an improvement to the inorganic salt, composites using reactive matrixes can be considered as an upgrade to the physical sorbent rather than the salt. This is mainly due to the pore volumes of inert matrixes being generally higher than the pore volume of reactive host matrixes (**Table 4**): the salt content of SIMs based on reactive matrixes generally reaches a maximum of 20 wt.-% and as a result reactive SIMs typically exhibit sorption behaviour that is closer to the physical sorbent than to the inorganic salt.

Zeolites are naturally occurring or artificially synthesised porous aluminosilicates. The pore network of zeolites, consisting primarily of micropores (diameter below 2nm), may accommodate and release water molecules through the mechanism of physisorption. When regenerated at 180°C / hydrated at 20°C and 10 mbar, zeolites alone demonstrate energy storage densities in the range 150 -160 kWh/m^3 [67]. Their adsorptive property and pore network has led to their investigation as host matrixes for inorganic salts. The low pore volume of zeolite, in the range 0.2 – 0.4 cm^3/g only allows for SIMs with a maximum of 20 wt.-% salt content. A summary of zeolite/salt composites in the TCS scientific literature is shown in **Table 5**. A potential drawback is that dispersing salt can be found to reduce zeolite's water sorption capacity. Impregnation into zeolites has been reported as damaging the pore structure of the matrix by reduction of the mesopores, leading to reduction in mass transfer and total water sorption capacity during hydration/dehydration compared to the pure zeolite [68–70]. In some cases this effect has led to pure zeolite to still be a more effective adsorbent (1.5 to 3 times higher water sorption capacity) than the salt dispersed composite [71].

Table 5 Physical properties of zeolite-based composites.

Salt	Salt Content	Zeolite Type	Zeolite pore volume	SIM pore volume	Energy Storage Capacity	Energy Storage Density	Cyclability	Ref
	wt%		cm^3/g	cm^3/g	kJ/kg	kWh/m^3		
$MgSO_4$	10 15 20	13X	0.374	 0.2		166		[60]
$CaCl_2$		13X						[72]
$CaCl_2$		13X		0.153	168	31.33		[69]
$CaCl_2$	17		0.3	0.18				[71]
$MgCl_2$	17.2	Na-X	0.2	0.08				[73]
$MgSO_4$	18.8	Na-X		0.16				
$MgCl_2$	15.3	Mordenite	0.17	0.01				
$MgSO_4$	14.9	Mordenite		0.15				
$MgCl_2$	13	Faujasite	0.32	0.27				
$MgSO_4$	15.6	Faujasite		0.24				
$MgSO_4$	5	13X		0.21				[74]
	10			0.16	1817		12.9% / 100 cycles	
$ZnSO_4$	5			0.28				
	10			0.23	1586		16.6% / 100 cycles	
$MgSO_4$	5	4A		0.08				
	10			0.02				
$ZnSO_4$	5			0.11				
	10			0.04				
$CaCl_2$ $MgCl_2$ $MgSO_4$		X	0.19					[75]
$MgCl_2$	7.1	13X	0.3	0.26				[76]
	10.1			0.24				
	15.1			0.22				
	19.2			0.21				
	24.5			0.18	1368	308		
$MgSO_4$	3.22	13X	0.28	0.27	500 - 550			[77]
	6.01			0.21	515 - 610			
	8.05			0.22	530 - 630			
	10.84			0.19	550 - 640			

Some authors hypothesised that the constrained space in which the salt is deposited does not allow for the salt to crystalise into its hydrated form which is generally accompanied by an expansion of the crystal lattice [78], and also found that the reduction sorption capacity is proportional to the amount of dispersed salt, but only for humidities below the deliquescence humidity of the impregnated salt. This behaviour is attributed to the deliquescence of the salt leading to a formation

a salt solution which may access the otherwise unused secondary pore volume of the zeolite (Donnan equilibrium). The salt is still found to contribute to the overall water sorption capacity of the composite. Thus, on the one hand, impregnation of salt limits the water sorption capacity of the composite due to pore blockage, but on the other the salt plays a role in the overall water uptake of the composite material and contributes to improve the power output during hydration [73,79]. There is therefore a balance to be found when combining zeolites with inorganic salts in order to produce a high performance TCS material.

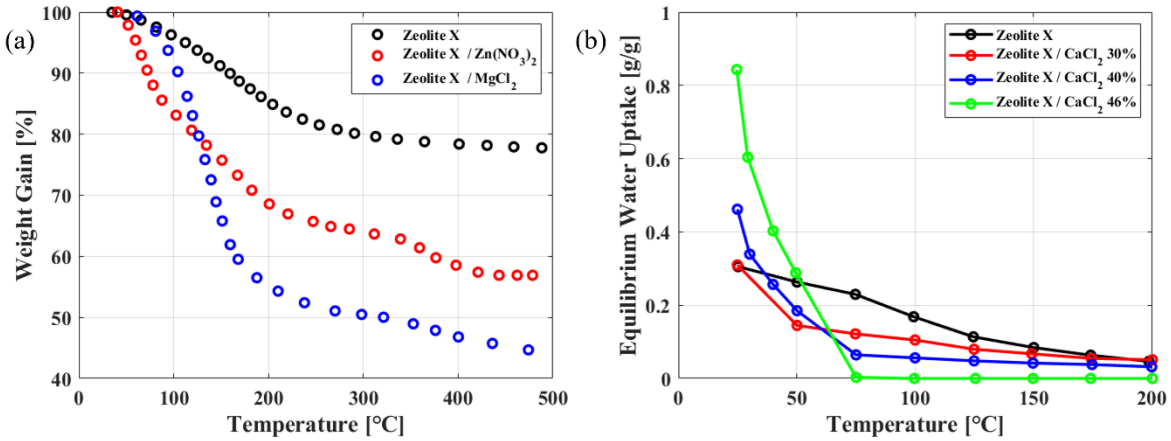

Figure 7 (a) TG-DSC measurements at an unspecified partial pressure of zeolite X, zeolite impregnated with $Zn(NO_3)_2$, zeolite impregnated with $MgCl_2$, data extracted and adapted from [80]**, (b) Zeolite 13X and Zeolite 13X / $CaCl_2$ composite sorption isobars at partial pressure 870 Pa adapted from** [72]**.**

The desorption behaviour of a typical zeolite both in pure form and with dispersed salts is shown in **Figure 7**. Dehydration mass loss peaks at a temperature of approximately 180°C for pure zeolite-X, whereas the zinc-nitrate impregnated zeolite-X material exhibits a peak dehydration temperature of approximately 120°C, and the zeolite-X / $MgCl_2 \cdot 6H_2O$ material a major dehydration peak at 80°C and a smaller dehydration peak at 170°C. These results highlight the structural interactions that occur when impregnating an inorganic salt into a zeolite. Rather than separated peaks at the respective dehydration temperatures of the salt and zeolite, the dehydration of the salt-in-(reactive) matrix material occurs at a new temperature level, below the regeneration temperature of the zeolite. Multiple dehydration peaks also occur in the case of salt-impregnated material, which is likely due to the multistep nature of the inorganic salt dehydration/hydration ($MgCl_2 \cdot 6H_2O$ first dehydrates to $MgCl_2 \cdot 4H_2O$, then followed by $MgCl_2 \cdot 2H_2O$, rather than a direct transition from hexahydrate to dihydrate). Thus, pure zeolite's dehydration temperature can be significantly lowered by salt impregnation to levels that are a potentially achievable for the heat sources envisioned for TCS (solar heat, industrial waste heat). Integration of inorganic salt to a reactive matrix has also been shown to provide improved cycling stability over multiple hydration/dehydration runs compared to the equivalent pure salts. Rehman et al. showed that after 100 cycles, the hydration enthalpy of $ZnSO_4$/zeolite and $MgSO_4$/zeolite composites decreased by 16.6% and 12.9% respectively, whereas for the same pure salts the enthalpy decreased by 41.0% and 45.4% respectively [74]. Silvester et al.

demonstrated near negligible enthalpy change over 5 cycles for a $CaCl_2$/silica gel composite [81], despite the well-known stability issues of pure $CaCl_2$.

2.4 Conclusions

The most suitable inorganic salts, their sorption reactions, and composites derived from these salts have been discussed in **Section 2**. Other than their equilibrium conditions and thermochemical properties, sorption reactions are also characterised by their unique kinetic behaviour. In the context of TCS, the power output during charge and power input during discharge depend respectively on the kinetics of hydration and dehydration. Thus in order to evaluate with precision the performance of different reactions for TCS applications, an in-depth understanding of their kinetics and how they differentiate from one-another is required. The following section reviews the current understanding of inorganic salt and SIM hydration/dehydration kinetics.

3 Solid-gas reaction kinetics

3.1 Solid-state kinetics framework

Solid-state kinetics deal with the parameterisation and measurement of reaction rates in gas-solid reactions, with particular focus on processes which are stimulated through a change in temperature [82]. Through the process of solid-state kinetics analysis, model equations are developed to predict the reaction behaviour of specific materials while accounting for realistic physical behaviour observed through experimentation. Furthermore, these models derived from milligram scale experiments can then be used in simulations for large, kilogram to ton scale TCS systems. Thus, reaction kinetics are an excellent means through which to tie material scale knowledge obtained through experimentation to the numerical analysis of TCS at the reactor and system scales. The reaction rate of a solid-state reaction process such as the hydration or dehydration of inorganic salts is generally expressed as a function of reaction advancement α, temperature T, and partial pressure p.

$$\frac{d\alpha}{dt} = k(T)f(\alpha)h(p) \tag{7}$$

The dependence on temperature of the reaction rate is expressed through the rate constant k, which is calculated by an Arrhenius expression:

$$k(T) = A_f \exp\left(\frac{-E_a}{RT}\right) \tag{8}$$

Where E_a is the activation energy, and A_f the frequency factor. This relationship leads to the differential form of the expression of the reaction rate:

$$\frac{d\alpha}{dt} = A_f \exp\left(\frac{-E_a}{RT}\right) f(\alpha) \quad (9)$$

The dependence of the reaction rate on the extent of conversion is expressed through the kinetic model $f(\alpha)$. A chemical process can be considered as a series of physical-chemical mechanisms that occur either successively or in parallel. The overall rate of the reaction therefore depends on the rate of the slowest of these mechanisms, called the rate-limiting process. The choice of kinetic model $f(\alpha)$ aims to reflect the physical phenomena underlying a particular rate-limiting process.

3.2 Inorganic salt sorption kinetics

In the following section, the current knowledge surrounding some of the most promising salts for TCS, along with the solid-state kinetic modelling of their hydration/dehydration reactions will be reviewed. The hydration and dehydration of inorganic salts are heterogeneous reactions taking place at the solid-gas phase interface. These reactions are characterised by two main steps: diffusion and reaction. These two reaction steps occur in series typically at the interface between a gas and a solid phase, as opposed to homogenous diffusion and reaction which take place simultaneously, in the entire volume and in the same phase. The presence of at minimum two chemical processes occurring during the hydration/dehydration reactions leads to the question: which of these dominates the chemical reaction? Identifying the rate-limiting process of the entire reaction opens the possibility of improving the efficiency of these reactions, which is intrinsically linked to the power input (for dehydration) and output (for hydration) of TCS.

It is broadly accepted that inorganic salt hydration/dehydration are well characterised by a function of the equilibrium drop (first-order reaction models), which is a particularly well-suited model for humid air conditions, typical of the hydration step in open sorption heat storage reactors [83]. However further refinement is required to progress the understanding of these adsorption reactions. Indeed order-based models do not imply any particular rate-controlling mechanism. They simply indicate that the reaction rate is proportional to the remaining unreacted fraction of the sample raised to a power. The identification of the rate-limiting processes of a gas-solid reaction can be carried out through solid-state kinetic analysis.

In **Table 6** can be found a summary of the kinetic studies present in the literature on the chemical reaction of water sorption onto inorganic salt. This table includes adsorption, desorption, and is only concerned with pure inorganic salts. The kinetic models ‘R2’, A2’ etc... refer to standard solid-state kinetic models [84]. These models result from the mathematical implication of some limiting mechanistic assumption that controls the overall rate of the reaction, such as nucleation (‘A’ models), diffusion (‘D’ models), geometrical contraction (‘R’ models) or order-based models (‘F’ models), with the number implying some variation on the actual mathematical derivation. A more detailed description of these models is provided later in this thesis in Chapter III. As can be seen from the table, desorption has been addressed in more detail than adsorption. This is likely due to water sorption being bivariant with regards to both temperature and humidity, as opposed to desorption

being monovariant with temperature. For these reasons, researchers tend to prefer carrying out solid-state kinetic studies on water desorption, while staying away from hydration when using the solid-state reaction framework. However, chemical reactions of solids with gases, that are bivariant by definition, can be studied within the framework of solid-state kinetics, as discussed by Vyazovkin et al. [82]. Upon further observation of **Table 6**, it can also be seen that studies are focused on a limited number of salts. The desorption of lithium sulphate $LiSO_4 \cdot H_2O$ has been the subject of a number of these studies. However, with a very low energy storage density of 250 kWh/m^3 [19] that is due to $LiSO_4$ being able to adsorb a single water molecule, lithium sulphate is not likely to be viable for TCS applications. The reaction kinetics of two salts, K_2CO_3 and $MgCl_2$, will now be reviewed in detail. These two salts are among the 5 inorganic salts which are (a) most promising for TCS applications due to their thermochemical properties and low cost, and as a result (b) are currently motivating research activity in the TCS community.

Table 6 Summary of kinetic studies conducted for pure inorganic salts. [a]n signifies the stoichiometric coefficient of the chemical reaction.

Dry Material (n)[a]	Reaction	Model	Method	Kinetic Parameters	Ref.
$MgSO_4.H_2O$ (6)	Desorption	[-]	Initial TG slopes	E = 20.92 kJ/mol (T>47.35°C)	[85]
$MgSO_4.H_2O$ (5)		[-]		E = 37.66 kJ/mol (T<47.35°C)	
$LiSO_4$ (1)	Desorption	R2	[-]	E = 80.10 ± 3.4 kJ/mol, A = 6.90 ± 0.5 s^{-1}	[86]
		R3		E = 79.90 ± 3.4 kJ/mol, A = 6.80 ± 0.5 s^{-1}	
		A2		E = 80.20 ± 3.4 kJ/mol, A = 7.20 ± 0.5 s^{-1}	
		D4		E = 91.60 ± 1.8 kJ/mol, A = 9.20 ± 0.3 s^{-1}	
		R3		E = 93.00 ± 1.9 kJ/mol, A = 9.90 ± 0.3 s^{-1}	
		F1		E = 92.20 ± 1.8 kJ/mol, A = 10.40 ± 0.3 s^{-1}	
		R2		E = 65.60 ± 3.2 kJ/mol, A = 6.10 ± 0.5 s^{-1}	
		R3		E = 65.20 ± 3.2 kJ/mol, A = 6.00 ± 0.5 s^{-1}	
		A2		E = 65.80 ± 3.3 kJ/mol, A = 6.40 ± 0.5 s^{-1}	
$LiSO_4$ (1)	Desorption	[-]	[-]	E = 146.44 ± 12 kJ/mol, A = 42.6 min^{-1}	[87]
$LiSO_4$ (1)	Desorption	Nucleation Growth	Fitting + Arrhenius Plots	E = 88.4 kJ/mol, A = 1.9.107 s^{-1}	[88]
$LiSO_4$ (1)	Desorption	[-]	[-]	E = 87.1 ± 0.8 kJ/mol, A = 1.4.108 $kg/m^2/s$	[89]
$LiSO_4$ (1)	Desorption	[-]	Fitting + Arrhenius Plots	E = 50.6 kJ/mol	[90]
$LiSO_4$ (1)	Desorption	See paper	[-]	E = 87.1 ± 0.8 kJ/mol, A = 1.7.1014 s^{-1}	[91]
$LiSO_4$ (1)	Desorption	See paper	[-]		[92]
$CaCl_2$	Desorption	[-]	[-]	E = 48.1 kJ/mol	[93]
$CaCl_2$	Desorption	First order	[-]	E = 48.6 kJ/mol	[94]
$MgCl_2$ (6)	Desorption	Multiple models	[-]		[95]
$MgCl_2$ (6)	Desorption	Multiple models	Sharp	E = 103.74 kJ/mol, A=2.088·1013 s^{-1}	[16]
K_2CO_3 (1.5)	Desorption	R3	Fitting + Arrhenius Plots	E = 91 kJ/mol	[96]
K_2CO_3 (1.5)	Desorption	[-]	[-]	E=1.54.10-19 J, k = 6.65.108 m.K1/2/s	[97]
K_2CO_3 (1.5)	Adsorption	$d\alpha/dt = A.\exp(E/RT).(1-\alpha)^{2/3}.(p_{eq}/p_v)$	Fitting + Arrhenius Plots	E = 46.22 kJ/mol, A=1.08.106 min^{-1}	[98]
	Desorption	$d\alpha/dt = A.\exp(E/RT).(1-\alpha)^{2/3}.(p_{eq}/p_v)$	Kissinger	E = 78.31 kJ/mol, A=8.90.1010 min^{-1}	

Table 7 Summary of kinetic studies carried out for salt-in-matrix composite materials. [a]WSS signifies 'Wakkanai Siliceous Shale'.

Materials	Hydration / Dehydration	Model	Method	Kinetic Parameters	Ref.
$CaCl_2$ (33.7%) + Silica Gel	Adsorption	Fink's Diffusion Model	[-]	De = (0.24±0.12)*10^{-6} m^2/s	[99]
LiCl (30%) + Attapulgite	Desorption	[-]	Kissinger	Ea = 51.29 kJ/mol	[100]
$CaCl_2$ (15%) + Silica Gel	Desorption	[-]	Kissinger / Ozawa	E = 64±1 kJ/mol	[101]
	Adsorption	Diffusion Model	[-]	k = 9.26.10^{-5} s^{-1}	
$CaCl_2$ (15%) + Alumina	Desorption	[-]	Kissinger / Ozawa	E = 67.5±1.5 kJ/mol	[101]
	Adsorption	Diffusion Model	x	k = 9.60.10^{-5} s^{-1}	
$CaCl_2$ (15%) + Bentonite	Desorption	[-]	Kissinger / Ozawa	E = 66.5±1.5 kJ/mol	[101]
	Adsorption	Diffusion Model	[-]	k = 1.07.10^{-4} s^{-1}	
$CaCl_2$ + Zeolite Ca-X	Adsorption	LDF	[-]	[-]	[102]
$CaCl_2$ (33.7%) + Silica Gel	Desorption	[-]	[-]	E = 23.4 kJ/mol	[93]
LiCl (9.6%) + WSS[a]	Desorption	[-]	Kissinger	E = 87.7 kJ/mol	[66]
LiCl (22.4%) + WSS	Desorption	[-]	Kissinger	E = 124.7 kJ/mol	
$CaCl_2$ + Silica Gel	Desorption	1st order	[-]	E = 23.5 kJ/mol	[94]

The kinetics of potassium carbonate's reaction with water (hydration and dehydration) have so far been investigated in some early work by Stanish and Perlmutter [96,97], and more recently by Gaeini et al [98]. In Gaeini's study, the kinetics of potassium carbonate hydration and dehydration were evaluated using a Simultaneous Thermal Analysis (STA) apparatus by Netzsch, with samples of approximately 10mg. In these setups, the sample is held inside an aluminium crucible. Hydration was carried out for several temperatures between 26°C and 57°C at a constant vapour pressure of 13 mbar. The kinetic parameters were calculated by drawing the Arrhenius plot. Results indicated that the hydration behaviour is best modelled by a contracting sphere model. The final hydration model of K_2CO_3 is:

$$\frac{d\alpha}{dt} = 6.5\ 10^7 \exp\left(-\frac{46.22\ 10^6}{RT}\right)(1-\alpha)^{\frac{2}{3}}\left(\frac{P_v}{P_{eq}}\right) \qquad (10)$$

Dehydration kinetics were carried out for temperatures ranging from 85°C to 150°C, and for different heating rates. Kinetic parameters were calculated using Kissinger's method. The final dehydration model of K_2CO_3 is:

$$\frac{d\alpha}{dt} = 5.3\ 10^{12} \exp\left(-\frac{78.31\ 10^5}{RT}\right)(1-\alpha)^{\frac{2}{3}}\left(\frac{P_{eq}}{P_v}\right) \qquad (11)$$

In the case of $MgCl_2$, only the dehydration kinetics have been investigated so far. Huang et al. [95] carried out a solid-state kinetic study to identify the different steps and corresponding kinetic mechanisms of the thermal decomposition of $MgCl_2 \cdot 6H_2O$. The experiment was carried out on an integrated thermal analyser, with 10mg samples heated from ambient temperature to 600°C at a heating rate of γ=2 K/min. The kinetic analysis was carried out using Doyle's **equation (12)**, and Coats-Redfern's **equation (13)**. These methods are designed for the kinetic analysis of thermal decomposition reactions performed under constant or linearly varying heating rates γ. With Doyle's method [103], plotting $\ln\left[\int_0^\alpha \frac{d\alpha}{f(\alpha)}\right]$ vs 1/T yields a straight line which enables the calculation of activation energy Ea and frequency factor A. With Coats-Redfern's method [104], the same can be achieved by plotting $\ln\left[\left(\int_0^\alpha \frac{d\alpha}{f(\alpha)}\right)/T^2\right]$ vs 1/T. The authors use both methods as a basis for comparison.

$$\ln\left[\int_0^\alpha \frac{d\alpha}{f(\alpha)}\right] = \ln\left(\frac{AE_a}{\gamma R}\right) - 5.3305 - 1.052\frac{E_a}{RT} \qquad (12)$$

$$\ln\left[\left(\int_0^\alpha \frac{d\alpha}{f(\alpha)}\right)/T^2\right] = \ln\left(\frac{AR}{\gamma E_a}\left(1-\frac{2RT}{E}\right)\right) - \frac{E_a}{RT} \qquad (13)$$

They found that the decomposition takes place over 6 distinct steps. 4 molecules of water were lost during the two first steps of the reaction. Steps 3 and 4 consisted in the dehydration and hydrolysis of

the material. 0.3 molecules of water were removed during step 5. Finally, decomposition (production of HCl) took place during the 6th and final step. The authors proposed the following models for each individual step:

Step 1, the first dehydration step taking place from 27°C to 108°C and producing $MgCl_2 \cdot 4H_2O$, was best modelled by spherical shrinkage model R2, for which more details can be found in **Chapter III** or in the reference [84], (**equation (14)**), with the following kinetic parameters:

$$\frac{d\alpha_1}{dt} = \gamma * 1.8 * 10^9 \exp\left(\frac{-66.8 * 10^3}{RT}\right) * 2(1-\alpha_1)^{1/2} \qquad (14)$$

Step 2 the second dehydration step taking place from 108°C to 144°C and producing $MgCl_2 \cdot 2H_2O$, was best modelled by R3 (see **Chapter III** or [84]), with following kinetic parameters:

$$\frac{d\alpha_2}{dt} = \gamma * 4.4 * 10^{17} \exp\left(\frac{-138.0 * 10^3}{RT}\right) * 3(1-\alpha_2)^{\frac{2}{3}} \qquad (15)$$

Step 3, the final dehydration step and first decomposition step taking place from 144°C to 178°C and producing $MgCl_2 \cdot nH_2O$ ($1 \leq n \leq 2$) and MgOHCl was best modelled by nucleation model A3 (see **Chapter III** or [84]), with the following kinetic parameters:

$$\frac{d\alpha_3}{dt} = \gamma * 2.3 * 10^9 \exp\left(\frac{-77.2 * 10^3}{RT}\right) * 2(1-\alpha_3)[-\ln(1-\alpha_3)]^{2/3} \qquad (16)$$

The final three steps, studied by the authors, are outside the scope of this study since these reactions are not reversible and therefore cannot be used to store heat thermochemically.

Mamani et al. [16] also carried out the kinetic study of the dehydration of $MgCl_2$ and of Bischofite, an extraction process by-product with approximately 95% $MgCl_2$ content. The kinetics of the dehydration of this material were compared to that of the pure salt to demonstrate the potential of certain waste products to be used as TCMs. Dehydration was carried out at 70°C, 80°C, 90°C and 100°C in a coupled TG-DSC apparatus, with samples of mass 10 to 20 mg in 70µL platinum crucibles. Depending on the reaction temperature, $MgCl_2 \cdot 6H_2O$ was dehydrated to various states up to $MgCl_2 \cdot 3.66H_2O$. Kinetic models (see **Chapter III** or [84]) were fitted to the experimental data using the Sharp method. They found that the dehydration of $MgCl_2 \cdot 6H_2O$ was best modelled by:

- R2 at 70°C
- R2 and A2 at 80°C
- A2 at 90°C
- A3 at 100°C

For the first dehydration step of $MgCl_2 \cdot 6H_2O$, the authors found an activation energy of 74 kJ/mol and an Arrhenius frequency factor of 2.088 10^{13} s^{-1}.

3.3 Composite sorption kinetics

In **Table 7** a summary can be found of the kinetic studies carried out for chemical reactions involving water sorption onto salt-in-matrix in composites. As can be seen, all kinetic studies on composites have been exclusively carried out on combinations of either $CaCl_2$ or LiCl with a matrix. $CaCl_2$ is the only salt to have kinetic studies carried out as both a pure material and as part of a composite. This shows the significant gap in the literature surrounding the effect of integrating a salt to a host matrix on the dynamic behaviour of the water (de)sorption reaction. Also, it can be seen that solid-state kinetic studies have only been carried out for desorption. The adsorption of water into SIMs is almost exclusively modelled with the linear driving force model or Fink's model for gas diffusion into spherical particles [105]. Finally, it can be seen that kinetics of hydration/dehydration of salt impregnated into specifically vermiculite have not been studied despite vermiculite being a popular matrix for SIM fabrication.

3.4 Conclusions

A summary of the current knowledge surrounding the kinetics of inorganic salt and SIM hydration and dehydration was presented in **Section 3**. The existing kinetic models for the most promising salts were discussed. Macro-scale simulations of thermochemical storage devices can make use of these kinetic models to inform specifically on the connection between performance and microscale physical phenomena [106]. In the following section current TCS reactor prototypes and how the kinetics of TCS reactions are modelled in macroscale simulations will be reviewed.

4 Kinetics at the reactor scale

4.1 TCS Reactor Designs

Low temperature TCS systems can be classified according to the following design choices [107]:

- Open or closed systems.
    - In open systems, heat and mass are in direct contact with the ambient and can only operate with water as the sorbate. Such systems do not use either an evaporator or condenser, and operate at atmospheric pressure, which limits overall system complexity and size. Since ambient air is used as both the carrier and source for the sorbate, overall transport rate of water to the sorbent may be limited, which can lead to the need for an additional humidifier to ensure sufficient humidity, which in turn guarantees a sufficient power output during hydration. Mass transport of the sorbate is generally the limiting factor to open systems performance [108].
    - In closed systems, only heat is in contact with the ambient, whereas the sorbate (mass) is contained within its own circuit and is provided to the system during heat discharge by an evaporator, and recovered during heat charge by a condenser. While systems not using water as the adsorbate are exclusively closed, water is often used in closed systems since using pure water vapour rather than humid air favours the reactor in

terms of mass transport. However, water vapour has a lower thermal conductivity than humid air, and in closed systems an additional circuit is needed to extract thermal energy during heat discharge. Consequently, differently from open systems, closed systems are generally limited by thermal transport.

- Fixed, transported and moving bed reactor systems.
    - In fixed systems, the entire mass of the sorbent is contained within the reactor.
    - In transported systems the sorbent is transported to the reactor from a storage to be hydrated/dehydrated, to then be extracted and stored until the reverse part of the cycle is conducted. This design has the advantage of keeping the reaction area small, which enables good control of the reaction mechanisms. However, space is needed for two storages (reacted and unreacted material), the reactive bed and the connections between all three.
    - In moving bed reactors (which are either screw, rotary or gravity-assisted bulk flow reactors [109]), thermal power output/input during discharge/charge respectively is kept constant through motion of the reactive bed [110], ensuring that the inlet air flow is consistently in contact with unreacted thermochemical material. A exemplary design is the vibrating moving bed reactor [111], which averages 356 W adsorptive heat power, with an electrical consumption of ~80 W.

A summary of the working principles of open and closed systems is shown in **Figure 8**.

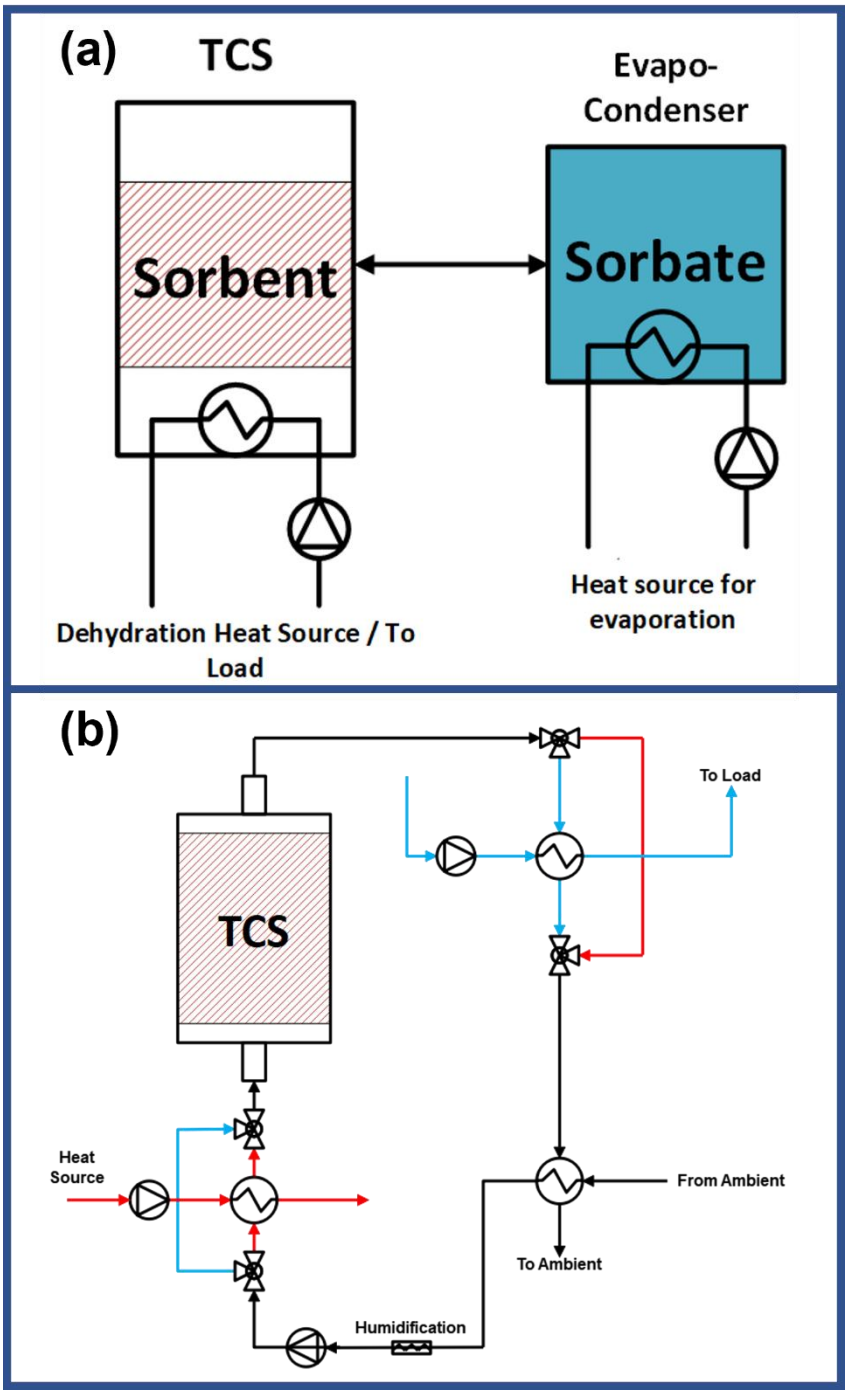

Figure 8 (a) Open and closed (b) operation modes of low-temperature TCS systems. Red lines are used during desorption, blue during sorption. Adapted from [112] **and** [113]**.**

4.2 TCS reactor prototypes

The work presented in this thesis is targeted towards *open fixed* TCS systems. Such reactive systems are generally designed as single packed bed reactors or arranged modularly in order to not have to

handle the entire mass of material during heat storage [112]. **Table 8** summarises the findings of the literature review surrounding current open TCS prototypes using inorganic salts or SIMs, with both inert and reactive matrices featured. Pure inorganic salts are rarely used in TCS prototypes due to stability issues: two prototypes in the table use pure inorganic salts. Zondag et al. reported severe blockage during the hydration of ~30 kg of $MgCl_2$ [114], and Farcot et al. [115] carried out the hydration of $SrBr_2$ in a moving bed reactor. This type of reactor ensures that the material does not agglomerate through constant motion of the reactant, at the expense of electrical power which hinders the final energy efficiency. Thus, at the prototype scale, composites are favoured over pure inorganic salts.

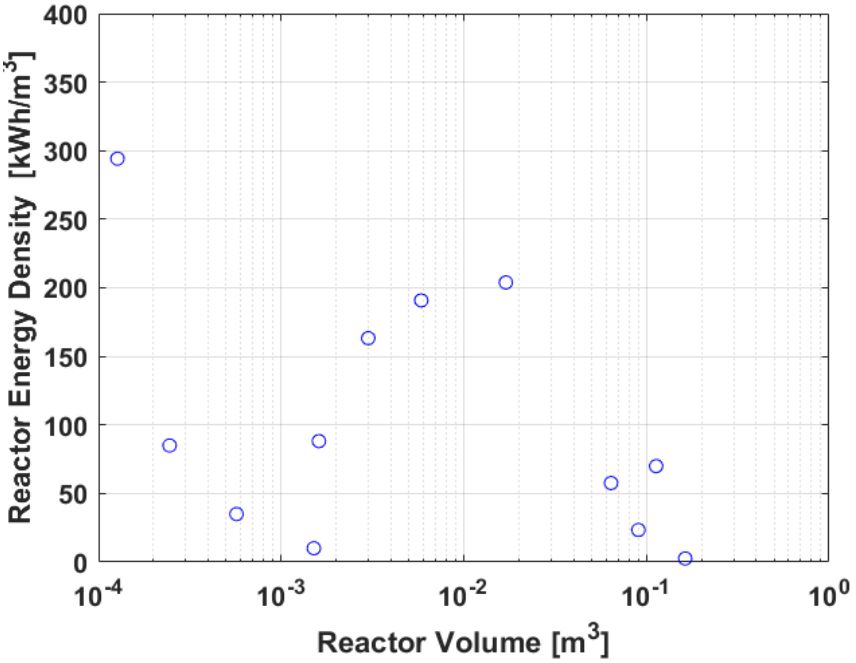

Figure 9 Reactor-scale energy storage density as a function of reactor volume in open low-temperature TCS prototypes.

Currently, one of the main issues with upscaling TCS from material to reactor and eventually process and system scales is the drop in reported energy storage density. **Figure 9** shows that the select few reactor prototypes with reactive volumes above 0.1 m^3 display energy storage densities below 100 kWh/m^3. However, the energy storage densities of the TCMs measured at the material scale are often above 200 kWh/m^3 and can easily reach values above 500 kWh/m^3 as shown in **Figure 10** where energy storage densities reported at the material scale, i.e. measured using sample-scale experimental methods such as TG-DSC, are significantly higher than the energy storage reported at the reactor scale, which are generally measured by integrating the temperature difference between the outlet and inlet air during hydration/heat discharge.

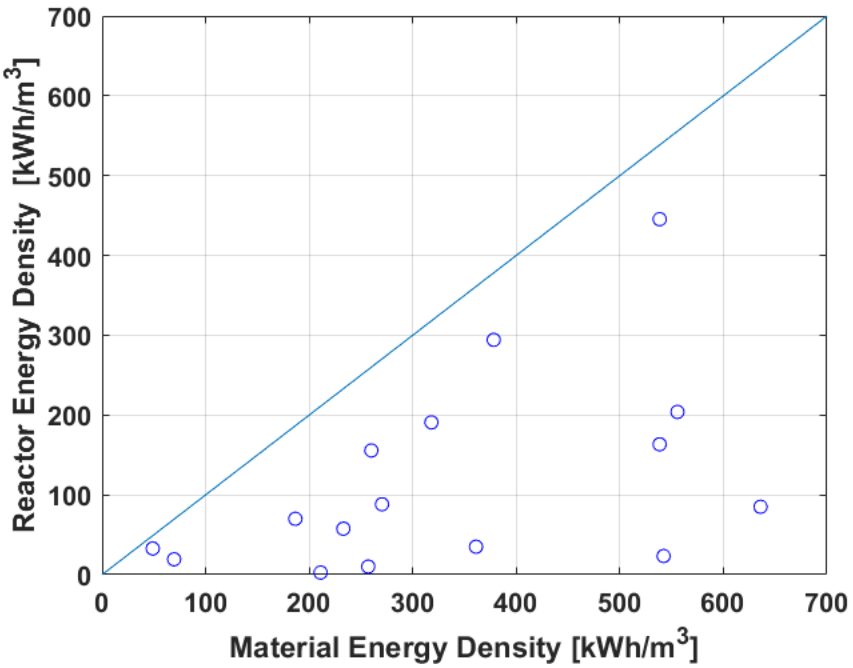

Figure 10 Reactor-scale energy storage density as a function of material-scale energy storage density in open low-temperature TCS prototypes.

In many cases, the volumetric energy storage density reported at prototype scale is less than half the material energy storage density of the TCM, which has been reported by some authors [116,117]. Various factors contribute to this discrepancy:

- Particle level energy storage density is often reported, whereas bulk level energy storage density will be lower due to material porosity.
- Unreacted zones in reactor prototypes reduce the effective energy storage density.
- Material scale energy density measurements generally include the sensible heat needed to increase the temperature of the reactants to the reaction equilibrium, whereas that sensible energy is lost during measurement of energy released during reactor discharge if time has expired between heat charge and release.
- Heat losses and power distribution.

The temperature level of the released heat is generally a source of inefficiency: heat released below the required temperature for the desired application (for example underfloor heating requires temperatures above 40°C). As was discussed previously, the power output of reactors is at least partially dependent on the reaction kinetics taking place within. Thus, having reviewed promising salts and SIMs hydration reactions, the current literature surrounding their reaction kinetics, and overviewed existing open TCS reactor prototypes, the final section of the literature review aims to summarise the current kinetic models used for reactor scale modelling of reactions for TCS.

Table 8 Summary of open TCS reactor prototypes, with key performance indicators, either provided or calculated with the available data. [a] SG stands for silica gel, [b] V stands for vermiculite.

Material Unit	Material Mass kg	Reactor Volume m^3	Maximum Power Density kW/m^3	Average Power Density kW/m^3	High Power Density kW/m^3	Medium Power Density kW/m^3	Low Power Density kW/m^3	Max φT °C	Material Energy Density kWh/m^3	Reactor Energy Density kWh/m^3	Ref -
Z13X + $MgSO_4$	0.40	1.51E-03	4.3	1.8	2.8	0.8	0.1	12.6	257.0	10.1	[118]
SG[a] + $CaCl_2$	2.00	1.63E-01	3.2	2.0	2.2	2.1	1.8	8.5	211.0	2.6	[111]
Matrix + $MgCl_2$	3.60	1.61E-03	4.6	3.8	3.2	4.2	3.7	18.1	270.3	88.2	[119]
V[b] + $CaCl_2$	6.00	1.13E-01	4.9	3.0	3.4	2.9	2.4	37.1	186.6	70.0	[120]
V + $CaCl_2$	0.13	1.27E-04	71.3	22.3	35.0	7.4	3.5	22.0	378.2	294.2	[121]
$MgCl_2$	31.62	1.70E-02	8.0	4.5	6.1	5.1	2.2	12.9	555.6	203.9	[114]
$SrBr_2$	0.22	9.03E-02	3.1	2.4	1.7	2.9	3.0	8.7	542.3	23.4	[115]
SG + $CaCl_2$	0.25	5.00E-04	142.0	77.5	98.0	66.4	39.6	16.0	538.4	445.4	[122]
LiCl + Activated Alumina	6.52	5.85E-03	49.9	19.2	28.5	10.3	3.4	19.3	318.0	190.8	[123]
SG + $CaCl_2$	2.20	3.00E-03	182.1	127.5	158.5	135.6	88.4	16.5	538.4	163.3	[110]
$MgSO_4$	0.62	2.45E-04	31.0	11.4	19.8	9.8	2.8	14.8	635.9	85.0	[124]
V + $CaCl_2$	0.13	5.70E-04	1.7	1.1	0.8	1.5	1.1	9.5	361.1	35.0	[125]
Z13X + $MgSO_4$ + LiCl	0.10	6.40E-02	46.0	16.7	28.0	21.1	0.1	47.6	233.0	57.6	[126]

4.3 TCS reactor-scale kinetics

Table 9 summarises the kinetic models used for reactor-scale simulations of salt based TCS. There are sufficiently few simulations for both open and closed systems to be included in this table, in which is clearly shown that the 1st order model is exclusively used. The table also shows that simulations are currently being carried out for reactors using pure inorganic salts as TCM, despite (a) pure salts not being suitable for direct use in TCS reactors, and (b) actual experimentation on TCS reactors is overwhelmingly being carried out using composite materials.

Table 9 Kinetic models used for simulations of low temperature salt based TCS. The original reference the authors used to justify their choice of kinetic model is shown in the Kin. Ref column.

Kin. Model	Parameters	Material	Type	Reaction	Dim.	Kin. Ref	Ref
1st Order	E_a = 5,000 J/mol A_f = 7.45 10^{-4} s^{-1}	Pure $MgCl_2$	Closed	Hydration	1D	-	[127]
1st Order	E_a = 55 kJ/mol A_f = 1.67 10^5 s^{-1}	Pure $MgSO_4$	Closed	Hydration	2D	[128]	[129]
1st Order	E_a = 55 kJ/mol A_f = 1.67 10^5 s^{-1} E_a = 20.849 kJ/mol A_f = 0.94 s^{-1} E_a = 82.84 kJ/mol A_f = 1.42 10^9 s^{-1}	Pure $MgSO_4$ Pure $CuSO_4$ Pure $CaSO_4$	Closed	Dehydration	2D	[128]	[130]
1st Order	E_a = 55 kJ/mol A_f = 1.67 10^5 s^{-1}	Pure $MgSO_4$	Closed	Dehydration	2D	[130]	[131]
1st Order	E_a = 55 kJ/mol A_f = 1.67 10^5 s^{-1}	Pure $MgSO_4$		Dehydration		[34]	[128]
1st Order	E/R = 10038 A_f = 1.9 10^{10} s^{-1} E/R = 11428 A_f = 2.2 10^{10} s^{-1}	Pure $MgCl_2$ 1st step Pure $MgCl_2$ 2nd step	Open	Dehydration	2D	[132]	[133]
1st Order	k = 5.5 10^{-6} s^{-1}	Pure $SrBr_2$	Open	Hydration	2D	[134]	[83]
1st Order	E_a = 55 kJ/mol A_f = 5.5 10^5 s^{-1}	Pure $MgCl_2$	Closed	Dehydration	2D	[135]	[136]
1st Order	k = 10^{-4} s^{-1}	Pure $SrBr_2$	Both	Both	2D	[137]	[108]
1st Order	E_a = 55 kJ/mol A_f = 1.63 10^5 s^{-1}	Pure $SrBr_2$	Closed	Both	3D		[138]
1st Order	k = 5.10^{-4} s^{-1}	Pure K_2CO_3	Open	Hydration	Quasi 2D	[139]	[140]
1st Order	k = 1.10^{-4} s^{-1}	Pure $SrBr_2$	Open	Both	2D	[108]	[141]

5 Conclusions

TCS generates high interest in the scientific literature. Some of the current knowledge and trends of this research have been presented and discussed in this chapter, with the overarching aim of answering Q1: What are typical materials used for low-temperature TCS? What kinetic models exist to capture their dynamic reaction behaviour at material and reactor scale? The literature review has also highlighted some of the current gaps in the TCS literature.

- Inorganic salts dispersed into host matrices are the most obvious candidates for low temperature TCS. Physical sorbents have either too low of an energy storage density or too high of a desorption temperature for low-temperature heat sources. Pure inorganic salts, while showing promising thermochemical properties for TCS, are limited in practice by instability issues which can be either a lack of cyclability, or a tendency to agglomerate and cause blockage in a packed bed reactor.

- At the material scale, the kinetics of pure inorganic salts have partially been addressed. Dehydration kinetics have generally been studied in more depth that hydration. However, the knowledge surrounding the impact of dispersing these salts into a matrix is limited. The influence of the matrix on kinetic behaviour requires further investigation. The kinetics of SIMs are further complicated by the number of possible salt/matrix combinations. These factors have motivated the work presented in **Chapter III**, which aims to evaluate the hydration kinetics of two of the inorganic salts highlighted in this chapter, the impact of dispersal into a host matrix on the kinetics, and the most accurate kinetic models for predicting the hydration behaviour.

- At reactor scale, order-based modelling is exclusively used for reaction kinetics. Current models tend to consider pure inorganic salts as the TCM, whereas research points towards SIMs being the preferred material at and beyond reactor scale. As a result, there is some uncertainty on how this systematic choice of kinetic model impacts the prediction of TCS reactor performance. The impact of kinetic model on reactor performance prediction motivates the work presented in **Chapter IV**.

Chapter III. Dynamic Study of Salt and SIM Hydration Kinetics

Chapter I *and* ***Chapter II*** *highlighted how the use of pure salt for low-temperature TCS is impractical due to severe mass transfer limitations, salt agglomeration and deliquescence. It is understood from an experimental point of view that integration within a host matrix partly addresses these issues. However, the extent to which the presence of a matrix affects the reaction is not fully quantified in terms of solid-state reaction kinetics. Thus, one of the research questions of this thesis (Q2) was formulated in order to assess the impact of salt impregnation on (a) kinetic behaviour during hydration and (b) on kinetic model selection. The work in this chapter is therefore oriented towards evaluating the effect of salt impregnation on hydration kinetics.*

The investigation was carried out with four materials: two inorganic salts ($MgCl_2$ and K_2CO_3), and two composites based on the dispersion of these salts into a vermiculite host matrix. The salt selection was informed by the literature review in ***Chapter II****, and the selection is further justified in this chapter. Composite material preparation is discussed in the light of the preparation methods reviewed in the previous chapter. The hydration of these materials is carried out in a dynamic vapour sorption (DVS) apparatus. Thermogravimetric data is analysed and discussed in view of identifying key rate-limiting processes. The chapter then addresses the solid-state kinetic analysis of the hydration reactions. A database of kinetic models, formulated from physical assumptions aligned with inorganic salt hydration, is assembled. These models are numerically fitted and optimised with two different methods to the hydration thermogravimetric data. From the combined analysis of the raw experimental data and of the results of the solid-state kinetic analysis, the rate-limiting processes during these hydration reactions are inferred.*

1 Introduction

The dynamic behaviour of the hydration of various thermochemical materials is studied and presented. The selected materials ($MgCl_2$, K_2CO_3 and their composite variants by integration into vermiculite) are hydrated under controlled temperature and humidity conditions using a Dynamic Vapour Sorption (DVS) apparatus. The thermogravimetric data obtained from these experiments were then used to analyse and discuss the dynamic behaviour of the chemical reaction. Focus was placed on the identification of the so-called rate-limiting process of the reaction. The dynamic behaviour of salt and salt-in-matrix composite hydration was further investigated through solid-state kinetic analysis. This numerical method allows for deeper analysis of chemical reaction's kinetic behaviour by measuring and parameterising the various rate processes involved in terms of temperature, reaction advancement, and humidity.

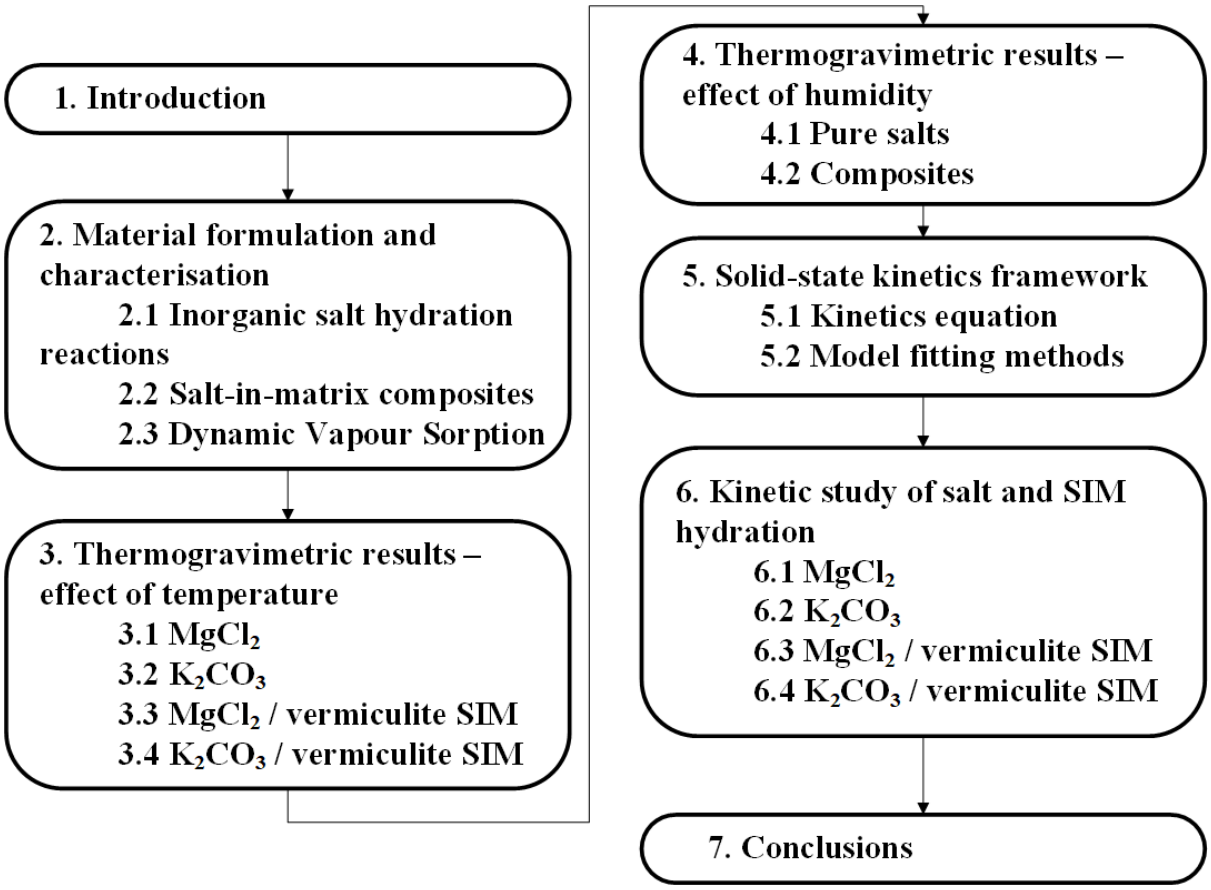

Figure 11 Chapter III mapped structure.

While the kinetic analysis of pure salt dehydration for certain specific salts has been partially investigated in the literature, the analysis of salt hydration through the lens of solid-state kinetics is still largely unaddressed. Solid-state kinetic analysis of salt-in-matrix composite (de)hydration is even more sparse in the literature. Consequently, the identification of the rate-limiting process during salt hydration, and the modification of this rate-limiting process induced by impregnation of the salt within a supporting matrix scaffold, are still largely absent. Therefore, this part of the study also covers the numerical modelling of the selected material which made it possible to infer the dominant reaction mechanism through the most suitable kinetic models. This numerical study helps consolidate the findings obtained through analysis of the experimental data from thermogravimetric analysis. The overall methodology is illustrated in **Figure 12**.

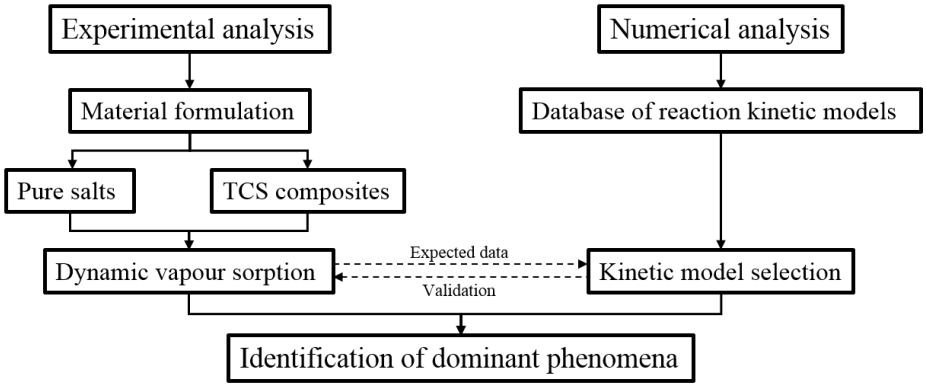

Figure 12 Chapter III methodology flowchart.

2 Material formulation and characterisation

2.1 Inorganic salt hydration reactions

Magnesium chloride and potassium carbonate are the two salts considered in this work. These two materials can be considered among the most promising for low temperature long term TCS.

Magnesium chloride ($MgCl_2$) hydrates through a multistep process; increasing ambient humidity will cause the material to hydrate by stoichiometric steps of two water molecules. $MgCl_2$ distinguishes itself from other inorganic salts by its low equilibrium vapour pressure in the range of temperatures considered for low temperature TCS: an equilibrium water vapour pressure of 1 mbar at 25°C (**Figure 13**) means that, in a sample holder and in ambient conditions of a laboratory, the material will adsorb water from the surrounding atmosphere. As such this material is particularly subject to deliquescence and overhydration, as has been observed experimentally [119]. The kinetics of the magnesium chloride dehydration have been extensively researched [16,95], however hydration kinetics are largely unaddressed. A relatively high theoretical energy density (~528 kWh/m^3 or 1.9 GJ/m^3), combined with the aforementioned practical issues, makes $MgCl_2$ a suitable candidate for impregnation into a host matrix. The detailed reactions constituting the hydration steps of magnesium chloride are shown in **equations (15)**, **(16)** and **(17)**:

$$MgCl_2 + 2\,H_2O \Leftrightarrow MgCl_2 \cdot 2H_2O,\ \Delta H = \text{-}1607535\ J/mol_{H2O},\ T_{10mbar} = 60°C \quad (17)$$

$$MgCl_2 \cdot 2H_2O + 2\,H_2O \Leftrightarrow MgCl_2 \cdot 4H_2O,\ \Delta H = \text{-}1279720\ J/mol_{H2O},\ T_{10mbar} = 90°C \quad (18)$$

$$MgCl_2 \cdot 4H_2O + 2\,H_2O \Leftrightarrow MgCl_2 \cdot 6H_2O,\ \Delta H = \text{-}1898990\ J/mol_{H2O},\ T_{10mbar} = 120°C \quad (19)$$

Reaction equilibrium is bivariant with temperature/humidity, the indicated reaction temperatures are given assuming a vapour pressure 10 mbar, using phase diagram shown in [142]. The corresponding mass uptakes after water adsorption to each hydration level are 37.8% (anhydrate to dihydrate, **equation (15)**), 75.7% (anhydrate to tetrahydrate, **equations (17)** and **(18)**) and 113.5% (anhydrate to hexahydrate, **equations (17)**, **(18)** and **(19)**), respectively.

Potassium carbonate hydrates to the sesquihydrate (1.5 moles of water per mole of salt) according to a single step adsorption process shown in **equation (20)**. During this hydration reaction the K_2CO_3 sample is expected to uptake 19% of its weight as water. Potassium carbonate presents a lower theoretical energy storage density (360 kWh/m^3 or 1.3 GJ/m^3) than $MgCl_2$, however good stability and an apparent improvement of hydration performance with cycling [29] make it a strong candidate for low temperature TCS. This material is generating increasing amount of attention from the TCS scientific, yet so far, outside of some very early studies by Stanish and Perlmutter [96,97,143], the kinetics of hydration have been investigated by a single author [98]. The investigation of potassium carbonate integrated to a host matrix is also relatively unaddressed, with the study by Shkatulov et al. the only material study so far considering this possible use for K_2CO_3 [47].

$$K_2CO_3 + 1.5\,H_2O \Leftrightarrow K_2CO_3 \cdot 1.5H_2O \qquad (20)$$

Potassium carbonate has been identified as a candidate for sorption heat storage in several reviews [19,26]. Although it displays a relatively low theoretical energy density of 360 kWh/m^3 [19] compared to other inorganic salts, potassium carbonate has shown good stability, such that the practical energy storage density could be close to the theoretical energy density [28]. K_2CO_3 was characterized by Gaeini et al. [98]. They found that the extent of conversion during hydration/dehydration of the material improved from 0.67 to 0.95 by cycling up to 10 times, after which the material's mass uptake stabilized. More evidence for this cyclic behaviour was put forward by Beving et al. [144]. Stanish and Perlmutter provided some of the earliest work in the kinetic study of potassium carbonate hydration and dehydration [96,97,143,145]. They found that during the hydration of K_2CO_3, the sample size had a significant effect on the advancement of the reaction. They assumed that the flow of water vapour through the pores of the material was hindered by the layer formed by the initially reacted material. Spreading out the sample as thinly as possible was found to address this issue [143]. Finally, in a recent study, Donkers et al. studied the nature of the phase-transition occurring during the hydration of potassium carbonate [25], along with three other salts $CuCl_2$, LiCl and $MgCl_2$. They found that the hydration K_2CO_3 takes place as a solid-solid transition mediated by a wetting layer (as opposed to a dissolution followed by a recrystallisation). They also found that K_2CO_3 is metastable, i.e., there is a zone on the phase diagram of potassium carbonate close to equilibrium where hydration will necessarily be hindered at the nucleation stage.

The goal of this work is to study the hydration kinetics of these inorganic salts in conditions representative of TCS operating conditions. The hydration was therefore carried out at temperatures of 25°C and 40°C, with a water vapour pressure of 7.5 mbar. These (P,T) conditions represent the state of the air flow before it receives the discharged heat from the TCS. These temperatures are chosen so that an increment in temperature due to the discharge process would raise the temperature of the air to a sufficient level for domestic space heating (ideally above 45°C-50°C). This humidity is a typical water vapour pressure found in European climates during winter. Furthermore, for TCS process it is expected than some heat recovery device would help recover some energy from the outlet and exchange with the inlet air stream, allowing hydration of the materials at temperatures of 25°C to 40°C even during winter [15,140]. It is so far unclear whether TCS processes will need forced

humidification (i.e., a humidification system which enables higher humidity than the available ambient humidity), which is a question that will be explored later in the thesis – the hydration conditions selected here therefore represent the conditions for TCS process without humidification. The humidity/temperature conditions with relation to the two hydration reaction equilibrium conditions are presented in **Figure 13**. For $MgCl_2$ it can be seen in **Figure 13a** that a water vapour pressure of 7.5 mbar should enable the hydration of the salt to the hexahydrate ($MgCl_2 \cdot 6H_2O$), while also avoiding the deliquescence zone where high water vapour pressure causes the formation of a salt solution, which is a thermodynamically irreversible process.

The Clausius-Clapeyron diagram for potassium carbonate hydration is shown in **Figure 13b**. The metastable curves for K_2CO_3 hydration and dehydration are also presented on this graph with dashed lines. These dashed lines delimit the so-called metastable zone [25]. There are two metastable zones, for hydration and dehydration, respectively. In these areas, hydrated or dehydrated states of salt crystals remain the same even though the partial pressure and temperature conditions have been shifted in order to cross the equilibrium line. Thus, dehydrated K_2CO_3 will remain dehydrated if P-T conditions (**Figure 13b**) go above the equilibrium line but within the metastable zone (below the dashed line). In order for $K_2CO_3 \cdot 1.5H_2O$ to be obtained, temperature should be decreased, or water vapour pressure increased in order to leave the metastable zone. The presence of such an area in the Clausius-Clapeyron diagram has obvious implications for the application of salt hydration/dehydration for TCS – for example hydration conditions that are considered representative of real operating conditions could be close or within the metastable region, which could kinetically hinder the progress of the hydration process. For this work, the selected pressure-temperature conditions are either outside or at the border of the hydration metastable zone, as can be better appreciated through **Figure 13b.**

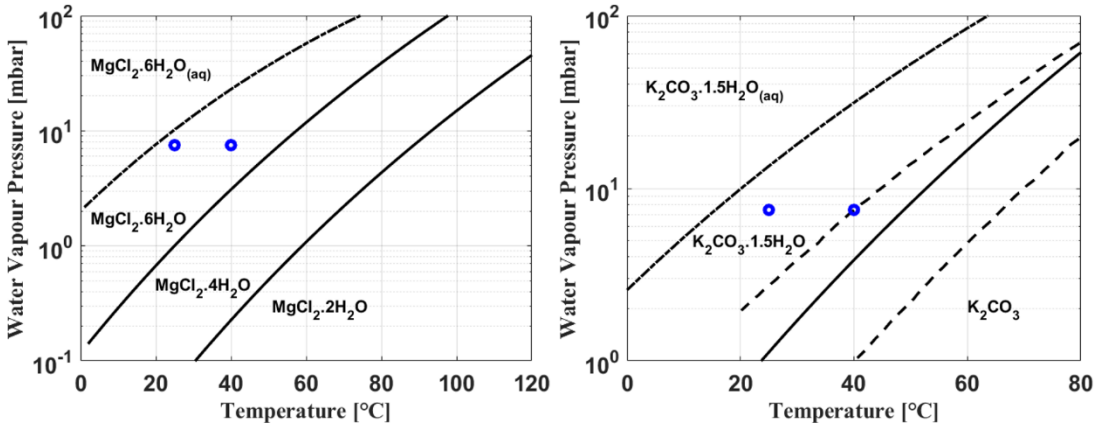

Figure 13 Clausius-Clapeyron diagrams (a) Magnesium chloride (b) Potassium carbonate - blue markers indicate hydration experimental conditions, full black lines separate the areas where different hydration states can exist, dashed lines indicate the metastable zone described in [25]**.**

2.2 Salt-in-matrix composites

Vermiculite was purchased from Dupre Minerals (SiO_2 34.46%, MgO 20.96%, AlO_3 12.79% and Fe_2O_3 8.98%). **Figure 14a** highlights the wet impregnation [50,146] salt-in-matrix fabrication process used to disperse the inorganic salt into the vermiculite.

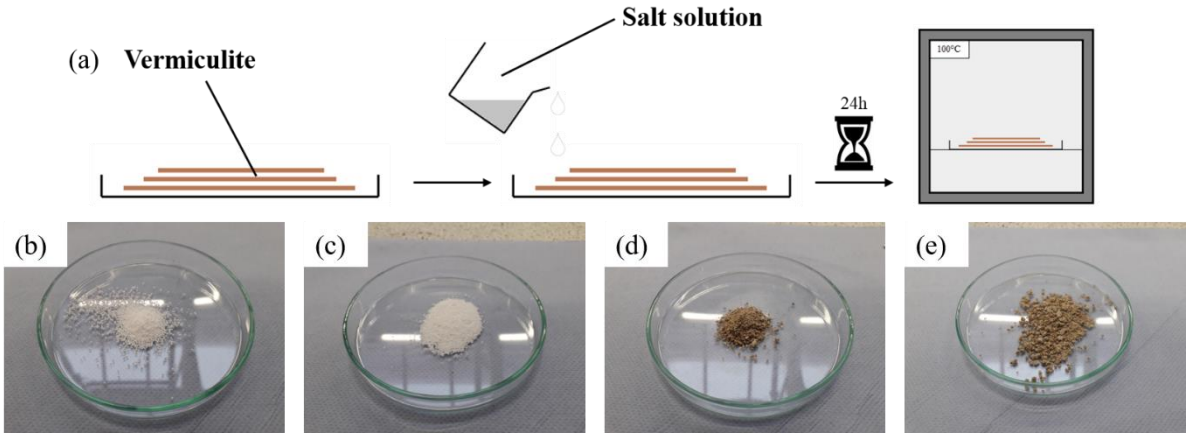

Figure 14 (a) Composite fabrication process, and dehydrated thermochemical material samples (b) K_2CO_3 (c) $MgCl_2$ (d) K_2CO_3/Vermiculite (e) $MgCl_2$/Vermiculite.

A salt solution is prepared by dissolving the inorganic salt into distilled water. The maximum potential concentration of salt in the solution is determined by the limit of solubility of the salt in water in the laboratory ambient conditions. The solubility limit of a number of salts, including $MgCl_2$ and K_2CO_3, is presented in **Table 10**. The solution is then poured into the vermiculite that has been ground beforehand to an average particle diameter of 3 mm. Vermiculite generally has a liquid absorption capacity of approximately 3 mL/g, and that is the case for the vermiculite used in this work.

Table 10 Limit of solubility of inorganic salts as a function of temperature.

g_{salt} /100mL$_{H2O}$	0 °C	10 °C	20 °C	30 °C	40 °C	50 °C	60 °C	70 °C	80 °C	90 °C	100 °C
$BaCl_2$	31.2	33.5	35.8	38.1	40.8	-	46.2	-	52.5	55.8	59.4
$CaCl_2$	59.5	64.7	74.5	100	128	-	137	-	147	154	159
$CaSO_4$	0.223	0.244	0.255	0.264	0.265	-	0.244	-	0.234	-	0.205
$CuCl_2$	68.6	70.9	73	77.3	87.6	-	96.5	-	104	108	120
K_2CO_3	105	109	111	114	117	121.2	127	-	140	148	156
LiCl	69.2	74.5	83.5	86.2	89.8	-	98.4	-	112	121	128
$LiSO_4$	36.1	35.5	34.8	34.2	33.7	-	32.6	-	31.4	30.9	-
$MgCl_2$	52.9	53.6	54.6	55.8	57.5	-	61	-	66.1	69.5	73.3
$MgSO_4$	25.5	30.4	35.1	39.7	44.7	50.4	54.8	59.2	54.8	52.9	50.2
$SrBr_2$	85.2	93.4	102	112	123	-	150	-	182	-	223

The composites mass composition can therefore be calculated theoretically from the salt solution concentration and volume of solution added to the vermiculite. The solution is added gradually, with frequent stirring of the wet vermiculite to ensure good dispersion within all of the support matrix's pore structure. This solid-liquid mix is then left for 24 hours in ambient conditions to enable the salt to bind to the vermiculite, before being placed into a furnace at 140°C for a further 24 hours. This step enables the full evaporation of the water, leading to the precipitation of the salt into the host matrix's pores and surface. Once the material has been fully dried, it is lightly ground in a mortar and pestle, and sieved to achieve particle size uniformity. Weighing of the vermiculite and composite samples at key steps of the preparation enables the measurement of the actual material's salt and matrix composition. The theoretically calculated and experimentally achieved mass compositions of the two fabricated SIMs are shown in **Table 11**. This table also shows standard deviations of the actual vermiculite and salt contents, which are the results of repeating the composite fabrication three times in order to ensure homogeneity of the results of the wet impregnation method. As can be seen the actual composition of the SIMs varies by approximately 1% according to the standard deviation calculation.

Table 11 Material compositions.

Material	Target Salt Content wt.-%	Actual Salt Content wt.-%	Vermiculite Content wt.-%
Bulk K_2CO_3	100.00	100.00	0
Bulk $MgCl_2$	100.00	100.00	0
K_2CO_3 / Vermiculite	40.00	37.11±1.29	62.89±1.29
$MgCl_2$ / Vermiculite	60.00	62.69±0.91	37.31±0.91

2.3 Dynamic vapour sorption

The materials were hydrated using dynamic vapour sorption (DVS). The hydrations were carried out in a DVS-Advantage 1 apparatus by Surface Measurement Systems [147] which can be seen in **Figure 15**, is represented schematically in **Figure 16**, and has its key parameters shown in **Table 12**. A DVS apparatus allows the control of specific values of temperature and partial pressure of a gas in an ambient around a sample holder connected to a microbalance. Therefore, it is possible to control the water vapour pressure and temperature around a sample of inorganic salt or composite to reach the hydration conditions discussed in **section 2.1** and specifically **Figure 13**. Thus, hydration experiments were carried out at 7.5mbar at temperatures of either 25°C or 40°C, and at 25°C, at water vapour pressures of 7.5 mbar, 10 mbar and 12 mbar. These conditions were chosen as they are representative of the potential discharge phase of a domestic TCS. In these systems it can be expected that a heat recovery system at the reactor outlet would enable preheating the inlet air temperature to temperatures of 25°C or 40°C. Vapour pressures around 7.5 mbar to 12 mbar enable on the one hand a large enough temperature lift during the discharge process, and on the other are low enough to avoid potential deliquescence.

Figure 15 DVS-Advantage apparatus [147]**.**

The materials were dried prior to the experiments at a temperature of 140°C. This value allows the dehydration of magnesium chloride without incurring the risk of thermal degradation in to HCl [28], which has been shown to occur at temperatures as low as 149°C [148]. Overall the control over $MgCl_2$ dehydration is not a trivial matter, as a number of studies point towards the overlapping of dehydration steps (from hexahydrate $MgCl_2 \cdot 6H_2O$, to tetrahydrate $MgCl_2 \cdot 4H_2O$ and to the dihydrate $MgCl_2 \cdot 2H_2O$) and thermal decomposition step in the range of temperatures 120°C-160°C [95,119,149,150].

Table 12 DVS Advantage-1: Key Parameters [151]

Parameter	Value	Unit
Temperature Range	5 - 60	°C
Oven Preheater Range	25-100	°C
Humidity Range	0 - 98%	-
Humidity Accuracy	+-1.5%	-
Gas Flow Rate Range	0 - 200	sccm
Actual Air Flow (dry)	76.9	sccm
Actual Wet Flow	23.1	sccm

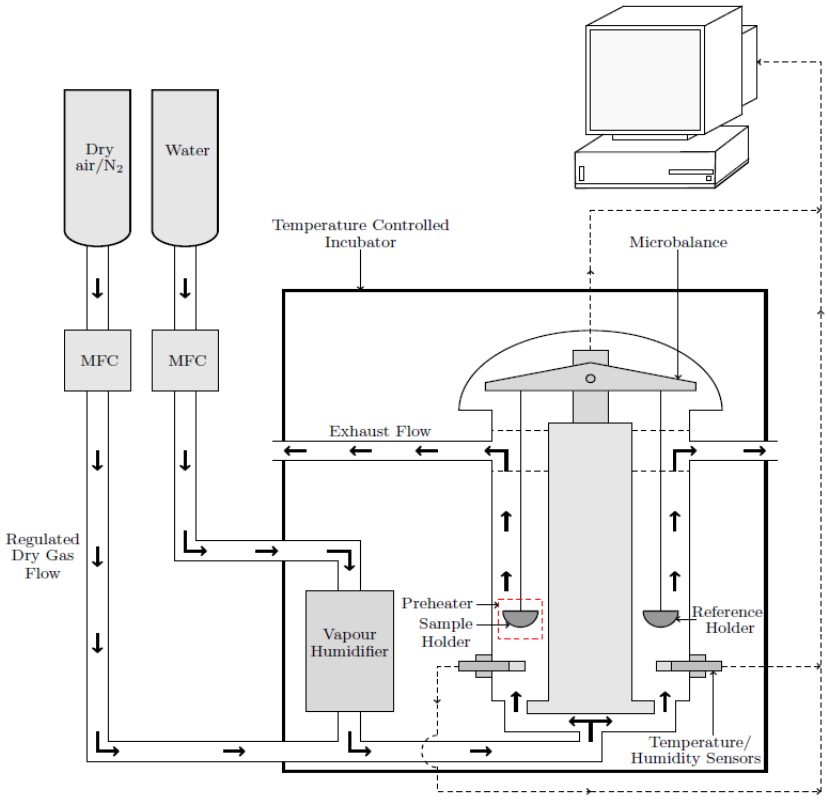

Figure 16 Schematic of Dynamic Vapour Sorption Advantage apparatus [152]**.**

The hydration experiments were each carried out three times to evaluate potential error which was calculated using the standard deviation of the experiment repetitions. At each time interval (20s time intervals) the mass of the sample was recorded, which, with the knowledge of the sample weight at the beginning of the experiment, enabled the calculation of the relative mass uptake β (**equation (21)**). Experiments were interrupted when either the relative mass uptake β did not change significantly or the rate of relative mass uptake $^{d\beta}/_{dt}$ reached a value of 0.

$$\beta = \frac{m(t) - m(t_o)}{m(t_o)} \tag{21}$$

An implicit but significant assumption is that of thermal equilibrium between solid (salt or salt-in-matrix) and gas (humid air) phases, which is often used in TCS scientific literature [108,128,138]. This assumption is also referred to as lumped-capacitance assumption by some authors. The general consensus [34,153,154] is that two requirements are needed to justify this assumption:

- Solid particles should be smaller than 1mm. As will be shown in **section 3.2**, particle diameters for these experiments are at the μm scale.
- Convective heat transfer resistance from solid to gas should be negligible compared to conductive heat transfer resistance within the solid. The dimensionless Biot number *Bi* is the ratio between convective and conductive heat transfer; thus, demonstrating a low Biot justifies

the assumption. Janna et al. [154] demonstrated that $Bi < 0.1$ is sufficient to justify the lumped-capacitance assumption. Biot number formula is shown in **equation**

- **(22**)

$$B_i = \frac{hL}{k} \quad (22)$$

Where h is convective heat transfer coefficient, L is a characteristic length which in a spherical particle is the ratio between volume and surface area i.e., $L = (4/3)R$ with R average particle radius equal to approx. 300μm, and k is solid thermal conductivity, which is easily shown to be between 0.5 and 1 W/K/m [155,156] for most inorganic salts. For TCS reactors heat transfer coefficient h in the range 10^1 to 10^2 W/m^2/K is typically used [21,157,158]. These conditions yield a Biot number in the range 3.10^{-3} to 6.10^{-3}, which meets the requirement for the lumped capacitance assumption. Thus, thermal equilibrium assumption between solid and gas phases is justified.

3 Thermogravimetric results – effect of temperature

3.1 Bulk $MgCl_2$

In **Figure 17** can be seen the measured time-dependent mass uptake of the $MgCl_2$ sample and the reaction rate during the hydration experiments, carried out at 25°C and 40°C. The right-hand plot also includes experimental error bars **Figure 17a.** The maximum error measured during the entire length of the experiments does not surpass 3%. Experiments were interrupted based on one of the three following criteria:

- No significant mass change was measured by the DVS's microbalance.
- The mass of the sample came within 3% of the theoretically expected value.
- The reaction rate came within a value close to 0.

As may be observed from **Figure 17a**, these criteria led to the total duration of each experiment (at each respective temperature) to be different. More specifically, the experiment at 40°C lasted longer and was overall slower than the experiment at 25°C. This observation is in line with Le Chatelier's principle, whereby exothermic reactions such as the hydration of inorganic salts are thermodynamically favoured at lower temperatures. This can be further appreciated through the Clausius Clapeyron diagram: increasing the temperature at a constant vapour pressure brings the sample closer to the equilibrium line between hydration stages, reducing the driving force of the reaction and therefore the overall rate of reaction.

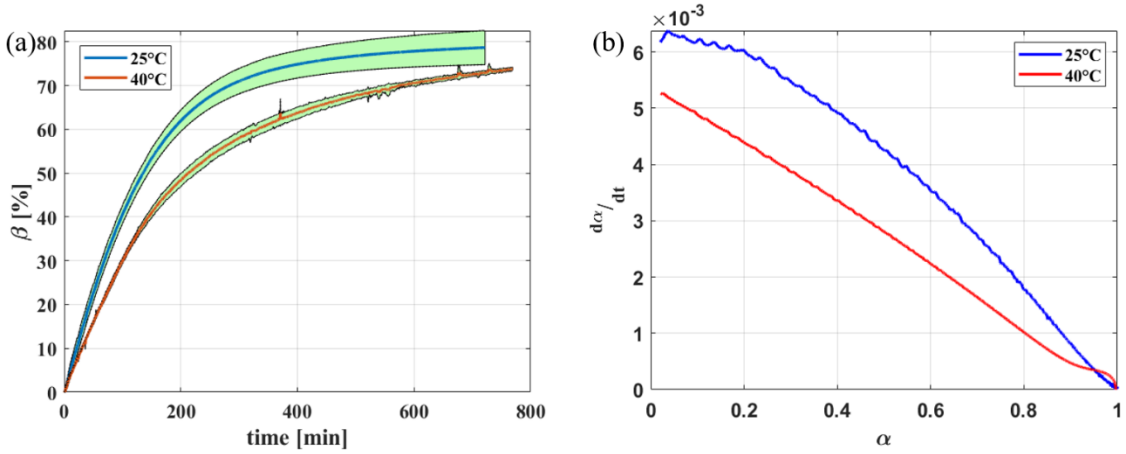

Figure 17 (a) Water mass uptake and (b) reaction rate of the hydration of $MgCl_2$ – area in green represents the standard deviation of the experiment over 3 repetitions.

At both experimental conditions, the $MgCl_2$ sample increased in mass through water uptake by approximately 75%. However, as can be calculated from a mass balance based on the stoichiometric reaction equation, the theoretical mass uptake during a full hydration to the hexahydrate (**equations (17)** through **(19)**) should be approximately 113%. A 75% mass uptake corresponds however to the following hydration reaction:

$$MgCl_2.H_2O + 5\,H_2O \Leftrightarrow MgCl_2.6H_2O \tag{23}$$

As was expanded on more extensively in the methodology section, a temperature of 140°C was used for the thermal pre-treatment of the magnesium chloride samples. This temperature was selected to dehydrate the sample as much as possible while also minimising the potential risk of thermal degradation, common to chlorides. It is therefore possible that during this pre-treatment the sample was dehydrated to the monohydrate $MgCl_2 \cdot H_2O$ rather than to the fully dehydrated state, which is compatible with the mass uptake observed in **Figure 17** and the mass balance of the reaction described in **equation (23)**. Particle size distribution of $MgCl_2$ sample is shown in **Figure 18**.

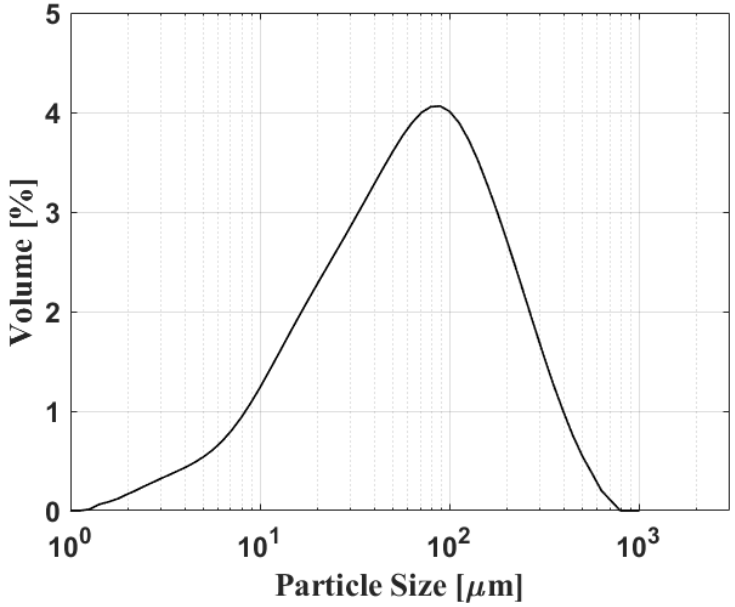

Figure 18 Particle size distribution of pure $MgCl_2$ particles used in DVS experiments.

This discrepancy between the theoretically expected and the experimentally observed behaviours during $MgCl_2$ could have significant consequences for the application in the context of TCS systems. The theoretical energy density of $MgCl_2$ is ~60 kJ/mol_{H2O} [19], which is now expected to decrease since full dehydration and hydration is likely not achievable in real operating conditions. Indeed, a temperature of 140°C appears to be insufficient to fully dehydrate the material, whereas the maximum achievable temperature of heat sources for real TCS system is not expected to be above 100°C. Thus, a 20% reduction of total energy density is to be expected based on the information presented here and in [19]. The presence of hindering mechanism which gradually limits the hydration and mass uptake of pure $MgCl_2$ is manifested by the overall reduction in reaction rate $d\alpha/dt$ with reaction progression ($\alpha \rightarrow 1$), visible in **Figure 17b**. The reaction rate at 25°C can be described as non-linear with respect to the reaction advancement, whereas the reaction rate at 40°C demonstrates clear linear behaviour. Furthermore, the mechanism hindering the mass uptake of $MgCl_2$ during hydration appears to scale with sample size. As is observable from **Figure 19a**, the overall rate of hydration clearly decreases with sample size increase. This is a sign that the limiting mechanism at least partially takes place at the interparticle level, i.e. water vapour diffusion through the space between particles contributes to the final reaction rate, which is in line with results of other studies in the literature [98]. These mechanisms are investigated further in **section 6** with the solid-state kinetic analysis of the experimental results. As discussed previously solid to gas heat transfer effects are negligible, convection heat transfer can be ignored as calculated by the system Biot number.

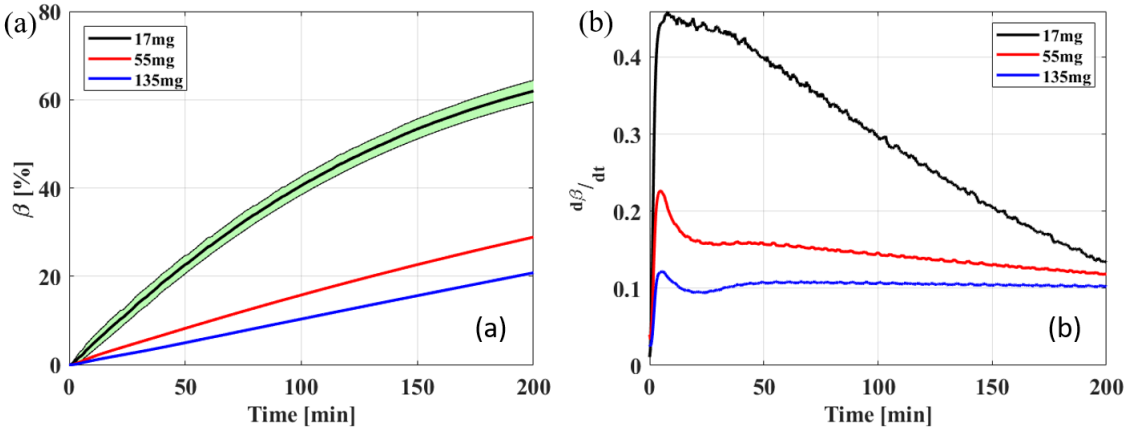

Figure 19 (a) Water mass uptake and (b) uptake rate during the hydration of $MgCl_2$ for different sample sizes at 25°C.

3.2 Bulk K_2CO_3

The thermogravimetric results of the hydration of potassium carbonate are presented in the following section. **Figure 20** shows the mass uptake evolution over time and the associated reaction rate of the K_2CO_3 samples at temperature 25°C, water vapour pressure of 7.5mbar and for sample sizes of 17mg, 55mg and 144mg. Water mass uptakes of 1.5% to 2% were measured; unlike what was observed for $MgCl_2$, this hydration level does not match a known hydrate of potassium carbonate, since the only known stable hydrate of K_2CO_3 is the sesquihydrate $K_2CO_3 \cdot 1.5H_2O$, the hydration to which yields a mass uptake of 19% (**equation (18)**). Furthermore, a decreasing water mass uptake and mass uptake reaction with increasing sample size was measured which supports the possibility that the rate-limiting mechanism to the hydration of potassium carbonate takes place at the interparticle level (i.e. bulk), rather than at the intraparticle (i.e. individual particle level). Additionally, from the observation of two distinct reaction regimes, the water mass uptake of K_2CO_3 appears to slow down significantly after what can be described as an initial relatively fast hydration stage.

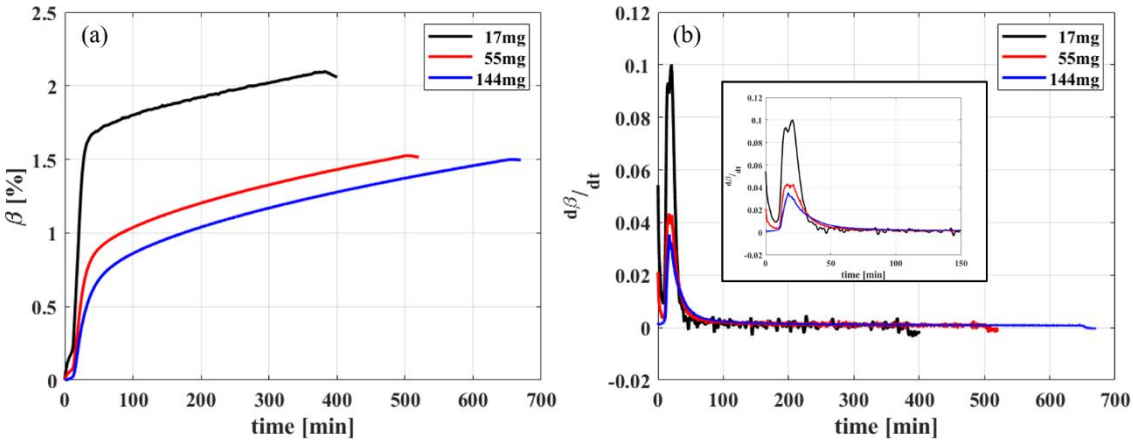

Figure 20 (a) Water mass uptake (b) and uptake rate during the hydration of K_2CO_3 for different sample sizes.

From the evidence shown in **Figure 20**, a hypothesis has been proposed relating to the formation of a sample diffusion barrier. The proposition is that during K_2CO_3 hydration a layer of hydrated salt is formed at the surface of the sample immediately in contact with the humid atmosphere and accessible by the water vapour. The hydration of K_2CO_3, in these circumstances, clearly deviates from being driven by the equilibrium conditions of the reaction. The projected mass uptake does not follow the stoichiometry of the chemical reaction in **equation (20)**.

Evidence in the literature supports this proposed hypothesis. Due to the observed effect of sample size on the hydration rate of potassium carbonate, Stanish et al. took the precaution of spreading out the particles in the sample at thinly as possible into a monoparticle layer in order to minimise diffusional resistance [143]. This practice led them to achieving the material's theoretical mass uptake of 19%. Sögütoglu et al. demonstrated that the hydration of potassium carbonate involved the presence of a metastable zone [25]. The hydration conditions in the present work were selected in order to avoid hydration hindrance due to this metastable zone. In the same work, the hydration of potassium carbonate was found to be mobilised by the formation of a liquid layer at the solid-gas interface. This wetting layer could be responsible for the clustering and agglomeration of hydrated K_2CO_3 particle, leading to the formation of the hypothetical sample diffusion barrier.

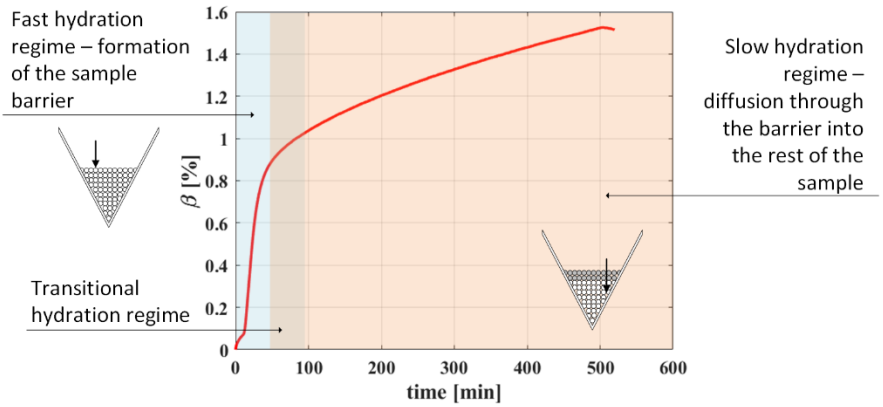

Figure 21 Hydration of K_2CO_3 at 25°C and diffusional barrier.

The steps leading to the formation of a sample diffusion barrier, manifested as hydration regimes, are presented in **Figure 21**. The salt particles directly in contact with the humid ambient hydrate first and quickly, leading to the formation of a hydrated particle barrier due to their swelling and the associated reduction in interparticle porosity, thereby reducing the accessibility of water molecules to the unhydrated regions of the sample. Indeed, volume change within the range of 22%-28% has been reported during water uptake of K_2CO_3 [19]. Additionally, the largely reported [119,159] phenomenon of particle agglomeration during salt hydration further adds to the role of a hydration barrier limiting water mass uptake, since particles will agglomerate together as they increase in diameter (assuming relative sphericity of the salt particles). The initial formation of the sample barrier takes place during the fast hydration regime. This resulting layer then hinders further hydration of the sample, leading to the slow hydration regime. Therefore, based on this proposed hypothesis, the hydration of K_2CO_3 in these conditions is controlled by water vapour diffusion through the area at

the interface between unhydrated solid and humid ambient (interparticle). The effect of temperature on the hydration behaviour was studied to gain further insight into this phenomenon.

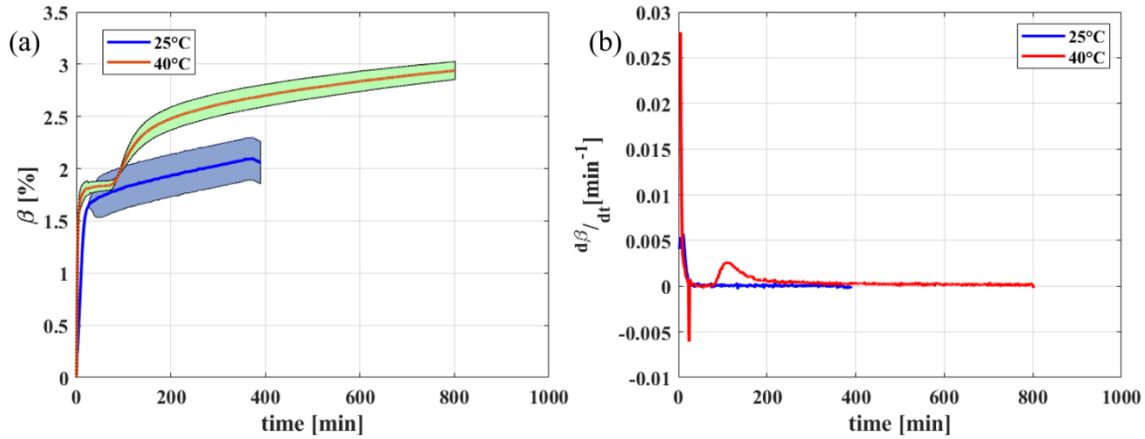

Figure 22 (a) Water mass uptake and (b) reaction rate of the hydration of K_2CO_3 – area in green represent the standard deviation of the experiment over 3 repetitions.

Figure 22 presents the time-dependent mass uptake and reaction rate of K_2CO_3 at temperatures of 25°C and 40°C. The figure also includes the experimental error bands, which are within the range of 0% to 0.5% over the entire experiment. As already observed previously, the experimentally measured mass uptakes (2% to 3%) are significantly lower than the expected mass uptake of 19%.

- The two hydration regimes can be clearly distinguished for the hydration at 25°C, with the initial fast uptake ($d\alpha/dt \sim 10^{-2}$ s^{-1}) followed by the slow hydration regime with almost negligible reaction rate.
- The change in hydration regime ascribed to the formation of a sample diffusion barrier may also be observed at 40°C, albeit with a different dynamic behaviour. In these experimental conditions, the relative mass uptake after the initial regime characterised by fast reaction kinetics reaches a plateau value, before increasing again in a regime that has the same characteristics as the slow kinetics regime observed at 25°C.

Thus, it can be seen that the hydration hindering mechanism of K_2CO_3 is dependent on temperature (or perhaps relative humidity, since the absolute water vapour pressure is kept constant despite the temperature variation).

Further observation of **Figure 22** reveals that the mass uptake rate increases with temperature, which is unexpected with respect to the Le Chatelier's principle for exothermic reactions and contrary to the behaviour of $MgCl_2$ hydration. The non-conventional behaviour observed is likely to be linked to the hypothesis of the sample diffusion barrier discussed in the previous paragraphs.
The behaviour of the entire sample does not follow the theoretically expected trend in terms of stoichiometry and equilibrium conditions. Yet, the kinetics of the hydration taking place at the scale of a single salt particle should be following equilibrium conditions. In particular, individual particles, part of the interface layer between sample and humid ambient, should hydrate faster at 25°C than at 40°C. This is because interparticle diffusional effects should be minimal at the solid-gas interface.

Since the formation of the sample diffusion barrier is tied to the hydration of the particles at the sample/ambient interface, if individual particles hydrate faster at 25°C, then the sample diffusion barrier should also form faster at 25°C than at 40°C. Therefore, counterintuitively, a larger number of water molecules may access deeper regions of the sample at 40°C than at 25°C before access becomes obstructed. Thus, the reaction will yield a higher mass uptake at 40°C than at 25°C (which is observable in **Figure 22**).

With the correct geometrical assumptions, it is possible to estimate the length of the barrier $\check{u}$ (see **Figure 23**) based on the mass uptake achieved during the fast regime β_{fast}. By assuming the sample holder to be an ideal cone (the sample holder is conical to a sufficient degree for the assumption to be realistic – the shape is not critical but impacts the following geometrical calculations from **equations** (24) to **(28)**), impermeable on all surfaces except the base, and that the hydration of the sample takes place from the base of the conical sample holder towards its vertex, the total volume of hydrated salt can be derived from the final mass uptake. The volume of the sample can be calculated with **equation (24)**:

$$V = \pi r^2 \, h/_3 \tag{24}$$

The volume of the unreacted sample is calculated with **equation (25)**:

$$V_{UR} = \pi r'^2 \, h'/_3 \tag{25}$$

The volume of the reacted part of the sample can be deduced:

$$V_R = V - V_{UR} = \pi r'^2 \frac{h'}{3} = \frac{\pi r^2}{3}\left(h - \frac{(h-\delta)^3}{h^2}\right) \tag{26}$$

The mass of reacted material can be determined with the ratio of actual mass uptake β_{fast} and the theoretical final mass uptake β_t, along with the sample mass m and ρ the anhydrated salt density.

$$m_R = \rho V_R = \frac{\beta_{fast}}{\beta_t} m \tag{27}$$

Barrier length $\check{u}$ can be deduced from **equation (28)**:

$$\delta = h - \sqrt[3]{h^2\left(h - \frac{3m}{\pi \rho r^2}\right)} \tag{28}$$

Table 13 K_2CO_3 sample characteristics.

Sample Size	m [mg]	β_{fast} [%]	h [cm]	δ [µm]
Small	17	1.613	0.35	46.9
Medium	55	0.816	0.45	46.3
Large	144	0.602	0.60	50.0

The calculated barrier layers *ŭ* are shown in
Table 13. As can be seen the barrier length was found to be constant for all sample sizes, at approximately 48μm. According to the particle size distribution of K_2CO_3 prior to hydration (**Figure 24**), this diffusional length is equal to approximately 8% of the average potassium carbonate particle diameter. The hydration of the sample of K_2CO_3 spans multiple layers of particles and begins with the rapid hydration of particles that are directly in contact with the humid air. Only a section of the top layer of particles that is within approximately 50μm of the solid/gas interface, or 8% of the average K_2CO_3 particle diameter, is affected by this fast reaction stage. Subsequent hydration of the rest of the particles is kinetically hindered by the diffusion of water through the layer of hydrated salt at the top of the sample. This mechanism is different from bulk $MgCl_2$, where intraparticle diffusion of water vapour from the outer layer of individual particles towards their core appears in this study to be the controlling reaction mechanism. This sheds light on potential practical issues that would arise with the hydration of K_2CO_3 in the context of TCS.

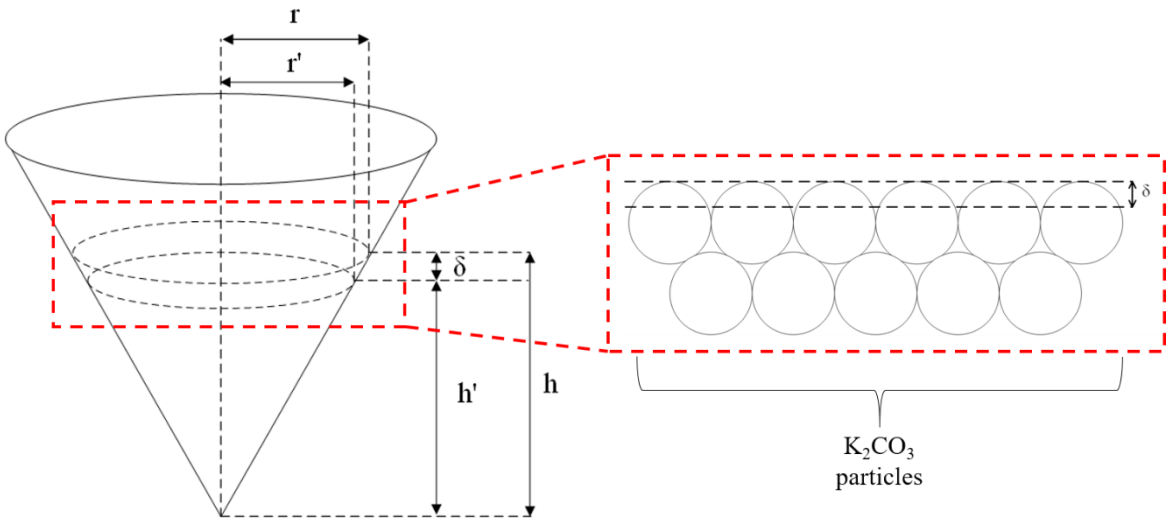

Figure 23 Schematic representation of the DVS sample holder and barrier length δ.

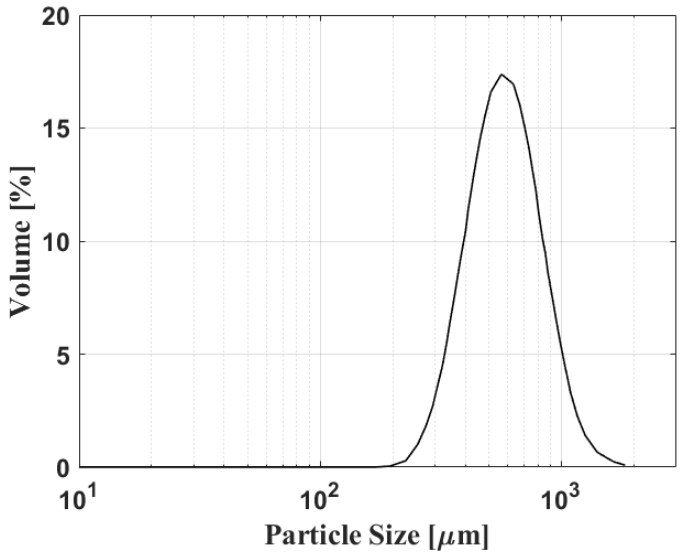

Figure 24 K_2CO_3 particle size distribution.

3.3 $MgCl_2$ / vermiculite SIM

Figure 25 shows the time-dependent mass uptake of $MgCl_2$/vermiculite and the corresponding reaction rate during hydration at 25°C and 40°C (7.5mbar). Since the composite salt content is estimated to be 62.7% (**Table 11**), and with the assumption that the composite fully hydrates during the experiment, a relative water mass uptake of 32.12% may be expected. As seen from **Figure 25a**, the experimentally measured mass uptake is within 5% to 15% of the expected value. Thus, this experiment demonstrates that the water mass uptake of $MgCl_2$ is favoured by the presence of a host vermiculite matrix, and is further evidence of the reliability of the wet-impregnation method in dispersing salt into a carrier.

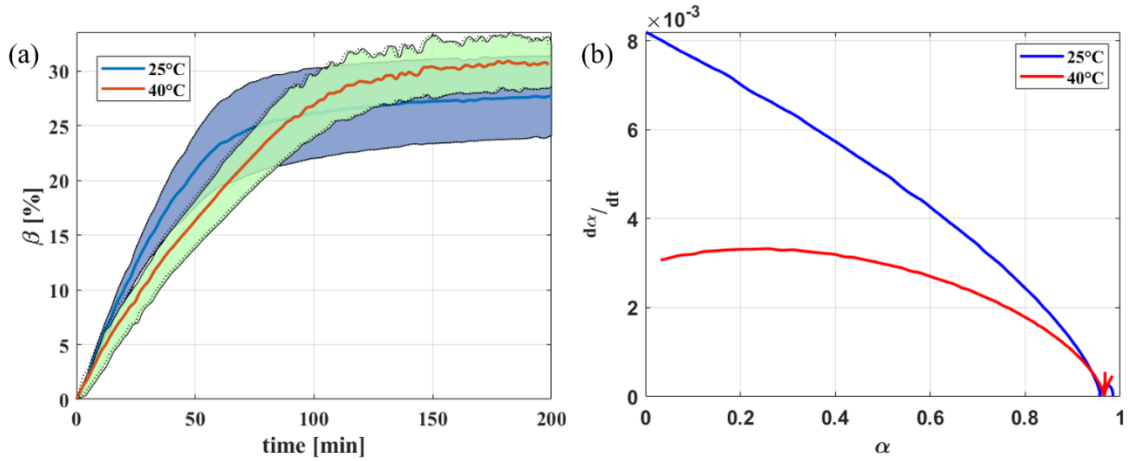

Figure 25 (a) Water mass uptake and (b) reaction rate of the hydration of $MgCl_2$ / vermiculite composite.

The variations in water mass uptake compared to the theoretical value are likely due to a combination of non-homogeneous distribution of the salt in the matrix, and experimental error during the calculation of the composition of the salt-in-matrix composite associated with the formulation of the material. Observation of the experimentally measured reaction rates shown in **Figure 25b** reveals that lower reaction rates are obtained at higher temperature, which is in line with Le Chatelier's principle. Furthermore, the highest uptake rates may be found towards the beginning of the reaction which can be attributed to the presence of the salt on the surface and in the easily accessed outer pores of the vermiculite. The outer pores and surface are reached first by water molecules during exposure to a humid ambient after simple diffusion through the macropores of the sample (i.e. through the interstitial void between particles of the sample). Relevant literature reports similar observations for vermiculite/salt composites [121,125,160], and SIMs based on different salts dispersed in a mesoporous matrix [66]. Thus, the hydration of the $MgCl_2$/vermiculite composite appears to be driven by two consecutive mechanisms: first, the hydration of the salt at the surface of the host matrix; then, the hydration of the rest (and majority) of the salt that is found within the pore structure of the composite and is more difficult to access for the water molecules. As was demonstrated earlier in **section 2.3** convective heat transfer from solid to ambient can be neglected as near instantaneous.

3.4 K_2CO_3 / vermiculite SIM

Figure 26 shows the time-dependent relative mass uptake of the K_2CO_3/vermiculite composite during hydration at 25°C and 40°C. Since the composite salt content is estimated to be 37.1% (**Table 11**), and with the assumption that the composite fully hydrates during the experiment, a relative water mass uptake of 6.62% may be expected. This value is reached to within 0.5% at both temperatures. Differently from pure K_2CO_3, the material therefore is able to achieve its theoretical mass uptake without significant kinetic hindrance. This is due to the known property of vermiculite that salts within its pore structure will hydrate and swell in the presence of water without impeding the transport of water vapour through pore blockage [49], which is clearly reflected in the fast hydration kinetics of the material. The hydration is therefore not limited by diffusional effects such as for pure K_2CO_3 due to the high porosity and multiple pathways for water vapour of the vermiculite matrix.

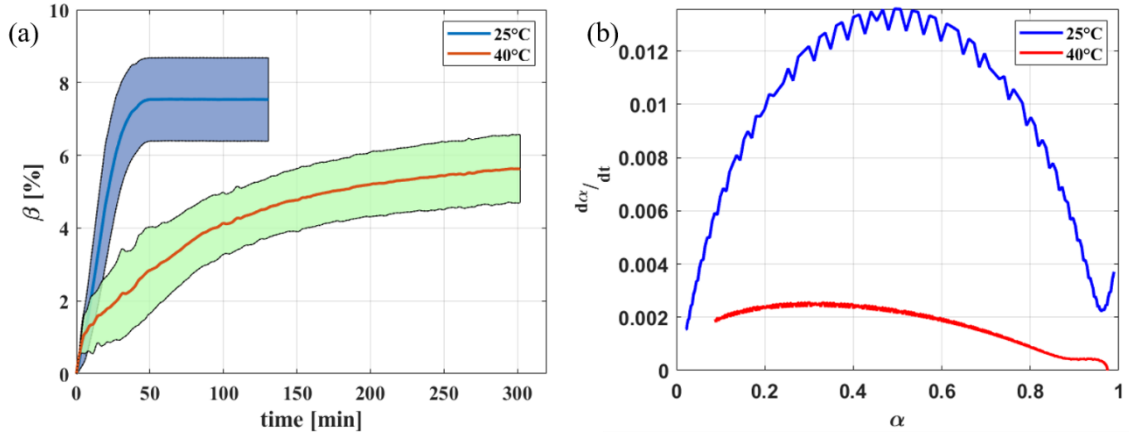

Figure 26 (a) Water mass uptake and (b) reaction rate of the hydration of K_2CO_3 / vermiculite composite experiments.

The kinetics of K_2CO_3/vermiculite composite hydration appear to be more dependent on hydration temperature than the magnesium chloride-based composite – this dependence is discussed in detail in **section 6** dealing with the kinetic assessment of the experimental results. Observation of the experimentally measured reaction rates shown in **Figure 26b** reveals that lower reaction rates are obtained at a higher temperature, which is in line with Le Chatelier's principle. Unlike its pure form, the hydration of K_2CO_3 impregnated into vermiculite follows standard equilibrium conditions. An inflexion at approximately α~0.3-0.4 (at 25°C) and α~0.4-0.5 (at 40°C), further points to the presence of two hydration mechanisms. Similarly to the $MgCl_2$/vermiculite composite, these distinguished hydration stages may be ascribed to the salt at the surface of the material hydrating prior to the salt found deeper within the pore structure of the composite.

From these results it can be seen that by dispersing the salt into a porous host matrix such as vermiculite, the kinetics of K_2CO_3 hydration may be vastly improved, and have wider implications when considering the material as a TCS material within a scaled thermochemical energy storage

system. On the one hand, the energy storage density of K_2CO_3 of 360 kWh/m^3 is low compared to other similar inorganic salts, while on the other, a host matrix is likely to be necessary to achieve a sufficiently high reaction rate (and therefore power output). Thus, a compromise is required in order to guarantee the material's kinetic performance while maintaining a sufficient energy storage density.

4 Thermogravimetric results - Effect of humidity

A set of experiments has been designed to study the impact of water vapour pressure on the water sorption performance and kinetics of inorganic salts and salt-in-matrix composites. This section presents the experimental results of the hydration of the four investigated materials at relative humidities 24.1%, 32.1% and 38.5% at a temperature of 25°C, which equates to absolute water vapour pressures of 7.5 mbar, 10 mbar and 12 mbar, respectively. These values of partial pressure were selected on the basis that they cover the typical humidities investigated in the TCS literature for salt hydration aimed at open low-temperature TCS. For multistep hydration reactions such as the hydration of magnesium chloride and differently from potassium carbonate hydrate, water vapour pressure may affect the total mass uptake of the material depending on the equilibrium conditions of the different hydration steps. Water vapour pressure is known to also affect the kinetics of such hydration reactions. This may be appreciated from the kinetics equations shown in **equation (29)**.

$$\frac{d\alpha}{dt} = k(T)f(\alpha)(1 - \frac{p_{eq}}{p}) \quad (29)$$

If it is assumed that the hydration reactions are carried out isothermally, such as in the conditions of Dynamic Vapour Sorption, then a higher vapour pressure results in a larger pressure term in turn leading to an overall higher reaction rate.

4.1 Pure salts

K_2CO_3

In the case of K_2CO_3, the selected operating conditions are located well beyond the hydration equilibrium line and above its metastable zone [25]. The selected operating conditions can be further appreciated through visualisation on the Clausius-Clapeyron diagram (**Figure 27**). The operated reaction should therefore theoretically lead to the hydration of the sample to the sesquihydrate $K_2CO_3 \cdot 1.5H_2O$ (**Section 2.1 equation (18)**) and a relative mass uptake of 19%. However, it is worth recalling from **section 3.2** that the hydration at 7.5 mbar of potassium carbonate was found to be hindered by a diffusion barrier caused by the hydration of the top layer of the sample. It will be seen in the following figures whether an increase in relative humidity around the sample affects this phenomenon.

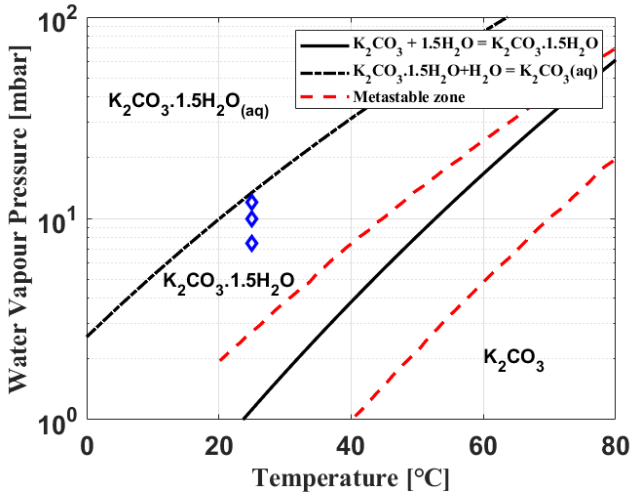

Figure 27 Clausius-Clapeyron phase diagram of K_2CO_3. The boundaries of the metastable zone, surrounding the hydration/dehydration equilibrium line, and the deliquescence zone are indicated. Experimental conditions are shown with the blue diamond-shaped markers.

The impact of water vapour pressure on the hydration of pure K_2CO_3 can be seen in **Figure 28**. **Figure 28 (a)** shows that regardless of the relative humidity the hydration follows the same behaviour observed in **section 3.2**:

- a fast but short mass uptake during the 'fast kinetics' regime, during which the achieved mass uptake appears to be unaffected by the vapour pressure, from the presented experimental data. Mass uptakes in the range of β~1.5%-3% are achieved during this hydration regime
- a slow linear mass uptake that appears to drift upwards towards no particular plateau value corresponding to a stoichiometric value of a reaction step. It can be seen that the relative mass uptake of the salt sample during this step does increase faster with higher relative humidities, as can be better appreciated through the reaction rates shown in **Figure 28 (b)**.

Thus, the hydration of potassium carbonate presents to a certain degree the expected dependency with relative humidity. The overall reaction behaviour characterised by the two hydration regimes remains unusual compared to other studies on the hydration of K_2CO_3 [98] or of inorganic salts in general. However, the increase in reaction rate with increased vapour pressure throughout most of the reaction is in line with the expected behaviour of the reaction.

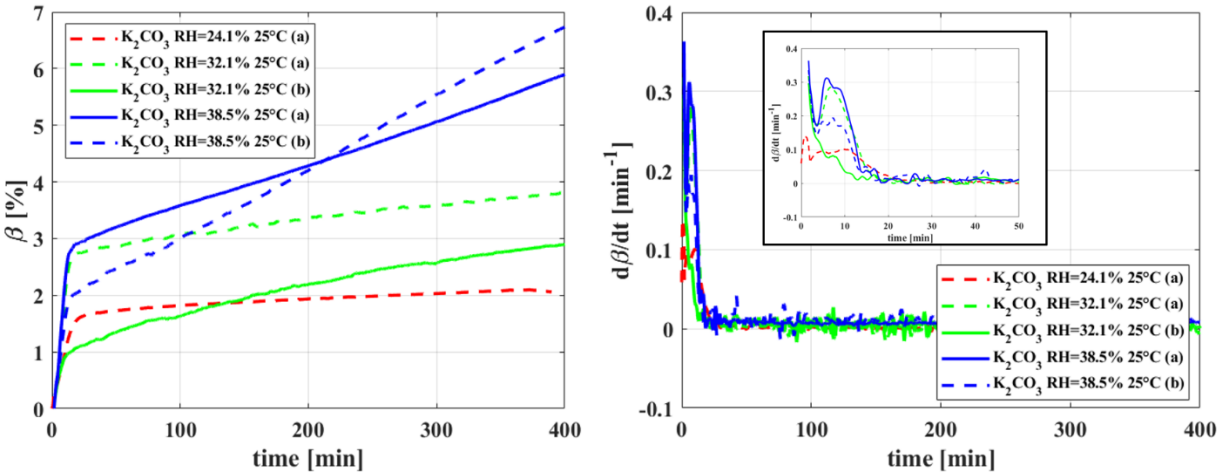

Figure 28 (a) Water mass uptake and (b) reaction rate of the hydration of K_2CO_3 for different humidity levels at 25°C.

$MgCl_2$

The same range of operating conditions was adopted for $MgCl_2$ (both in pure form and dispersed into vermiculite). These conditions can be visualised on $MgCl_2$'s Clausius-Clapeyron phase diagram. As can be seen from **Figure 29**, at 25°C the equilibrium pressure of magnesium chloride hydration (hydration to the hexahydrate at ~1 mbar, hydration to the dihydrate from the anhydrate state at ~ 8 10^{-7} mbar) is significantly lower than for K_2CO_3 hydration from anhydrate to sesquihydrate (~1 mbar). This is a characteristic feature of $MgCl_2$ whose hydration equilibrium conditions are exceptionally low compared to other similar inorganic salts –anhydrate $MgCl_2$ in open ambient conditions will hydrate and deliquesce in time.

Since, as has been discussed previously, the hydration kinetics of inorganic salts are primarily driven by the so-called pressure drop (difference between equilibrium water vapour pressure and actual water vapour pressure), with identical operating conditions it is expected that the kinetics of $MgCl_2$ hydration should be faster than for K_2CO_3 hydration. Furthermore, it can be seen that the hydration at 12 mbar / 25°C should bring $MgCl_2.6H_2O$ to deliquescence according to the theoretical phase diagram.

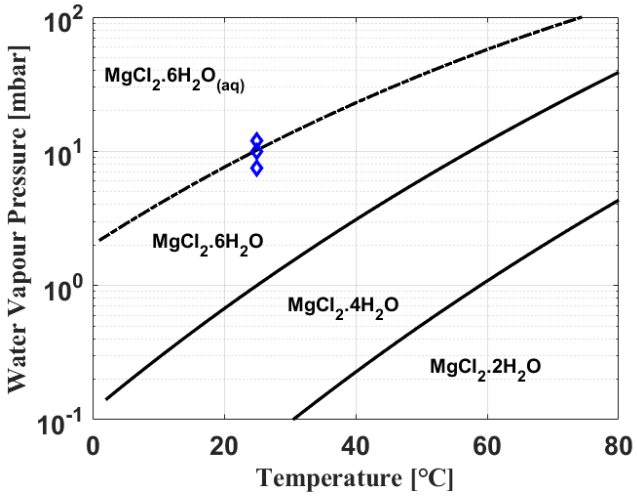

Figure 29 Clausius-Clapeyron phase diagram of $MgCl_2$. The boundaries of the deliquescence zone are indicated. Experimental conditions are shown with blue diamond-shaped markers.

Figure 30 shows the effect of water vapour pressure on the dynamic hydration behaviour of $MgCl_2$. The relative mass uptakes during the hydrations at 7.5 mbar / 25°C (RH = 32.1%) and 10 mbar / 25°C (RH = 38.5%) converge towards a plateau value of approximately 70%, with the hydration at the higher vapour pressure of the two (RH = 38.5%) presenting the higher uptake rate. However, it can be seen that the water mass uptake of $MgCl_2$ drifts upwards towards no particular plateau value when hydrated at 25°C / 12 mbar – this behaviour is characteristic of a deliquescing system, where the newly formed liquid phase continuously absorbs water from the ambient.

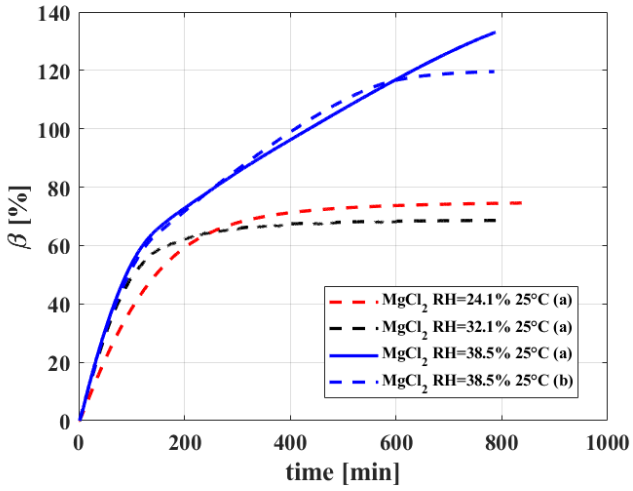

Figure 30 Water mass uptake of the hydration of $MgCl_2$ for different humidity levels at 25°C.

4.2 Composites

The effect of humidity on the dynamic sorption behaviour of $MgCl_2$-vermiculite and K_2CO_3-vermiculite composites is also investigated. The current body of TCS literature shows that the integration of the salt into a vermiculite host matrix does not directly affect the hydration equilibrium conditions which were seen for the pure salts in **Figure 28** and **Figure 29**. Thus, at identical humidity, the same level of hydration should be expected for each composite compared to the pure salt equivalent, relatively to the salt content of the composite. However, vermiculite host matrices have shown to affect the material's hydration behaviour around the deliquescence limit, i.e. the limit of the (P.T) conditions where the hydration of the material takes place via a direct solid to solution transition [161]. In the case of pure salts, deliquescence leads to the dissolution of the salt into the liquid phase mediating the hydration reaction. Experimentally, this phenomenon is generally characterised by an upward drifting of the mass uptake which does not appear to converge towards any particular mass uptake level that would be determined by reaction stoichiometry.

With regards to excess humidity leading to deliquescence, vermiculite host matrixes have been shown to prevent salt solution leakage due to capillary forces retaining the solution in the pore structure of the vermiculite. Thus, it can be expected that during the hydration of a SIM composite which would bring the system equilibrium beyond the deliquescence point, the sample would display mass uptake variation with similar behaviour to hydration below the deliquescence point, i.e. convergence of the mass uptake towards a value coinciding with the stoichiometry of a particular hydration step.

K_2CO_3 / vermiculite

Figure 31 shows the effect of relative humidity on the relative mass uptake of composite K_2CO_3/vermiculite during hydration. In each case the hydration takes place through a fast initial mass uptake during the first hour, before significantly slowing down and reaching a threshold mass uptake value of approximately ~8% of the original sample mass. Furthermore, from **Figure 31b** and from part of **Figure 31a**, the hydration reaction rate can be seen to increase with relative humidity. Thus, when comparing with the hydration behaviour of the pure salt when varying relative humidity and with the study on the effect of temperature on hydration kinetics (**sections 3.2** and **3.4**), it is evident that dispersion of this salt into vermiculite removes the apparent hydration diffusion barrier severely hindering the hydration of the pure salt and leads the material to behave more closely to theory.

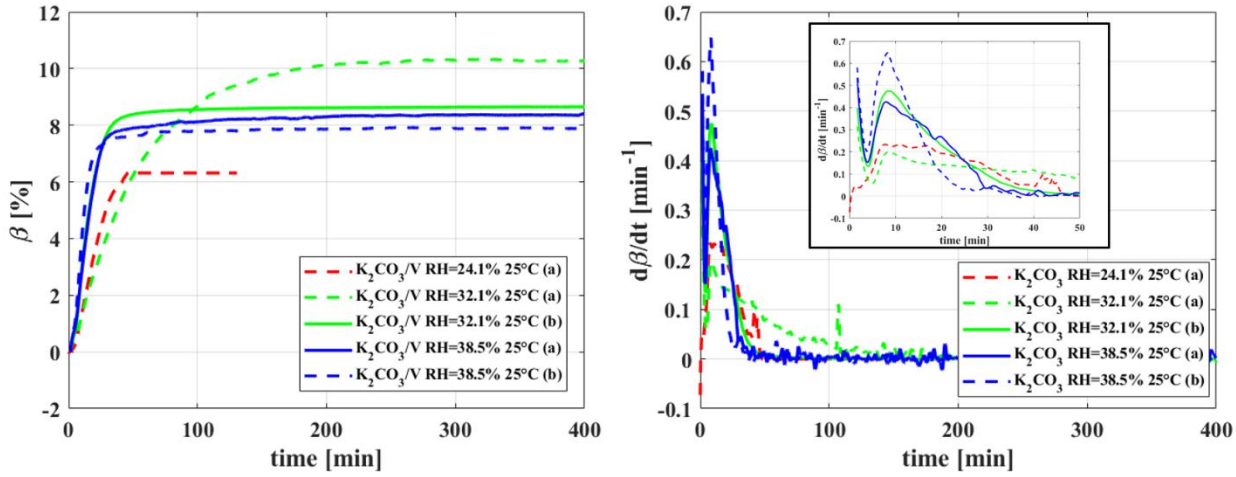

Figure 31 (a) Water mass uptake and (b) reaction rate of the hydration of K_2CO_3/vermiculite composite for different humidity levels at 25°C.

$MgCl_2$ / vermiculite

Figure 32 shows the effect of relative humidity on the relative mass uptake of the salt-in-matrix composite $MgCl_2$/vermiculite during hydration. Similarly to the hydration of the pure salt at 25°C / 7.5 mbar (RH = 24.1%) and 25°C / 10 mbar (RH = 32.1%), the mass uptake curves display the typical decelerating trend with the maximum reaction rate being found at the beginning of the reaction. However, differently from the pure material, the mass uptake during the hydration of the SIM at 25°C / 12 mbar (RH = 38.5%) stabilises to a plateau value after approximately ~5 hours reaction time.

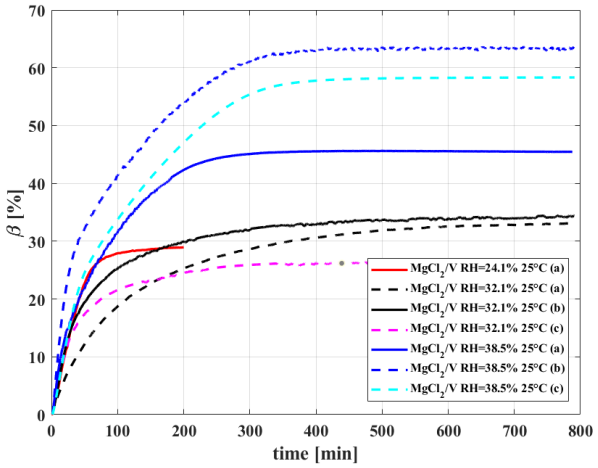

Figure 32 Water mass uptake of the hydration of $MgCl_2$/vermiculite composite for different humidity levels at 25°C.

It can be recalled from **Figure 30** that, during the hydration of pure $MgCl_2$ in these same conditions, the mass uptake curve drifted significantly upwards with no apparent slowing down or stabilisation of the reaction. The upward drift was a result of the operating conditions bringing the hydration of $MgCl_2$ into the deliquescence zone, see **Figure 29**, and therefore yielding a salt over-hydration through a liquid phase transition, with water absorption occurring from the gas phase to the new liquid phase.

Furthermore, it can be seen that the sample achieves a similar mass uptake at RH = 24.1% and RH = 32.1% of approximately β~30%, whereas in deliquescent conditions at RH = 38.5% the mass uptake stabilises at approximately β~55%. Thus the increased mass uptake capacity of the composite sample can be observed when hydrated in deliquescent conditions, which can be ascribed to the liquid absorption of the water vapour which comes in addition to the gas-solid transition achieved during adsorption (the water uptake capacity of vermiculite is approximately 5% of the total uptake and can be neglected as a contributor to the final mass uptake).

It has been shown in recent studies in the literature dealing with 'salt dispersed into vermiculite' composites that by capillary forces, water forms a liquid solution in the unoccupied pores of the vermiculite, creating a local RH different from the ambient humidity forced by the experiment. The local RH is higher than the salt's deliquescence humidity, and salt solution leakage can be observed for composites with too high a salt content (this threshold value appears to be salt-dependent). Such a phenomenon has been observed for $SrBr_2$ in vermiculite [48], K_2CO_3 in vermiculite [47] and LiCl in vermiculite [45]. It can thus be seen that this phenomenon of pore water accumulation due to capillary forces occurs for multiple salts impregnated into vermiculite, and it is conceivable that the same phenomenon occurs for $MgCl_2$ dispersed into vermiculite. Consequently, these capillary forces also prevent any salt in solution leaking from the material, i.e., deliquescence when the hydration conditions are brought into the theoretical deliquescence zone.

5 Solid-state kinetics framework

5.1 Kinetics equation

Since inorganic salt hydration is a thermally stimulated process, i.e. it can be initiated through a variation in temperature, its rate of advancement can be expressed through the solid-state kinetic equation [82], shown in **equation (30)** :

$$\frac{d\alpha}{dt} = k(T)f(\alpha)h(p) \tag{30}$$

The reaction rate of the reaction is therefore dependent on three terms: *k(T)*, the kinetic rate constant, $f(\alpha)$, the kinetic reaction model, and *h(p)*, generally referred to as the pressure-dependence term. For reversible solid-gas reactions of the type $A_{solid} = B_{solid} + C_{gas}$, the pressure dependence term can generally be expressed as:

$$h(p) = 1 - \frac{p_{eq}}{p} \tag{31}$$

It has been established that this expression is suitable for inorganic salt hydration [108,162], with p_{eq} the equilibrium vapour pressure and p the water vapour pressure. However, it should be noted that a modified expression is also adopted when relating the effect of water vapour pressure to the rate expression. The pressure term shown in **equation (31)** is sometimes used with an exponent *n*, as shown in **equation (32)**:

$$h(p) = (1 - \frac{p_{eq}}{p})^n \tag{32}$$

This equation is mainly used for decomposition reactions where the gaseous product may further react with the decomposing reactants such as in oxidation or autocatalytic reactions; in these cases the reaction total pressure may depend more strongly on the local concentration or partial pressure of the product, hence a power relationship [82]. This is not the case for inorganic salt hydration, thus in this work, it is assumed that the dependency on the pressure term is first order, therefore the expression in **equation (31)**, i.e. **equation (32)** with *n = 1* The equilibrium vapour pressure is determined using the Clausius-Clapeyron relation (**equation (33)**):

$$p_{eq} = \exp\left(\frac{-\Delta H}{RT} + \frac{\Delta S}{R}\right) \tag{33}$$

The water vapour pressure, considered to be an ideal mixture of gaseous water and air, was determined using the ideal gas law (**equation (34)**):

$$p = cRT \tag{34}$$

The temperature-dependent kinetic rate constant can be parameterised through an Arrhenius-type equation as shown in **equation (35)**:

$$k(T) = A_f \, exp\left(\frac{-E_a}{RT}\right) \tag{35}$$

Thus, for sufficiently small variations of temperature, the kinetic rate is effectively constant. Fully developing each element of the kinetics equation shown in **equation (30)** yields the developed expression of the kinetics equation shown in **equation (36)**:

$$\frac{d\alpha}{dt} = A_f \, exp\left(\frac{-E_a}{RT}\right) f(\alpha)(1 - \frac{p_{eq}}{p}) \tag{36}$$

A database of all the considered solid-state kinetic models in this study is presented in **Table 14**. Over the years, many solid-state kinetic models have been proposed for a variety of underlying assumptions, with several being proven to be erroneous. The models discussed here are some of the most commonly used and have not shown to be problematic during the many instances of their application [84]. These solid-state kinetic models can be categorised into classes of models, based on their mechanistic assumption. These model classes are discussed here in the context of inorganic salt hydration.

- **Nucleation and growth models (A)** (also called Avrami models) are based on the assumption that the limiting step is the formation of salt hydrate nuclei at nucleation sites, the latter being generally found at surface features of the solid reactant phase, such as defects, imperfections, fissures etc... Certain hydration reactions have been shown to be described by nucleation models [84,163].
- **Geometrical models (R)**: differently from Avrami models, nucleation is considered to be instantaneous, and the reaction is controlled by the rate of progress of the reaction interface from the outside surface of crystal particles towards their centre. The different variations on geometrical contraction models are based on assumptions for the geometrical shape of the crystals.

Table 14 Reactions model database.

Model	f(α)	Integral form g(α)
nucleation models		
Avrami-Erofeyev (A2)	$2(1 - \alpha)[-\ln(1 - \alpha)]^{1/2}$	$[-\ln(1-\alpha)]^{1/2}$
Avrami-Erofeyev (A3)	$3(1 - \alpha)[-\ln(1 - \alpha)]^{1/3}$	$[-\ln(1-\alpha)]^{1/3}$
Avrami-Erofeyev (A4)	$4(1 - \alpha)[-\ln(1 - \alpha)]^{1/4}$	$[-\ln(1-\alpha)]^{1/4}$
geometrical contraction models		
Contracting area (R2)	$2(1-\alpha)^{1/2}$	$1-(1-\alpha)^{1/2}$
Contracting volume (R3)	$3(1-\alpha)^{2/3}$	$1-(1-\alpha)^{1/3}$
diffusion models		
1-D diffusion (D1)	$1/(2\alpha)$	α^2
2-D diffusion (D2)	$-[1/\ln(1 - \alpha)]$	$[(1-\alpha)\ln(1-\alpha)]+\alpha$
3-D diffusion (D3)	$[3(1 - \alpha)^{2/3}]/[2(1 - (1 - \alpha)^{1/3})]$	(1-(1-α)1/3)2
Ginstling-Brounshtein (D4)	$3/[2((1 - \alpha)^{-1/3} - 1)]$	$1-(2/3)\alpha-(1-\alpha)^{2/3}$
Valensi-Carter (VC)	$[3(1/(z-1))(1+(z-1)\alpha)^{1/3}(1-\alpha)^{1/3}]/[2((1-\alpha)^{1/3}-(1+(z-1)\alpha)^{1/3}]$	$[(1+(z-1)\alpha)^{2/3}+(z-1)(1-\alpha)^{2/3}-z]/[2(1-z)/r_o^2]$
reaction-order models		
First Order (F1)	$(1 - \alpha)$	$-\ln(1-\alpha)$

- **Diffusion models (D)** hinge on the assumption that the product (in this case the layer of hydrated salt) forms a barrier at the surface of crystal particles which increases in thickness as the reaction progresses, which limits access of the mobile reactant phase (water vapour) to the nucleation sites in the solid reactant phase (anhydrate salt). Reactions controlled by reactant diffusion are also referred to as being mass-transfer limited, and may play a role in reversible reactions [84], which is the case of salt hydration/dehydration. Similarly to geometrical models, the variants of diffusion models depend on the assumed shape of the reactant particles and the direction diffusion occurs in.
- **Order-based models (F)** are not based on any physical phenomenon, differently from all the previous classes of solid-state kinetic model. Order-based models hinge on the assumption that the reaction rate depends on the fraction of remaining reactant – similarly to homogenous reaction kinetic models where the rate depends on the remaining reactant concentration.

The reaction advancement is calculated from the experimental thermogravimetric data. The reaction advancement requires the knowledge of the mass of the sample at the beginning of the experiment $m(t_0)$, at any given time t $m(t)$, and, crucially, the mass at the end of the experiment $m(t_f)$.

$$\alpha(t) = \frac{m(t) - m(t_0)}{m(t_f) - m(t_0)} \tag{37}$$

5.2 Model fitting methods

In solid-state kinetics the selected method for numerical fitting of the kinetic models generally depends on the type of experimental data available, which in turn will depend on the type of experiment carried out. Hydration of inorganic salts is by definition an exothermic reaction, and at a given water vapour pressure can only be carried out over a short range of temperatures of roughly 30°C for K_2CO_3 (to the sesquihydrate) and for $MgCl_2$ (to the hexahydrate). Therefore, the hydration experiments were carried out isothermally (differently from having a constant heating rate, i.e. with a heating rate *dT/dt = 0*) at a temperature where full hydration should be ensured. These experimental choices allow for the model-fitting to be carried out using so-called non-linear model fitting [82], and with the assumption that the hydrations take place as a single-step reaction. Linear and non-linear fitting methods can be distinguished between integral and differential methods. In order to rigorously inspect the hydration kinetics of the chosen materials, model fitting was carried out using both methods.

Differential method

The differential fitting method consists in resolving the kinetics equation, shown in **equation (38)**.

$$\frac{d\alpha}{dt} = k(T)f(\alpha)(1 - \frac{p_{eq}}{p}) \tag{38}$$

The differential equation is resolved using the numerical solver *ode45* in Matlab which relies on a 4th order Runge-Kutta method. The fitting is then carried out, also in Matlab, with a Levenberg-Maquardt algorithm implemented via the function *lsqcurvefit*. The fitting is optimised by using the kinetic rate constant *k(T)* as the fitting parameter for the least-squares method.

Integral method

Fitting was also carried out using the integral fitting method, which hinges on the integration of the differential form of the kinetics equations, **equation (36)**, to obtain the following **equation (39)**:

$$g(\alpha) = \int_0^{\alpha} \frac{d\alpha}{f(\alpha)} = \int_0^{t} k(T)dt = k(T)t \tag{39}$$

Fitting the differential form of the kinetics is relatively demanding computationally since it involves the optimised resolution of the 1st order differential equation which can be further complicated by the form of the chosen kinetic model. The integral method provides a simpler method by directly applying the mathematical function of each model to the experimental data outside of the resolution process. This alternative method can be used comparatively with the differential fitting method. After integrating the equation, the transformation provided by the integral kinetic function g(α) is applied to the experimental advancement α_{exp}, leading to an approximate linearisation of the experiment data to which is fitted the linear function of time found on the right-hand side of **equation (39)** by varying the fitting parameter k(T).

Evaluation of fitting quality

To evaluate the quality of the model fitting procedures, two statistical indicators were used: coefficient of determination R^2 (see **equation (40)**) and the corrected Akaike information criterion estimator (**equation (41)**).

The coefficient of determination is calculated from the square of Pearson's correlation coefficient:

$$R^2 = \left(\frac{n\sum y_{exp}y_{num} - (\sum y_{exp})(\sum y_{num})}{\sqrt{\left(n\sum {y_{exp}}^2 - \left(\sum y_{exp}\right)^2\right)\left(n\sum {y_{num}}^2 - (\sum y_{num})^2\right)}}\right)^2 \tag{40}$$

In the definition of the coefficient of determination **equation (40)**, the subscripts *exp* and *num* refer to experimentally obtained data and numerically calculated data, respectively.

$$AICc = nlog\left(\frac{R^2}{n}\right) + 2P \tag{41}$$

In **equations (40)** and **(41)**, *n* is the number of experimental points for each hydration experiment carried out in the DVS, and *P* is the number of estimable parameters, which is equal to 1, with the rate constant *k* the fitting parameter for both integral and differential methods. Models with the lowest AICc values and coefficient of determination R^2 values closest to 1 may be considered the most accurate.

Evaluation framework

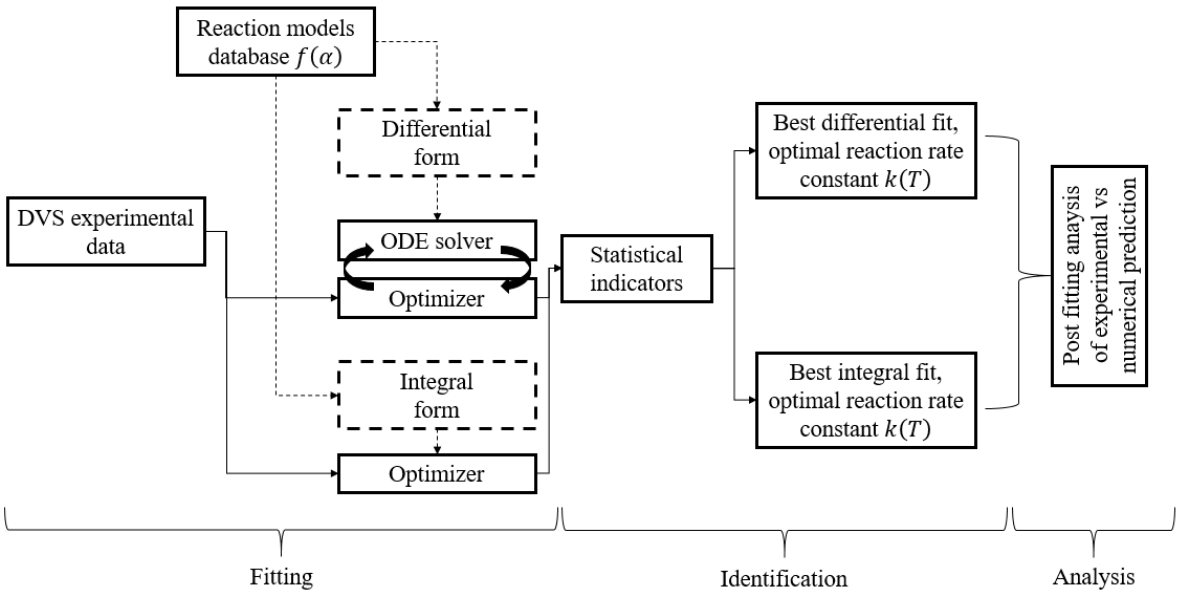

Figure 33 Framework for the evaluation of reaction models for salt hydration.

The complete evaluation procedure, starting from the thermogravimetric experimental data obtained via the DVS to the derivation of accurate kinetic models with the analysis of the rate-limiting processes, is shown in **Figure 33**. The evaluation framework consists of three key sub-steps:

- The fitting sub-step hinges on the coupling of an ODE solver (*ode45* in Matlab) with a numerical optimiser (least squares optimiser *lsqcurvefit* in Matlab), using both differential and integral fitting methods, to derive the best fitting parameter *k*.
- The identification sub-step is based on the quantitative comparison between fitting results obtained for both integral and differential fitting methods in order to clearly distinguish the best fitting solid-state kinetic models.
- The analysis sub-step hinges on the combination of the fitting results obtained through the two previous steps and the analysis of the pure thermogravimetric data to infer the rate-limiting process for each hydration reaction and achieve an improved understanding of the underlying dominant physical phenomena.

6 Kinetic study of salt and SIM hydration

In the following paragraphs the results emerging from the assessment of solid-state kinetic models for the thermogravimetric data presented in the previous section are discussed. For this study, the kinetic models presented in **Section 5** were selected on the basis that they encompass kinetic models considered by the scientific community for solid-gas reactions such as inorganic salt hydration. 11 models were selected and may be sorted within the following categories: (A) nucleation models, (R) geometrical contraction models, (D) diffusion models, (VC) the Valensi-Carter diffusion models and (F) the first-order model.

6.1 $MgCl_2$

In **Figure 34a** to **Figure 34d** the experimental thermogravimetric results obtained by DVS measurement with the most accurately fitted kinetic models are compared. As was discussed in **section 5**, two numerical fitting procedures were used to assess the precision of the different models in predicting the experimental method, the integral and differential methods. **Figure 34a** and **Figure 34c** show the comparison of the experimentally obtained mass reaction advancement ($\check{U}$) curves with solid-state kinetic models fitted using the differential method. In tandem, **Figure 34b** and **Figure 34d** show the comparison with solid-state kinetic models fitted using the integral procedure. A very strong agreement may be observed between experimental results and numerical values. Geometrical contraction kinetic model R3 and the diffusion model VC predict the reaction very well until α~0.8, after which the models tend to overestimate the rate of advancement of the reaction. First-order model F1 provides an excellent prediction of the reaction behaviour throughout the entire experiment. This latter model is based on the linear decrease of the reaction rate $d\alpha/dt$ as the reaction progresses (i.e., α trends towards 1), which explains its robustness for the considered reaction, accompanied by the assumption of near-equilibrium behaviour of the reaction.

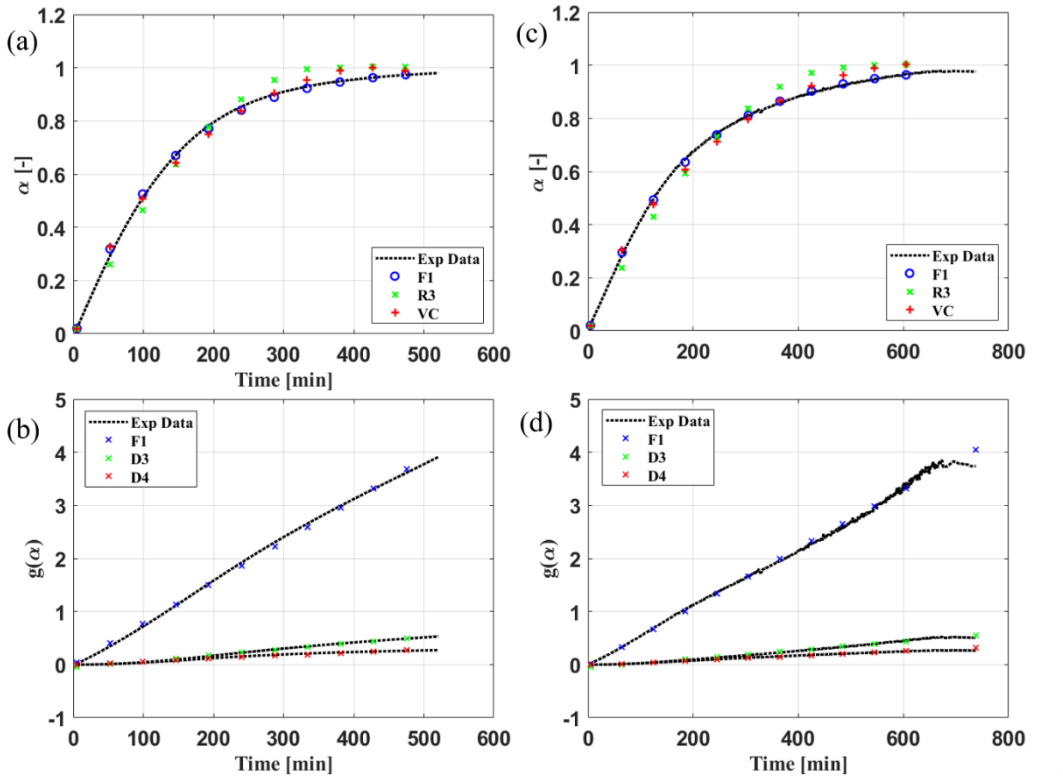

Figure 34 Differential and integral fit of kinetic models to $MgCl_2$ hydration at 25°C (a)(b) and 40C (c)(d).

However, due to the phenomenon (or lack of physical phenomenon) underpinning its derivation, the first-order kinetic model does not point towards any specific reaction mechanism, and as a result cannot be used to derive any understanding of the rate-limiting phenomena of the hydration reaction. On the other hand, the good fitting accuracy of the VC and R3 model (up to α~0.8) points towards the fact that bulk/intraparticle diffusion does not limit the hydration reaction – indeed these two models are derived from the assumption that the reaction is limited by phenomena occurring at the particle level (diffusion and solid-gas interface contraction, respectively), and that intraparticle diffusion time may be considered negligible and therefore non-limiting.

The detailed fitting accuracy of the different kinetic models to the hydration behaviour of $MgCl_2$, as evaluated by the statistical indicators R^2 (see **equation (40)**) and AICc (see **equation (41)**), are shown in **Table 15**. In most cases, a high value of R^2 is accompanied by a corresponding high value of AICc, with the only exception being the integral fitting of the VC model at both 25°C and 40°C– this exception can be explained by the mild non-linear behaviour towards the end of the reaction at 40°C that F1 is not able to capture.

	Differential Fit			Integral Fit		
	25°C					
	k [min^{-1}]	R^2	AICc	k [min^{-1}]	R^2	AICc
A2	6.71E-03	0.986	-5800	3.11E-03	0.951	-6955
A3	5.95E-03	0.968	-5010	1.98E-03	0.912	-7394
A4	5.25E-03	0.956	-4716	1.46E-03	0.887	-7899
R2	2.79E-03	0.992	-7258	1.58E-03	0.924	-8335
R3	2.05E-03	0.996	-8516	1.39E-03	0.959	-9734
D1	2.79E-03	0.970	-6770	1.98E-03	0.892	-7037
D2	2.10E-03	0.987	-6298	1.97E-03	0.953	-8472
D3	6.97E-04	0.983	-5471	1.16E-03	0.994	-13300
D4	5.36E-04	0.988	-5977	3.11E-03	0.976	-13217
F1	7.72E-03	0.999	-9703	7.77E-03	0.998	-8896
VC	3.23E-04	0.989	-6191	3.29E-04	0.972	-14798
	40°C					
	k [min^{-1}]	R^2	AICc	k [min^{-1}]	R^2	AICc
A2	4.83E-03	0.977	-7846	2.28E-03	0.962	-9684
A3	4.34E-03	0.957	-6885	1.47E-03	0.924	-9977
A4	3.86E-03	0.944	-6521	1.09E-03	0.899	-10528
R2	1.97E-03	0.985	-9521	1.19E-03	0.948	-11640
R3	1.46E-03	0.992	-10800	1.03E-03	0.977	-13879
D1	1.95E-03	0.964	-9892	1.52E-03	0.930	-10008
D2	1.48E-03	0.987	-9719	1.47E-03	0.981	-12883
D3	4.96E-04	0.988	-8394	8.16E-04	0.990	-16516
D4	3.79E-04	0.990	-9227	2.28E-03	0.995	-20190
F1	5.50E-03	0.999	-15943	5.51E-03	0.997	-11598
VC	2.28E-04	0.990	-9572	2.42E-04	0.992	-21793

Table 15 Kinetic model agreement with experimental data of $MgCl_2$ hydration.

While good agreement with the experimental data was obtained for most models, the highest accuracy was obtained, in the case of the differential fitting method, for models F1 and R3 (R^2>0.999) at 25°C, and for models F1, R3 and D4 at 40°C. By observing **Table 8**, it can be seen that the F1 was among the top three most accurate models in terms of either R^2 or AICc in six instances out of maximum of eight (two temperatures, two fitting methods and two statistical indicators). Thus, these results highlight the robustness of F1 in predicting $MgCl_2$ hydration behaviour. Additionally, models R3/D3/D4 were all among the top three most accurate models in four instances, showing accuracy very similar to F1 in terms of R^2 and AICc. These three models are all derived from the similar assumption that the limiting mechanism occurs at the scale of the individual particle, either intraparticle diffusion or solid-gas interface evolution from particle surface to the core. This results sheds light on $MgCl_2$ hydration's rate limiting phenomenon.

6.2 K_2CO_3

Figure 35 and **Table 16** show the results of fitting the solid-state kinetic models to the hydration data of pure potassium carbonate. Two points need to be highlighted in order to discuss these numerical results:

- The determination of the reaction advancement requires knowledge of the reactive samples final mass [164]. In this case the chosen final value of the sample mass is the final experimentally measured value, even if the mass would likely have continued to evolve had the experiment been continued.
- In these experimental conditions, as was discussed in **section 3.2**, the hydration of potassium carbonate displays very poor kinetics, with an obvious diffusional effect hindering the samples mass uptake.

Thus, in the present section, the kinetic analysis of the thermogravimetric data of K_2CO_3 hydration aims to assess the validity of the kinetic models in predicting the experimentally obtained behaviour, and therefore with particular focus on the early stages of this reaction (fast hydration regime leading to the slow hydration regime).

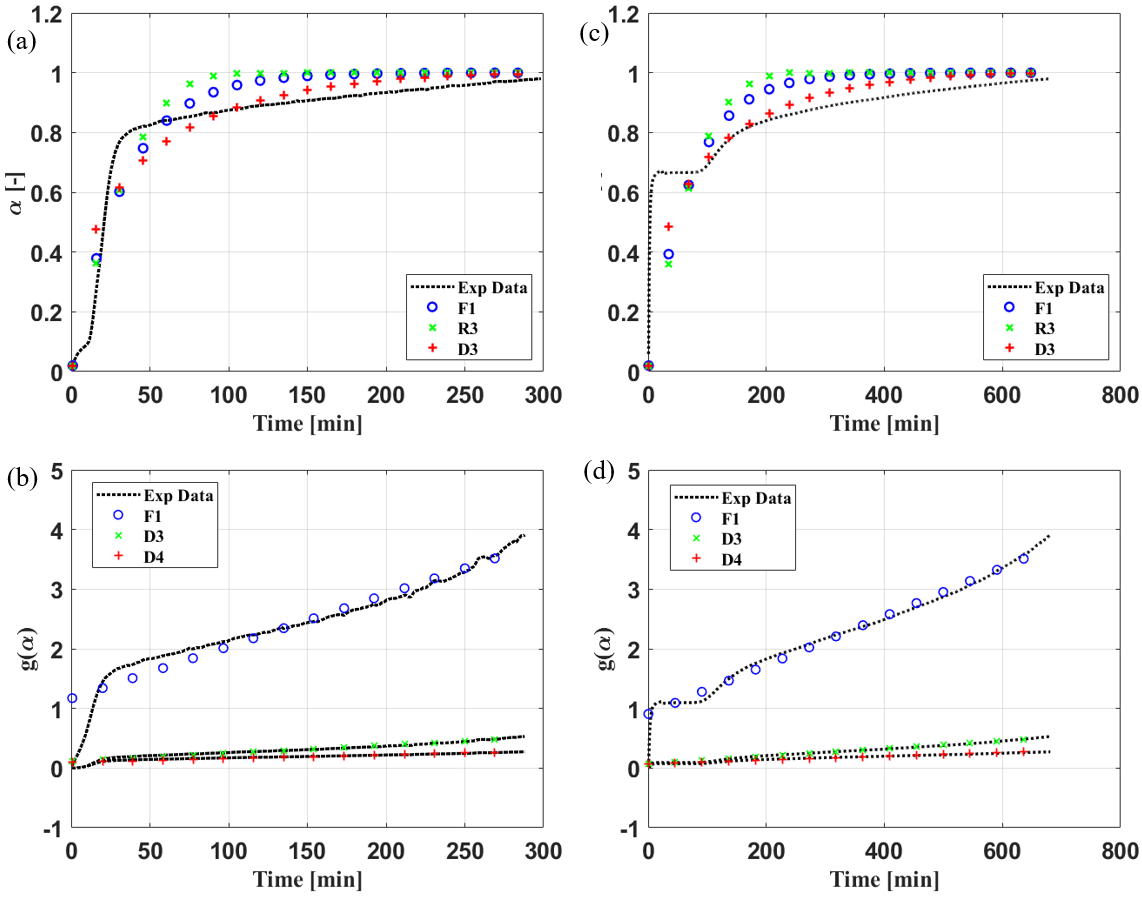

Figure 35 Differential and integral fit of kinetic models to K_2CO_3 hydration at 25°C (a)(b) and 40C (c)(d).

Table 16 shows the quality of the fit of the solid-state kinetic models to the thermogravimetric hydration data of K_2CO_3. Differently than for $MgCl_2$, it can be seen from the R^2 values that the models fitted very poorly with the differential method to the experimental data, with the standout models being F1 at 25°C (R^2 = 0.9089) and D2 at 40°C (R^2 = 0.9470). It was found in the analysis of the thermogravimetric data that the hydration of K_2CO_3 begins with a fast mass uptake, before entering a slow hydration regime with a linear and slow increase in water uptake. Observation of the fitted differential curves of the kinetic models to the experimental data (**Figure 35a** and **Figure 35c**) shows that the kinetic models are not able to capture the relatively complex thermogravimetric behaviour of the sample, in particular when shifting from fast hydration kinetics to the slow regime. The kinetic models also tend to end in a plateau, whereas the hydration of K_2CO_3 displayed a linear, albeit very slow, steady increase. Greater accuracy was achieved however when fitting the kinetic models using the integral fitting method. In this case models D3 and D4 consistently ranked among the top 3 models for both temperatures, closely followed by F1 and VC, which points overall to diffusion models being most suitable for predicting K_2CO_3 hydration behaviour in the case of integral fitting, particularly at 40°C where coefficient of determination values of R^2>0.95 were obtained.

	Differential Fit			Integral Fit		
			25°C			
	k [min^{-1}]	R^2	AICc	k [min^{-1}]	R^2	AICc
A2	5.66E-02	0.8907	-4013	3.03E-03	0.802	-3587
A3	5.10E-02	0.8785	-3935	1.81E-03	0.735	-4146
A4	4.49E-02	0.8714	-3900	1.30E-03	0.696	-4563
R2	8.63E-03	0.7521	-3107	1.44E-03	0.730	-4521
R3	1.58E-02	0.8917	-4141	1.37E-03	0.811	-5012
D1	5.19E-03	0.6202	-2689	1.67E-03	0.640	-3901
D2	6.05E-03	0.7546	-3520	1.93E-03	0.805	-4386
D3	3.73E-03	0.8826	-4765	1.36E-03	0.947	-6251
D4	2.18E-03	0.8323	-4131	3.03E-03	0.873	-6752
F1	5.23E-02	0.9089	-4348	8.73E-03	0.919	-2647
VC	1.26E-03	0.8225	-4024	3.39E-04	0.857	-7701
			40°C			
	k [min^{-1}]	R^2	AICc	k [min^{-1}]	R^2	AICc
A2	1.62E-02	0.4944	-7473	1.40E-03	0.969	-12288
A3	4.42E-02	0.2080	-7341	8.26E-04	0.951	-13500
A4	4.67E-02	0.1846	-7321	5.84E-04	0.939	-14430
R2	3.17E-03	0.9015	-7290	6.81E-04	0.940	-13826
R3	3.88E-03	0.7013	-8085	6.48E-04	0.966	-15266
D1	2.12E-03	0.9221	-6738	8.26E-04	0.885	-11586
D2	2.21E-03	0.9470	-8514	9.53E-04	0.949	-12815
D3	1.16E-03	0.8863	-10374	6.51E-04	0.992	-18320
D4	8.80E-04	0.8887	-9375	1.40E-03	0.973	-18799
F1	1.41E-02	0.7565	-8569	4.09E-03	0.988	-9913
VC	8.41E-04	0.8701	-7408	1.66E-04	0.969	-20997

Table 16 Kinetic model agreement with experimental data of K_2CO_3 hydration.

6.3 $MgCl_2$ / vermiculite composite

Table 17 shows the quality of the fit of the solid-state kinetic models to the thermogravimetric hydration data of the $MgCl_2$/vermiculite composite. AICc values in the range of 10^2-10^3 show that the fitting of the kinetic models is carried out with less accuracy for this composite than to the associated pure salt (AICc~10^4). This is due to numerical rather than physical reasons: the composite material achieves its maximum mass uptake significantly faster than the pure material, resulting in a lower number of datapoints, which for the least squares fitting method results in a lower quality fit. This phenomenon further explains the discrepancy in accuracy between the experiment carried out at 25°C (the shorter reaction leading to less accurate model fitting) and the hydration at 40°C (slower, resulting in higher fitting precision).

	Differential Fit			Integral Fit		
	25°C					
	k [min-1]	R^2	AICc	k [min-1]	R^2	AICc
A2	2.23E-02	0.9969	-1565	1.54E-02	0.968	-1642
A3	1.78E-02	0.9903	-1301	9.95E-03	0.940	-1719
A4	1.47E-02	0.9850	-1208	7.39E-03	0.920	-1816
R2	1.05E-02	0.9989	-2189	7.83E-03	0.947	-1934
R3	7.86E-03	0.9981	-1996	6.83E-03	0.970	-2231
D1	1.18E-02	0.9895	-1394	9.79E-03	0.920	-1625
D2	8.33E-03	0.9810	-1204	9.52E-03	0.957	-1869
D3	2.63E-03	0.9593	-1066	5.52E-03	0.973	-2425
D4	2.09E-03	0.9742	-1148	1.54E-02	0.969	-2820
F1	2.92E-02	0.9896	-1509	3.77E-02	0.989	-1405
	40°C					
	k [min^{-1}]	R^2	AICc	k [min^{-1}]	R^2	AICc
A2	1.30E-02	0.9980	-2668	1.15E-02	0.997	-3278
A3	1.03E-02	0.9924	-2149	7.62E-03	0.984	-2841
A4	8.57E-03	0.9874	-1974	5.75E-03	0.970	-2816
R2	6.18E-03	0.9991	-3351	5.99E-03	0.993	-3427
R3	4.57E-03	0.9964	-2744	5.06E-03	0.996	-3826
D1	6.88E-03	0.9882	-2028	7.64E-03	0.978	-2699
D2	4.73E-03	0.9737	-1785	7.04E-03	0.978	-2783
D3	1.45E-03	0.9497	-1610	3.70E-03	0.932	-2824
D4	1.17E-03	0.9658	-1715	1.15E-02	0.969	-3730
F1	1.68E-02	0.9980	-2217	2.59E-02	0.970	-1463

Table 17 Kinetic model agreement with experimental data of $MgCl_2$/Vermiculite composite hydration.

A notable observation that can be made from **Table 17** is that there is no significant change in ranking of most accurate kinetic models between temperatures. Indeed at 25°C, models R2 and R3 were fitted differentially with R^2>0.998 and with AICc<-1900, and at 25°C these same models are fitted

differentially with R^2>0.996 and AICc<-2700; these are amongst the top-ranking models, except for R3 which ranks lower than F1 and A2 at 40°C according to R^2 with the differential method.
A similar observation can be made for the integral method, with which model R3, D4 and D3 are the top-ranking models at 25°C (R^2 > 0.96 and AICc < -2.2 10^3) and 40°C (R^2 > 0.96 and AICc < -3.6 10^3). Interestingly, all (R) and (D) models share similar geometrical assumptions leading to their derivation, which suggests that for $MgCl_2$/vermiculite hydration as a whole (both fitting methods, both temperatures), mechanisms at the intraparticle level (either diffusion or interface mobility) are controlling the entire process at both temperatures.

Figure 36 shows the comparison between the experimental thermogravimetric results of $MgCl_2$/vermiculite hydration obtained by DVS measurement and the most accurately fitted kinetic models. Kinetic models R2 and R3 can be seen to fit with high fidelity the experimental data, even late into the reaction at α>0.8, which would point towards the hydration being limited by the mobility of the reaction interface, from particle surface towards its core. This rate-limiting process is in line with the findings discussed in **section 3**, where hydration was found to take place at the surface of the composite first (due to salt deposited on the surface), then followed by hydration salt found deeper within the pore structure of the vermiculite.

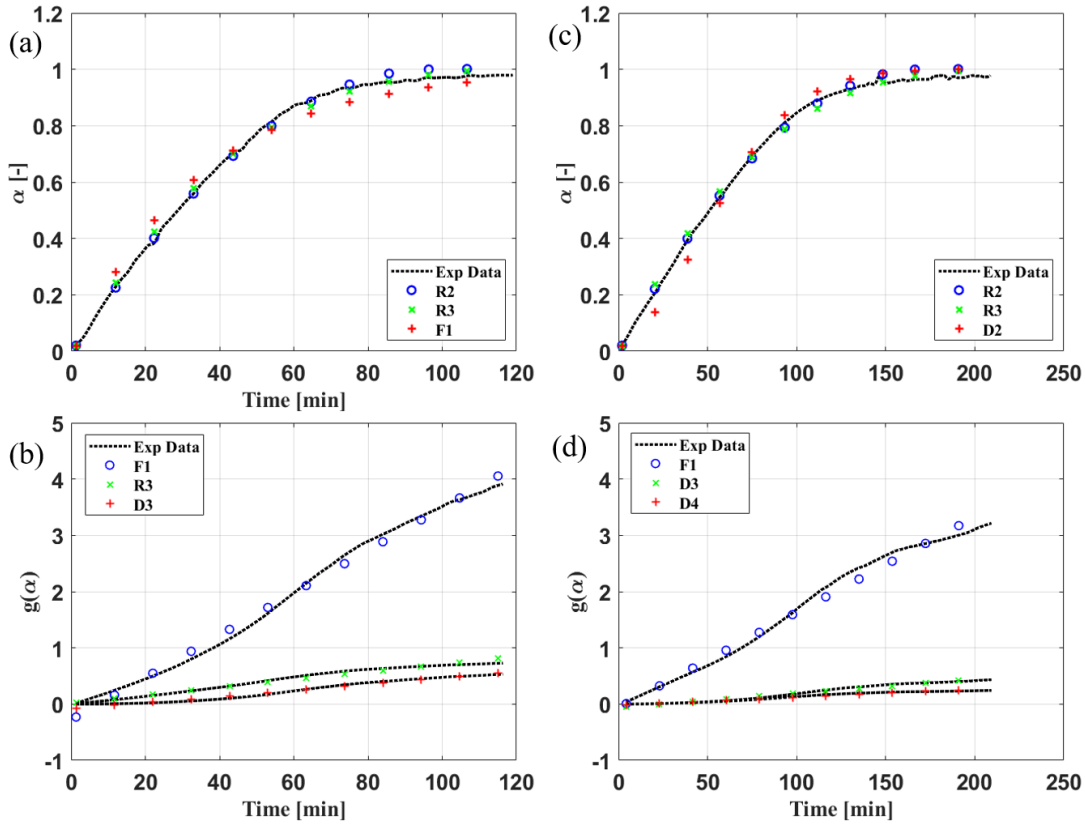

Figure 36 Differential and integral fit of kinetic models to $MgCl_2$/Vermiculite composite hydration at 25°C (a)(b) and 40C (c)(d).

Differently from pure $MgCl_2$, the first-order model F1 underestimates the sample mass uptake late into the reaction. This is indicative that the bulk diffusion mechanism, discussed for pure $MgCl_2$, is not a limiting mechanism in the case of the $MgCl_2$/vermiculite composite's hydration. This finding is supported by the known property of porous matrixes of substantially improving water mass transport compared to raw inorganic salts, and therefore minimising the impact of interparticle vapour diffusion as a rate-limiting process. Therefore, from the evidence and results presented here, it may be concluded that the rate-limiting mechanism of $MgCl_2$/vermiculite hydration takes place at the individual particle level (intraparticle diffusion or interface progression from particle surface to core), and that the interparticle/bulk diffusion phenomenon that was observed for pure $MgCl_2$ hydration is not a limiting factor when the salt is dispersed into vermiculite.

6.4 K_2CO_3 / vermiculite composite

Table 18 shows the quality of the fit of the solid-state kinetic models to the thermogravimetric hydration data of the K_2CO_3/vermiculite composite, as well as the associated kinetic rate constants. AICc values in the range 500~1000 show that the kinetic models are fitted to the K_2CO_3/vermiculite composite hydration data with less accuracy than for the $MgCl_2$/vermiculite (AICc values in the range 1000~5000); as discussed previously in **section 6.3** this is due to the lower water mass uptake of the K_2CO_3/vermiculite (~8% mass uptake, see **Figure 37**, whereas the $MgCl_2$/vermiculite showed a maximum uptake of ~30%, see **Figure 36**) resulting in a shorter experiment and therefore a lower number of experimental data points. The lower mass uptake of the K_2CO_3/vermiculite is due to:

- Raw K_2CO_3 has lower water uptake than raw $MgCl_2$ from a stoichiometric point of view.
- Vermiculite composite can accommodate more salt due to the respective solubility limits (see material salt and matrix contents in **Table 18**).

Furthermore, this effect of length of experiment correlating to fitting accuracy extends to the change in temperature during hydration. The accuracy of the fitting of the experimental data of the hydration is higher at 40°C (AICc~3000 to 8000) than at 25°C. Similarly, to the $MgCl_2$/vermiculite composite, this difference in accuracy can be attributed to the shorter experimental time due to faster mass uptake at 25°C than at 40°C, and thus a lower number of experimental data points.

Unlike what was observed for pure $MgCl_2$ and for the $MgCl_2$/vermiculite, a change in onset hydration temperature from 25°C to 40°C at constant water vapour pressure appears to change the best fitting kinetic models to the thermogravimetric data of K_2CO_3/vermiculite composite hydration, as can be observed from the fitting results shown in **Table 18**.

- At 25°C, nucleation models A3 and A4 (R^2 ~ 0.99, AICc ~ 1000, for both integral and differential fitting methods) are the best fitting models to K_2CO_3/vermiculite composite hydration.
- At 40°C, first order model F1 (R^2~0.99, AICc~5000) and geometrical contraction models R2 and R3 (AICc~5000, R^2~0.99 for differential fitting, R^2~0.97 for integral fitting) are the most accurate kinetic models.

	Differential Fit			Integral Fit		
			25°C			
	k [min^{-1}]	R^2	AICc	k [min^{-1}]	R^2	AICc
A2	4.20E-02	0.9960	-676	4.64E-02	0.992	-748
A3	3.38E-02	0.9997	-1004	3.27E-02	0.999	-1128
A4	2.81E-02	0.9986	-777	2.55E-02	0.996	-987
R2	1.99E-02	0.9820	-517	2.34E-02	0.978	-795
R3	1.44E-02	0.9742	-487	1.92E-02	0.964	-784
D1	2.13E-02	0.9465	-401	2.87E-02	0.947	-631
D2	1.37E-02	0.9196	-374	2.52E-02	0.918	-604
D3	3.91E-03	0.8883	-351	1.26E-02	0.835	-680
D4	3.31E-03	0.9088	-365	2.52E-02	0.896	-887
F1	5.08E-02	0.9557	-444	9.31E-02	0.906	-253
			40°C			
	k [min^{-1}]	R^2	AICc	k [min^{-1}]	R^2	AICc
A2	9.09E-03	0.9917	-3847	5.74E-03	0.979	-4421
A3	7.35E-03	0.9824	-3350	3.70E-03	0.955	-4479
A4	6.16E-03	0.9759	-3164	2.74E-03	0.939	-4696
R2	4.21E-03	0.9900	-4418	3.02E-03	0.965	-5025
R3	3.15E-03	0.9944	-5089	2.59E-03	0.987	-6063
D1	4.55E-03	0.9728	-4189	3.90E-03	0.947	-4255
D2	3.38E-03	0.9815	-3835	3.71E-03	0.987	-5489
D3	1.12E-03	0.9700	-3325	2.02E-03	0.983	-6257
D4	8.61E-04	0.9793	-3634	3.71E-03	0.995	-8215
F1	1.19E-02	0.9917	-5097	1.37E-02	0.996	-4307

Table 18 Kinetic model agreement with experimental data of K_2CO_3/Vermiculite composite hydration.

Thus, it may be inferred from these results that hydration of the K_2CO_3/vermiculite composite at 25°C is controlled by nucleation and growth of hydrate crystals $K_2CO_3 \cdot 1.5H_2O$ in the pores and surface of the vermiculite i.e. the transport of water molecules to adsorption sites can be seen as near-instantaneous compared to the actual adsorption and crystallisation step. On the other hand the dominant mechanism at 40°C (with a decreased water concentration in the air) is shifted to intraparticle reaction interface progress as the pores of the material are less saturated with water molecules which take more time to travel and occupy the adsorption sites.

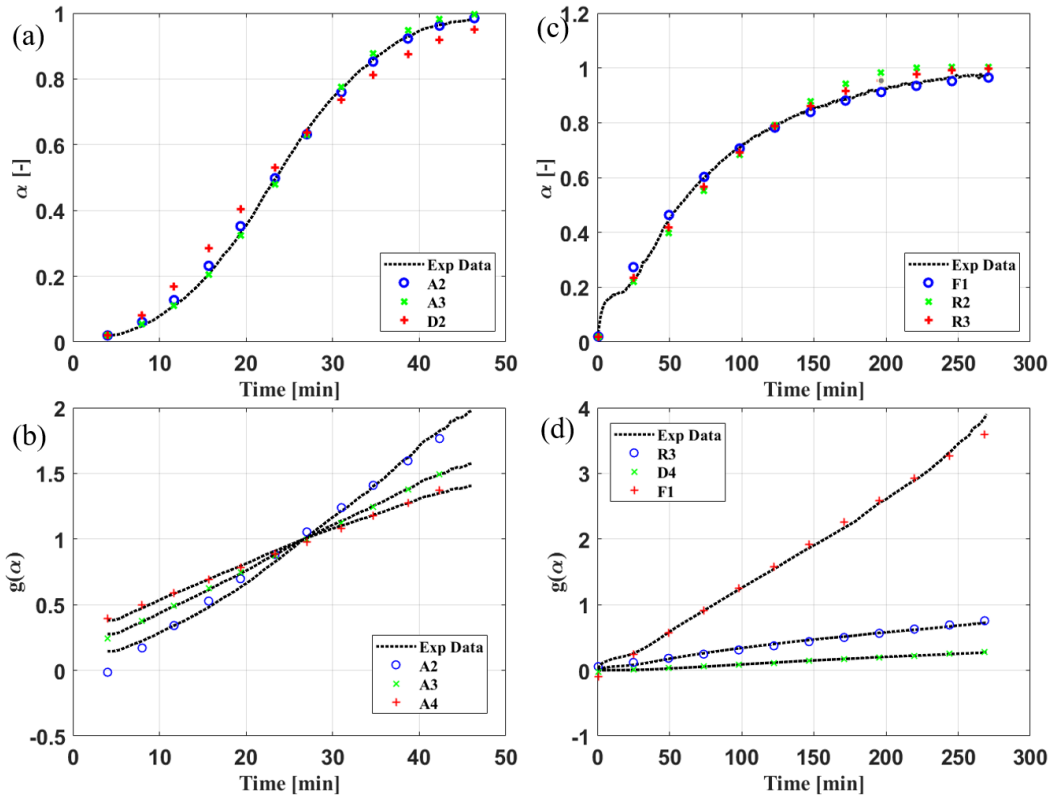

Figure 37 Differential and integral fit of kinetic models to K_2CO_3/Vermiculite composite hydration at 25°C (a)(b) and 40°C (c)(d)

In **Figure 37** the numerically fitted curves of the most accurate kinetic models in predicting the experimental outcome of K_2CO_3/vermiculite hydration can be appreciated. As was discussed in the previous paragraph, it can be seen from **Figure 37a** that the nucleation and growth models A2 and A3 fit very accurately the mass uptake of the composite at 25°C/7.5 mbar over the entire experimental duration, whereas **Figure 37c** shows the high accuracy of R2 and R3 in predicting the experimental outcome at 40°C/7.5 mbar.

Based on the data and evidence presented here and in the previous paragraph, it may be inferred that:

- At 40°C, the nucleation and growth of hydrate crystals from water molecules is faster than the transport of these water molecules to all of the unreacted regions of the sample. Thus, the hydration process is controlled by reaction interface progress (F1, R2 and R3 models).
- On the other hand, at 25°C, and therefore further from the equilibrium line (**Figure 13**) and at higher relative humidity than 40°C, humidity is sufficiently high for water transport to be non-limiting, i.e., all regions of the sample are in contact with water molecules, and therefore the rate-limiting mechanism of the reaction is nucleation and growth of new salt hydrate nuclei (A3 and A4 models).

7 Conclusions

In this chapter, the hydration kinetics of $MgCl_2$ and K_2CO_3, both in pure form and dispersed into a vermiculite host-matrix, were comprehensively assessed in view of TCS applications. The limiting processes underlying the hydration kinetics of these materials, the effect of dispersing the bulk salts into a host matrix on hydration kinetics, and the accuracy of solid-state kinetic models were all investigated. This work distinguishes itself from previous studies as it considers for the first time the hydration reaction of inorganic salts within the framework of solid-state kinetics. Through this framework the impact of salt dispersion into a host matrix was quantified, and suitable kinetic models were proposed for hydration outside of the typical order-based modelling. Key conclusions of this chapter are the following:

- In the conditions of the DVS, the hydration of $MgCl_2$ took place between the monohydrate and the hexahydrate during an adsorption reaction that appears to be kinetically controlled by a combination of bulk and particle-level diffusion. On the other hand, the hydration of K_2CO_3 from anhydrate state to the sesquihydrate was found to be severely kinetically hindered by the formation of a so-called diffusion barrier. This diffusional barrier was found to scale with sample size, which indicates that the rate-limiting mechanism occurs at the bulk sample scale rather than at the intraparticle level.

- The hydration of $MgCl_2$ is likely dominated by the movement of a reactant/product phase boundary that progresses from the surface to the core of individual salt particles and was found to be best modelled by first-order model F1 and diffusion model D4. Chemical reaction dictates the reaction rate at the beginning of the hydration before gradually being taken over by intraparticle diffusion. Due to the so-called diffusional barrier along with hydration conditions departing from equilibrium conditions leading to non-conventional behaviour, the hydration of K_2CO_3 was poorly modelled by typical solid-state kinetic models.

- Dispersion of the two salts in a vermiculite host matrix, with salt contents approximately 50 wt% increased the reaction rate 5 to 10-fold. In the case of K_2CO_3, the diffusional barrier was eliminated through impregnation. Analysis of the thermogravimetric data points in both cases towards a two-step hydration process: hydration of the salt particles on the surface of the host matrix, followed by hydration of the salt located in the bulk of the matrix.

- Dispersion of the two salts in vermiculite results in a notable shift in dominant reaction mechanism. Hydration of $MgCl_2$-vermiculite was best modelled by R2 and R3, phase-boundary control models, without significant change due to temperature. Differently, the rate-controlling mechanism during hydration of K_2CO_3-vermiculite was affected by temperature: nucleation controls the reaction at 25°C, with the best models being A2 and A3, whereas particle diffusion or phase boundary controls the hydration at 40°C which was best modelled by R2 and R3.

Kinetic models identified in this work are valid within the range of sample sizes from 10 mg to 100 mg, in temperature/humidity conditions typical of low-temperature TCS in open systems, and for composites with ~50 wt. % salt content. The specific results may be used in future works operating in the same parameter range; however fundamental behaviour behind salt/SIM hydration has been discussed which extends the range of applicability of the present findings. The local kinetic models developed here are intended to complement large scale kinetic models in the literature rather than replace them. These models will be used in the next chapter to evaluate how the choice of kinetic models may impact the predicted performance of larger scale TCS systems.

Chapter IV. Techno-Economic Performance of TCS Processes for Space Heating in Dwellings

*A review of the TCS literature in **Chapter II** revealed that advanced kinetic models for the hydration of inorganic salts and salt-in-matrix composites were lacking. Consequently, in **Chapter III**, the dynamic behaviour of the hydration of two promising salts, K_2CO_3 and $MgCl_2$, in bulk form and dispersed into a vermiculite host matrix, was evaluated with solid-state kinetic analysis. Insight was gained into the dominant mechanisms of these hydration reactions, and more advanced solid-state kinetic models were derived as alternatives to the generally used first-order model. Indeed, from the literature review it was also shown that the majority of time-dependent TCS simulations use first-order models for the reaction kinetics. As has been discussed, improving the understanding surrounding hydration behaviour is necessary to progress TCS, and work in **Chapter III** attempted to address this. However, from an end-user's standpoint it is also of how material scale kinetics affect the overall performance of TCS processes, i.e. research objective Q3 (What impact do the selected thermochemical material (TCM) and the reaction kinetics have on the performance of sorption-based low-temperature TCS processes?) discussed in **Chapter I**.*

*The aim of **Chapter IV** is to quantify the impact of choice of TCM and kinetic model on the performance of a TCS process, in the context of an integrated storage system in a dwelling for solar heat from a solar thermal system. To achieve this research objective, the chapter is structured as follows. A general discussion on the background to this chapter is carried out in **section 1**. Then **section 2** shows the reference scenario accounting for realistic operating conditions and for heating demand, a presentation of the TCS and its basic operation strategy, a description of the relevant chemical process, and finally the justification for the choice of TCMs. In **section 3**, the modelling methodology is presented. The main elements of the model are a reduced geometry quasi-1D reactor model, a model for the solar collector that gathers solar energy for storage and a model for the two heat exchangers. Model validation and the behaviour of the process in a so-called "basic" constant operating conditions are presented in **section 4**. A techno-economic analysis of the TCS process is carried out in **section 5** after having introduced the set of KPIs used to quantify performance. The analysis is then completed in **section 6** through a sensitivity analysis with regards to the selected kinetic model and the kinetic rate constants, using models developed in **Chapter III** and in the literature.*

1 Introduction

The energy storage density and overall performance of inorganic salts are well quantified at the material scale so that their theoretical performance is now well known [19,23]. Energy storage density at the sample scale can be measured with a variety of different methods, the most common being

differential scanning calorimetry which can also be combined with thermogravimetric analysis. While the performance of TCS sorption reactors and processes depends on the performance of the TCM, it is also tied to the mechanisms of heat and mass transfer driving the hydration/dehydration reaction at the reactor scale, which can limit the theoretical performance predicted at the material scale.

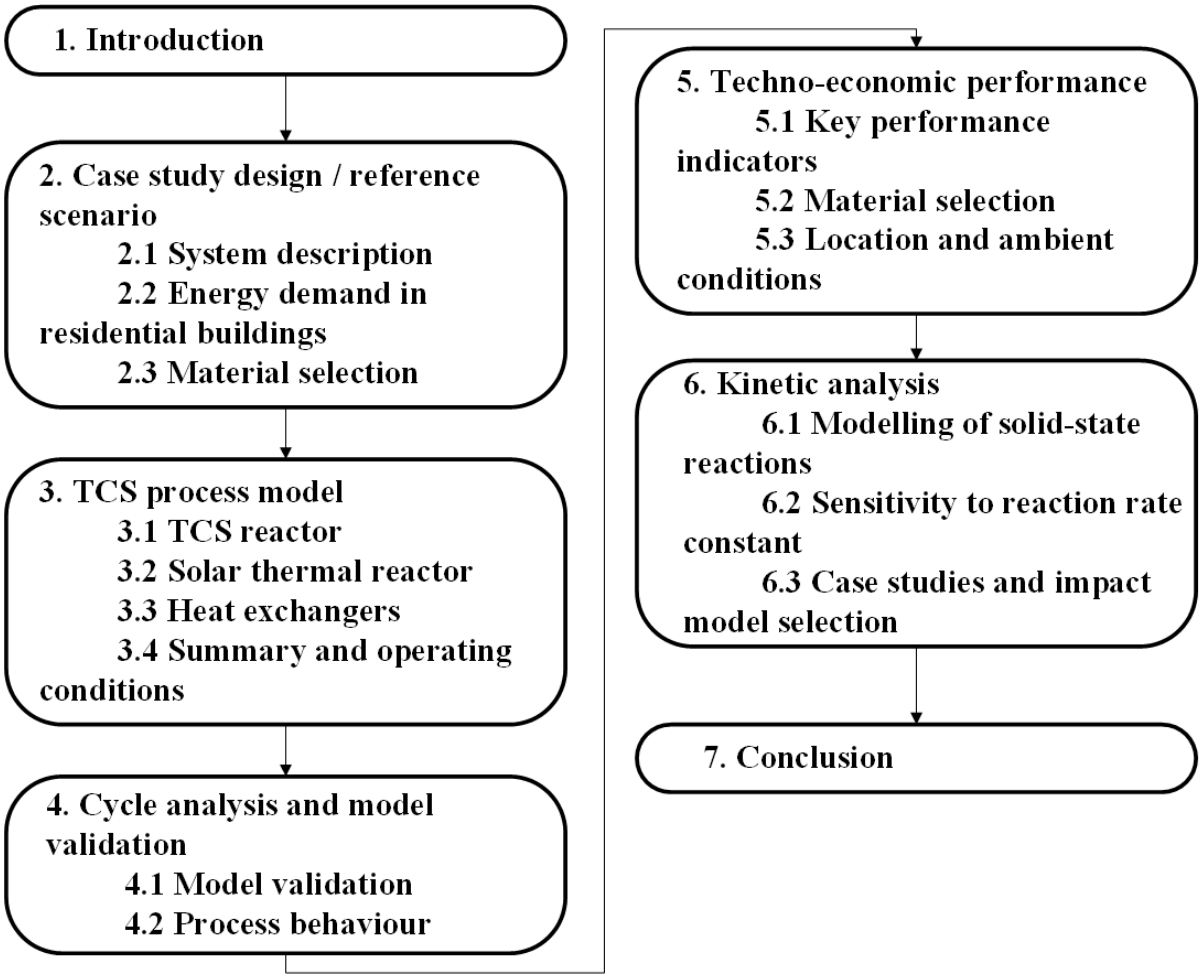

Figure 38 Chapter IV mapped structure.

In addition, kinetics play as important a role as thermodynamic properties and heat and mass transfer in affecting the power output of TCS systems [108,127] (in **Chapter II** a review of the current literature surrounding inorganic salt hydration/dehydration kinetics was covered). The role of dynamic effects (i.e. chemical kinetics, and heat and mass transfer) on overall performance can be appreciated when introducing larger amounts (kilograms and above) of material in a TCS reactor compared to the typical amounts used for material characterisation (milligrams). The calculated energy storage density at the reactor scale is typically much lower than the material-scale measured energy storage density (see **Figure 39**). The presence of parts of reactor structure and process elements such as fans, humidifiers or heat exchangers further increases the total volume of the process and contributes to decreasing the energy storage density measured at the process scale compared to material and reactor scales.

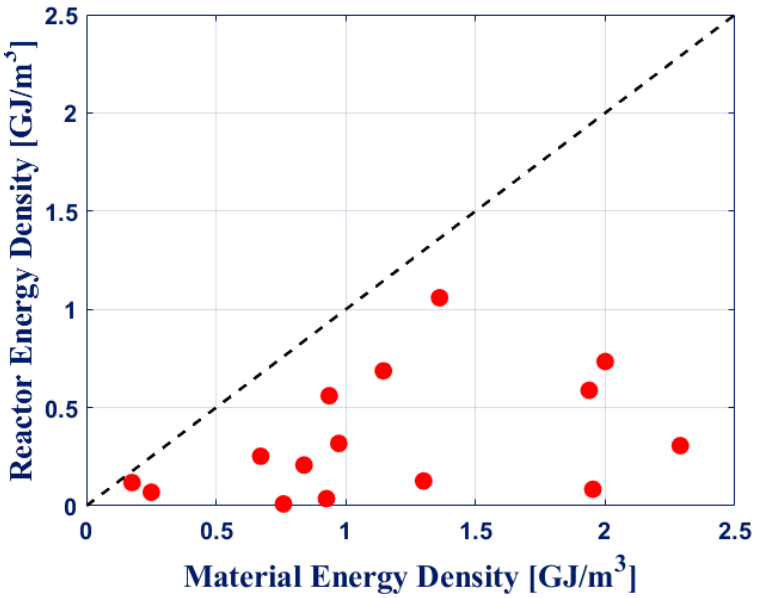

Figure 39 Comparison of energy storage densities at material and reactor scales for various open TCS reactors and materials, taken from the literature.

Although a number of continuum models have been proposed to study reactor performance based on the TCM, on reactor geometry, and system layout, numerical studies on specifically water-based system-integrated open TCS reactors for domestic applications are lacking. Furthermore, while techno-economic evaluations of TCS systems have been carried out for a variety of materials based on their thermodynamic and physical properties [15], there are fewer techno-economic studies of TCS systems that account for reaction kinetics and dynamic effects. The literature features some discussion surrounding kinetic limitation of open TCS performance. However, the effect of material scale kinetics on reactor scale performance with a thorough cross-comparison for multiple candidate salts and consolidating the link between material properties and process techno-economic performance still needs some addressing. This gap in the knowledge justifies the aims of the present chapter.

2 Case study design / reference scenario

A TCS process used for space-heating in a domestic context is under scrutiny in this chapter. For this study, the TCS store is used to cover space-heating demand only, which generally accounts for over 60% of a typical European household's energy usage (**Figure 40**). It is assumed that warm air discharged from the TCS is used directly for warm air heating inside the dwelling. Further in this thesis (**Chapter V**) an analysis will be carried out for a dwelling with underfloor heating. Additionally, implementation of open TCS for hot water production (less than 20% dwelling energy use) incurs significant financial costs, particularly due to the necessity of efficiently transferring the released thermal energy from an air flow to water during the discharge phase. Furthermore, the necessary minimum heat discharge temperature by the TCS for domestic hot water (DHW) is higher than for space heating; 35°C for space heating via warm air heating as opposed to 40°C for DHW or

space heating with underfloor heating, leading to a lower overall amount of exploitable energy for DHW and further reducing the economic incentive of a TCS for domestic applications.

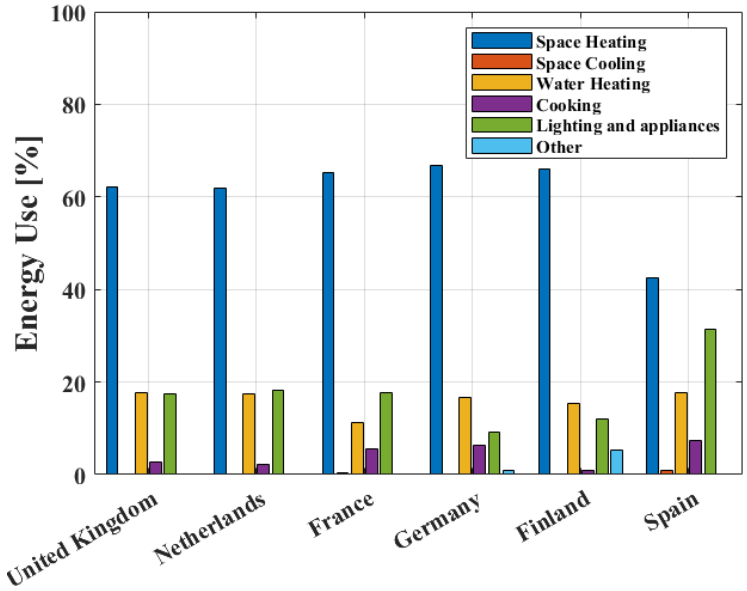

Figure 40 Final energy consumption in the residential sector by end use, 2019, for selected European countries. Source: Eurostat [165]**.**

2.1 System description

The role of the dwelling-integrated TCS storage unit is to store solar heat recovered from roof-top solar thermal collectors. Solar heat is recovered by a flat plate solar thermal collector (FPC) on the south-facing roof of the dwelling and captured in a heat transfer fluid (HTF), which is passed through an HTF-to-air heat exchanger (HX). FPCs typically operate at a temperature of around 65°C to 90°C [166], which overlaps with the temperature range required for the dehydration of most inorganic salts (temperature which can be further reduced by integration into a host matrix).

Since the TCS is an open process, during both heat charge and discharge, air acts as a heat carrier fluid and is supplied by an electric fan. During heat charge, when solar heat is transported to the TCS, water is desorbed from the hydrated material as the thermal energy from the hot air is captured as chemical energy in the reactor and triggers the dehydration reaction. Once the material is fully dehydrated, the air flow circulating through the system is interrupted, and the reactor isolated from the ambient by closing inlet and outlet valves. In the absence of any humidity the energy is stored with no losses until needed later, such as during winter.

When heat is needed from the storage, air is extracted from the ambient and transported to the reactor. The humidity naturally present in the air triggers the exothermic hydration reaction, causing the flow of air to dry and heat up as it passes through the reactor. Depending on the climatic conditions air may require additional humidification, which implies more financial investment. One of the goals of

this chapter will be to evaluate the necessity for forced humidification of open TCS systems in domestic environments. The extracted hot dry air may then be used directly for space heating. **Figure 41** shows the process flow diagram. As recommended in the case of TES systems integrated to applications [167], the boundaries of the process are clearly indicated, along with the heat sources and sinks. The heat sources are the solar thermal collectors in the case of desorption or the ambient and the HTF store in the case of adsorption, and heat sinks are the ambient in both cases and the space-heating system for adsorption.

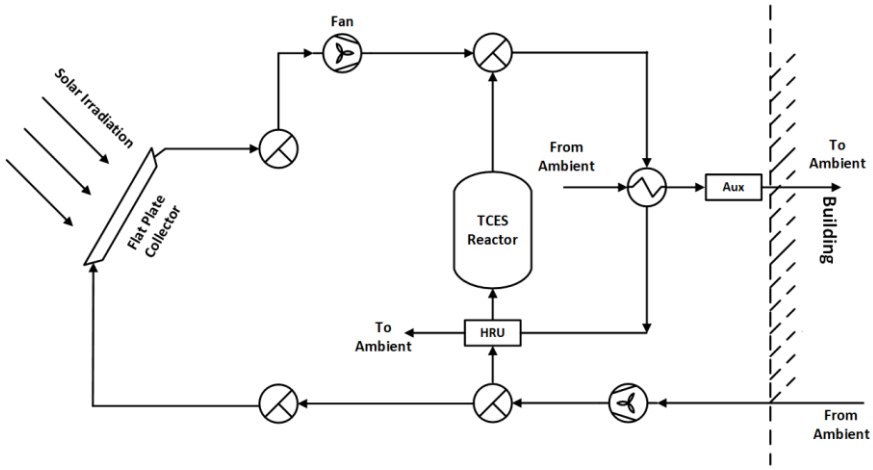

Figure 41 Process flow diagram of the TCS system for domestic space heating.

Figure 42 shows the elements of the process used specifically for heat charge and discharge, respectively. The strategy for using the TCS for solar energy storage for domestic space heating consists in four operating modes [168]:

- Solar energy is available while there is no demand for heating in the building: solar energy is stored.
- Solar energy is available while there is a demand for heating in the building: solar energy is supplied to the building space heating system.
- Solar energy is not available, while there is a demand for heating in the building: if stored energy is available, energy from the storage is supplied to the building space heating system.
- Solar energy is not available, while there is a demand for heating in the building: if stored energy is not available, energy from an auxiliary source is supplied to the building space heating system, typically an air-to-air heat pump, or an electrical resistance heater supplied with electricity bought from the grid.

The final operating mode raises the question of the need for an auxiliary energy source, and whether the coupled solar collector and TCS process is expected to provide for 100% of the building's heating demand. The design choice is likely to be driven by economic factors [169].

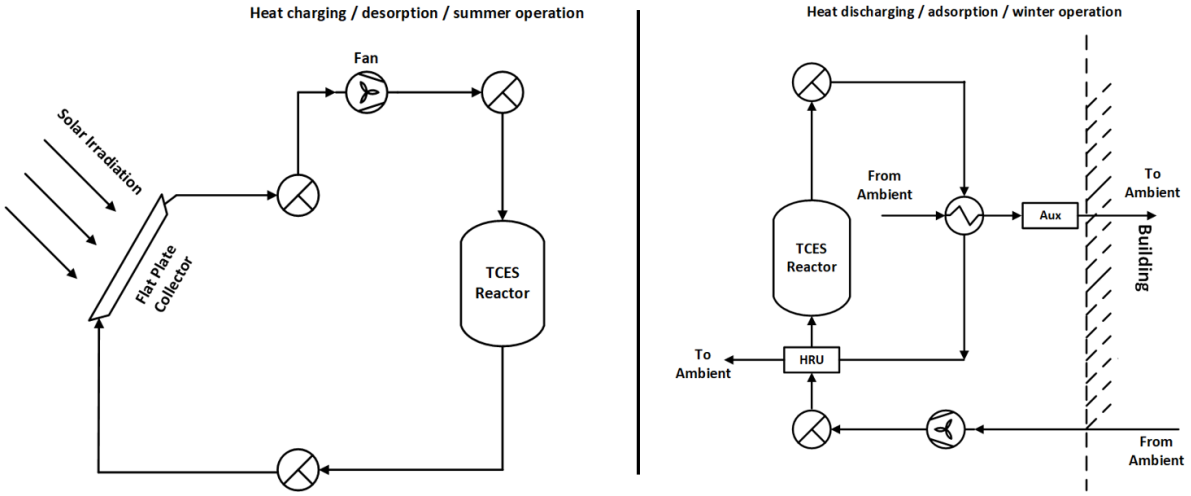

Figure 42 Process flow diagram of the TCS system for domestic space heating. Left-hand side desorption/heat charge. Right-hand side adsorption/heat discharge.

The basic open TCS reactor concept was covered in **Chapter II** and revisited here. The open TCS reactor is in this case considered to be a fixed bed reactor in which a TCM is packed. Air flows into the reactor inlet and through the TCM due to its porous state. Dehydration requires the heating of the entire mass of TCM, which can involve large thermal inertia and lead to low performance and reduced control over the process [139]. During hydration, high volumes of TCM can lead to reactive 'dead zones', where humidity carried by the air flow does not access parts of the TCM bed. Therefore, it is advantageous to keep the reactive area as small as possible. To achieve this, the TCS storage is divided into modules in order to minimise these heat and mass transfer issues while also reducing the pressure drop across the reactor, in turn decreasing the mechanical power required from the fan [15]. **Figure 43** shows examples of prototypes and concepts of segmented/modular reactors found in the TCS literature.

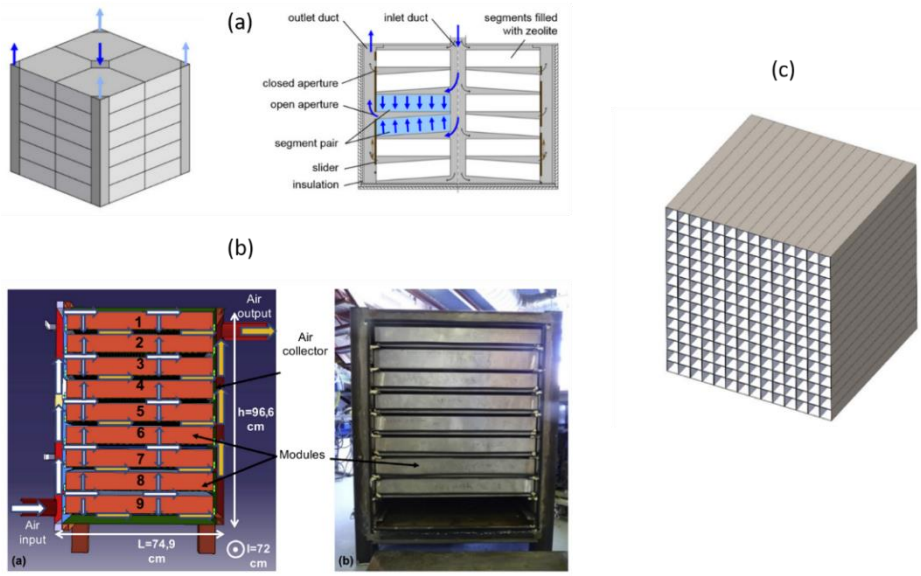

Figure 43 Prototypes and schematic concepts of segmented open reactors for TCS. Images taken from (a) [170] **(b)** [171] **(c) [15].**

2.2 Energy demand in residential buildings

In this study, the system considered is a low-energy two-story single-family house in Western Europe (200 m^2 of living surface area). This dwelling is expected to require an annual space-heating demand of 10 GJ / 2777 kWh, which is consistent with the values reported in the literature for a family-house located in Western Europe expected to potentially feature a TCS. Mahon et al. based their feasibility study of a Zeolite-$MgSO_4$ composite for thermochemical energy storage on a winter space heating demand of 5737 kWh (20 GJ) for a house of unspecified size located in the UK with an 8m^2 solar collector [172]. De Jong et al. estimate a 10 GJ annual space-heating demand for a typical well-insulated dwelling in the Netherlands, and also mention the concept of subdividing the storage in multiple modules for daily heat demands that is further investigated by Scapino et al. [15]. In their review, Kuznik et al. estimate the annual space heating demand for a low-energy building in Western Europe to be 25 kWh/m^2 of living space, i.e., 18 GJ for the house used in their study. The same value is given by Grekova et al. for low energy buildings in Europe [43]. Values of 8.3 GJ / 2300 kWh for a single family house by Van Beek et al. [173] and 1,861 kWh for an average Dutch household by Trausel et al. [174] have been reported.

As discussed in the previous section, the thermal store is considered to be subdivided into a number of individual modules that each store and release the heat required for 24 hours of space heating. Furthermore, in the current scenario it is expected that there are 212 days requiring space heating throughout the year. An individual storage unit should therefore be able to release at least 47.2 MJ of heat throughout the course of a day [15,175], yielding a system that should deliver an average thermal power of 0.55 kW over a 24 hour period. In the case of low to medium temperature domestic space-

heating, air should be provided at a temperature of approximately 35°C during the 24-hour period [15,175].

2.3 Material selection

Various inorganic salts have been investigated as potentially suitable TCMs to carry out the reversible exo/endo-thermic sorption reaction to release/store heat. As was discussed in more detail in the literature review in **Chapter II**, the suitability and theoretical performance of these salts have been extensively compared over the past 10 years in several screenings. Donkers et al. concluded that K_2CO_3 is the most promising salt for TCS applications, whereas in an earlier work N'Tsoukpoe et al. preferred $SrBr_2$ and $LaCl_3$ [19,26]. These comparisons were carried out at the material scale: theoretical thermal storage capacity, cyclability and other relevant properties for TCS were evaluated at the milligram scale. Since the publishing of these reviews, most of the literature concerning salt hydrates for TCS has revolved around approximately 10 to 15 salt hydrates. One of the aims of this chapter is to compare the techno-economic performance of the TCS process using these different materials.

Inorganic salts and hydration reaction

In this study, a number of salts were considered as potential TCMs for the system in consideration. These salts were selected on the basis that their ability to store and release heat in the context of open low-temperature TCS has been demonstrated in the current literature or in previous chapters of this thesis, either at the material scale through thermogravimetric methods or at the reactor scale through prototypes. These salts were all at least identified as promising through the inorganic salt reviews published in the past years [19,23,26].

An additional consideration that is not always mentioned in these aforementioned reviews is the hydration and dehydration level that is to be realistically expected in the operating conditions of low-temperature TCS.

$$MgCl_2 \cdot 6H_2O + \Delta H \rightleftarrows MgCl_2 + 6H_2O_{(g)} \qquad (42)$$

As an example, when describing the hydration reaction of magnesium chloride, some authors might assume the reversible hydration reaction described in **equation (42)**, hydrating anhydrous magnesium chloride up to the hexahydrate. However it can be seen through numerous studies on the dehydration of various hydrates of magnesium chloride and in the previous chapter (**Chapter III.2.1**) that achieving full dehydration of $MgCl_2$ with solar thermal (60 to 100°C) is unlikely, since removal of the final molecule of water was found to be achieved at temperatures of approximately 140-160°C [95,148], overlapping with the typical degradation temperature of chlorides of approximately 140°C. Fully dehydrating the material is therefore not only unrealistic in terms of energy availability, but for some salts also incurs the risk of irreversibly degrading the material and damaging the material's

cyclability and ultimately energy storage and release capacity. In the magnesium chloride example, a more realistic hydration reaction to expect would be as shown in **equation (43)**.

$$MgCl_2 \cdot 6H_2O + \Delta H \rightleftarrows MgCl_2 \cdot 2H_2O + 4H_2O_{(g)} \quad (43)$$

Similar reasoning can be applied to most salts which can theoretically hydrate up to hexahydrate or more: the amount and temperature level of heat typically required to fully dehydrate one of these salts ($MgCl_2$, $CaCl_2$, $SrBr_2$ and $MgSO_4$) is expected to be superior to power available in residential solar energy systems. Thus, for many inorganic salts it is more realistic to assume their dehydration to the monohydrate or dihydrate during heat charge. The candidate inorganic salts, their reversible (de)hydration reaction considered for this study, and some of their relevant thermal and chemical-physical properties are shown in **Table 19**.

Table 19 Summary of thermo-physical properties of inorganic salts and their hydration reactions considered in this study. Reaction enthalpy and entropy were calculated from the formation enthalpies and entropies of the salt in hydrated and dehydrated state. Density and heat capacity for the dehydrated state. Unless specified, data was retrieved from NBS database of thermophysical properties [176]**.**

Reaction	ρ [kg/m^3]	Cp [J/kg/K]	ΔH [J/mol]	ΔS [J/mol/K]	Cost [€/t]
$SrBr_2 \cdot H_2O + 5H_2O = SrBr_2 \cdot 6H_2O$	2,396	455.49	58,162.00	143.6	2,400 [174]
$MgSO_4 \cdot H_2O + 6H_2O = MgSO4 \cdot 7H_2O$	2,570 [34]	801.56	55,950.33	147.9	77 [174]
$CaCl_2 \cdot 2H_2O + 4H_2O = CaCl_2 \cdot 6H_2O$	1,850 [177]	1,170.00 [178]	59,432.00	154.9	116 [174]
$MgCl_2 \cdot 2H_2O + 4H_2O = MgCl_2 \cdot 6H_2O$	1,860 [19]	1,213.31	63,007.00	142.3	154 [174]
$K_2CO_3 + 1.5H_2O = K_2CO_3 \cdot 1.5H_2O$	2,430	827.97	63,635.33	157.0	900
$BaCl_2 + 2H_2O = BaCl_2 \cdot 2H_2O$	3,856	360.85	58,932.00	149.2	537
$CaSO_4 + 2H_2O = CaSO_4 \cdot 2H_2O$	2,960	736.08	56,877.00	146.0	447
$CuCl_2 + 2H_2O = CuCl_2 \cdot 2H_2O$	3,386 [19]	534.62	58,782.00	159.4	3132
$LiCl + 2H_2O = LiCl \cdot 2H_2O$	2,068 [19]	5,731.94	30,202.00	148.9	27,000
$Li_2SO_4 + H_2O = Li_2SO_4 \cdot H_2O$	2,221	1,069.40	49,481.00	140.3	27,000

The equilibrium conditions of these reactions can be visualised in the Clausius-Clapeyron diagram (**Figure 44**). The red and blue areas on this figure encompass the hydration and dehydration conditions, respectively. The deliquescence conditions have not been considered in the equilibrium, and neither have the recently discovered metastable zones for K_2CO_3 and $CuCl_2$ [25]. Metastable zones were discussed earlier in **Chapter III.2.1**.

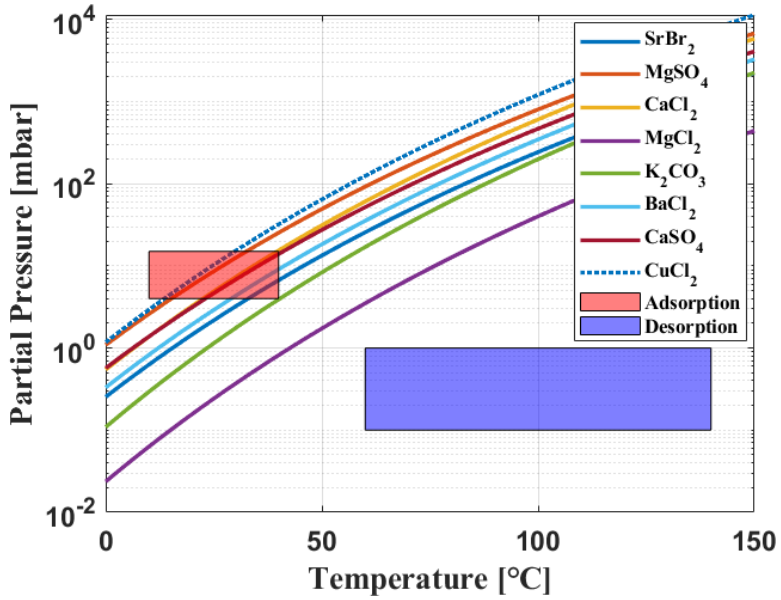

Figure 44 Clausius-Clapeyron diagram for all investigated salts, and temperature/partial pressure ranges for hydration and dehydration.

Host matrix selection

The TCS reactor contains either pure salts or composite SIMs as the active materials. The underlying stability issues associated with pure salt hydration/dehydration, such as deliquescence or agglomeration are well documented in the TCS literature. This topic was discussed in detail in **Chapter II.2.3**, but is briefly summarised here. Dispersing inorganic salts into a host matrix provides the benefits of:

- mechanically supporting the salt.
- creating an available volume for salt to expand and contract during hydration/dehydration cycles.
- preventing from leaking in the case of deliquescence if subjected to high humidity.
- Increasing the energy storage density compared to the pure inorganic salt by the capillary force / deliquescence effect. Due to capillary forces, the salt solution formed through deliquescence is contained within the pores of the host matrix and provides additional heat storage capabilities due to water absorption by the salt solution.
- Reduction of dehydration temperature by improving thermal conductivity and lowering equilibrium conditions.

The main disadvantage of using such host matrixes is the reduction of material-level energy storage density, since part of the volume of the composite is taken up by an inert material that has no contribution to the energy storage process. Such host matrices therefore enforce a design choice relating to the mass compositions of the salt and matrix respectively in the composite, where increasing amounts of host matrix will provide material stability, cyclability and kinetic improvement

at the cost of energy storage capacity. Because SIM composites are formulated by wet impregnation which consists of pouring salt solution into the host matrix before evaporating the water to precipitate the salt into the matrix, the maximum salt content of a SIM composite depends on (1) the liquid absorption capacity of the host matrix, and (2) the solubility of the salt in the experimental conditions. The limit of solubility of inorganic salts was discussed in more detail in **Chapter II.2.2**. The maximum energy storage density of any salt/matrix pair may be calculated from the maximum salt content, the energy storage density of the pure salt and the bulk properties of the two respective materials.

In this work, inorganic salts are considered dispersed into vermiculite, due to low cost, low density (and therefore low thermal mass which reduced sensible heat loss due to material heating to the equilibrium temperature), and high specific porosity (3 cm^3/g vermiculite). The composite materials are assumed to have been prepared using the wet impregnation method, which was described in detail in **Chapter III**. Due to the high porosity of vermiculite, it is assumed that 50 wt.-% composite SIMs were formulated which is a realistic estimate based on existing SIMs formulated in the literature (see **Chapter II.2.3**).

3 TCS process model

A quasi 1D physics-based model is used to simulate the behaviour of the TCS reactor. The reactor model is coupled to models for heat exchangers and a flat plate collector (in the case of dehydration) to formulate the entire process model. The numerical implementation is carried out in Matlab. The final equation system is resolved using the numerical ordinary equations system solver *ode15s*. The following elements of the complete model will be presented:

- Equations for the TCS reactor model
- Equations for the flat plate collector
- Equations for the heat exchangers
- Summary of system equations
- Calculations of key performance indicators

3.1 TCS Reactor

The reactor model consists in a series of individual nodes (1D-partitioning) where heat flows, state of hydration, air humidity and equilibrium humidity are locally defined as functions of time, combined to simulate the complete reduced geometry (**Figure 45**).

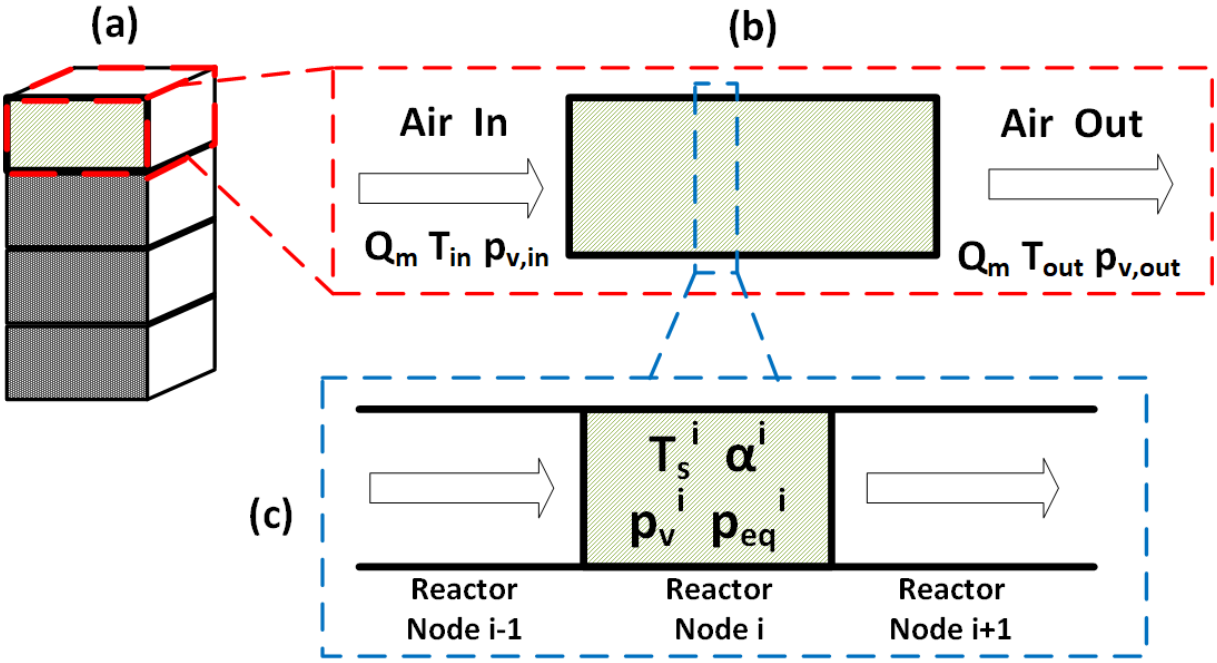

Figure 45 Segmentation and 1-Dimensional partitioning of TCS reactor. The complete TCS reactor is shown schematically in (a), one of the reactor subsections in (b), and the partitioning of a subsection into nodes in (c).

The key assumptions for the model are the following:

- Thermal equilibrium between solid and gas phases. The reactor is filled with a porous TCM. Generally, in the TCS literature, the TCM is treated numerically as either a single homogenous medium with a single temperature, or as two distinct homogenous zones (solid and gas) with each their own temperature and that are in constant heat exchange. Both methods have been shown to be viable [179]. In this study thermal equilibrium and a single homogenous medium have been assumed.
- Thermal losses to the ambient are neglected, as it is assumed the TCS reactor is appropriately insulated.
- Constant heat capacities for solid and gas phases.
- All hydration/dehydration reactions are considered as single step reactions between their lower and higher hydration levels, according to the stoichiometry in **Table 19** in **section 2.3**.
- Deliquescence is assumed to be counterbalanced by the dispersion of the salt into a vermiculite host matrix, while metastable zones, if existent depending on the selected salt, are neglected.

The reactor is segmented into modules which operate independently. The modelled reaction takes place in one subsection that is partitioned into nodes according to a quasi 1D scheme (**Figure 45**). The system of equations determines the temperature, advancement, vapour pressure and equilibrium pressure at each node. By adapting boundary and initial conditions, the same system of equations may be used for both hydration and dehydration steps.

The energy balance for each node can be found in **equation (44)**, where m_s and Cp_s are the mass and heat capacity of inorganic salt in the composite, m_m and Cp_m the mass and heat capacity of the matrix, ΔH the reaction enthalpy, κ the reaction stoichiometric coefficient, Q_m the air mass flow rate, Cp_f the air heat capacity, α^i the local reaction advancement at node i, and T_s^i and T_s^{i-1} the temperature inside the reactor at nodes i and i-1 respectively. The variation in energy inside a reactor node (left-hand side term) is due to the heat supplied through convection by the air flow which depends on the temperature at the outlet of the previous node (second right-hand side term) and the energy either released or stored by the chemical reaction (first right-hand side term).

$$\frac{dT_s^i}{dt}(m_s Cp_s + m_m Cp_m) = \frac{d\alpha^i}{dt}\Delta H \frac{\kappa m_s}{N M_{H2O}} + Q_m Cp_f (T_s^{i-1} - T_s^i) \tag{44}$$

In this model, the reaction rate depends on the advancement and the equilibrium drop, which is the main driving force of the reaction [82,108,162,164], as seen in the solid-state kinetic **equation (45)** where p_{eq}^i and p_v^i are water and equilibrium vapour pressures at node *i* respectively and k_{cin} the kinetic rate constant.

$$\frac{d\alpha^i}{dt} = k_{cin} f(\alpha^i)(1 - \frac{p_{eq}^i}{p_v^i}) \tag{45}$$

The energy equation and reaction kinetics are tied by the water mass balance in **equation (46)**, where M_s is the molar mass of the salt. The flow of water transported from gas to solid phase by the reaction's driving force (right-hand side) is equal to the increase in water loading of the material (left-hand side).

$$\frac{d\alpha^i}{dt}\kappa \frac{M_{H2o}}{M_s}\frac{m_s}{N} = 0.62198 Q_m (\frac{p_v^{i-1}}{101325 - p_v^{i-1}} - \frac{p_v^i}{101325 - p_v^i}) \tag{46}$$

The equilibrium conditions are defined by the Clausius-Clapeyron **equation (47)**, where ΔS is the reaction entropy and R the gas constant.

$$p_{eq} = 101325 e^{\frac{-\Delta H}{RTs} + \frac{\Delta S}{R}} \tag{47}$$

Thus, **equations (44)** to **(47)** constitute the equation system for the reactor model.

3.2 Solar thermal collector

Solar thermal is the thermal energy generation technology used to charge the TCS. The solar thermal collector is considered to be a flat plate solar air heater, with a single tempered glass cover above the

selectively absorbent plate, as represented schematically in **Figure 46**. Cold air circulates and is heated through the collector's internal manifold area.

The effective useful energy extracted from the incident solar irradiation by the FPC is equal to the total incident irradiation minus heat losses associated with heat loss coefficient U_L. The heat loss coefficient lumps together all thermal losses due to convection, conduction, and infrared radiation. The energy balance is carried out in the FPC energy **equation (48)**:

$$\dot{Q}_u = A_p(S - U_L(T_{pm} - T_a)) \tag{48}$$

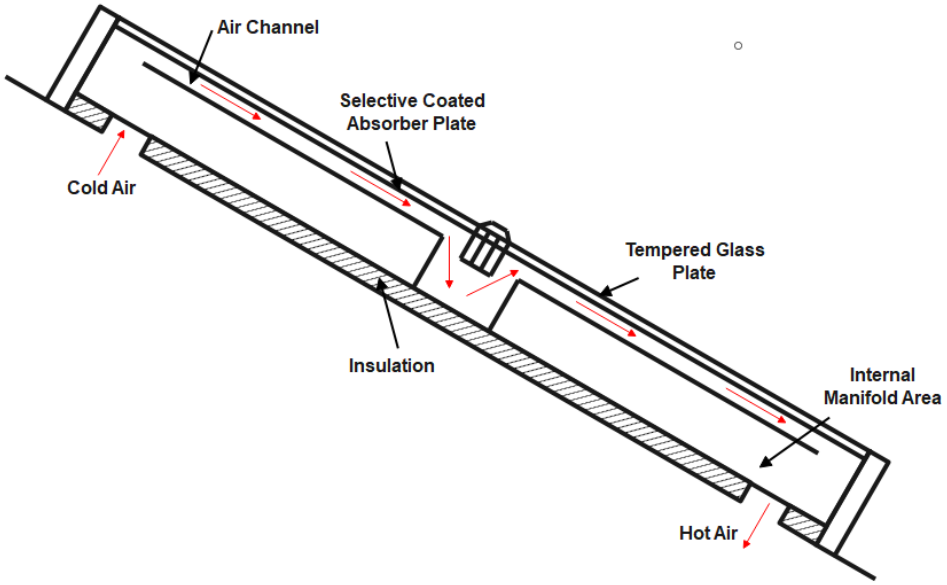

Figure 46 Cross-sectional diagram of a flat plate solar air heater (adapted from [168]**).**

Alternatively, the effectively transferred heat $\dot{Q}_u$ to the heat transfer fluid can be expressed as a function of the total incident irradiance through the so-called flat plate collector efficiency η_{coll}, as shown in **equation (49)**, where the efficiency of the FPC is defined as the ratio of useful extracted energy over the total available energy by solar irradiance:

$$\eta_{coll} = \frac{\dot{Q}_u}{I_t A_c} \tag{49}$$

The solar air heater was assumed to be a Lubi air heater manufactured by Enerconcept Distribution. To avoid heat transfer calculations outside the scope of this chapter, the efficiency of the solar collector was found from the manufacturer's data, shown graphically in **Figure 47**. The efficiency is mainly a function of the specific heat transfer fluid volumetric flow rate, and of the solar irradiance. The data provided showed the performance of the FPC for solar irradiances 300 W/m^2 and 900 W/m^2. Performance for other irradiance values are extrapolated by weight averages from these two curves,

as shown in **Figure 47** for 600 W/m^2. The efficiency for a given solar irradiance I' and surface specific HTF flow rate is extrapolated using **equation (50)**:

$$\eta_{coll}(I') = \eta_{coll}\left(300\frac{W}{m^2}\right) - \frac{\eta_{coll}\left(300\frac{W}{m^2}\right) - \eta_{coll}\left(900\frac{W}{m^2}\right)}{\left|300\frac{W}{m^2} - 900\frac{W}{m^2}\right|} * (I' - 300\frac{W}{m^2}) \quad (50)$$

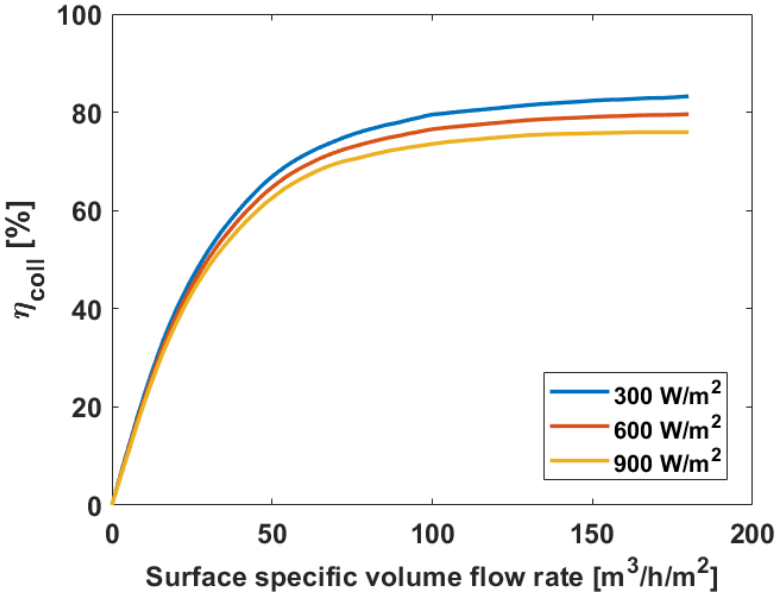

Figure 47 Lubi solar air heater performance curves, data provided for direct solar irradiance values of 300 W/m^2 and 900 W/m^2 [180]**.**

For a given instantaneous solar irradiance and a heat transfer fluid flow rate selected by design, the efficiency of the system and therefore effectively transferred heat can be determined. The thermal load transferred to FPC working fluid is calculated with **equation (51)**.

$$T_{FPC,out} = T_{FPC,in} + \frac{\dot{Q}_u}{\dot{m}_{FPC}\dot{C}p_{FPC}} \quad (51)$$

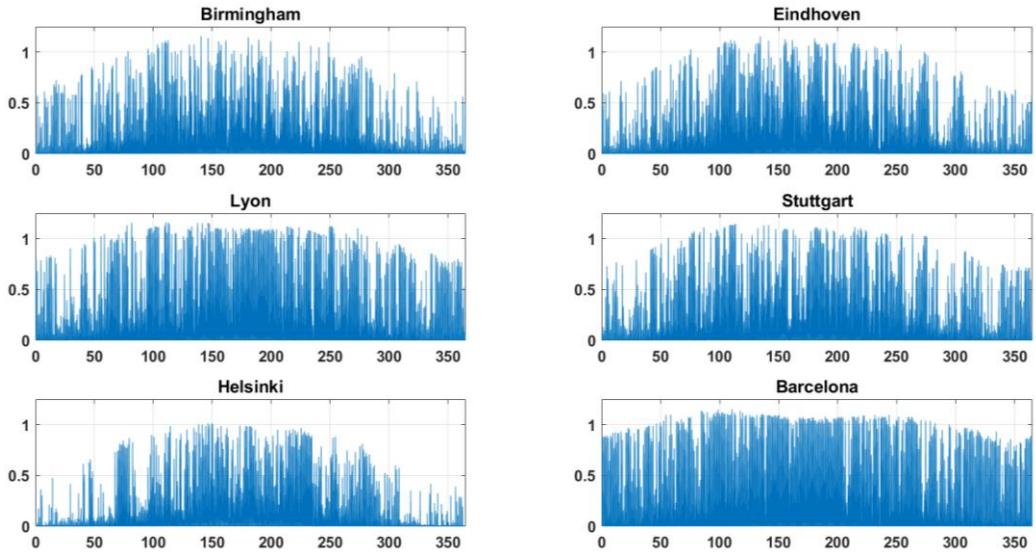

Figure 48 2015 annual total irradiance [kW/m^2] at six different locations in Europe.

The total incident irradiance is determined through hourly solar irradiance data (direct and diffuse irradiance), temperature and wind data from 2015 at six different European locations which were retrieved from Renewables.ninja [5,181] and presented in **Figure 48**. The data for these 6 locations will be used for the analysis in location-specific case studies (see **section 5.3** later in this chapter).

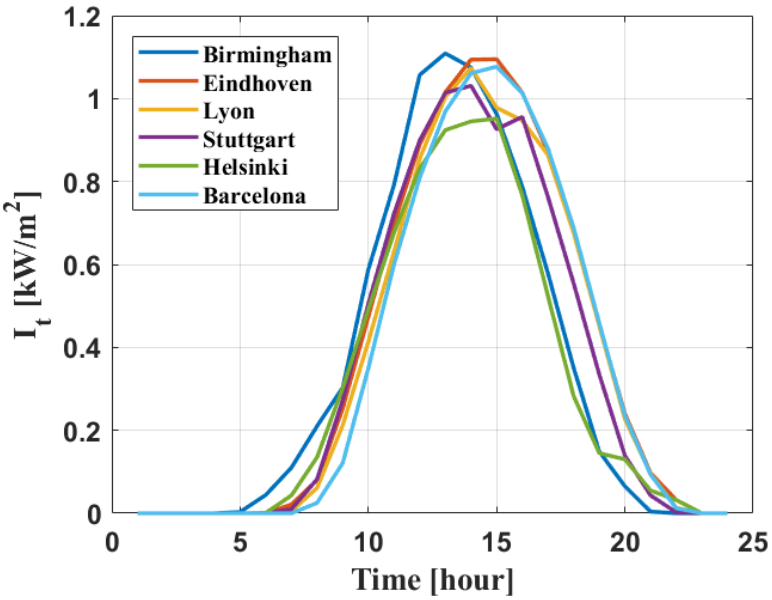

Figure 49 Daily total irradiance [kW/m^2] at six different locations, clear summer day.

To convert the FPC output temperature data from discrete data points to a continuous function that is required for the methodology used for solving the system of equations presented in **paragraph 3.1**, the fluid outlet temperature profile was fitted in a least-squares sense to a modified Weibull function (**equation (52)**).

$$f(x) = \gamma \frac{\beta}{\eta} (\frac{x}{\eta})^{\beta-1} \exp\left(-\left(\frac{x}{\eta}\right)^{\beta}\right) + \varepsilon \quad (52)$$

Using weather data in the case of Birmingham, the resulting FPC output temperature profile and fitted curve are presented in **Figure 50**.

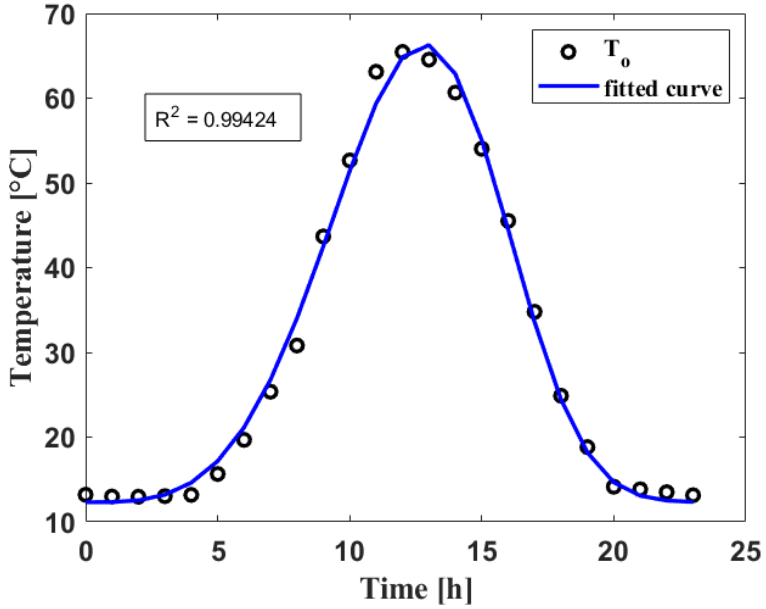

Figure 50 FPC output temperature and fitted modified Weibull function, in the case of a clear sky summer day in Birmingham.

The obtained parameters from fitting the modified Weibull function to the FPC output temperature data at 6 different European locations can be found in **Table 20** along with the associated coefficient of determination R^2.

Table 20 Fitting parameters and coefficient of determination for the fitted Weibull distribution function to the modelled FPC output temperature at 6 different locations.

	β	η	γ	ε	R^2
Birmingham	4.37	13.59	444.08	285.47	0.994
Eindhoven	4.24	14.80	510.16	292.81	0.991
Lyon	4.34	15.12	525.76	290.62	0.979
Stuttgart	4.18	14.79	546.63	282.57	0.972
Helsinki	4.53	13.79	360.91	286.72	0.986
Barcelona	4.63	14.90	451.48	298.39	0.985

3.3 Heat exchangers

The following section details the design and modelling of the two heat exchangers that are used in the TCS system, which are (1) the heat exchanger (denoted HX) at the outlet of the reactor that collects the heat released by the exothermic hydration reaction (heat discharge during winter) and transports it to the building load, and (2) the heat recovery unit (denoted HRU) which uses the heat not extracted by the HX heat exchanger from the air flow exiting the reactor to preheat the air flow entering the reactor during hydration.

Process to load heat exchanger HX

The HX air-to-air heat exchanger is in a crossflow configuration. This configuration has the advantage of achieving high energy transfer effectiveness (η>80%) and is feasible for air flows, although such a design may require special manifolds. The disadvantages of crossflow heat exchangers are generally considered to be low resistance to fouling (an issue that is mitigated since the exchanging fluids are both clean air) and low operating pressure. This latter issue is also mitigated since the entire system operates at atmospheric pressure, with a slight pressure increment imposed by the air blower to compensate for the system's pressure drop, notably due to the packed bed in the TCS reactor.

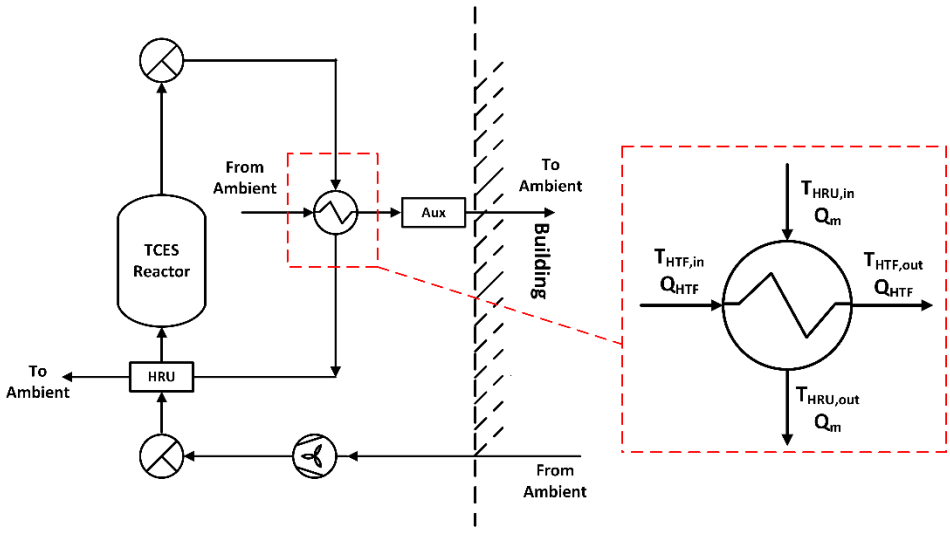

Figure 51 Diagram of inlet and outlet flows of heat exchanger HX during the hydration process.

HX was initially modelled with the rest of the system equations with an idealized effectiveness (**equation (53)**):

$$\varepsilon_{HX} = \frac{Q_m(T_{HTF,out} - T_{HX,out})}{\min(Q_m, Q_{HTF})(T_{HTF,out} - T_{amb})} \quad (53)$$

This initial estimation of HX performance leads to solving the *heat exchanger design problem*, i.e., determining the heat exchanger's size (heat transfer surface A), and overall heat transfer coefficient U. The ε-NTU method is used to provide a realistic heat-exchanger model and is recommended for carrying out *heat exchanger performance calculations*. The number of thermal units NTU is calculated using **equation (54)**:

$$NTU = \frac{UA}{C_{min}} \tag{54}$$

The typical overall heat transfer coefficient values of U for air to air heat exchangers, are generally found between 25 and 50 W/m^2/K [182]. U = 37 W/m^2/K is used in this study as an average value.

NTU	ε for indicated capacity-rate ratios, Cmin / Cmax							
	0	0.25	0.5	0.7	0.75	0.8	0.9	**1**
0.00	0.000	0.000	0.000	0.000	0.000	0.000	0.000	0.000
0.25	0.221	0.216	0.210	0.205	0.205	0.204	0.202	0.200
0.50	0.393	0.378	0.362	0.350	0.348	0.345	0.339	0.333
0.75	0.528	0.502	0.477	0.457	0.452	0.447	0.438	0.429
1.00	0.632	0.598	0.565	0.538	0.552	0.525	0.513	0.500
1.25	0.713	0.675	0.635	0.603	0.595	0.587	0.571	0.556
1.50	0.777	0.735	0.691	0.655	0.645	0.636	0.618	0.600
1.75	0.826	0.784	0.737	0.697	0.687	0.677	0.657	0.636
2.00	0.865	0.823	0.775	0.733	0.722	0.711	0.689	0.667
2.50	0.918	0.880	0.833	0.788	0.777	0.764	0.740	0.714
3.00	0.950	0.919	0.875	0.829	0.817	0.804	0.778	0.750
3.50	0.970	0.945	0.905	0.861	0.848	0.835	0.807	0.778
4.00	0.982	0.962	0.928	0.886	0.873	0.860	0.831	**0.800**
4.50	0.989	0.974	0.944	0.905	0.893	0.880	0.850	0.818
5.00	0.993	0.982	0.957	0.921	0.909	0.896	0.866	0.833
5.50	0.996	0.988	0.968	0.933	0.922	0.909	0.880	0.846
6.00			0.975	0.944		0.921	0.892	0.857
6.50			0.980	0.953		0.930	0.902	0.867
7.00			0.985	0.960		0.939	0.910	0.875
7.50			0.988	0.966		0.946	0.918	0.882
8.00			0.991	0.971		0.952	0.925	0.889
8.50			0.993	0.975		0.957	0.931	0.895
9.00			0.994	0.979		0.962	0.936	0.900
9.50			0.996	0.982		0.966	0.941	0.905
10.00			0.997	0.985		0.970	0.945	0.909
inf	1.000	1.000	1.000	1.000	1.000	1.000	1.000	1.000

For a given heat exchanger effectiveness and capacity-rate ratio C_{min} / C_{max}, the required number of heat transfer units NTU is given in Error! Reference source not found., taken from Kays and London ADDIN CSL_CITATION {"citationItems":[{"id":"ITEM-

1","itemData":{"ISBN":"0070334188","abstract":"This is the third edition of a standard text book which has beem revised to take into consideration conversion to SI system of units. However, in view of the lack of uniformity in the world for conforming to the new system, the authors have used a dual system of units in this edition. A unique feature of their book is that virtually all the basic text data come from a single reasearch programme under the supervision of the authors. So there is no question about the comparability of test results of one surface to another. Additional data have come from other sources but the authors have chosen to maintain 'the original tradition' so that internal consistency remains almost complete. (R.A.H.)","author":[{"dropping-particle":"","family":"Kays","given":"W. M.","non-dropping-particle":"","parse-names":false,"suffix":""},{"dropping-particle":"","family":"London","given":"A. L.","non-dropping-particle":"","parse-names":false,"suffix":""}],"id":"ITEM-1","issued":{"date-parts":[["1984"]]},"title":"Compact heat exchangers. Third Edition.","type":"book"},"uris":["http://www.mendeley.com/documents/?uuid=24af1502-aa85-4ee2-87c4-28f44d7b9dda"]}],"mendeley":{"formattedCitation":"[183]","plainTextFormattedCitation":"[183]","previouslyFormattedCitation":"[183]"},"properties":{"noteIndex":0},"schema":"https://github.com/citation-style-language/schema/raw/master/csl-citation.json"}[183]. Thus, for an effectiveness $\varepsilon_{HX} = 0.8$ and an assumed capacity rate ratio of 1 (i.e., two air flows with equal flow rate) the required number of transfer units is NTU = 4, which with a known minimum capacity ratio of $C_{min} = Q_m\, Cp_{air}$, with $Q_m = 0.0671$ kg/s and $Cp_{air} = 1004$ J/kg/K results in a heat transfer capacity of C=67 W/K and required heat exchange surface area of $A_{HX} = 8.95\ m^2$. This heat exchanger surface area will be used in the economic evaluation later in this chapter. From the thermal effectiveness of HX, the instantaneous amount of transferred heat may be calculated, considering that the maximum amount of transferred heat is equal to $(T_{in} - T_{amb})C_{min}$, with C_{min} the minimum heat capacity rate between hot and cold sides of HX:

$$q = (T_{in} - T_{amb})C_{min}\varepsilon_{HX} \tag{55}$$

From the amount of transferred heat, the temperatures at the outlet of HX, on both hot and cold sides, may be calculated with **equations (56)** and **(57)**:

$$T_{HTF,out} = T_{HTF,in} + \frac{q\varepsilon_{HX}}{Q_{HTF}Cp_{air}} \tag{56}$$

$$T_{HX,out} = T_{HX,in} - \frac{q\varepsilon_{HX}}{Q_m Cp_{air}} \tag{57}$$

Heat recovery unit HRU

The heat recovery unit is modelled using the definition of the heat exchanger effectiveness [182], and is represented schematically in **Figure 52**. The fluid flowing through this heat exchanger is air. The air flows at the same rate on both the hot and cold sides of the heat recovery unit.

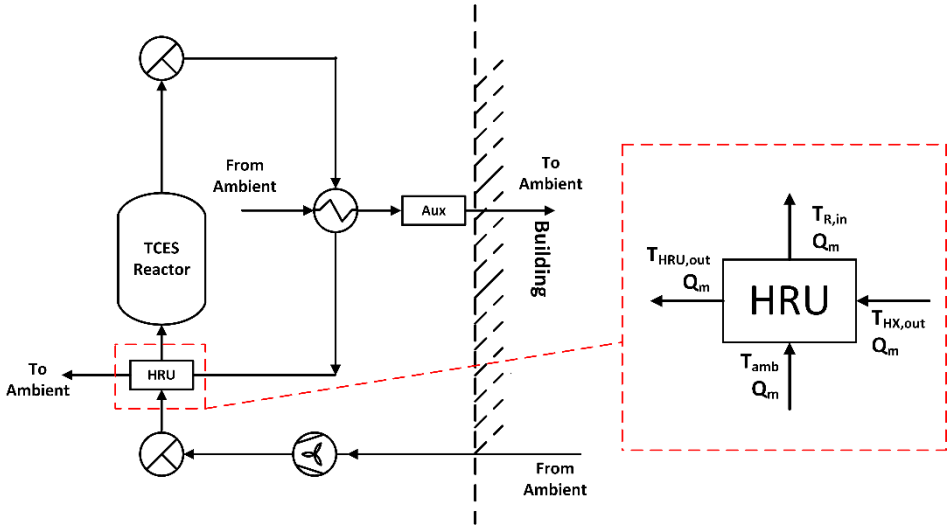

Figure 52 Diagram of inlet and outlet flows of heat recovery unit HRU during the hydration process.

The effectiveness of the heat recovery unit is therefore defined in **equation (58)**:

$$\varepsilon_{HRU} = \frac{T_{R,in} - T_{amb}}{T_{HX,out} - T_{amb}} \tag{58}$$

As for heat exchanger HX in the previous section, the capacity ratio is 1 and effectiveness of 80% is desired and assumed, leading to an overall heat exchanger area A_{HRU} = 8.95 m^2.

3.4 Summary and operating conditions

A total *4N+2* differential algebraic equations (DAEs) constitute the system of equations modelling the behaviour of the TCS system, where *N* is the number of reactor subdivisions as discussed in **section 3.1**: **equations (44)** to **(47)** are solved n times, and **equations (57)** and **(58)** are solved once. A summary of equations and variables is shown in **Table 21**.

Table 21 Summary of constituting variables and equations of TCS system model.

Variables	Equations	
$T_s^{i...N}$	$\frac{dT_s^i}{dt}(m_s Cp_s + m_m Cp_m) = \frac{d\alpha^i}{dt}\Delta Hr \frac{m_s}{nM_{H2O}} + Q_m Cp_{air}(T_s^{i-1} - T_s^i)$	(44)
$\alpha^{i...N}$	$\frac{d\alpha^i}{dt} = k_{cin} f(\alpha^i)(1 - \frac{p_{eq}^i}{p_v^i})$	(45)

$p_v^{i\ldots N}$	$\frac{d\alpha^i}{dt}\kappa\frac{M_{H2o}}{M_s}\frac{m_s}{n} = 0.62198Q_m(\frac{p_v^{i-1}}{101325-p_v^{i-1}} - \frac{p_v^i}{101325-p_v^i})$	(46)
$p_{eq}^{i\ldots N}$	${p_{eq}}^i = 101325e^{\frac{-\Delta H}{RTs}+\frac{\Delta S}{R}}$	(47)
$T_{HX,out}$	$T_{HX,out} = T_s^n - \frac{q\eta_{HX}}{Q_m Cp_{air}}$	(57)
$T_{R,in}$	$\eta_{HRU} = \frac{(T_{in}-T_{amb})}{(T_{HX,out}-T_{amb})}$	(58)

The variables' initial values for both hydration and dehydration are presented in **Table 16**.

Table 22 Initial values of system variables for hydration and dehydration.

	Hydration	**Dehydration**
$\boldsymbol{T_s^{i\ldots N}}$	19°C	25°C
$\boldsymbol{\alpha^{i\ldots N}}$	0	1
$\boldsymbol{p_v^{i\ldots N}}$	p_{eq}(19°C)	p_{eq}(25°C)
$\boldsymbol{p_{eq}^{i\ldots N}}$	0 Pa	0 Pa
$\boldsymbol{T_{HX,out}}$	T_{amb}	T_{amb}
$\boldsymbol{T_{R,in}}$	T_{amb}	T_{amb}

4 Cycle analysis and model validation

4.1 Model Validation

Validation of the model was carried out in order to confirm that the model's prediction is a realistic representation of TCS reactor behaviour. The reactor model was validated with experimental data presented in Michel et al. [109]: they investigated the behaviour of an open TCS reactor prototype containing pure $SrBr_2$ and consisting of 9 individual modules stacked one on top of another. The model is validated for the operation of an individual module. In this case a reactor module is a rectangular cuboid with dimensions 0.694m x 0.651m x 0.075m (0.034 m^3) containing 44.4 kg of $SrBr_2$ (Ed_{Srbr2} = 528 kWh/m^3, ρ_{SrBr2} = 2396 kg/m^3). Validation relies upon the temperature profiles measured by 4 thermocouples at different heights of the reactive salt bed which coincide with a subdivision of the reactor module into 5 segments. The temperature profiles obtained at each thermocouple with data from the model were compared, for both heat charge and discharge modes (**Figure 53** and **Figure 54**).

Hydration

During hydration (**Figure 53**), the air volumetric flow rate is 32.2 m^3/h, calculated from the total flow rate of 290 m^3/h reported by the authors as used for all 9 modules simultaneously through the assumption that the air flow is evenly divided between the reactor modules. The air enters the reactor with an inlet temperature of 25°C and an inlet water vapour pressure of 980 Pa. A kinetic rate constant of $k_{cin} = 10^5$ s^{-1} was used for the simulation. This value was found to be the best match between

simulation and experimental data once all other parameters were selected to emulate the experimental conditions.

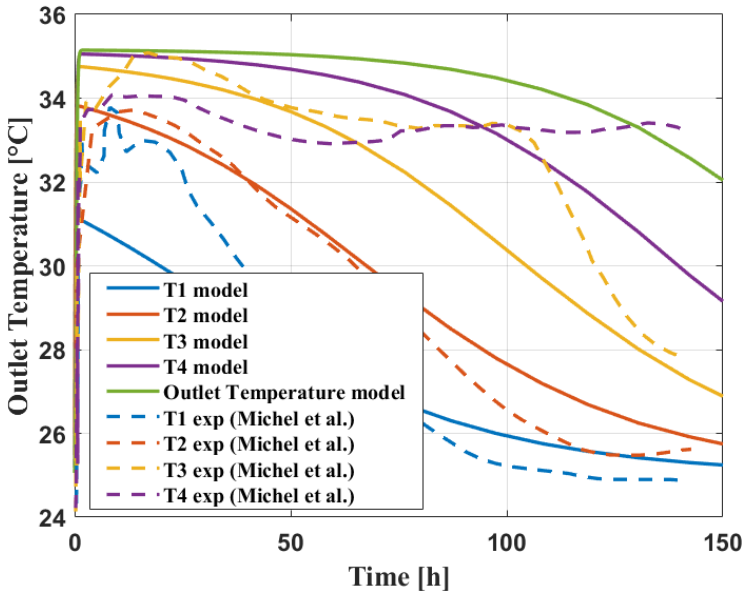

Figure 53 Comparison of hydration experimental data from Michel et al. (temperature profiles at different locations of the reactor) with modelled data.

The model predicts within approximately +-3°C the temperature levels at the different locations of the reactive bed, in particular the maximum temperature lift ΔT of approximately 10°C. Deviation can be observed for the temperature profiles measured by thermocouples T3 and T4. This deviation, increasing further along the reactive bed, never exceeds a 3°C difference, the maximum difference between experimental data and simulation being found at 100 hours for the temperature measured by thermocouple T3.

The overall rate of the reaction is well reproduced, with the temperatures at T1 and T2 stabilizing to the inlet temperature after approximately 120h-150h of reaction. Around this time the temperature profiles measured by thermocouples T3 and T4 exhibit severe non-conventional behaviour. This behaviour can be attributed to physical phenomena occurring within the reactive bed which affect heat and mass transfer; agglomeration/deliquescence of the salt due to hydration and the subsequent morphological change, or to the uneven distribution of the air flow due to localized porosity gradients caused by either the packing procedure of the reactor or crystalline structure changes caused by the hydration reaction. At the worst point, at 100 hours, the deviation reaches the previously mentioned maximum of ~3°C for thermocouple T3. In any case, even computationally demanding 2D or 3D models are not able to capture this physically complex behaviour, as reported during model validation by the authors themselves [137], and by others [184].

Dehydration

In the reference work, dehydration was carried out experimentally by providing air into the reactor module at a 34.73 m^3/h flow rate, temperature of 80°C and humidity 2557 Pa (RH = 5.4%). A kinetic rate constant of $k_{cin} = 10^{-5}$ s^{-1} was used for the simulation. **Figure 54** the temperature profiles along the reactor as a function of reaction advancement, for both experiment and simulation, can be seen. In both cases, the temperatures all along the reactor increase almost immediately to a plateau, before each increasing in turn just below the inlet temperature, to approximately 78°C. A notable difference between experiment and simulation is the equilibrium temperature plateau that is reached almost immediately by all sections of the reactor, which was found to be just under 65°C for the simulation, as opposed to a lower value of ~60°C for the experiment. Similarly, the temperature at the outlet of the reactor toward the end of the dehydration process is predicted by the model to reach the inlet temperature of 80°C, whereas the temperatures measured for the experimental setup reach values of 78°C.

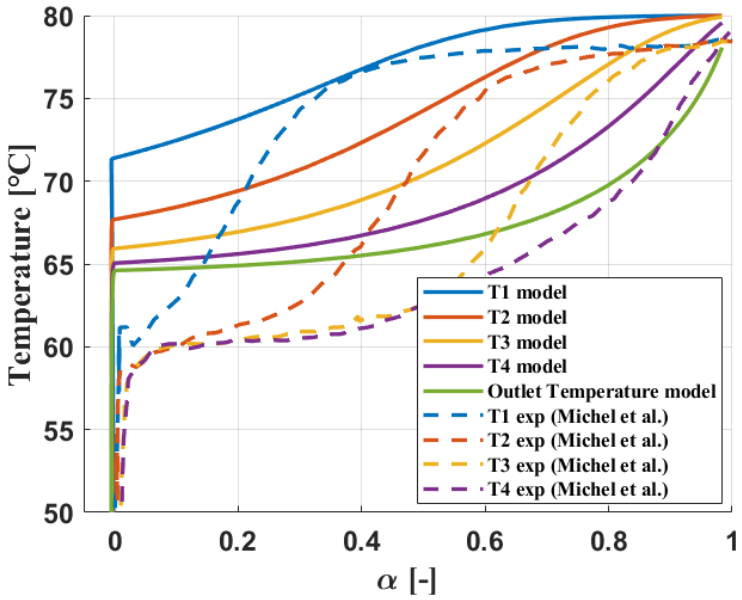

Figure 54 Comparison of dehydration experimental data from Michel et al. (temperature profiles at different locations of the reactor) with modelled.

An aspect of the dynamic behaviour that is well captured by the model is the temperature at thermocouple T4 beginning to increase (above equilibrium) when the temperature at thermocouple T1 reaches the inlet temperature. A segment of the reactor reaching inlet temperature is an indicator that this segment has been completely dehydrated (i.e., has the maximum amount of thermal energy loaded) since the solid material is being heated sensibly to the inlet temperature which is only possible if the heat provided into the reactor is no longer being absorbed by the dehydration reaction.

The simulation results best fit the experimental behaviour close to the inlet where ideal, conventional reaction behaviour can be observed. On the other hand, the simulation deviates for the reaction furthest from the inlet where the experimental data departs from conventional, expected reaction

behaviour. This behaviour is discussed in the reference study by the authors who attribute this unexpected behaviour to either the flow of the moist air following preferential paths in the salt bed rather than an evenly spread out flow across the reactor subsection, formation of diffusion paths due to the dehydration, or leakage of the reactor module. These complex phenomenological behaviours cannot be captured by the 0.5D model used in this study, and would also be difficult to replicate with higher-order models. Thus, the reactor model captures the progress of the hydration/dehydration level sufficiently to expect a realistic performance prediction of TCS reactors.

4.2 Process behaviour

In the previous paragraph, the TCS reactor model was validated with experimental data. The TCS reactor model successfully captures the temperature lift, reaction rate, overall reaction time and dynamic behaviour of temperature profiles along the reactor. The analysis may be carried out with confidence that the prediction of the reactor model is representative of TCS reactor behaviour. The following paragraph aims at studying the overall TCS process behaviour during so-called 'basic' hydration and dehydration stages. For this section, the considered case scenario is a TCS used in a dwelling as described in further detail in **sections 2.1**, **2.2** and **2.3**, to store heat during summer and release heat during winter in Birmingham, UK. The materials used in this scenario are a K_2CO_3 based salt-in-matrix composite for hydration, and a $SrBr_2$ based salt-in-matrix composite for dehydration. The mass of pure salt in the reactor is determined by the total yearly heat demand of 10 GJ / 2777 kWh divided by the number of heating days estimated to be 212 days [15], from which the mass of matrix can be calculated assuming 60 wt.% composite SIMs. Thus, reactor volume varies with material energy storage density, with an assumed constant aspect ratio of AR=L/D=4. Hydration is carried out with a flow of air at constant inlet temperature and humidity, whereas the dehydration is carried out with an air flow heated by solar energy captured by the solar thermal collector over the course of a day. The main parameter values are presented in **Table 23** and material amounts for hydration and dehydration in **Table 24.** A choice of C=1 for the main heat exchanger, i.e., equal flow rates was chosen. This choice was made for simplicity but could be optimised with different flow rates for C≠1. This optimisation was not carried out in the present work.

Table 23 Model parameters for basic hydration and dehydration simulations.

	Value	Unit	Description
Q_m	0.0671	kg/s	Reactive air flow
Q_{HTF}	0.0671	kg/s	Air flow to building load
k_{cin}	$5\ 10^{-4}$	1/s	Kinetic constant
Cp_m	960	J/kg/K	Matrix Heat Capacity
ρ_m	800	kg/m^3	Matrix Density
D_p	0.001	m	Particle Diameter
ε	0.5	[-]	Material Porosity
γ	60%	[-]	Salt wt-content

Table 24 Materials for hydration and dehydration steps.

	Hydration	Dehydration
Salt	K_2CO_3	$SrBr_2$
Matrix	Vermiculite	
m_{salt} [kg]	68	43
m_{matrix} [kg]	45	29

Hydration

The hydration/heat discharge stage is carried out during winter with cold humid air. The inlet air is considered to be pumped from the ambient surrounding the dwelling at a temperature of 5°C, and a water partial pressure of 1200 Pa, a humidity level that is frequently used in the TCS literature at the material scale for characterisation and at reactor scale for prototype operation and simulations. Realistic water vapour pressures in European climates in winter are generally significantly lower; however, for the analysis of this basic hydration/dehydration cycle the commonly used value from the literature was selected in order to provide a basis for comparison with literature works.

Feeding humid air to the reactor inlet immediately triggers the exothermic hydration reaction in the first node of the reactor. This can be seen by the rapid increase in temperature, at the outlet of the first reactor node, from the inlet temperature of 278K to the equilibrium temperature of ~304K at the inlet vapour pressure (**Figure 55**). The air passing through the unreacted material gathers heat released from the exothermic reaction, while water transported in the vapour phase of the air flow is loaded into the TCM via the chemisorption process. The heated air passes through the rest of the reactor, generating a temperature lift at each reactor node. Air passing through the rest of the reactor with lower humidity than equilibrium will not gather any more heat as it will not release water vapour, as can be seen by ~304K limit to the temperature inside the reactor. Pressure drop across the reactor was calculated using Ergun's equation for gas flowing through a packed bed (see **Annex II**). Using the parameters shown previously in **Table 23** and **Table 24** pressure drop was evaluated as $\Delta P = 1.02\ 10^4$ Pa, for a reactor length of 1.2m and flow rate 0.0671 kg/s which results in an air flow velocity of 0.67 m/s. The same pressure drop is calculated for the dehydration phase shown in the next section. With a volumetric flow rate of 0.559 m^3/s, this resulted in a pumping power of 571 W.

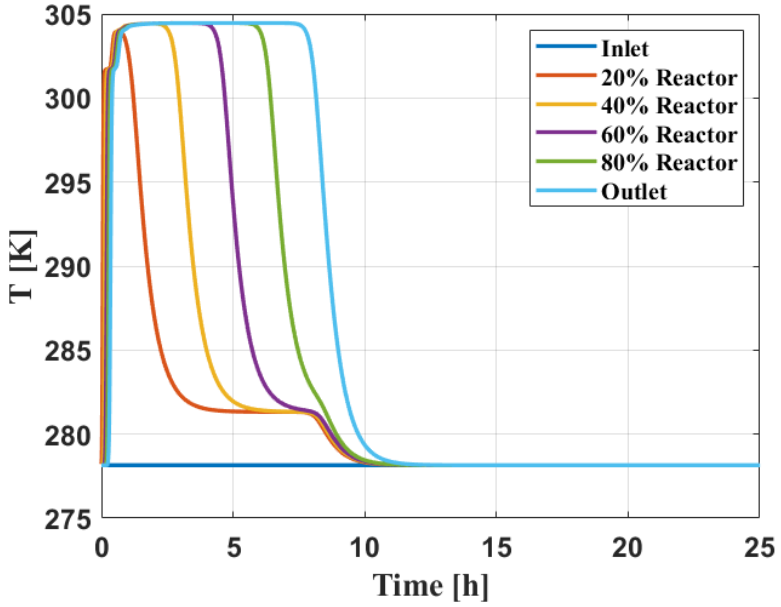

Figure 55 Local reactor temperatures during hydration/heat discharge, normalized over the inlet temperature in degrees Celsius.

The local advancement profile in **Figure 56** shows that the TCM nodes hydrate in successive order from the inlet, demonstrating the progress of a reaction front. The material in the reactor node immediately at the inlet adsorbs water from the air flow, until the local air humidity reaches equilibrium, or the material is fully loaded. In the present case, the final node of the reactor begins to hydrate when the local advancement of all previous nodes has reached unity. This behaviour mainly varies with air flow and kinetic rate constant.

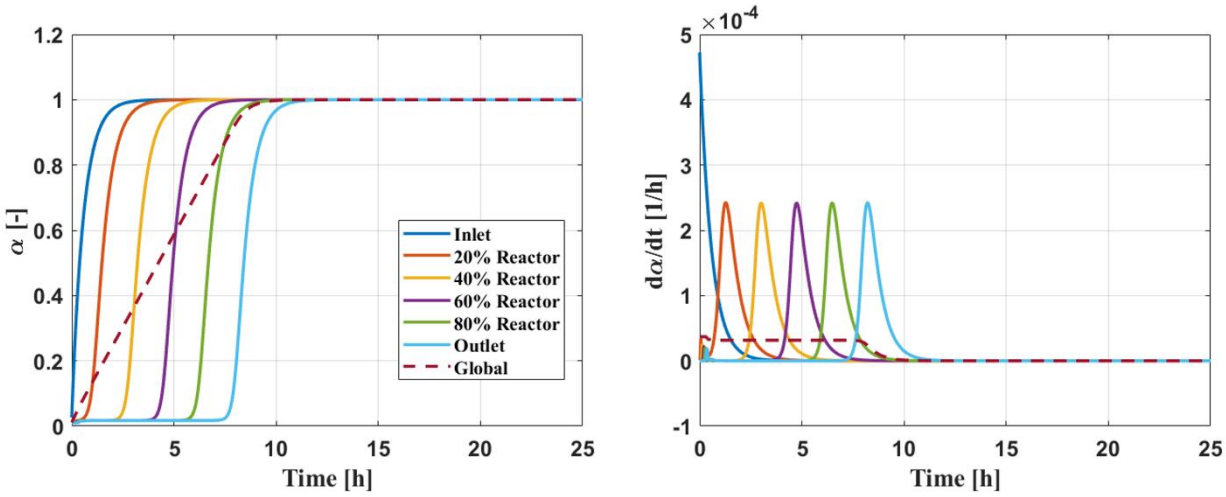

Figure 56 Local (full lines) and global (dashed red line) reaction advancement during hydration/sorption/heat discharge.

Figure 57 shows the humidity profile of the air at the outlet of the reactor nodes. Whilst the humidity at each reactor node is initially 0, humidity at the reactor nodes that are not yet in contact with humid air rapidly rises to equilibrium. Equilibrium humidity is achieved by the initial flow of air as it reacts with the first reactor nodes. At each node, once the material is sufficiently hydrated, humidity gradually increases back to match the inlet water vapour concentration as more humid air passes through the reactor and no more water is extracted from the air at that location in the reactor.

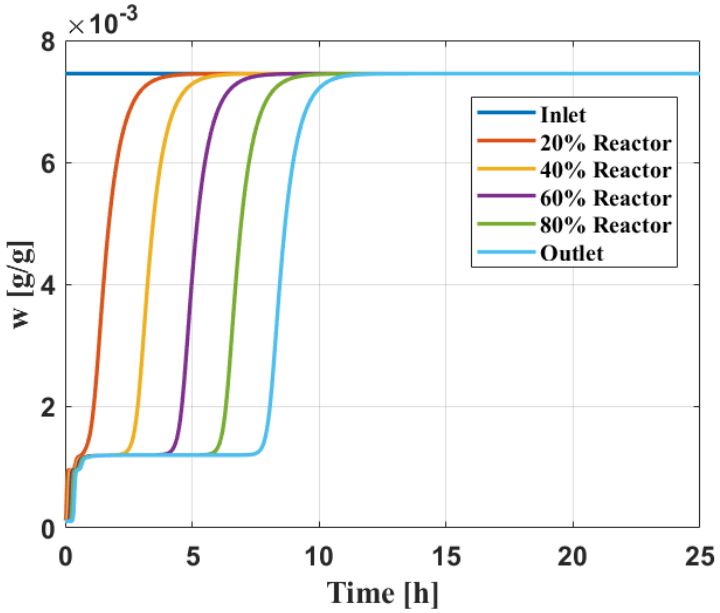

Figure 57 Local reactor non-dimensional absolute humidities during hydration/heat discharge, normalized over the inlet humidity in kg_{H2O}/kg_{air}.

The presence of the reaction front is also visible as the humidity at the outlet of each node can be seen to increase from the equilibrium plateau to the inlet humidity, from the inlet of the reactor to the outlet. The temperature profiles at different locations of the process during the hydration stage are shown in **Figure 58**: the temperature profile of the air flow being sent to the building load for space heating and the temperature sent out of the process by the heat recovery unit after exchanging with the reactor inlet. At the reactor inlet, the heat recovery unit (HRU) enables an increase of reactor inlet temperature of approximately 3°C, from the ambient temperature of 5°C to 8°C. At the outlet of the reactor, a temperature of 32°C at a mass flow rate of Q_m = 0.0671 kg/s is achieved. After heat transfer from the air flowing through the reactor to the air loop connected to the building space, the TCS process is capable of delivering heated air to the building load at a temperature of approximately 28°C, with a mass flow rate of Q_{HTF} = 0.0671 kg/s corresponding to a power output of 1.2 kW, over ~10 hours. The total amount of energy discharged at maximum power is 12 kWh. When considering the total storage capacity of the module is 10 GJ divided by 212 i.e., 13.1 kWh, the TCS delivered approximately 90.2% of the stored energy at maximum power.

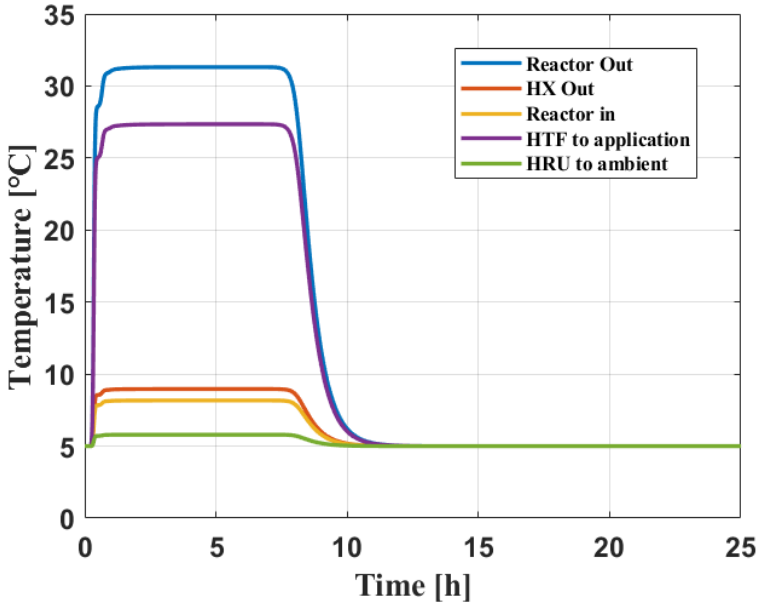

Figure 58 Hydration process – temperatures at different locations of the process.

Dehydration

Heat charge / desorption step of the thermochemical energy storage cycle is shown in this section. **Figure 59**, **Figure 60** and **Figure 61** respectively show the temperature profile, advancement, and humidity profiles at the outlet of each reactor node. Heat captured by a solar thermal collector is provided throughout the day to the TCS reactor, with the temperature profile matching the trend of total incident solar irradiation onto the FPC (**Figure 59**).

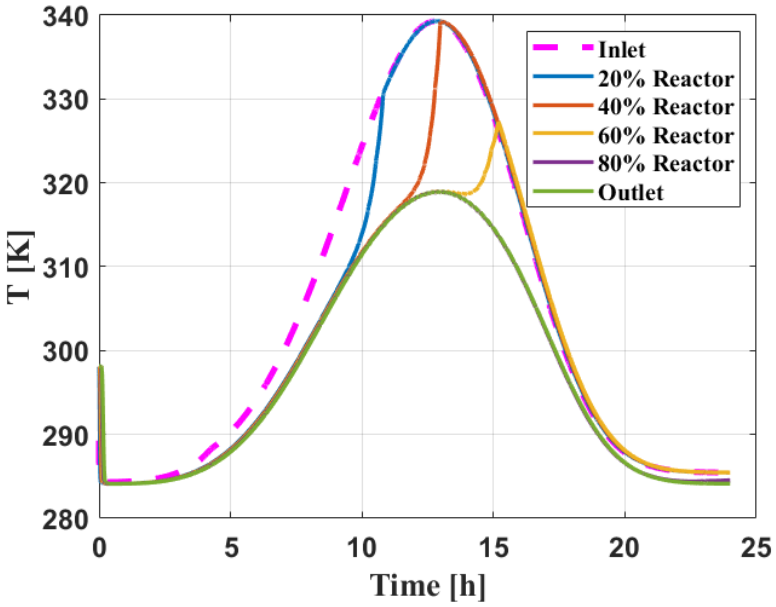

Figure 59 Reactor temperature profiles during desorption.

The low total captured solar energy compared to the reactor module's maximum heat storage capacity can be appreciated from **Figure 60** where the state of charge of the reactor does not reach 0 after the full 24 hours. It can be seen that just as the first 20% of the reactor has been completely desorbed after 12 hours, the dehydration reaction begins in the next segment of the reactor, displaying the reaction front. The dehydration reaction clearly takes place from the inlet towards the outlet of the reactor, resulting in a reaction front where all of the material upstream of the front has been dehydrated and all the material downstream of the reaction front has yet to be dehydrated; the TCS material reacts as far as the equilibrium conditions will allow. Any excess heat not consumed by the reactor at a certain level will be used further down the reactor, resulting in the reaction front.

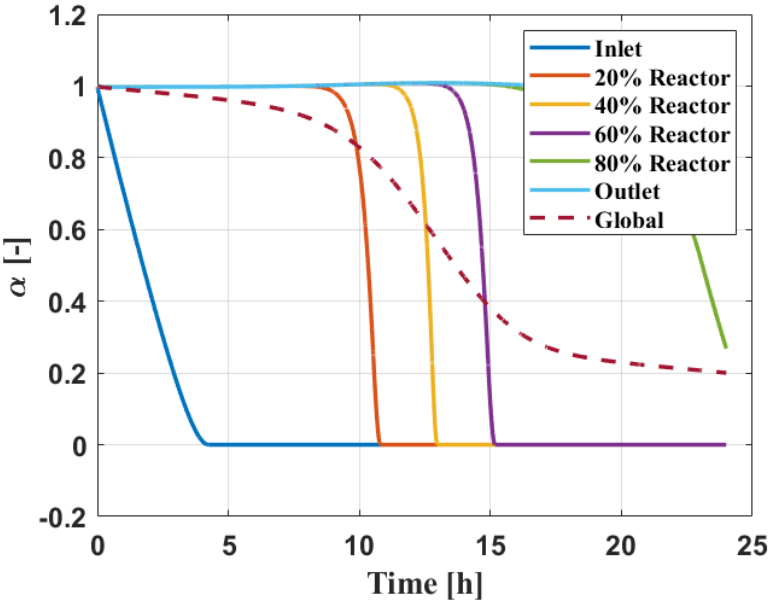

Figure 60 Local advancement profiles and global advancement during desorption.

As dehydration takes place, an increasing amount of water vapour is released by the TCM and is transported to the outlet of the reactor by the reactive air flow. **Figure 61** shows the humidity level at the outlet of each reactor node, and the increasing humidity level with increasing distance from the reactor inlet which exemplifies the accumulation of water vapour by the air flow at each node of the reactor, finally reaching its maximum at the outlet of the reactor. After some reaction time, the humidity at the outlet of each reactor node drops back down to the inlet humidity of almost 0 g/g, signalling that the entirety of the material upstream of that reactor node has fully been dehydrated, matching the reaction advancement level reaching close to 0 as seen in the previously in **Figure 60**. In this chapter, partial desorption/adsorption with successive cycles is not addressed. During a dehydration process the reactor inlet and outlet valves are closed once solar input is negligible, and the TES is maintained in a partially dehydrated state, with the remaining hydrated material located towards the outlet end of the reactor. If the next cycle is hydration to release the stored energy, only part of the total TES capacity as heat is released, with hydration beginning from the inlet of the reactor.

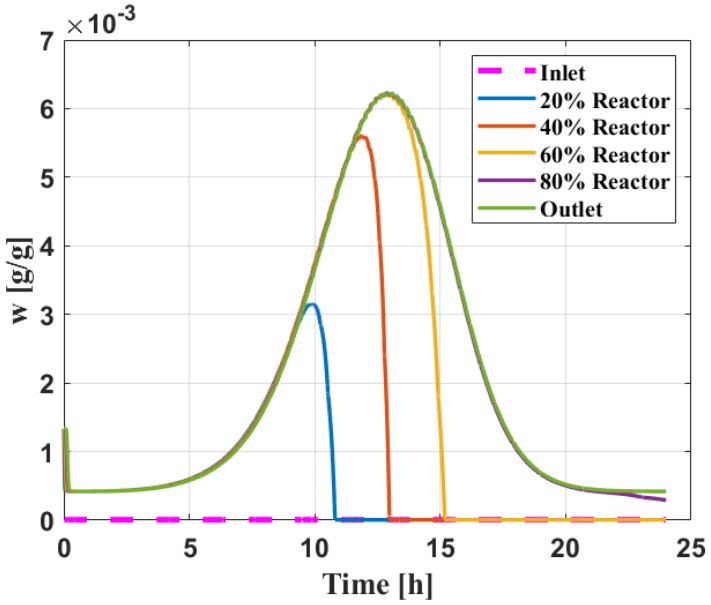

Figure 61 Reactor air humidity profiles during desorption.

5 Techno-economic performance

Having described the TCS process model, validated its accuracy using experimental data from the literature and analysed the basic hydration and dehydration cycles using a reference case scenario, the aim of **Section 5** is to analyse the impact of 1. material selection and 2. ambient temperature/pressure conditions tied to the geographic location on the techno-economic performance of the process.

5.1 Key performance indicators

Key performance indicators are a helpful means to compare the performance of different thermal energy storage solutions. The TCS scientific literature highlights the need for a common comparison framework of the different renewables-driven technologies, and in particular for different TES [166,167]. The KPIs selected here are aimed at assessing the performance of the TCS process in terms of:

- system size: a reasonable volume for a reactor installed in a family house is approximately 1 m^3 [185].
- nominal power: evaluation of the different heat fluxes during charge and discharge.
- cost efficiency: the system's competitivity compared to traditional space-heating technologies.

The KPIs used in this study are therefore the following:

(1) **Maximum temperature lift**, ΔT_{max}, the maximum achieved temperature increase between the air flow entering the TCS process and the hot air flow transporting the discharged heat used for domestic space heating.

(2) **Energy storage capacity**, ESCv expressed in kWh/m^3, is defined as the amount of energy stored in the reactor during charge for a fixed reactor volume [186]. In the case of open sorption systems for thermal energy storage, ESCv can be calculated according to **equation (59)**.

$$ESCv = \frac{\kappa \frac{|\Delta H_n^o|}{M_n} m_s}{V} \tag{59}$$

Where M_n is the molar mass of the higher hydrate, m_s the total mass of salt in the hydrated state, ΔH_n^o the reaction hydration enthalpy, κ the stoichiometric coefficient of the reaction and V the total volume of the system.

(3) **Useful energy density**, Ed_{useful} expressed in kWh/m^3, is defined as the total amount of heat released at or above the system's nominal power during the discharge step. This value can be calculated using the discharge response time (t_R) and nominal power discharge time (t_{NP}), with **equation (60)**. Differently from the energy storage capacity, only heat released above the minimum temperature of 30°C contributes to the useful energy density.

$$Ed_{useful} = \frac{1}{V}\int_{t_R}^{t_R+t_{NP}} P(t)dt = \frac{Cp_{HTF}}{V}\int_{t_R}^{t_R+t_{NP}} Qm_{HTF}T_{HTF,out}(t)dt \tag{60}$$

(4) **Average power density** P_{av}, expressed in W/m^3, is the time averaged power output of the process divided by the volume of the reactor, and is shown in **equation (61)**:

$$P_{av} = \frac{1}{V}\frac{1}{t}\int_0^t P(t)dt \tag{61}$$

(5) **Storage capacity cost**, SCC, expressed in €/kWh and calculated using **equation (62)** proposed by Scapino et al. [15]

$$SCC = \frac{reactor\ cost + solid\ material\ cost + fan\ electrical\ costs}{Ed_{useful}V} \tag{62}$$

- Solid material cost: A universal price of inorganic salts does not exist since it depends on the amount purchased, the purity of the salt and on the supplier. The prices of each salt were recovered from Alibaba.com, taking the first five entries with a minimum purity of 95%. A minimum and maximum price are provided which depend on the amount purchased. Both these values were considered, averaged, and plotted in **Figure 62** along with the standard

deviation. As can be seen, there exists a difference in price of up to several orders of magnitude, the cheapest being magnesium sulphate $MgSO_4$ at 0.16 €/kg, several orders of magnitude cheaper than Strontium Bromide $SrBr_2$ at 24.03 €/kg.

- Reactor cost depends on the energy density and volumetric density of the selected inorganic salt. The total amount of steel used for the reactor is derived from the total volume of reactive material, with an added 10% margin to account for space between modules, diffusers at the inlet and other potential components.
- Process costs, composed of (a) Fan electrical costs: the duration of the hydration and dehydration cycles depends on the selected salt. Both the total amount of energy to release and the rate and duration of heat release will impact the costs associated with operating the fan. Fan electrical costs are capital costs of the fan installation and cost of electricity expenditure to operate. Fan consumption is calculated with Ergun's pressure drop equation as explained previously. (b) Heat exchanger costs: the two air-to-air heat exchangers (HX and HRU) are HVAC type heat exchangers, as manufactured by Toshiba [187]. Minimum and maximum effectiveness provided by the manufacturer were used in combination with Kays and London [183] to determine the NTU for each heat exchanger, and therefore the cost per NTU is derived for the corresponding flow rate (~200 m^3/h)

Table 25 Air-to-air heat exchanger costs [187]

Parameter	Unit	Models				
Model	-	VN-M150HE	VN-M250HE	VN-M350HE	VN-M500HE	VN-M650HE
Flow Rate	m^3/h	150	250	350	500	650
Price	£	1181	1217	1397	1692	1880
min ε	%	81.5	78	74.5	76.5	75
max ε	%	83	81.5	79.5	78	76.5
NTU (C/C=1)	-	4.75	4	3.5	3.5	3.25
Cost per NTU	£/NTU	248.6	304.3	399.1	483.4	578.5

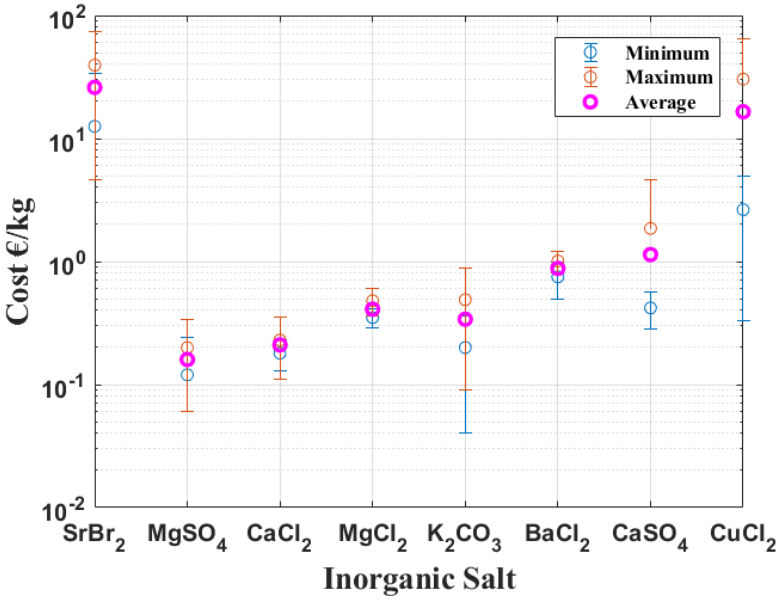

Figure 62 Minimum, maximum and average bulk prices of inorganic salts. Prices recovered from the first 5 entries when entering the name of each salt on the search engine of Alibaba.com, with a minimum of 95% purity.

Table 26 Summary of evaluated KPIs.

KPI		Unit
Maximum Temperature Lift	ΔT_{max}	K
Energy storage capacity	ESC_v	kWh/m^3
Useful Energy Density	Ed_{eff}	kWh/m^3
Average Power Density	P_{av}	W/m^3
Storage Capacity Cost	SCC	€/kWh

5.2 Material selection

The thermal performance of a number of inorganic salt hydration reactions in view of low-temperature TCS is discussed in the literature. Some early material scale reviews screened several hundred different potential hydration reactions, with mixed results that only account for steady state thermophysical properties of the sorption reactions. For example, N'Tsoukpoe et al. screened 125 salts in their 2014 review [26], with 17 being found suitable, and $SrBr_2$, $MgSO_4$ and $LaCl_3$ being considered the 'top 3'. However, in their 2017 review Donkers et al. screened 563 different hydration reactions [19], shortlisting 25 salt hydrations as the most suitable: neither $SrBr_2$ nor $MgSO_4$ were included in the shortlist, yet these two salts have attracted more attention than $LaCl_3$. The motivation for the following section is therefore twofold:

(1) the discrepancy in the assessment of different salt/water pairs have led to no definitive consensus on the most suitable salt based TCM, although some candidates emerge from the frequency at which they are studied in TCS literature.

(2) the need for a comparison of TCS systems techno-economic performance with different inorganic salt hydration reactions.
The effect of material selection on the dynamic behaviour of the system during hydration is therefore studied in the following section.

Hydration of the TCS with constant operating conditions and variation of the TCM is carried out in this section. Inlet conditions of the humid air flow are water vapour pressure of p_{in} =1200 Pa and inlet temperature of 5°C which are the assumed average winter temperature and humidity surrounding the family house. These operating conditions are kept constant and identical for all considered materials throughout this section. The total mass of salt in a module is calculated from the daily heat demand divided by the TCM theoretical energy storage density. The volumetric energy storage density of a salt-in-matrix composite can be calculated with **equation (63)**.

$$Ed_{SIM} = \frac{Ed_{salt}\varepsilon}{1 + \frac{(1-comp)}{comp}\frac{\rho_{salt}}{\rho_{matrix}}} \quad (63)$$

Where $comp$ is the weight fraction of salt in the composite, Ed_{salt} the volumetric energy storage density of the pure salt and $\mathring{U}$the bulk porosity of the composite, assumed to be 50%. The TCM is a 60 wt.-% salt content composite with vermiculite as supporting matrix. The salt to matrix ratio was kept the same for all cases, although solubility, which determines the maximum concentration achievable when dissolving the salt into water for the wet impregnation synthesis method, varies between salts. **Table 27** summarises the selected parameters for the simulations presented in this section.

Table 27 Model parameters for basic hydration and dehydration simulations.

	Value	Unit	Description
T_{amb}	16	°C	Ambient Temperature
P_{in}	1200	Pa	Inlet Water Vapour Pressure
k_{cin}	5 10^{-4}	s^{-1}	Kinetic Rate Constant
N	50	[-]	# of Reactor Nodes
T_{in}	5	°C	Inlet Temperature
p_{in}	1200	Pa	Inlet Vapour Pressure
Q_m	0.0671	kg/s	Air flow rate in reactor loop
Q_{HTF}	0.0671	kg/s	Ai flow rate to building load

Figure 63 shows the time-dependent temperature profile of the air flow sent to the building load for different salts during hydration with the conditions outlined in **Table 27**. At fixed operating conditions, the energy output of the TCS system during hydration varies significantly in magnitude and duration with salt selection, with the temperature lift compared to the ambient varying between a minimum of +6.1°C for the hydration of the $CuCl_2$-based composite and a maximum +23.6°C for the $MgCl_2$-based composite. Thus, in these conditions, only the $MgCl_2$, K_2CO_3 and $SrBr_2$-based TCS can discharge heat above the minimum temperature requirement of 30°C for domestic space heating.

The temperature lift achieved during inorganic salt exothermic adsorption depends mainly on the thermodynamic properties of the reaction, in particular the equilibrium conditions of the reaction, and on the inlet operating temperature and humidity conditions. These heat discharge performances can also be controlled with variation in mass flow rates of either the main reactive air flow or the heat transfer air flow to the building load.

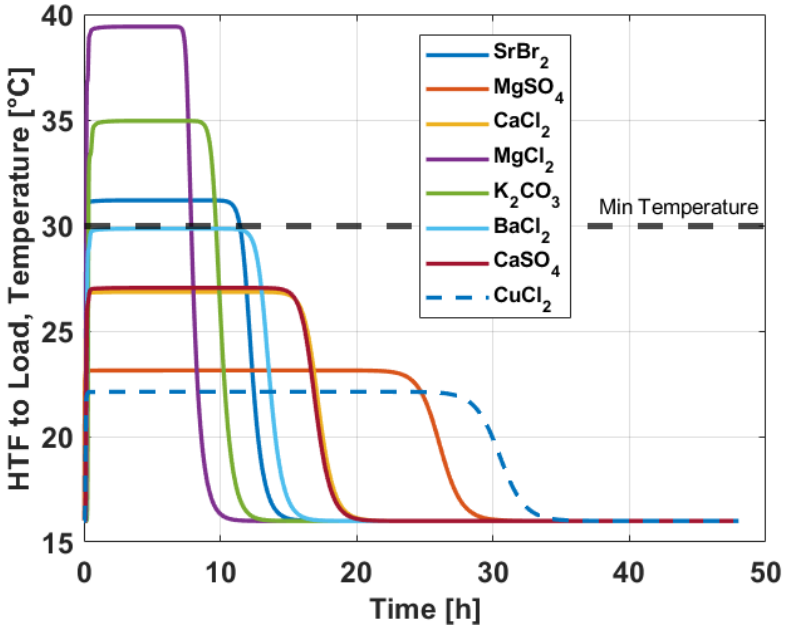

Figure 63 HTF to space heating temperature at mass flow rate Q_{HTF} = 0.0671 kg/s, for different salts in a 60 wt.-% composite, p_{in} = 1200 Pa, T_{amb} = 16°C

By recalling the Clausius-Clapeyron equilibrium diagram of the investigated salt hydration reactions (**Figure 44**), the equilibrium vapour pressure of the $MgCl_2$ hydration is seen to be the lowest among all the selected salts over the temperature range 0°C to 150°C (roughly the temperature range encompassing maximum and minimum temperatures during the entire storage cycle, hydration and hydration included). Therefore, the so-called pressure drop Δp_w, i.e. the difference in water vapour pressure between the vapour pressure introduced into the reactor and equilibrium water vapour pressure at these reaction conditions, is largest for $MgCl_2$ hydration than for any other salt hydration amongst those considered. Upon further investigation of the correlation between pressure drop and achieved temperature lift, it becomes evident that the higher the pressure drop for a hydration reaction, the higher the temperature lift. This behaviour is due to salt hydration reaction rate being strongly tied to the equilibrium pressure drop (a common feature of many solid-gas reversible reactions) [82,108,162,164], with the reaction rate driving the power output of the system. Several studies in the literature, including work in earlier chapters of this thesis (see **Chapter III.4** on the effect of humidity on hydration kinetics), show the correlation between hydration reaction rate and humidity, at both material scale [98,188,189] and reactor scale [118,120,123].

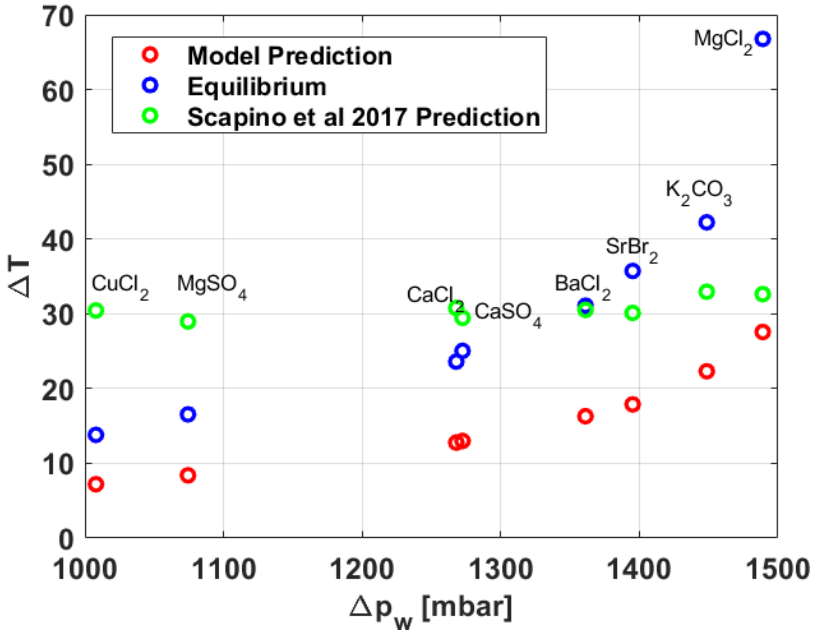

Figure 64 Temperature lift during hydration as a function of equilibrium pressure drop, according to the present model, the equilibrium temperature and the expression given by Scapino et al. [15].

Figure 64 investigates the relationship between achieved temperature lift at the outlet of the reactor and equilibrium pressure drop, according to the present simulations, to the equilibrium temperature predicted by the Clausius-Clapeyron equation **equation (64)**, and the temperature lift prediction formula proposed by Scapino et al [15] **equation (65)**. The latter is predicated on a simple heat balance between the amount of heat that may be released from the TCM based on the available humidity and the thermal capacity of the air flow carrying the humidity into the reactor and the thermal energy out of the reactor.

$$p_{eq} = 101325e^{\frac{-\Delta H}{RT}+\frac{\Delta S}{R}} \tag{64}$$

$$\Delta T = \frac{p_{H2O}\Delta H}{RT\rho_{air}Cp_{air}} \tag{65}$$

It can be seen that at low pressure drops (such as for $CuCl_2$ hydration or $MgSO_4$ hydration), the TCS process model predicts a lower temperature lift than the two other methods which are in agreement. However, as equilibrium pressure drop increases, the equilibrium predicts an ever increasing temperature lift difference with Scapino's formula and the prediction with the present model, which in turn increasingly agree. For both the present model and equilibrium predictions, temperature lift and pressure drop are positively correlated, whereas Scapino's method is less sensitive to the material choice and tends to predict a constant temperature lift of ~25K to ~30K.

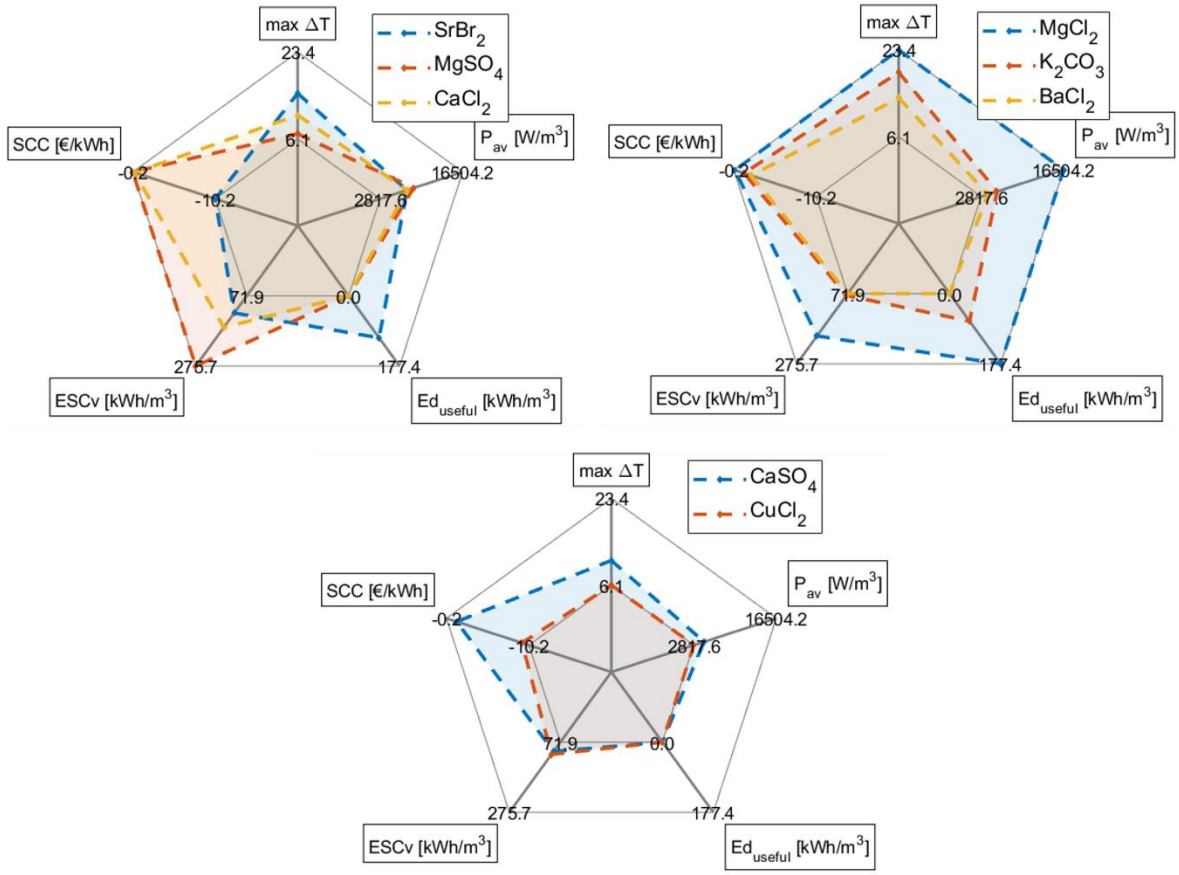

Figure 65 System KPIs for constant operating conditions and different salts.

The performance of the TCS system is therefore impacted by the ambient temperature and water vapour pressure, and by the reaction's equilibrium conditions which depend on salt/water pair thermochemical properties. KPIs calculated from the system's simulation data (partially presented in **Figure 52**) are shown in **Table 28** and **Figure 65**. These 5 KPIs were selected on the basis that they enable the performance achieved by the system operating with the different materials in terms of power output (P_{av}), energy quality (Ed_r), total energy capacity (Ed_{useful}), storage capacity cost (1/SCC) and maximum achieved temperature lift (ΔT_{max}). Storage capacity cost is inverted so that performance measurement improves when the value of the KPI increases.

System KPIs can be visualised in a radar chart in **Figure 65**. The system operating with the $MgCl_2$-based composite is the system showing overall the most promising performance according to the selected KPIs. An effective storage density of 177 kWh/m^3 was achieved for a total energy storage density of 195 kWh/m^3. The discrepancy observed between Ed_{useful} and Ed_r is explained by Ed_r being based on the total energy released by the process through the HTF, whereas Ed_{useful} only accounts for the energy transported by the HTF that is above the minimum acceptable temperature level of 30°C.

Table 28 KPIs for constant operating conditions (P_{in} = 1200 Pa, T_{amb} = 5°C), and different salts.

	ΔT_{max}	P_{av}	Ed_{useful}	Ed_r	SCC
	K or °C	W/m^3	kWh/m^3	kWh/m^3	[€/kWh]
$SrBr_2$	15.2	7276	106	122	10.2
$MgSO_4$	7.1	8383	0	276	0.2
$CaCl_2$	10.8	7275	0	164	0.4
$MgCl_2$	23.4	16504	177	195	0.3
K_2CO_3	19.0	5478	69	77	1.4
$BaCl_2$	13.8	3961	0	72	2.3
$CaSO_4$	11.0	4509	0	99	1.4
$CuCl_2$	6.1	2818	0	108	9.3

Thus, response time and power output profile towards the end of the reaction, which are the main phases during discharge where heat is released at low temperature, are responsible for a 25% reduction in energy storage density in the case of $MgCl_2$. An interesting case worth mentioning is the TCS process using $MgSO_4$, for which the total energy storage capacity is 276 kWh/m^3, is the highest among all the TCMs, the lowest SCC, while providing no useful energy to the building load due to a low equilibrium pressure drop that can be seen in **Figure 64**.

In terms of average volumetric power density, large variations from 2.8 kW/m^3 up to 16.5 kW/m^3 may be observed between TCS systems operating with different reactive materials. However average power output does not appear to be proportional to the equilibrium pressure drop discussed previously; while equilibrium pressure drop enables the prediction of maximum temperature lift, it does not provide any information regarding the thermal behaviour towards the end of the reaction. Recalling **Figure 63**, it can be seen that for some materials, the tail end of the temperature profile is long which signifies that some thermal energy is released with low to negligible temperature lift. Illustrating this, the TCS system operating with barium chloride $BaCl_2$ exhibits an average power density of 3.9 kW/m^3 for a maximum temperature lift of 13.8°C, whereas with $CaSO_4$ the TCS system provides a smaller maximum temperature lift of 11.0°C with a larger average power density of 4.5 kW/m^3.

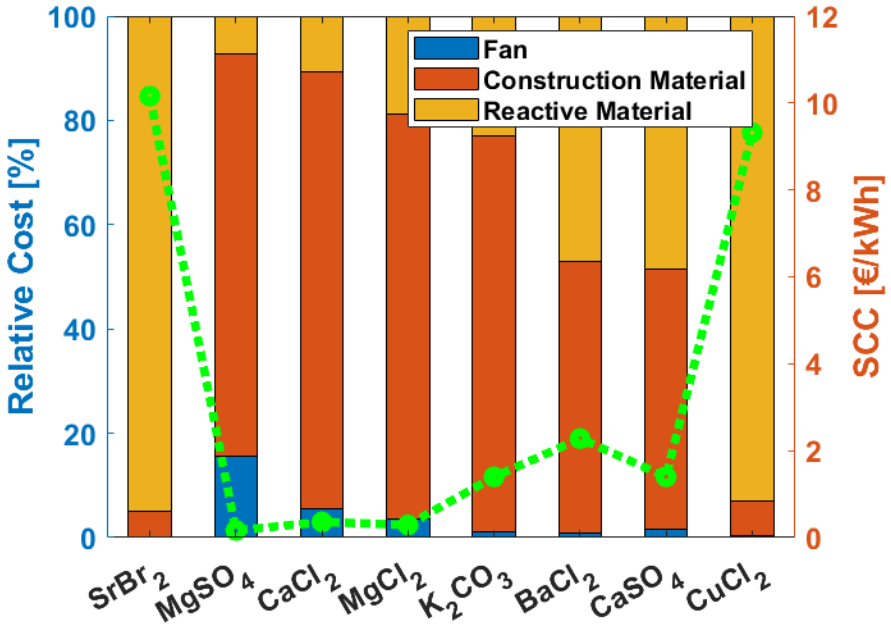

Figure 66 Left axis and bar plot: relative cost of reactive materials, reactor construction materials and fan electrical costs during hydration, for different salts. Right axis and black markers: KPI storage capacity cost (SCC in €/kWh installed storage capacity), for different salts.

Figure 66 reports both the cost breakdown of the TCS system for the different considered salts, and the storage capacity cost. It would be expected that the materials enabling the best thermal performance would also be the most expensive, and therefore a payoff between thermal performance as measured by P_{av} and $E_{d,eff}$, and economic performance (SCC) would be expected. Interestingly, systems using the aforementioned $MgCl_2$ / $CaCl_2$ / $MgSO_4$ which showed the best overall technical performance, exhibit the lowest storage capacity costs, at 0.23 €/kWh, 0.28 €/kWh and 0.11 €/kWh, respectively. Systems operating with SIMs based on K_2CO_3 / $BaCl_2$ / $CaSO_4$ exhibit SCCs in the range 1 €/kWh – 1.25 €/kWh. For the least economically viable TCS systems, which are $SrBr_2$ and $CuCl_2$, reactive material costs account for over 90% of the total cost breakdown, while exhibiting SCCs over 8 €/kWh, which is in line with salt cost comparison carried out earlier in **Figure 62**. Furthermore, according to an estimation by Rathgeber et al. [190], a residential TES running a maximum of two cycles a year should exhibit a SCC below 1.43 €/kWh. The system analysed in this study could be economically viable if containing a composite with any of the considered salts except $SrBr_2$ and $CuCl_2$.

The calculation of storage capacity cost could ultimately be refined with a more detailed cost calculation of the process units; in this case storage capacity costs encompass material costs, fan costs and reactor material costs, which gives a basis for comparison for system economic viability with different salt-in-matrix composites. From these results it can be seen the economic viability of the TCS system depends strongly on the selected salt/water pair. Notable outliers are $MgCl_2$ which has the higher potential equilibrium pressure drop leading to the highest power output for the TCS system, $MgSO_4$ which has the highest energy storage density and lowest storage capacity cost, but delivers

heat at low temperature, and K_2CO_3 which shows the second highest power output after $MgCl_2$ combined with low cost. Despite showing good technical performance, the high bulk material cost of $SrBr_2$ strongly impacts final economic viability at the reactor scale.

5.3 Impact of location and ambient conditions

Specific locations

Other than material selection, the performance of the TCS system is tied to the operating conditions of the process, which are in turn dependent on local weather conditions. Thus, performance will vary with geographic location. For the hydration step in particular, inlet water vapour pressure and ambient temperature are the main parameters affected by geographic location that will impact performance. Hydration/heat discharge is expected to mainly be carried out during winter, which in Europe is characterised by low temperatures and low relative humidities (in the range of 4.5 mbar to 9 mbar). As has been highlighted in a critical overview of TCS systems for domestic household applications [116], the hydration conditions often reported in TCS studies of ~12 mbar to ~25 mbar are not representative of winter conditions, which leads to the following two issues with the outcomes:

(1) the reported performance of the TCS material/reactor/system is calculated for unrealistic, overly favourable conditions.

(2) the calculated economic viability is overestimated as studies do not consider the need to include additional humidification in the case of open systems, which replaces the evaporator found in closed systems.

Table 29 Average winter weather conditions for selected European locations.

Location	Outdoor Temperature [°C]	Relative Humidity [%]	Water Vapour Pressure [mbar]
Birmingham	5	86	7.35
Eindhoven	4	90	7.17
Lyon	4	83	6.61
Stuttgart	1	88	5.66
Helsinki	-2	89	4.59
Barcelona	10	74	8.92

The objective of this section is therefore to explore the impact of location on domestic TCS process performance. The locations, shown in **Table 29**, are selected on the basis that they present weather conditions considered as suitable [43] for domestic low-temperature TCS for space heating:

- sunny warm summers where, for a household equipped with a flat plate solar collector, daily available solar energy exceeds the required daily heat demand.

- cold dark winters that drive a high space heating demand that isn't covered by available solar energy.

Considering that the air used for hydration during winter is extracted from outside the building and assuming no humidification system is present, the hydration conditions depend on ambient air temperature and water vapour pressure. Visualisation of the different salt hydration reaction equilibriums in a Clausius-Clapeyron diagram in **Figure 67** reveals that at the selected geographical locations, equilibrium pressures of the reactions are only marginally lower than the ambient water vapour pressures. With such a low potential equilibrium drop, the performance of the system can be expected to be low.

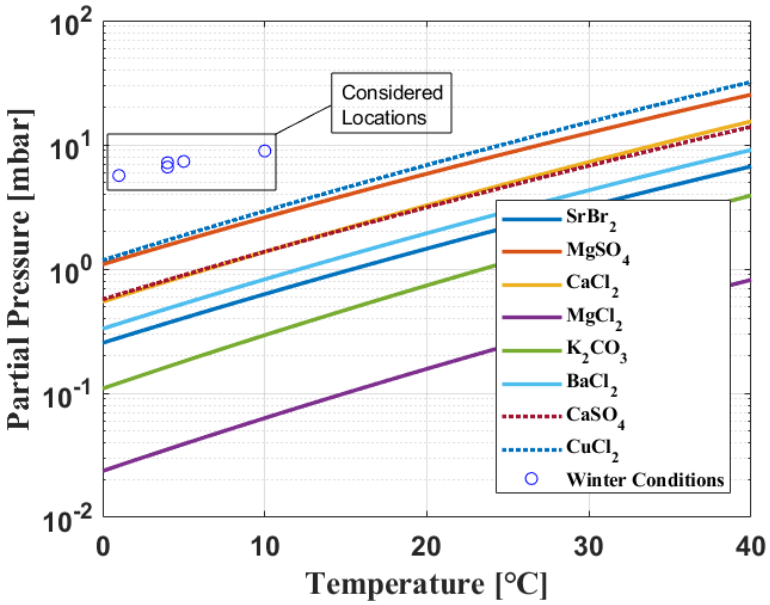

Figure 67 Clausius-Clapeyron diagram for inorganic salt hydration, with winter weather hydration conditions at each considered location.

Since pressure drop may be low but not negligible, hydration of these salts will still yield a temperature lift in the humid air flow. The equilibrium vapour pressure of $MgCl_2$ hydration at outdoor temperature is the lowest among the considered inorganic salts, which results in the highest potential for system performance. This is reflected in the performance of the TCS process using $MgCl_2$ at different locations presented in **Figure 68**. While total system storage capacity cost is unaffected by location, maximum temperature lift φT_{max} varies from 10 K in Helsinki to 16.8K in Barcelona, with a corresponding variation in average volumetric power density P_{av} from 3.2 kW/m^3 to 5 kW/m^3. For all locations, however, the achieved temperature lift is insufficient to provide air above the threshold value of 303.15K, which is reflected by KPI Ed_{useful} being 0 kWh/m^3.

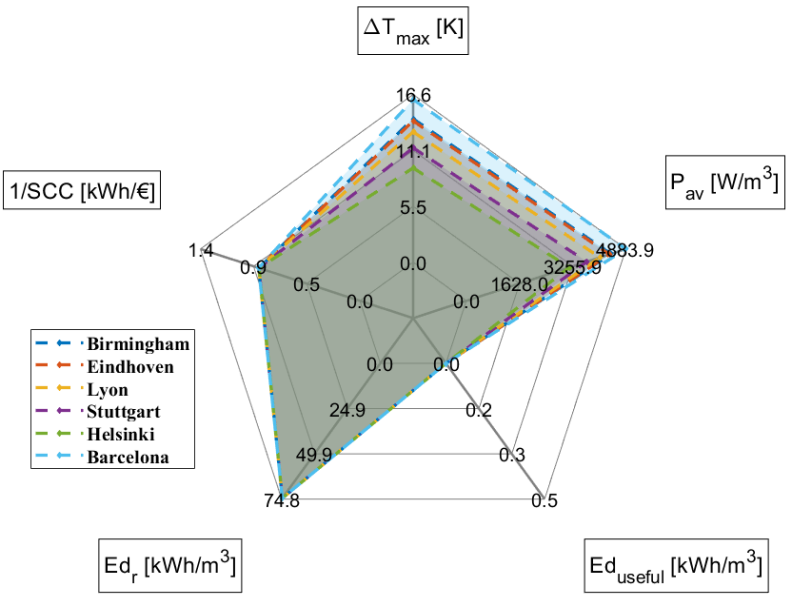

Figure 68 System KPIs for reactor carrying out the hydration of $MgCl_2$-based composite at various locations during winter.

Thus, in winter at different locations in Europe and using realistic weather conditions, the system is not able to deliver heat at the required temperature. Since $MgCl_2$ has the lowest equilibrium vapour pressure of all the considered salts over the temperature range [0°C - 40°C], it will achieve the highest temperature lift among all the selected salts, as was simulated in the previous section. Therefore, in realistic winter conditions (ambient temperature between -5°C and +10°C, water vapour pressure between 4 mbar and 10 mbar), the TCS process will not deliver the necessary heat at the required temperature level at any of these locations without additional humidification, which entails additional costs to consider for system economic viability and total system volume. The following section explores the possibility of controlling the inlet vapour pressure through the integration of a humidification system to the process and its impact on performance.

Impact of humidity

Assuming an indoor starting temperature of 16°C, the following section analyses the impact of inlet water vapour pressure on the process performance as measured by the KPIs, over partial pressures varying from ambient winter conditions to humidities achieved through a forced humidification system. The adsorption process with the additional forced humidification system is shown in **Figure 69**. The water vapour pressure varies between 500 Pa and 1800 Pa. Air can't be taken directly from the outside in winter as air at ~5°C such as during winter in Birmingham can only be hydrated to ~ 800 Pa before saturation, whereas at 16°C a maximum of 1800 Pa can be achieved. These operating conditions may be visualised on the Clausius-Clapeyron phase diagram shown in **Figure 71**.

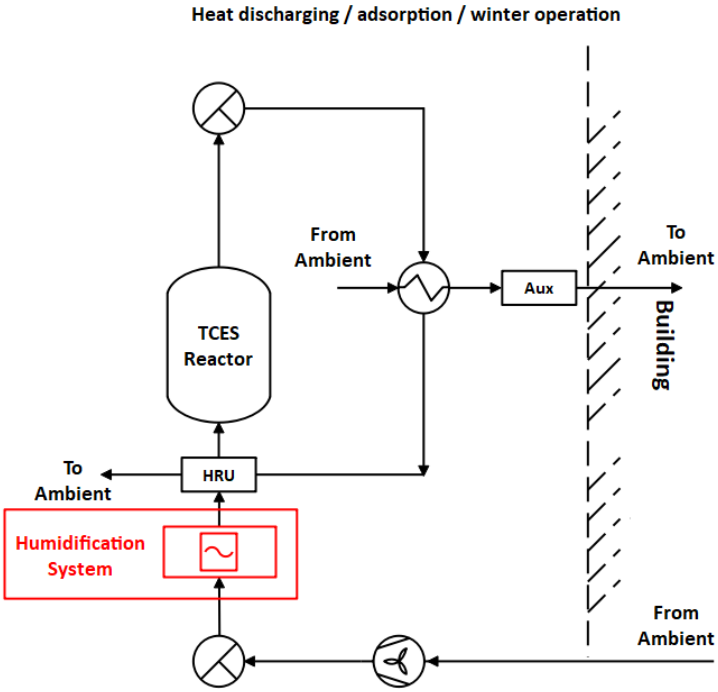

Figure 69 Process flow diagram of TCS system during adsorption, with additional humidification system (in red).

The humidification system is assumed to be based on evaporative humidification, which implies a cooling effect of the humidified air. The induced cooling effect on the air flow can be determined from a Mollier / humid air diagram shown in **Figure 70**, with the key assumption that the humidification takes place with constant enthalpy, as the only variation is that of the enthalpy of water vapour which is negligible compared to the dry air enthalpy [191].

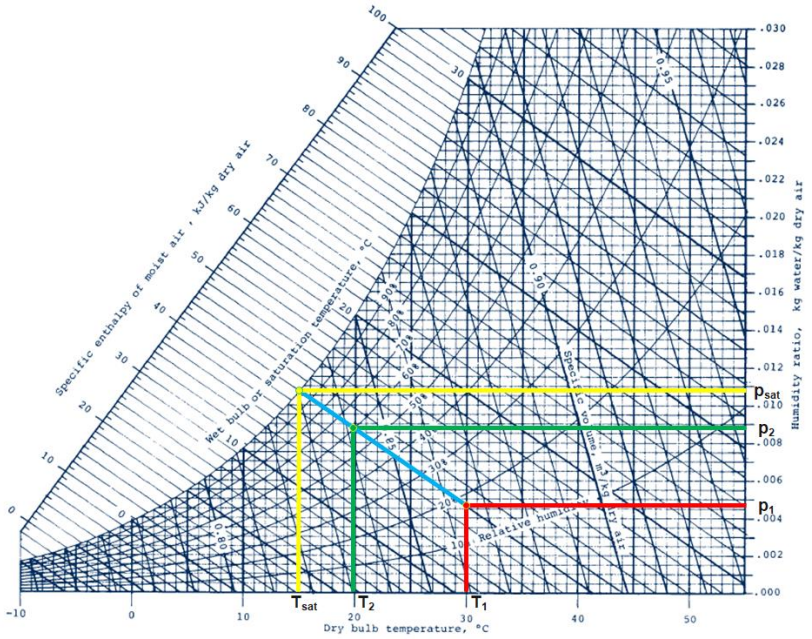

Figure 70 Mollier (or humid air) diagram. Red represents the starting conditions of an air flow to be humidified, yellow the saturation conditions in the case of maximum humidification, and green the final temperature of the air after humidification-induced cooling.

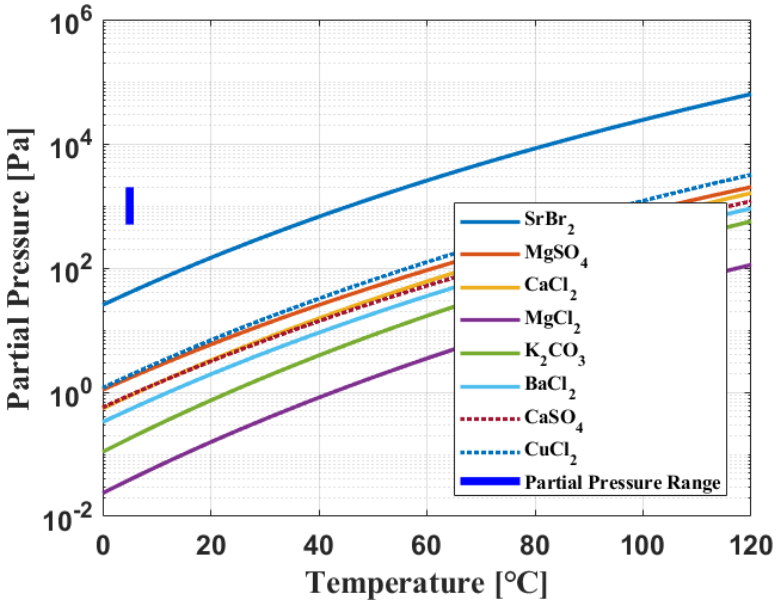

Figure 71 Clausius-Clapeyron phase diagram for all salts with water vapour pressure range.

As can be recalled from previous sections, the temperature lift and therefore the power output are highly correlated to the inlet humidity and the associated equilibrium drop. Variation in system performance over the range of inlet vapour pressure is shown in **Figure 72**, **Figure 73,** and **Figure**

74. **Figure 72** shows that the maximum temperature lift varies between 5 K and 35 K for all salts for water vapour pressures between 900 Pa and 1800 Pa, corresponding to an average power density varying between 3 kW/m^3 and 25 kW/m^3.

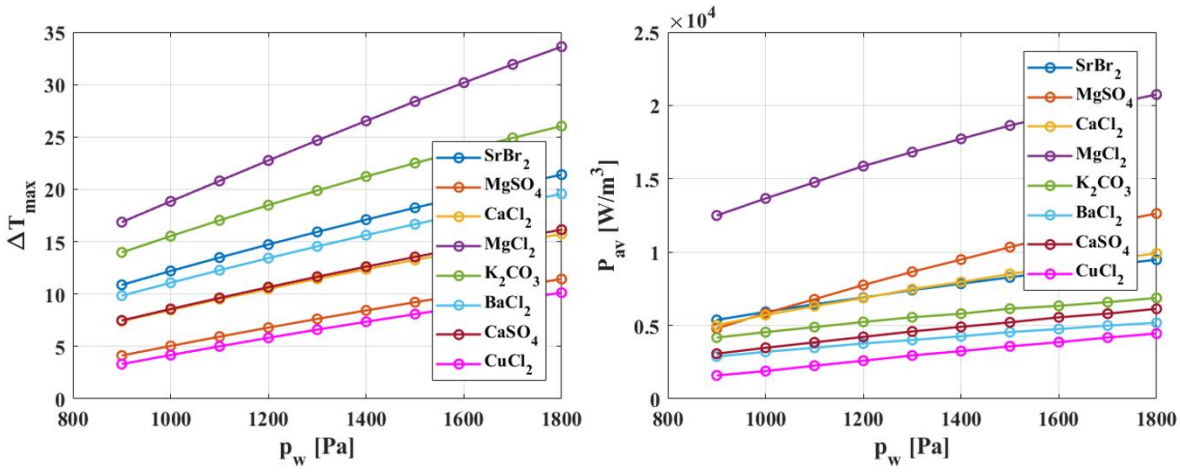

Figure 72 Influence of inlet water vapour pressure on (left hand side) maximum achieved temperature lift and (right hand side) average power output.

As can be appreciated by **Figure 71** there is a minimum water vapour pressure threshold for useful energy storage to be extracted. Below inlet water vapour pressures of 1000 Pa, no useful energy is extracted resulting in the system delivering 0% of the household's daily space heating demand apart from $MgCl_2$ and K_2CO_3 based systems. For each material there is a minimum water vapour pressure which allows for useful energy to be released. Increasing onset vapour pressure increases the options for useful TCS storage.

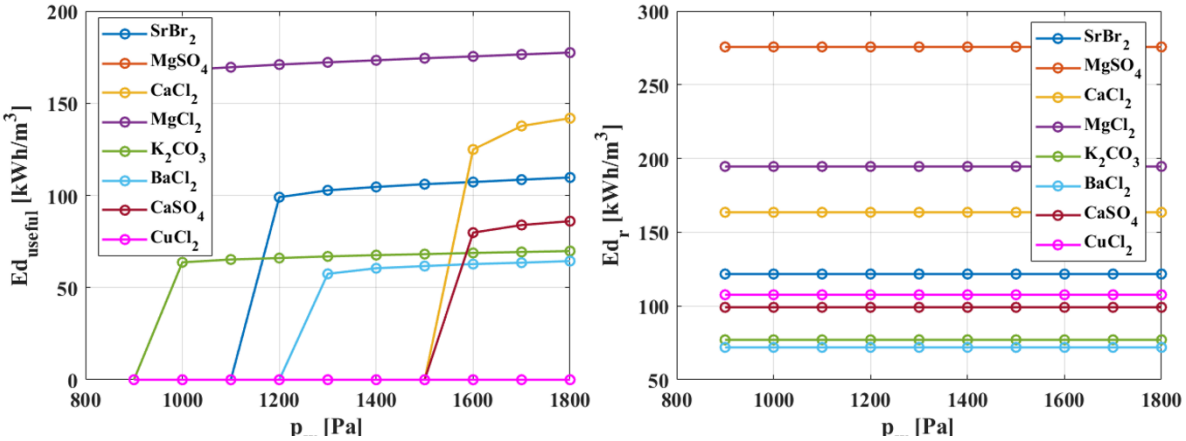

Figure 73 Influence of inlet water vapour pressure on (left hand side) useful energy density and (right hand side) system self-sufficiency.

To take the example of $SrBr_2$ hydration dispersed into a host matrix, if a sufficient water vapour pressure is achieved then a useful energy density of 112 kWh/m^3 is obtained for the system and approximately 87% of the theoretical daily energy demand can be met. The highest achievable effective energy storage density of 175 kWh/m^3 is achieved with $MgCl_2$ hydration. Notably, the hydration of $MgSO_4$ yields the highest potential of reactor energy density of 265 kWh/m^3, combined with one of the lowest possible temperature lifts which varies between 5 K and 19 K for inlet water vapour pressures in the range 500 Pa to 2000 Pa. This result further highlights the potential for magnesium sulfate hydration as a viable TCS reaction. However additional technical efforts to humidify the inlet air stream are necessary to achieve sufficient temperature lift with this material.

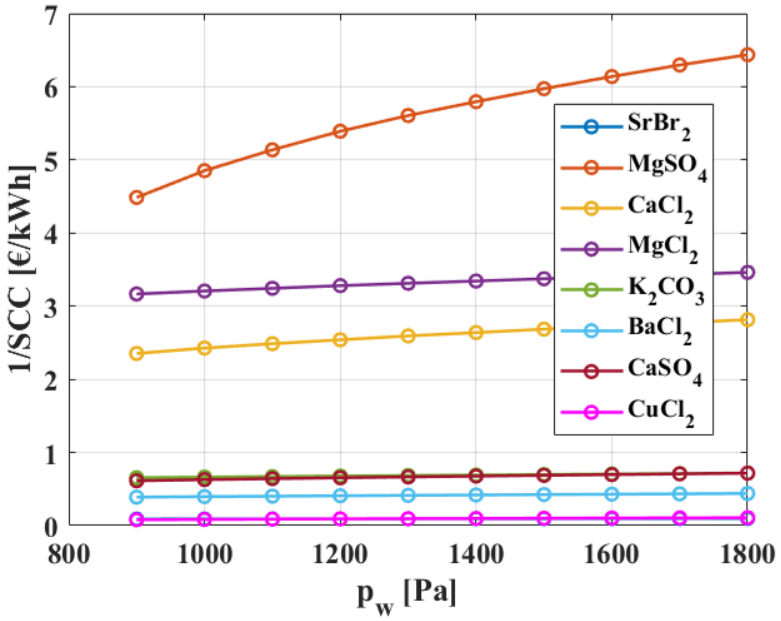

Figure 74 Influence of inlet water vapour pressure on inverse system storage capacity cost.

The dependence of the system storage capacity cost for each material on inlet water vapour pressure is shown in **Figure 74**. Above each material's threshold vapour pressure, the system storage capacity cost stabilises quickly and loses its dependency on vapour pressure. This can be explained by the fact that SCC depends strongly on the total amount of energy released by the process, and not the quality of the released heat; only for very low water vapour pressures is the maximum potential for heat release of the TCS reactor not achieved. Overall, the TCS system displays low storage capacity costs above the threshold vapour pressure for each material, except strontium bromide. This latter material displays a minimum storage capacity cost of 11 €/kWh, which is above the maximum acceptable value of 1.43 €/kWh discussed in **Section 5.2**. While use of this material in the TCS process shows one of best performances, the high cost of the material makes strontium bromide unlikely to be viable in open TCS for residential space heating. Systems operating with a $MgCl_2$ or $MgSO_4$ and to a lesser extent $CaCl_2$ based composite show the best economic viability.

6 Kinetic analysis

The following section is aimed at studying the impact of kinetic model selection and kinetic rate constant on the performance of the TCS system. Solid-state kinetics of inorganic salt hydration and dehydration are typically evaluated at the milligram sample scale through various experiments under different isothermal temperature programs or water vapour pressures. Representative kinetic models are generated through the parameterisation of the reaction rate with the temperature and/or partial pressure. The resulting kinetic models can then be ideally used for a reaction occurring under any experimental condition providing it does not deviate too far from the conditions of the kinetic measurements.

6.1 Modelling of solid-state reaction kinetics

Solid-state kinetics were discussed in detail in **Chapter II.3.1** and **Chapter III.5**. The solid-state kinetic equation is briefly discussed here, shown in **equation (66)**. The equation describes the rate of a solid-state reaction at a location inside the reactor.

$$\frac{d\alpha}{dt} = k_{cin} f(\alpha)(1 - \frac{p_{eq}}{p_v}) \tag{66}$$

With the rate constant determined through an Arrhenius expression:

$$k_{cin} = A_f exp(\frac{-E_a}{RT}) \tag{67}$$

Where A_f and E_a are the kinetic parameters: A_f the frequency factor and E_a the activation energy [82]. As was shown in the literature review, in **Chapter II.3.2** and **Chapter II.3.4**, the majority of models coupling heat/mass/kinetics equations in simulations in the literature use the first order (F1) kinetic model. This can be observed for models of both open and closed systems, for a wide variety of different inorganic salts, and for both hydration and dehydration. **Table 30** shows a summary review of reactive system models used for the hydration/dehydration of pure inorganic salts. This table is not a definitive review of all existing simulations yet is representative of the very narrow range of kinetic models for these types of reactors for TCS. The table presents the kinetic parameters, which are either the direct kinetic rate constant k_{cin}, or the Arrhenius parameters that enable calculation of the kinetic rate constant through the temperature-dependent relation (**equation (67)**).

Table 30 Summary of existing pure salt hydration and dehydration simulations in TCS literature, with kinetic model and parameters.

Model	Parameters	Material	Type	Reaction	Dimensions	Ref
F1	E_a = 5 kJ/mol A_f = 7.45 10^{-4} s^{-1}	$MgCl_2$	Closed	Hydration	1D	[127]
F1	E_a = 55 kJ/mol A_f = 1.67 10^5 s^{-1}	$MgSO_4$	Closed	Hydration	2D	[129]
F1	E_a = 55 kJ/mol A_f = 1.67 10^5 s^{-1} E_a = 20.1 kJ/mol A_f = 0.94 s^{-1} E_a = 82.84 kJ/mol A_f = 1.42 10^9 s^{-1}	$MgSO_4$ $CuSO_4$ $CaSO_4$	Closed	Dehydration	2D	[130]
F1	E_a = 55 kJ/mol A_f = 1.67 10^5 s^{-1}	$MgSO_4$	Closed	Dehydration	2D	[131]
F1	E_a = 55 kJ/mol A_f = 1.67 10^5 s^{-1}	$MgSO_4$	Closed	Dehydration	2D	[128]
F1	E/R = 10038 A_f = 1.9 10^{10} s^{-1} E/R = 11428 A_f = 2.2 10^{10} s^{-1}	$MgCl_2$ 1st step $MgCl_2$ 2nd step	Open	Dehydration	2D	[133]
F1	k = 5.5 10^{-6} s^{-1}	$SrBr_2$	Open	Hydration	2D	[83]
F1	E_a = 55 kJ/mol A_f = 5.5 10^5 s^{-1}	$MgCl_2$	Closed	Dehydration	2D	[162]
F1	k = 10^{-4} s^{-1}	$SrBr_2$	Both	Both	2D	[108]
F1	E_a = 55 kJ/mol A_f = 1.63 10^5 s^{-1}	$SrBr_2$	Closed	Both	3D	[138]
F1	k = 5.10^{-4} s^{-1}	K_2CO_3	Open	Hydration	Quasi 2D	[140]

While all of the reviewed simulations use the F1 model, the few available material-scale kinetic analyses of salt hydration (in this thesis, see **Chapter III**, and in the literature, as will be expanded on in **section 6.2**) point towards alternative models amongst the standard solid-state kinetic model database being more accurate. Experimental evidence put forward in this thesis in **Chapter III** and in recent works in literature point towards the hydration of inorganic salts being mainly dominated by diffusion, which is the basis of derivation of the 'D' class of models. Coincidently, in **Chapter**

III, diffusion-class models were also found to accurately model hydration $MgCl_2$-vermiculite hydration.
Power output (respectively input) of TCS systems is proportional to hydration (resp. dehydration) reaction kinetics. Analysing the discrepancy in predicted performances with either the standard first-order (F1) model or specifically designed models which better reflect physical reality (for example, diffusion models D2, D3 or D4 when considering the experimental evidence discussed previously) could therefore shed light on the accuracy of current TCS reactor simulations presented in the literature.

Furthermore, for many of the cases shown in **Table 30**, it is often unclear how the kinetic parameter pair activation energy E_a / frequency factor A_f (or direct values for the reaction rate constant k_{cin}) were determined. Since (a) conclusions are drawn from these case studies on the performance of the simulated systems, and (b) the performance of the simulated systems depends on the kinetic rate constant (or parameters), therefore (c) a sensitivity analysis of system behaviour on kinetic reaction rate can clarify the accuracy of performance predictions in relation to the assumptions made by authors on the reaction rate parameterisation.

6.2 Sensitivity to reaction rate constant

Before addressing the impact of the nature of the kinetic model on TCS performance, the effect of kinetic rate constant for a given kinetic model needs evaluating. The sensitivity of the TCS system behaviour to variations in kinetic rate constant value is presented in the following paragraph. The hydration of a 60wt.-% potassium carbonate-based composite in the conditions detailed in **Table 31** was simulated for different values of rate constant, using the first-order (F1) kinetic model. **Figure 75** and **Table 32** show the sensitivity of the KPIs to variations of the rate constant.

Table 31 Parameters for the simulation of the TCS process for kinetic analysis.

	Value	Unit	Description
T_{amb}	5	°C	Ambient Temperature
p_{in}	1200	Pa	Inlet Water Vapour Pressure
Q_m	0.0671	kg/s	Air mass flow rate
N	50	[-]	Reactor Subdivisions

While KPIs that are dependent on the total energy released during discharge (reactor energy storage density Ed_r and useful energy storage density Ed_{useful}) show very little sensitivity to variations in k_{cin} values, average power P_{av} was found to vary from 2.94 kW/m^3 to 8.27 kW/m^3 when varying the value of the kinetic rate constant from 10^{-4} s^{-1} to 5.10^{-3} s^{-1}. An increase from k_{cin} = 10^{-4} s^{-1} to k_{cin} = 5.10^{-4} s^{-1} (two typical k_{cin} values according to **Table 30**) leads to a two-fold increase in average volumetric thermal power output (**Figure 75a**). The increase in average volumetric power of the discharge cycle can be explained by the impact of the kinetic rate constant on the TCS outlet power profile (**Figure 75b**).

Table 32 KPIs for TCS system with a 60wt.-% potassium carbonate-based composite with constant operating conditions (P_{in} = 1200 Pa, T_{amb} = 5°C), and different kinetic rate constants for the first order (F1) model.

k_{cin} [s^{-1}]	ΔT_{max} K or °C	P_{av} kW/m^3	Ed_{useful} kWh/m^3	Ed_r kWh/m^3	SCC [€/kWh]
10^{-4}	22.31	2.94	0.00	77.06	1.381
5 10^{-4}	22.48	6.23	0.00	77.06	1.382
10^{-3}	22.48	7.21	0.00	77.06	1.383
5 10^{-3}	22.67	8.27	0.00	77.06	1.421

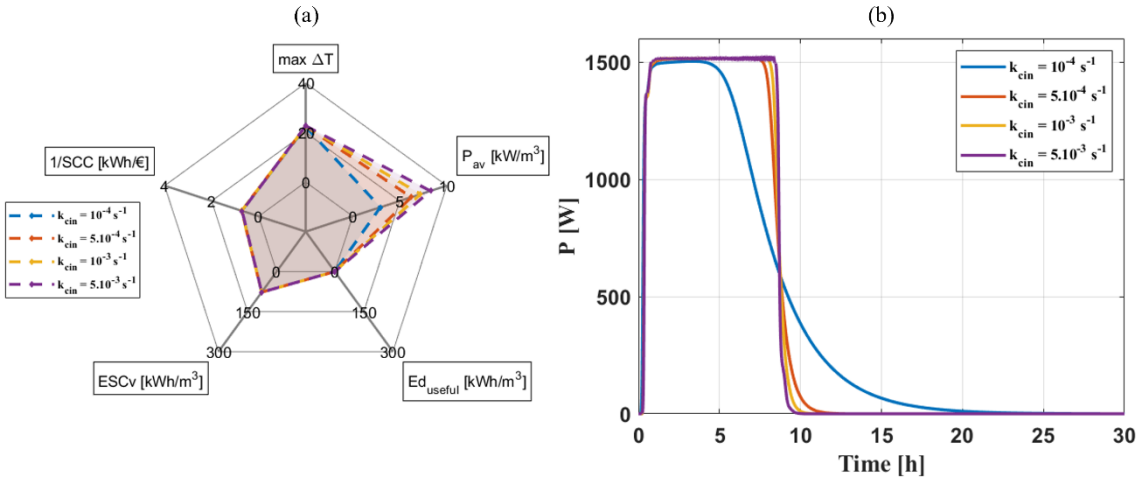

Figure 75 Evaluation of TCS KPIs during hydration of a 60wt.-% potassium carbonate-based composite, impact of kinetic rate constant value using first order (F1) model.

Figure 75b demonstrates the difference in power profile for rate constants k_{cin} = 10^{-4} s^{-1} to k_{cin} = 5.10^{-4} s^{-1}. Decrease in rate constant value leads to increasing the slope and length of the tail end of the power profile, which indicates that energy is effectively released below the maximum achievable power for the selected operating conditions and material. On the other hand, increase in rate constant increases the rate water adsorption from the air flow to the TCM, which results in a faster discharge, i.e. higher power discharge for the same amount of storage capacity. This proportional increase is limited to ~ k_{cin} = 10^{-3} s^{-1}, beyond which the rate of heat extraction is no longer limited by the kinetics of the reaction, but rather by the equilibrium conditions of the reaction which determines the reaction temperature, and the air flow rate which determines the amount of heat that can feasibly be removed. It can therefore be seen how the choice of rate constant affects volumetric power density.

Thus, KPIs dependent on the overall dynamic behaviour of the TCS system are more strongly impacted by changes to the kinetic rate constant than the other KPIs. Furthermore, it appears that the theoretical performance, and perhaps the viability, of the entire system could hinge on the selected kinetic rate constant, with the achieved temperature lift added to the inlet temperature varying around the threshold value of 30°C with kinetic rate constant value.

6.3 Case studies and impact of model selection

As has been discussed in the literature review (**Chapter II**), a small number of kinetic models have been proposed in the literature for the hydration and dehydration reactions of inorganic salts. The majority of these kinetic studies were focused on the dehydration reaction, whereas kinetic studies focusing on the hydration are sparse. Furthermore, application of these models for the reaction kinetics modelling in TCS simulations are largely absent, with authors generally preferring the first order (F1) model as an approximation of reaction kinetics rather than physically representative kinetic models such as diffusion-based models. The following section aims to study the impact kinetic models on the overall performance of the TCS system to evaluate the discrepancy between simulation and reality due to the selection of simpler models.

Kinetic models in the literature

These aforementioned kinetic models are shown in **Table 33** for the solid-state kinetic models developed in this work, and in **Table 34** for the available solid-state kinetic models in the literature. While **Table 34** does not cover the entirety of available models for predicting the water uptake or removal of inorganic salts and salt-in-matrixes, to the best of the author's knowledge all models formulated within the solid-state kinetic framework for kinetic equations (detailed in [82]), with explicit kinetic parameters (E_a and A_f) applicable over approximately the range of temperatures envisioned for TCS are shown in this table. Alternative models for the hydration of inorganic salts exist in literature, particularly models derived from Fick's diffusion equation in porous media [192], which have been used to show that the hydration of pure potassium carbonate is diffusion-limited [193]. This type of model has most often been used for the simulation of salts impregnated in reactive matrixes or pure physical sorbents such as silica gel or zeolite [93,101,194]. Fickian models were not considered, with solid-state kinetic models being the focus of this study.

Table 33 Solid-state kinetic models for inorganic salt and salt-in-matrix/water adsorption, developed in this work (Chapter III). Kinetic parameters calculated through fitting and the Arrhenius relation. [min^{-1}] can be conventionally used as a unit for reaction rate constants.

Material (stoichiometric loading)	Step	Model	Kinetic Parameters
K_2CO_3 (0-1.5)	Adsorption	D3	$E_a = 3.58*10^4$ J/mol $A_f = 9.34*10^5$ min^{-1}
		F1	$E_a = 3.92*10^4$ J/mol $A_f = 3.52*10^6$ min^{-1}
$MgCl_2$ (2-6)	Adsorption	R3	$E_a = 1.63*10^4$ J/mol $A_f = 5.22*10^2$ min^{-1}
		F1	$E_a = 2.25*10^4$ J/mol $A_f = 5.79*10^2$ min^{-1}
K_2CO_3 (0-1.5) / Vermiculite	Adsorption	A2	$E_a = 7.92*10^4$ J/mol $A_f = 1.64*10^{13}$ min^{-1}
		F1	$E_a = 7.51*10^4$ J/mol $A_f = 3.42*10^{12}$ min^{-1}
$MgCl_2$ (2-6) / Vermiculite	Adsorption	R3	$E_a = 2.81*10^4$ J/mol $A_f = 4.82*10^4$ min^{-1}
		F1	$E_a = 2.86*10^4$ J/mol $A_f = 6.01*10^4$ min^{-1}

Table 34 Solid-state kinetic models for inorganic salt/water adsorption and desorption, available in the literature. For reference [16]**, multiple models for the different reaction steps of $MgCl_2.6H_2O$ desorption were proposed, differently from the other references which proposed a single model.**

Material	Step	Model	Parameters	Ref.
K_2CO_3 (1.5)	Adsorption	Prout-Tompkins	E_a = 46.22 kJ/mol A_f=1.083.10^6 min^{-1}	[98]
	Desorption	Prout-Tompkins	E_a = 78.30 kJ/mol A_f=8.898.10^{10} min^{-1}	[98]
$MgCl_2.6H_2O$ (6-4)	Desorption	R2	E_a = 66.8 kJ/mol A_f =3.6·10^9 s^{-1}	[95]
$MgCl_2.6H_2O$ (4-2)	Desorption	R3	E_a = 138.0 kJ/mol A_f =8.8·10^{17} s^{-1}	[95]
$MgCl_2.6H_2O$	Desorption	Various	E_a = 103.74 kJ/mol A_f =2.088·10^{13} s^{-1}	[16]

Hydration of potassium carbonate

In this specific example, pure potassium carbonate was considered as the TCM. It is assumed that hydration of this TCM in the considered reaction takes place without being hindered by deliquescence / agglomeration etc. The kinetics for both hydration and dehydration reactions have been studied in the literature [98], and in a previous chapter of this work (**Chapter III**) for the water sorption reaction. The hydration of potassium carbonate at 25°C and 7.5 mbar, carried out in **Chapter III**, was kinetically hindered and most of the kinetic models were fitted to the experimental data with poor accuracy (R^2<0.95 in many cases), particularly when fitted with the differential method. On the other hand, it was found using the integral method that the first-order model F1 and the spherical diffusion model D3 modelled with K_2CO_3's hydration behaviour with relatively high accuracy (R^2>0.98). The fitted kinetic rate constants were found to be 1.36 10^{-3} min^{-1} and 8.76 10^{-3} min^{-1} for the two models, respectively. **Equation (68)** shows the resulting first order model F1 suitable for the hydration of potassium carbonate at 25°C:

$$\frac{d\alpha}{dt} = 5.87\ 10^4 \exp\left(-\frac{3.92\ 10^4}{RT}\right)(1-\alpha)\frac{p_w}{p_{eq}} \qquad (68)$$

Equation (69) shows the resulting diffusion model D3 suitable for the hydration of potassium carbonate at 25°C:

$$\frac{d\alpha}{dt} = 1.56\ 10^4 \exp\left(-\frac{3.58\ 10^4}{RT}\right)\frac{3(1-\alpha)^{2/3}}{2(1-(1-\alpha)^{\frac{1}{3}})}\frac{p_w}{p_{eq}} \qquad (69)$$

The shrinking core / contracting sphere model (i.e. R3) was identified as a suitable solid-state kinetic model for the hydration of potassium carbonate by Gaeini et al. [98], and the associated kinetic equation is shown in **equation (70)**:

$$\frac{d\alpha}{dt} = 6.05\ 10^4 \exp\left(-\frac{46.22\ 10^3}{RT}\right)(1-\alpha)^{\frac{2}{3}}\frac{p_w}{p_{eq}} \qquad (70)$$

Simulations were carried out for a TCS system with a potassium carbonate packed reactor with the three aforementioned kinetic models. The results of the simulation and comparison between different kinetic models are presented in the following figures (**Figure 76**, **Figure 77** and **Figure 78**).

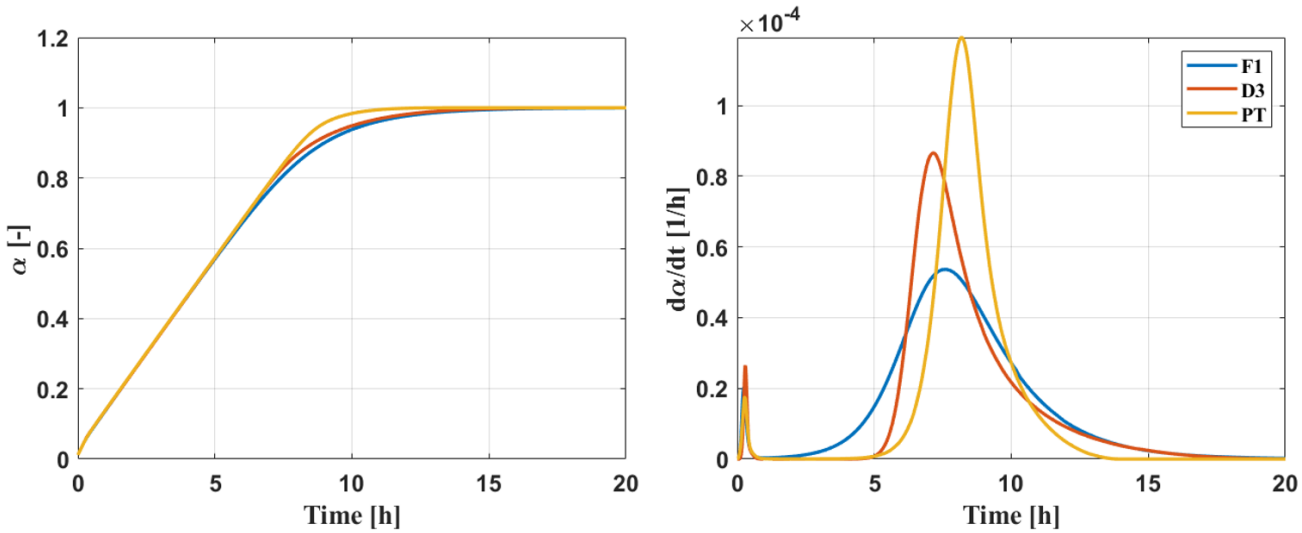

Figure 76 Comparison of simulation results for potassium carbonate hydration: (left) Global reaction advancement and (right) reaction rate with first order model F1, diffusion model D3 and Prout-Tompkins model investigated in [98]**.**

As can be seen from the comparison of the reaction advancements and reaction rates for different kinetic models (**Figure 76**), the Prout-Tompkins / shrinking core model predicts higher reaction rate peaks, with the reaction driven by the shrinking core model reaching a maximum reaction rate of approximately 1.18 10^{-4} h^{-1}, whereas with the D3 and F1 models maximum reaction rates of 8.65 10^{-5} h^{-1} and 8.36 10^{-5} h^{-1} are achieved. Ultimately the change in reaction model results in a sharper slope for the reaction advancement profiles over the entire length of the reactor. These results are logical since the kinetic model by Gaeini et al. was for hydration reactions that were faster with overall better mass transport than the hydration reactions carried out in this work. As a result, the temperature-dependent kinetic rate constant *k(T)*, calculated through the Arrhenius expression and kinetic parameters E_a and A_f, is higher than the kinetic rate constant calculated in this work.

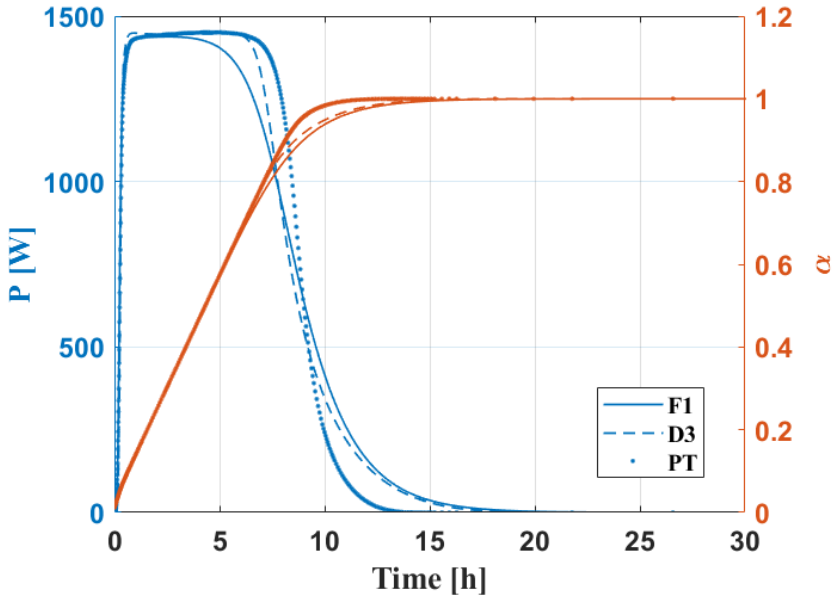

Figure 77 Comparison of simulation results for potassium carbonate hydration: process power output and global reaction advancement profile for different kinetic models.

While the selection of the kinetic reaction model has a noticeable influence on local advancement profiles (**Figure 77**), the global reaction advancement is only slightly affected by the choice of reaction model; the simulation of the TCS with the shrinking core model predicts a faster reaction progress between ~40% and 60% of the total reaction time, which notably results in a sharper temperature profile/power output slope once the temperature begins decreasing after approximately 4 hours (first-order) to 6 hours (shrinking core) of discharge. A sharper temperature profile slope is preferable in terms of process operating performance, as it generally signifies that heat is being discharged at a high temperature for a longer period of time, and less heat is discharged below the minimum acceptable temperature of 30°C for the space-heating purposes. As a result, the reactor carrying out the hydration reaction driven by the shrinking core model maintains a constant maximum power output of 1,425W for 6.8 hours, whereas with the same reaction driven by first-order kinetics that level of power output can only be sustained for 3.4 hours, resulting in a 50% decrease in effective heat space-heating time compared to the Prout-Tompkins kinetics.

Certain KPIs being intrinsically tied to the power output, the difference in power output is reflected on the overall system performance. The effect of kinetic model selection on the power profile of the reactor, and the associated performance considerations discussed in the previous paragraph, can be further appreciated through visualisation of the KPIs (**Figure 78**).

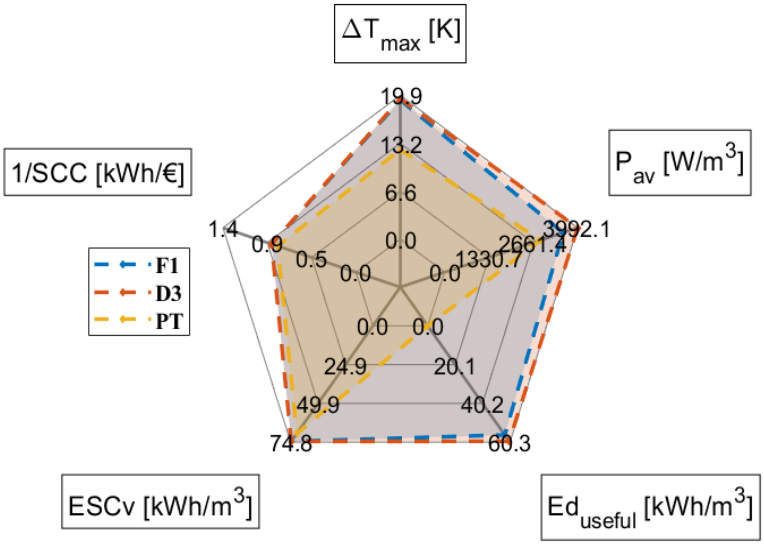

Figure 78 Comparison of key performance indicators from simulation results for potassium carbonate hydration with first order, diffusion and shrinking core (PT) kinetic models.

The two KPIs that are most sensitive to the selection of solid-state kinetic model are the useful energy and average power output. It can be seen from the mapping of the performance indicators that the total useful energy storage density increases from 165 kWh/m^3 to 178 kWh/m^3, i.e., an 8% increase. The average system power output is affected even more significantly by the kinetic model selection: a variation from approximately 10 kW/m^3 to 17 kW/m^3, i.e., a 70% increase in average power output.

Hydration of magnesium chloride

The next considered case scenario is a TCS system using pure $MgCl_2$ as the thermochemical storage material. This material was used in two different prototype open sorption reactors in some early studies by Zondag et al. In the first case [119], the material in the reactor behaved very poorly due to the overhydration causing agglomeration of the salt particles and formation of a hard salt layer that was impenetrable by an air flow: significant pressure drop was measured in the packed bed, and the authors abandoned attempts to hydrate $MgCl_2$ with that prototype. In a later study by the same authors, however [114], magnesium chloride was hydrated successfully without the material issues described above in a 17 L reactor prototype under a humidity of 12 mbar (which the authors described as realistic winter conditions), air flow rate of 500 L/min. A pressure drop of 100 Pa was measured, and a temperature lift of 14°C was achieved. Thus, a kinetic study of $MgCl_2$ hydration in the context of a TCS system is relevant as this material has shown the potential to be useable as a TCM in pure form in a reactor.

In the previous chapter (**Chapter III**) of this thesis, first order (F1) and geometrical contraction (R3) kinetic models were fitted to magnesium chloride hydration thermogravimetric data and were found to accurately predict the experimental reaction behaviour. These two kinetic models were used for

the TCS simulation to analyse the potential variation in performance prediction. **Equation (77)** shows the resulting first order model F1 suitable for the hydration of magnesium chloride at 25°C:

$$\frac{d\alpha}{dt} = 8.7\ 10^{1} \exp\left(-\frac{2.25\ 10^{4}}{RT}\right)(1-\alpha)\frac{p_w}{p_{eq}} \qquad (71)$$

Equation (78) shows the resulting contracting volume model R3 suitable for the hydration of magnesium chloride at 25°C:

$$\frac{d\alpha}{dt} = 2.9\ 10^{1} \exp\left(-\frac{1.63\ 10^{4}}{RT}\right)3(1-\alpha)^{2/3}\frac{p_w}{p_{eq}} \qquad (72)$$

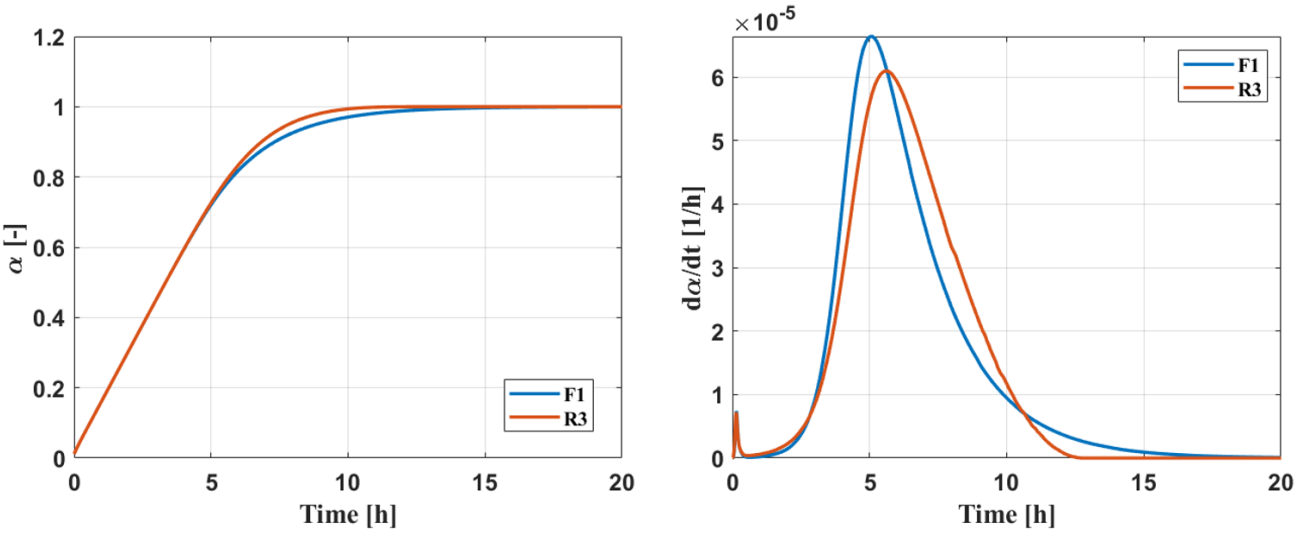

Figure 79 Comparison of simulation results for magnesium chloride hydration: (left) Global reaction advancement and (right) reaction rate with first order model F1 and geometrical contraction model D3.

The difference in dynamic behaviour due to the change in reaction kinetic model can be appreciated from **Figure 79** and **Figure 80**, and the induced variation of KPIs can be seen in **Figure 81**. As in the previous cases, the main aspect of the process dynamic behaviour affected by kinetic model choice is output power profile; the duration of maximum power delivery and steepness of the profile slope once the reaction nears the end. It can be noted again that a steeper power profile is favourable as it signifies a larger amount of heat released at maximum temperature and reduces the duration of the transient regime. This translates into a significantly different average volumetric power output over the discharge period which can be visualised by the performance chart of the process mapping its key performance indicators.

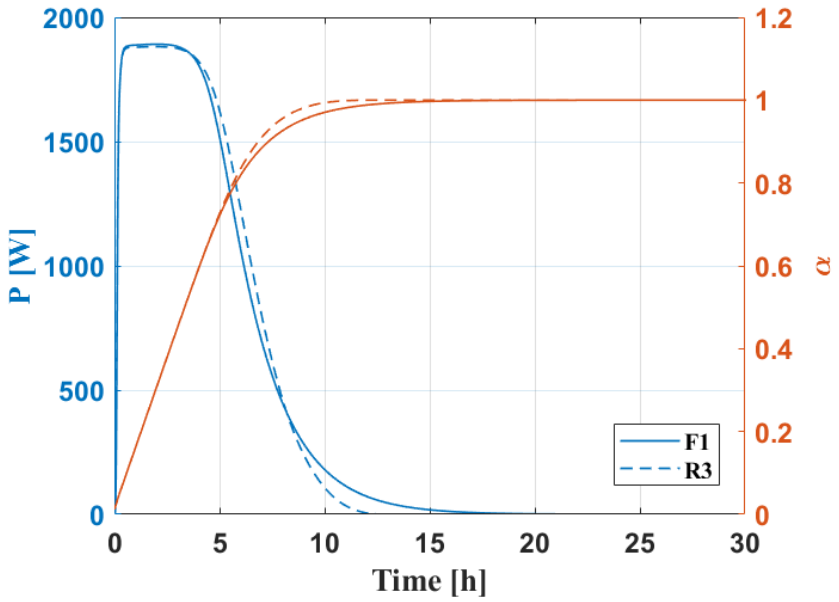

Figure 80 Comparison of simulation results for magnesium chloride hydration: process power output and global reaction advancement profile for different kinetic models.

Similarly to the hydration of potassium carbonate, it can be seen (**Figure 81**) that useful release energy Ed_{useful} and average power P_{av} are the two most affected KPIs by a shift in reaction kinetics. On the other hand, maximum achieved temperature lift is only marginally affected. Storage capacity cost is also largely unaffected due to the calculation being based on the *total* energy release irrespectively of the quality of the released heat (i.e., irrespective of the heat being released below or above the minimum temperature of 30°C).

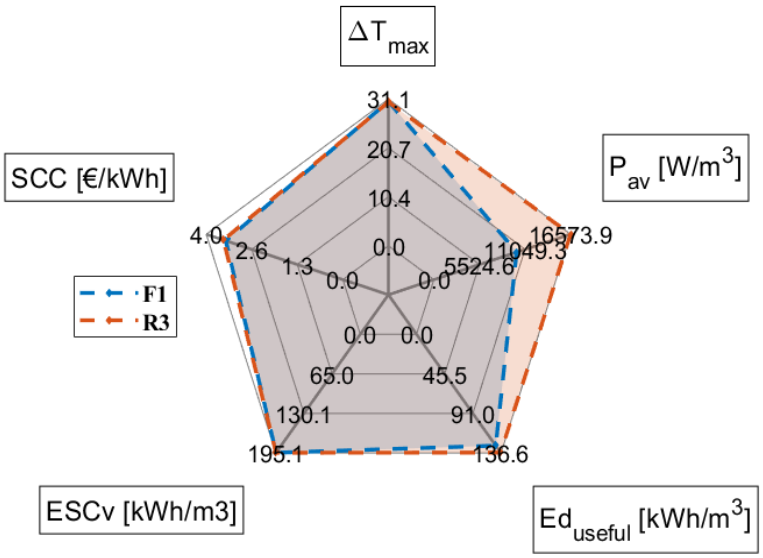

Figure 81 Comparison of key performance indicators from simulation results for magnesium chloride hydration with first order and shrinking core kinetic models.

Useful energy density of heat released above 30°C can be seen to vary from 162 kWh/m^3 to 170 kWh/m^3 between F1 and R3, i.e., an approximate 5% variation. Since, as was discussed previously, the effective energy density reported by studies on TCS reactors and prototypes could be lower by up to 50% than the reported value, a variation in 5% of the total useful energy released by the process due to the choice of kinetic model is relevant.

Hydration of potassium carbonate / vermiculite composite

In **Chapter III**, the solid-state kinetic analysis of the hydration of a potassium carbonate-based composite, using vermiculite as the host matrix, was carried out. To the knowledge of the author, this study represents, one of the only solid-state kinetic analyses for the hydration of a salt-in-matrix composite using vermiculite as the supporting matrix. The nucleation model A2, also known as the Avrami-Erofeyev equation was found to correctly well this material's dynamic hydration behaviour. **Equation (73)** shows the resulting nucleation model (A2) suitable for the hydration of the potassium carbonate / vermiculite composite:

$$\frac{d\alpha}{dt} = 2.73\ 10^{11} \exp\left(-\frac{7.92\ 10^4}{RT}\right) 2(1-\alpha)[-\ln(1-\alpha)]^{1/2} \frac{p_w}{p_{eq}} \qquad (73)$$

Equation (74) shows the fitted and parameterised first-order model (F1) suitable for the hydration of potassium carbonate:

$$\frac{d\alpha}{dt} = 5.7\ 10^{10} \exp\left(-\frac{7.51\ 10^4}{RT}\right) (1-\alpha) \frac{p_w}{p_{eq}} \qquad (74)$$

Finally, **equation (75)** shows the standard first-order model ($F1_{std}$) with the constant kinetic rate constant.

$$\frac{d\alpha}{dt} = 5.\ 10^{-4} (1-\alpha) \frac{p_w}{p_{eq}} \qquad (75)$$

Figure 82 and **Table 35** present the KPIs of the TCS hydration process operating with the K_2CO_3/vermiculite composite for the simulation carried out for the different kinetic models and their associated parameters. As for the previous kinetic studies for the pure salts, the main performance indicators affected by kinetic model selection are maximum temperature lift and average power output. Modelling the reaction mechanisms with a nucleation model resulted in an average volumetric power output of P_{av} = 8109 W/m^3 and a temperature lift of 24°C. On the other hand, the TCS system using first-order kinetics showed P_{av} = 6604 W/m^3 / ΔT_{max} = 23.2°C and P_{av} = 6248 W/m^3 / ΔT_{max} = 22.5°C, with a temperature-dependent and constant kinetic rate model, respectively.

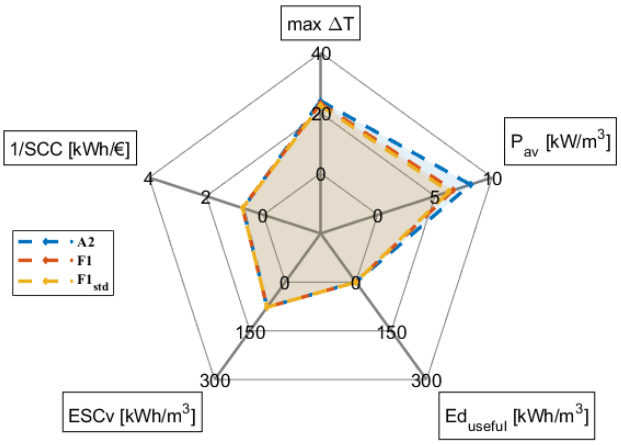

Figure 82 Comparison of key performance indicators from simulation results for 60wt-% salt content potassium carbonate / vermiculite composite hydration with first order and nucleation kinetic models.

Thus, in this case, kinetic model selection had a stronger impact than the variation of the kinetic rate constant on TCS the power output. Furthermore, TCS processes using nucleation-limited kinetics show good performance compared to first-order kinetics. Nucleation models are characterised by a sigmoidal advancement curve, i.e., a slow start with a marked acceleration during the first half of the reaction. Comparison of the advancement curves for different classes of solid-state kinetic model, as can be found in [84], shows that nucleation-limited reactions will reach completion the fastest, which explains the increased performance at the TCS system level.

Table 35 KPIs for TCS system a 60wt.-% potassium carbonate-based composite with constant operating conditions (p_{in} = 1200 Pa, T_{amb} = 5°C), and kinetic models.

k	ΔT_{max}	P_{av}	Ed_{useful}	Ed_r	SCC
[s-1]	K or °C	kW/m^3	kWh/m^3	kWh/m^3	[€/kWh]
A2	24.0	8.1	0	77.06	1.401
F1	23.2	6.6	0	77.06	1.369
$F1_{std}$	22.5	6.2	0	77.06	1.370

7 Conclusions

In this chapter, the dynamic behaviour and performance of open TCS systems operating with SIM composites was assessed through the measurement of KPIs. A scenario whereby a dwelling is equipped with solar thermal collectors and an open TCS process designed for space heating was conceived. A dynamic, 0.5D reactor model was coupled with relevant process unit equations to model process operation. The effect of material selection, location, ambient weather conditions and reaction kinetics on process performance was evaluated.

- With realistic winter ambient conditions and without forced humidification, the achieved temperature lift was generally below the minimum required temperature of 30°C for thermal comfort. Only TCS systems operating with $MgCl_2$ and K_2CO_3 composites achieved the required temperature lift, which is mainly explained by these salts' low equilibrium vapour pressure with water. When accounting for porosity, the inert host matrix and losses, energy storage capacities in the range 70 kWh/m^3 to 177 kWh/m^3 were measured, which represents a 75%-80% drop compared to the ESCv measured at the material scale. The volume occupied by a humidifier would further reduce the overall energy storage capacity of the system but increase the thermal power output to achieve thermal comfort.

- In economic terms, calculation of the system SCCs showed that, for most salts, the TCS sorption system could be affordable for industrial users, with most SCCs below the recommended 1.5 €/kWh. TCS with strontium bromide $SrBr_2$ and copper chloride $CuCl_2$ shows high SCC due to their bulk material costs. The high SCC is not mitigated by an improved overall system performance compared to other materials. On the other hand, TCS operating with $MgSO_4$ composites displayed the highest volumetric energy storage density and lowest overall cost which could offset the additional cost of forced humidification that would allow sufficient thermal power for space heating.

- Variation of the kinetic rate constant within a typical range of values and model selection resulted in a non-negligible uncertainty to the TCS system final performance. The performance in terms of volumetric power density during the hydration of K_2CO_3, K_2CO_3/V and $MgCl_2$ varied by up to 16%, 22% and 36% respectively. Future modelling of TCS system performance should carry an uncertainty analysis associated with the kinetic modelling of the chemical reactions.

Chapter V. Techno-Economic Viability of Power-to-Heat Coupled with Sorption Low Temperature Thermochemical Energy Storage for Domestic Space Heating

*In **Chapter IV** the dynamic performance of a TCS system integrated to a dwelling for the storage of solar heat for space heating, with a focus on the heat discharge phase was studied. It was concluded that on the technical side the TCS system may struggle to deliver sufficient power to fulfil the system thermal energy demands. On the economic side, such a system would be viable provided some of the most expensive inorganic salts are avoided (namely $SrBr_2$ and $CuCl_2$). The temperature achieved by solar thermal collectors (up to 100°C above ambient temperature) may also be insufficient to completely desorb the TCM (salt desorption temperatures in the 50°C - 150°C range), and therefore the economic viability of such a system may be jeopardised.*

Outside of the techno-economic challenges highlighted in the previous chapter, the application of solar-driven TCS is also limited to areas with sufficient solar resources and with sufficient need for space heating. On the other hand, various areas have an obviously high need for space heating but with very little sunlight, due to harsh winters for example. Nevertheless, in all these areas the penetration of renewable electricity is increasing, and thus the electrification of heat is an increasingly used solution. However, the intermittency of both the heat demand and the renewable energy supply still needs to be managed.

Advances in other chemical engineering fields have led to efficient electrical heating of chemical reactors, thus opening the door to coupling TCS with electrical energy sources which could be a means to manage the intermittency of renewable electricity supply and heat demand. Thus, in the specific context of this thesis, this chapter is aimed at investigating TCS reactors coupled with power-to-heat technology integrated to dwellings. In this chapter the dynamic behaviour of open low-temperature sorption based TCS with electrically driven dehydration, integrated into a dwelling with solar PV is simulated, and the techno-economic viability of this system named TCS/P2H/PV is evaluated. Power-to-heat is attractive as it unlocks the potential to exploit off-peak electricity for use in domestic space heating. Since the main technical issue is the mismatch between available off-peak electricity and domestic space heating demand, conversion of electrical energy to thermal for storage within a TCS could be a viable solution.

The aim of this chapter is to evaluate the potential for integrating TCS in a residential space heating system which features solar PV. In order to carry out the evaluation, a TCS process model is used to simulate the dynamic performance within the TCS/P2H/PV system. The process model consists of a quasi-1D reactor model coupled with relevant process equations to simulate the full dynamic

behaviour of the TCS system. Electrical heating strategies were formulated within the framework of the quasi-1D model in order to predict the transient behaviour of TCS/P2H/PV. From the dynamic simulation results, an evaluation of the techno-economic performance of TCS/P2H/PV was derived in terms of efficiency, solar fraction, final cost of energy and energy saving. The specific purpose of the techno-economic evaluation is to determine whether the proposed TCS/P2H/PV systems show economic potential. Commercially available renewable domestic heating systems, such as solar PV, have well established payback times. Implementation of electrically driven TCS can be expected to affect the viability and dynamic behaviour of heating systems and improve return on investment times by matching supply/demand of otherwise intermittent energy sources. Part of the aim of the study is therefore to also quantify this impact on renewable energy system viability.

1 Introduction

During heat charge, the thermally activated dehydration of inorganic salt hydrates occurs in the temperature range 50°C - 150°C. Furthermore, heat obtained from solar thermal technologies can be recovered in that temperature range, up to 100°C above ambient temperature using flat plate collectors [168]. Thus, solar thermal energy can be considered as the main target energy source for low-temperature seasonal TCS. For low-temperature open TCS, the conventional charging strategy consists in heating circulating air extracted from the ambient with solar thermal energy and guiding it into a packed bed reactor containing the TCM, whereupon heat is exchanged conductively between the air flow and the solid [13,195]. However, TCM dehydration driven by direct thermal energy can face limitations, such as:

- insufficient thermal energy provided by the solar collector to fully desorb the TCM.
- heat at too low power to desorb the TCM to the lowest hydration level, impinging total energy storage capacity. Dehydrating chlorides (such as $CaCl_2$ or $MgCl_2$) and removing the final water molecule occurs at temperatures of approximately ~140°C, which is a challenging temperature to reach with solar thermal technologies.
- cost-efficiency due to the installation of new solar collector systems, whereas solar photovoltaic (solar PV) systems or other renewable electrical energy systems may already be in place.
- inefficient and slow heating due to (a) the heating of the medium surrounding the TCM or the reactor vessel, followed by (b) the conductive heat transfer between the air flow and the solid material.

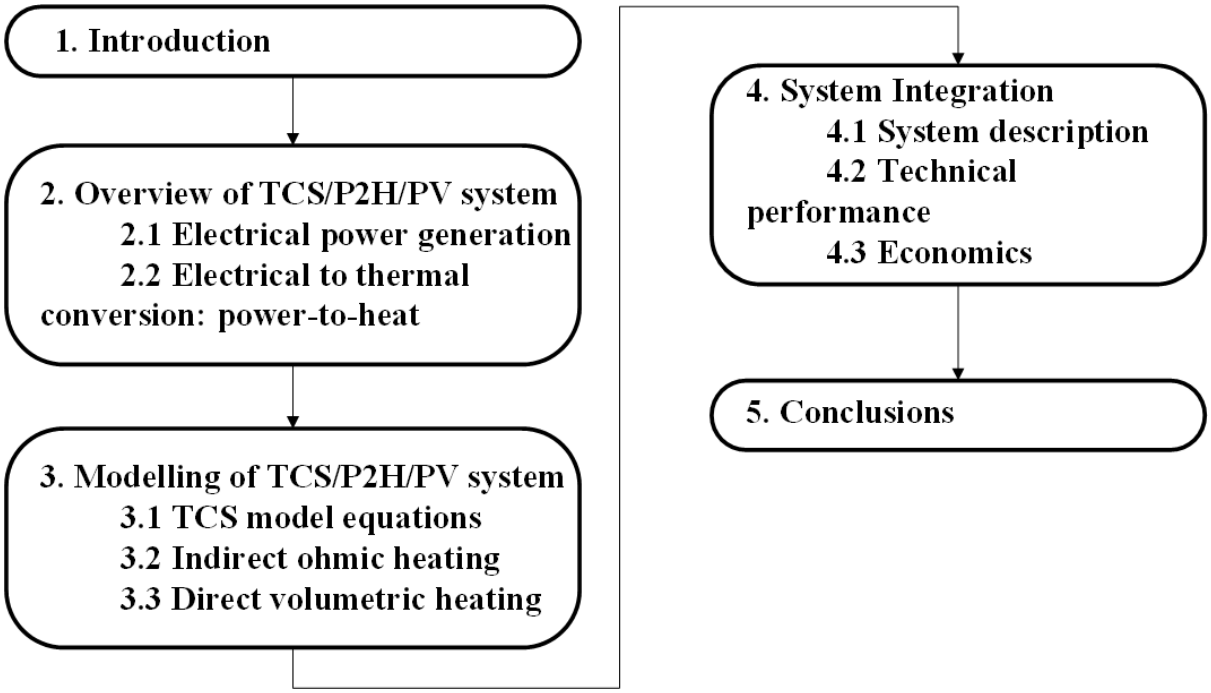

Figure 83 Chapter V mapped structure.

Thus, alternative energy sources or charging strategies should be considered such as electrification of chemical reactors via power-to-heat (P2H). P2H is a designation encompassing all methods used to convert electrical energy to thermal energy. P2H opens the door to increased flexibility of domestic use of electricity, whether it be sourced through the district network or decentralised solar PV. It is therefore proposed in this work to explore different potential electrified heating strategies for the charging step of an open seasonal TCS system for domestic space heating. The outline of the chapter's structure is shown in **Figure 83**.

First, a review of the available electrical dehydration strategies is carried out, where the physical fundamentals on which the electrified dehydration methods are based are discussed, along with their application to gas-solid reactions and, more specifically, desorption. Then, an overview of existing electrically heated reactor designs is presented. A TCS system and reactor design is proposed for the conventional electrified dehydration method. The simulation of the transient behaviour of these systems is carried out through a dynamic process model coupled to a quasi-1D TCS reactor model. The resulting system of differential equations is solved in Matlab using a variable step, variable order ordinary differential equation solver based on backwards differentiation formulas, *ode23t*. Finally, system technical and economic performance is evaluated through the calculation of relevant key performance indicators (KPIs) and levelized cost of energy (LCOE) analysis.

2 Overview of P2H/TCS process

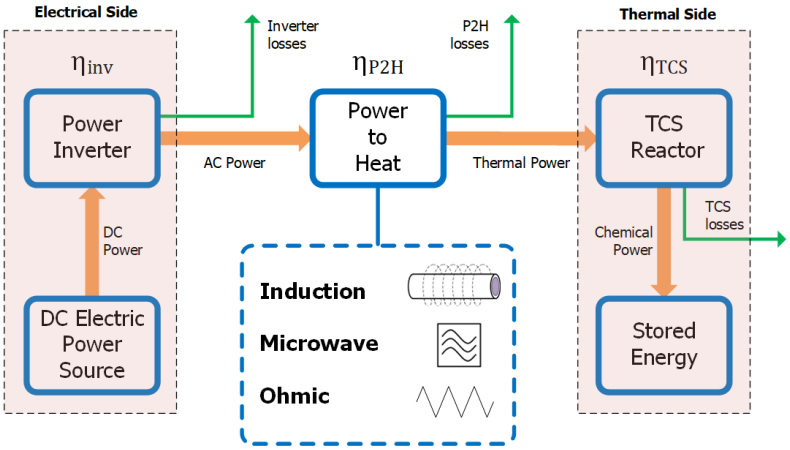

Figure 84 Conceptual overview of power-to-heat coupled to thermochemical energy storage.

An overview of the P2H/TCS process is presented in **Figure 84**. The system can be viewed as having an electrical side and a thermal side, which are interconnected by the P2H element. Solar energy is harnessed and converted to an alternating current on the electrical side which powers the P2H element, which, as will be discussed at length further in the chapter, can be based on either indirect heating of the reactive area (ohmic) or direct heating (induction or microwave). On the thermal side the generated heat is managed by either being stored in the TCS or sent directly to the heat load.

2.1 Electrical power generation

PV system

Solar PV energy systems in dwellings are generally organised as shown in **Figure 85a**. A solar PV array generates electrical DC power. The power rating of solar PV for dwellings is generally in the range 1 kW – 7 kW depending on the total solar cell surface area of the PV array. The generated DC can be either (a) sent directly to suitable appliances, (b) stored in a lead-acid battery (the most typical type of electrical energy storage in small-scale solar domestic applications [196]) or lithium ion battery, directly used in DC appliances, or converted to AC for either (c) suitable AC appliances or (d) sold back to the grid if advantageous with arbitrage. Since the domestic system is connected to the grid (AC current), in the considered case scenario it is assumed that PV generated DC electricity is inverted to AC for compatibility. However, for other systems nothing prevents using a DC heater without inverting the PV generated electricity.

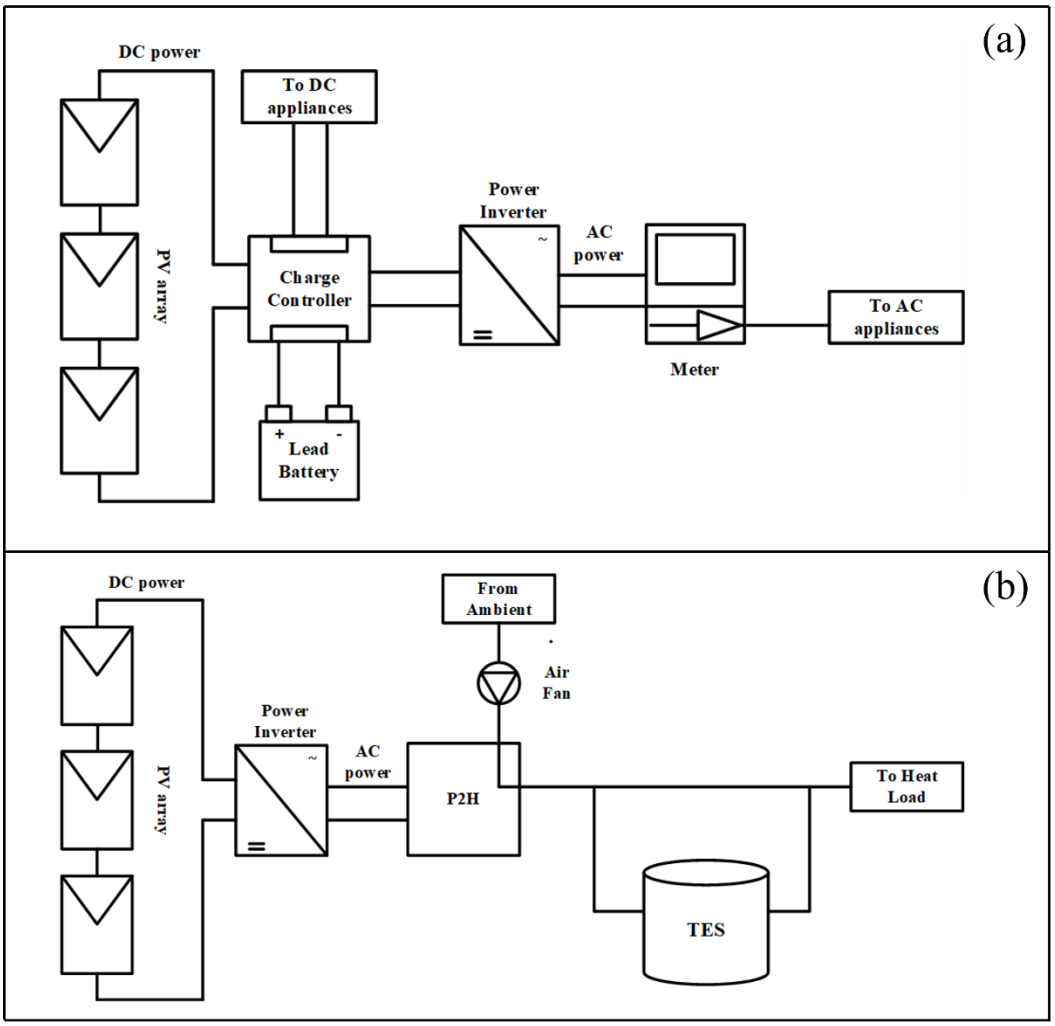

Figure 85 (a) Typical arrangement of grid-connected photovoltaic system, with consumption of both DC and AC electrical power, and lead-battery storage [196] **(b) Envisioned arrangement of photovoltaics coupled with P2H and TES.**

The coupling of PV systems with P2H and TES is envisioned according to the diagram in **Figure 85b**. DC power is converted to AC with a power inverter. AC powers the P2H element, and the generated heat is either sent directly to the heat load of the dwelling if needed instantaneously or stored in the TES. In this system, energy is never returned to the grid for potential sale via arbitrage and the aim is to maximise solar energy use for space heating. This design decision is made on the basis that the dwelling's total annual space heating demand is likely to exceed the total annual amount of energy generated annually by the PV system, and that reconverting thermal energy delivered from the TCS to electrical energy for sale is not technically practical in a dwelling.

Power inverter

The direct current (DC) generated by the PV system is converted to alternating current (AC) by a power inverter. The power inverter is assumed to be an SMA Sunny Boy model [197]. The rating of the power inverter depends on the current intensity, which is mainly tied to the power rating of the PV system and the available solar irradiance. Typical efficiency curves for domestic solar power inverters are shown in **Figure 86**. By assuming that the power inverter operates at the optimal ratio of generated PV power over PV power rating, the power inverter may be assumed have an efficiency of $\eta_{inv} = 92\%$. If P_{DC} is the power generated by the PV system, then the alternating current power at the output of the inverter is calculated with **equation (76)**:

$$P_{AC}(t) = \eta_{inv} P_{DC}(t) \tag{76}$$

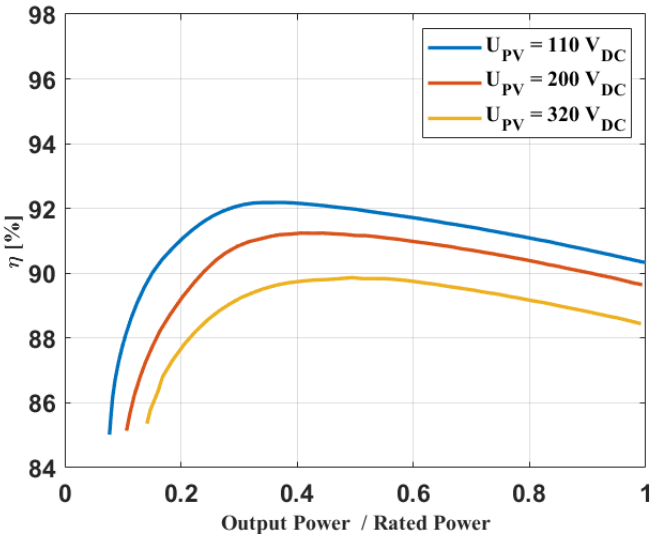

Figure 86 Typical solar power inverter efficiency curves, for different input voltages. Conversion efficiency of the inverter depends on the ratio of PV power output over the PV array rated power.

2.2 Electrical to thermal conversion: power-to-heat

Power-to-heat methods for the electrified heating of chemical reactors may be subcategorised into *direct* and *indirect* heating [198]. During *direct* heating, i.e., microwave (MW) and radiofrequency (RF) heating methods, thermal energy is recovered directly in the material and thus occurs without the need for a heat transfer medium. *Direct* heating may also be seen as *volumetric* heating. During *indirect* heating, such as ohmic heating, electrical energy is converted to thermal energy outside the chemical reactor, and the obtained heat is subsequently transported to and exchanged with the reactive area. *Indirect* heating may also be described as *conventional* heating. Thus, in this study, the two P2H methods, *indirect* heating (ohmic heating of the circulating airflow), and *direct* heating (MW and RF heating) coupled with low-temperature TCS, will be evaluated.

Indirect Conventional Heating: Ohmic Heating of the Air Flow

The first strategy to consider for the electrified heating of the TCS reactor is indirect ohmic heating. A heating element is used to heat an air flow. Heated air circulates through the TCS packed with porous thermochemical material. This method is typical for most laboratory-scale TCS setups [122,123]. Ohmic heating, or direct resistance heating, or Joule heating, is derived from the heat loss that occurs when passing an electric current through a material. The heating power is calculated through **equation (77)**.

$$P_{ohm} = I^2 Res \tag{77}$$

Where I is the current (Amps) and Res the resistance value of the heating element. A typical process diagram of laboratory-scale setup with an electrical heater in shown in **Figure 87**.

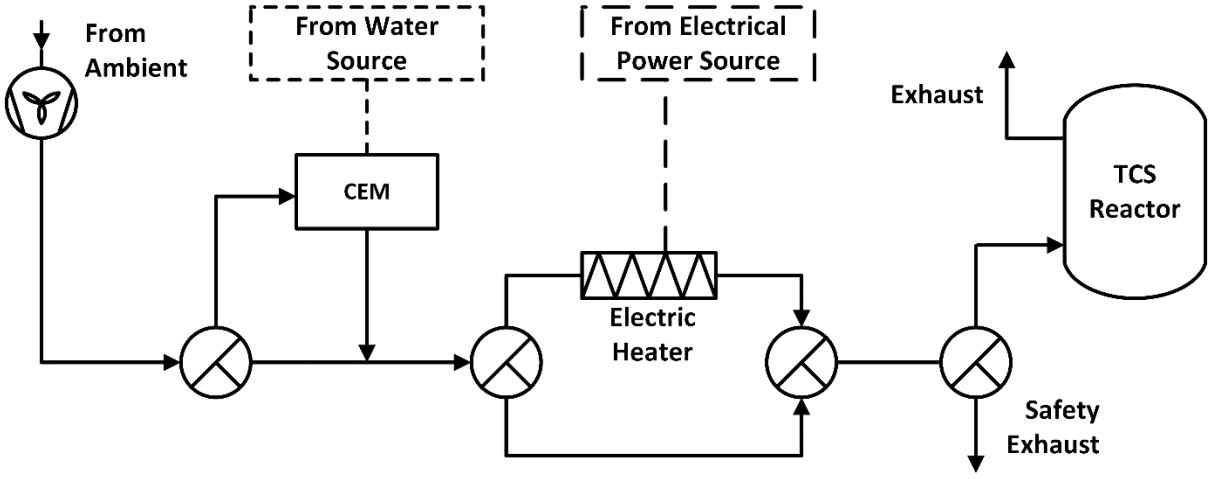

Figure 87 Typical conventionally heated TCS lab-scale setup with electrical ohmic heating of the air flow for the desorption phase.

Such a system shows similarities with the typically envisioned coupling of TCS with solar thermal. The heat source is located outside the TCS and is used to transfer energy to the air flow which transports both thermal energy to and water out of the reactor during charge (and water to the reactor and thermal energy out during discharge). The main difference and advantage is that at constant heating power from the TCS element, the mass flow rate of air can be controlled to achieve relatively high temperatures to ensure complete dehydration. Air duct heaters are an example of heating element that could be used for this application.

Direct Volumetric Heating: Microwave Heating

Direct volumetric heating can be achieved in chemical reactors by converting electromagnetic energy to thermal directly within the reactive area. This is achievable either through microwave heating or radio-frequency (also referred to as induction heating). Microwave heating will first be discussed.

Microwaves are electromagnetic waves in the frequency range 0.3 GHz to 300 GHz [199]. MW heating shows several promising properties with regards to application for physical adsorbents, inorganic salt and SIM composite desorption [200].

- Direct heating of the solid reactants leads to a different temperature profile than conventional heating, with the higher temperature found within the solid which reduces with increasing proximity to the reactor walls.
- Volumetric heating leads to the entirety of the material being heated simultaneously.
- Instantaneous heating due to the direct and volumetric nature of microwave heating.
- Selective heating due to microwave heating interacting more strongly with certain compounds compared to others, which can be controlled and exploited to preferentially heat up certain reactants in the reactor such as the constituting components of a composite material.
- The consensus from the literature is that MW-assisted heating is more efficient than conventional heating, leading to higher yields and faster reactions.

The main technical limit to microwave use in chemical reactors is the penetration depth which is in the range of several centimetres (dependent on the heated material). The use of large volume microwave-assisted reactors is therefore restricted. In the case of TCS, the application of microwave reactors seems suitable when combined with modular, segmented reactors where the depth of the reactive area may be designed to match the penetration depth of microwaves. Another solution could be to design a microwave cavity, through which the TCM is transported and exposed to an electromagnetic field, such as with a conveyor belt or a moving-bed reactor which is a topic of interest in TCS literature [111].

The physical process by which heating can be achieved through microwaves will now be discussed. The electromagnetic energy of microwaves may be converted to thermal energy inside solid materials through several mechanisms. For inorganic salts the main process by which heating occurs is ionic conduction. As ionic materials, electronically neutral compounds resulting from the association of an anion and a cation, inorganic salts exposed to electromagnetic energy at the MW frequency will be heated by the mechanism of ionic conduction. Ionic conduction consists in the movement or transit of ions from one site to another via defects in the crystal lattice, with this movement instigated by the influence of oscillation of the electric field. The collision of these charged particles (ions) with neighbouring molecules leads to heating of the material [201]. The dissipation of electromagnetic energy into heat by materials depends on their dielectric parameters, and in particular the dielectric loss coefficients. The dielectric loss coefficients of some of the considered inorganic salts are shown in **Table 36**. Desorption of various sorbates (water, CO_2, etc.) has been demonstrated as achievable using microwaves: physical sorbents such as zeolites [202–204], silica gel [205] but also salt-in-

matrix composites ($CaCl_2$ in silica gel) [206] have been successfully desorbed at various scales using microwaves.

Table 36 Dielectric loss coefficients of some inorganic salts.

Salt	Dielectric constant	Reference
$MgSO_4 \cdot 7H_2O$	6.20	[207]
	5.46	[208]
$MgSO_4 \cdot 1H_2O$	7.36	[207]
$MgSO_4$	8.20	[208]
$CuSO_4 \cdot 5H_2O$	6.55	[207]
$CuSO_4 \cdot 1H_2O$	10.10	[207]
$BaCl_2$	9.81	[208]
$BaCl_2 \cdot 2H_2O$	9.00	[208]
K_2CO_3	4.96	[208]

Microwave-assisted reactors and pure microwave heated reactors have been studied in the fields of catalysis [209–211], organic chemical synthesis [212] and heterogenous inorganic chemistry [213,214]. A summary of MW-heated reactors found in the literature is shown in **Table 37** and **Figure 88**. Other MW-assisted reactors may be found in the literature; however, these examples are generally designed for very low amounts of reactive material and experiments at the sample scale. The examples selected here display a variety of sizes to explore the complexity of upscaling MW-assisted reactors for the processing of ~$10^0 – 10^2$ kg of TCM which would be required in the context of P2H/TCS. The low penetration depth of microwaves combined with the need for a cavity within which to resonate electromagnetic waves strongly limits the available reactive area. Some reactor designers have attempted to circumvent this limitation by designing continuous flow reactors: reactive material is transported, by a conveyor belt for example, in the reactive area where microwaves are deployed.

The electrical energy consumption of the transport system is offset by the amount of material which can be heated in the limited area of the MW reactor. In such a reactor, a final energy efficiency of 37% was reported by Esveld et al. [215], who attributed 41% of the losses to the conversion of electric energy to electromagnetic energy in the magnetron, and 22% of the losses to the undesired heating of reactor components. These figures are coherent with the electric-to-electromagnetic conversion efficiencies at the magnetron of 50%-65% reported in [216]. Others have reported higher magnetron efficiencies of 85% [205]. The temperature range of 0°C to 350°C achieved by these MW reactors is well suited to the low-temperature desorption of TCMs. Additionally, it should be noted that the temperatures needed to achieve the full reaction in MW reactors is often lower than the same reaction taking place in a conventionally heated reactor.

Table 37 Review of electrified MW-heated chemical reactors. MW power designates the electrical power consumed by the magnetron(s). Real power designates the volumetric power measured in the reaction zone. EFI designates the range of electric field intensities measured or calculated. Reactive zone volume designates the volume inside the reactor that is occupied by reactive material. Total volume designates the total volume of the reactor including walls, casings etc. Volume ratio designates the ratio between reactive zone volume and total volume. Volumes are either provided in the references or estimated from available diagrams and data.

Process	Phase	MW Power	Real Power	EFI	Average EFI	Temp. Range	Reactive Zone Volume	Total Volume	Volume Ratio	Notes	Ref
	s/g/l	kW	kW/m^3	V/m	kV/m	°C	m^3	m^3	[%]		
2-propanol dehydrogenation	s/l	-	1	$0 - 2.44.10^5$	-	0 - 350	5.31E-07	2.00E-04	0.27%	• Batch reactor • Reaction rate increased 17 to 38-fold • Generation of local hotspots due to MW	[217]
polymer synthesis	l	2	-	$0 - 2.5*10^4$	-	0 - 250	5.00E-03	8.10E-03	61.74%	• Batch reactor • MW and conventional heating hybrid reactor • Reaction rate increased 2.65-fold	[218]
esterification of stearic acid with stearyl alcohol	s/l	4.4	-	$0 - 1.2 *10^4$	15 ± 4	0 - 200	4.68E-03	2.10E-01	2.23%	• Continuous microwave dry-media reactor • MW heating of 10 kg/h to 100 kg/h solid material using conveyor belt • Reaction rate increased 20 to 30-fold • Final efficiency 37% (41% loss to magnetron, 22% loss to heating parts of the reactor) • 25% loss to heating reactor elements is typical	[215]
extraction	s/l	6	-	-	-	-	-	-	-	• Continuous-flow microwave reactor	[219]
zeolite ad/de-sorption	s/g	3	1 - 2	-	-	0 - 120	0.0061	-	-	• Batch reactor • Full desorption achieved at temperature 70°C lower than CH • Less energy required for equivalent desorption with CH	[220]

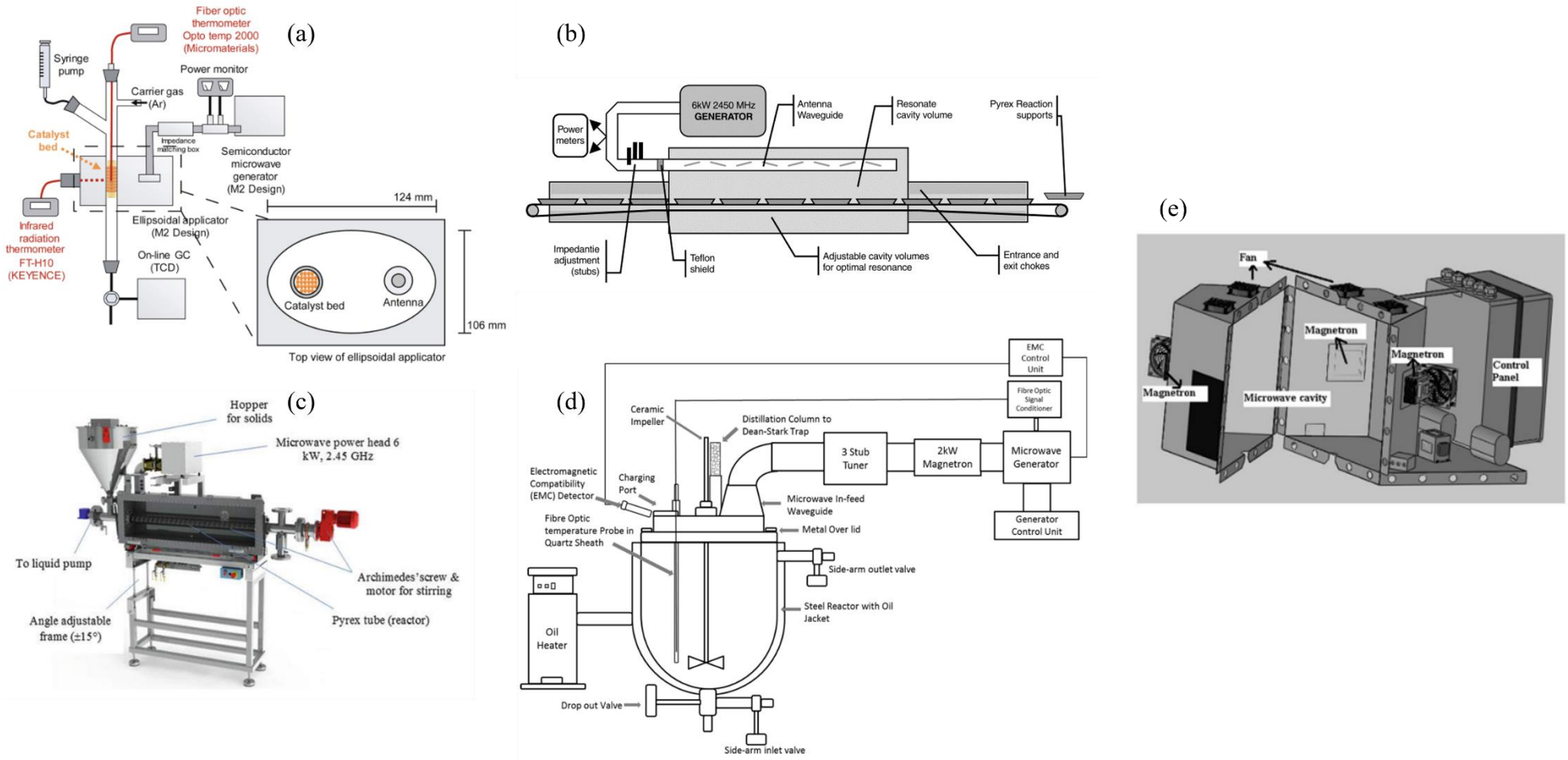

Figure 88 Review of electrified MW-heated chemical reactors. References for the examples (a) [217]**, (b)** [215]**, (c)** [219]**, (d)** [218]**, (e)** [220]

Direct Volumetric Heating: Radiofrequency / Induction heating

Radio frequency (RF) heating provides thermal energy to materials by electromagnetic energy transfer with longer wavelengths than MW heating, resulting in a more effective albeit slower heating due to increased penetration depth. Indeed, the main issue often cited with MW-assisted reactions is the low depth of penetration of microwaves leading to the heating ability of the setup to decrease drastically with an increase in reactive material volume. In principle, RF heating can heat up larger volumes than MW-heating due to increased penetration depth. The principle of applying inductive heating to reactive systems hinges on electromagnetic force fields in the presence of ferromagnetic elements in the reactor, or ferromagnetic supports. These supports may be arranged in a coil around the reactive system or dispersed within the reactive system. These ferromagnetic elements are powered by an electrical power source supplying an alternating electrical field. The induced opposite alternating magnetic field, i.e. eddy currents, leads to the solid material located within the coil (workpiece) to be heated to the selected temperature [221].

RF induced desorption was demonstrated at the pellet level using zeolite-based /water and silica gel-based composite/water pairs [222]. In addition to a binder, iron particles were dispersed in the pellets to act as RF susceptors. The role of iron particles in the heating performance was demonstrated by the increased RF power transferred to the pellets with increasing iron mass fraction in the composite pellet. Application of RF-heating to larger scale sorption systems has been carried out by SaltX Technology AB [223]. In their patent a TCS reactor system is shown, consisting in a tube-shaped reactor through which is conveyed either hydrated or dehydrated thermochemical material, which is presented in **Figure 89(e)**. Authors of the patent specified that the reactive material could be any of the usually encountered inorganic salts for TCS, including low temperature salts. The material could potentially be dehydrated with either of solar heat, waste heat or electricity. The issue of thermally treating large amounts of TCM using RF-heating is resolved by transporting the TCM to the RF-heated zone.

RF-reactor designs have been proposed where the entirety of the bulk of the reactant is heated, such as the reactors shown in **Figure 89(a)**, **Figure 89(b)** and **Figure 89(c)**. In these designs, the reactive material contains a ferromagnetic nanoparticulate component and the reactive area is enveloped by an induction coil. However, scaling up such designs to provide thermal energy to much larger amounts of TCM such as for domestic space heating is not obvious and not discussed in the mentioned references. Fernandez et al. proposed a scale-up methodology for an RF-heated reactor (**Figure 89(d)**) and were able to achieve a scale-up factor of approximately 700, thermally treating 0.5 kg material /day.

Thus, (a) thermal desorption is achievable with RF-induced heating, (b) the specific chemisorption (desorption) of inorganic salts may be carried out in this manner, (c) heating kilogram amounts of TCS could be challenging, but achievable with some progress in either the design of induction heaters or the design of transported/conveyor belt reactors, or through the use of modular reactors. Therefore, through a combination of material transport to the RF-heated area, segmentation of the reactor and

potential scale-up methodologies, it is assumed in the following sections of the present chapter that RF-heating is an option for electrified P2H-TCS.

Conclusion to the overview of electrified chemical reactors

Promising volumetric heating solutions based on electromagnetic energy are available to provide heat to endothermic reactions. These methods have also been shown, in principle, to be applicable to physical desorption (zeolites, silica gel…) and chemical dehydration of inorganic salts. Having demonstrated the feasibility of electrically powered volumetric and conventional heating of TCS, the techno-economic potential of residential heating systems integrating these processes will be evaluated.

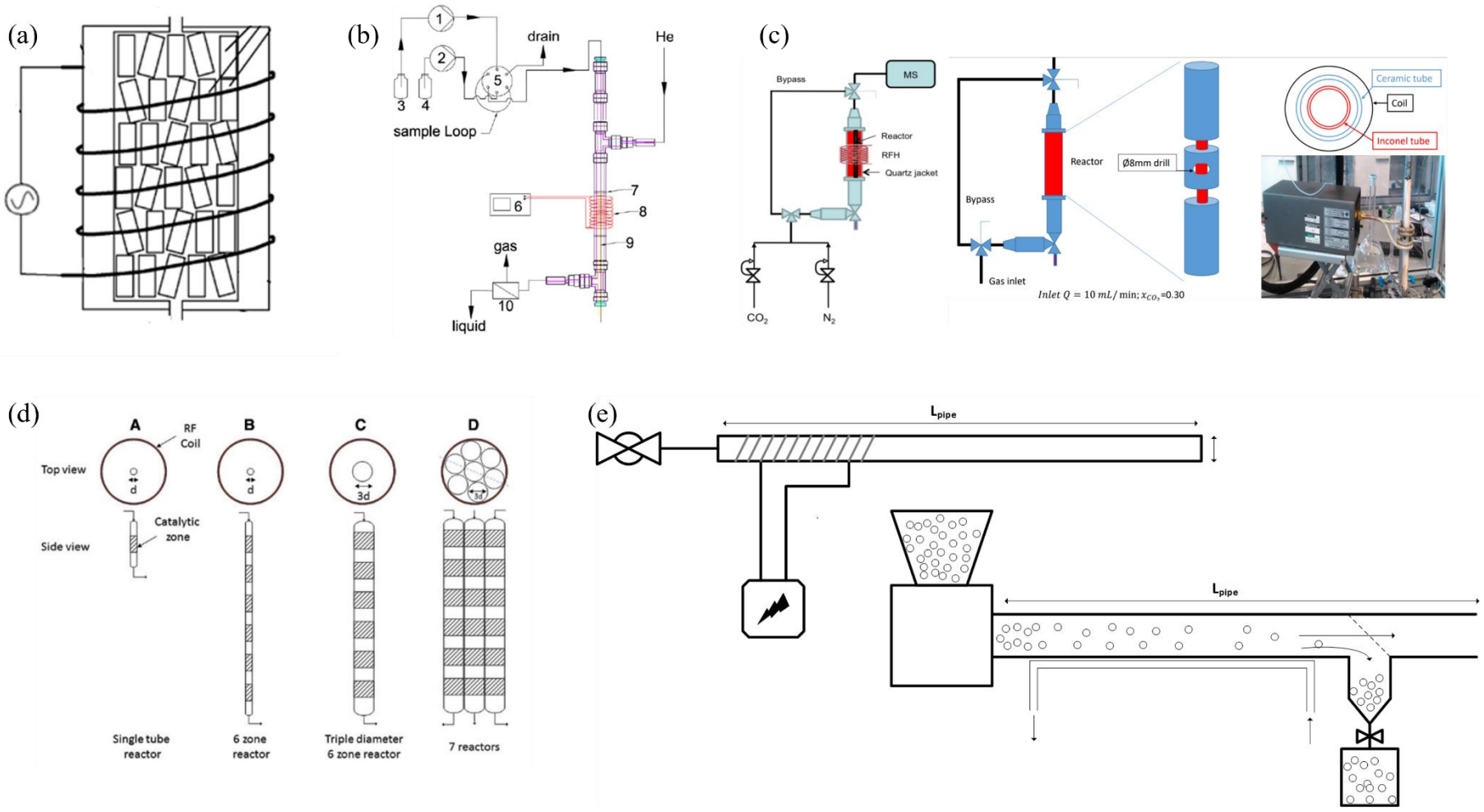

Figure 89 Review of electrified RF-heated chemical reactors. (a) RF-heated packed bed chemical reactor principle [224]**, (b) micro-trickle RF reactor** [225]**, (c) RF reactor for calcium looping** [226]**, (d) proposed RF-reactor scale-up methodology** [227]**, (e) RF heated TCS reactor in principle, Salt-X patent** [223]**.**

3 Modelling of the TCS/P2H/PV system

This section discusses the modelling strategy of the TCS/P2H/PV system which includes the TCS, its secondary components (heat exchangers, fans, humidifier), and the power-to-heat component.

3.1 TCS model equations

A numerical model is formulated to predict the dynamic behaviour of a reactor embedded within a TCS process during desorption. This TCS process model, discussed extensively in **Chapter IV Section 3.1**, is briefly described here. In open systems, mass transfer is the main limitation for large scale TCS. Large amounts of TCM can lead to non-negligible pressure drop, increasing fan power and reducing overall system efficiency [15]. Therefore, the material within the reactor is subdivided into individual reactor modules. Air flowed during sorption/desorption travels only within a single reactor module, and any volumetric heating (MW-heating, RF-heating…) or conventionally heated air flow is applied to a single reactor module at a given time. If more heat is required or needs to be stored, multiple reactor modules may be used in series. The concept of the modular reactor is presented schematically in **Figure 90**. As can be seen, the TCM is arranged into modules so that, during desorption, for example, hot air / thermal energy / volumetric heating Q_v is only provided to a fraction of the total TCM material, reducing pressure drop and mass transfer limitations and providing additional control over reactor operation.

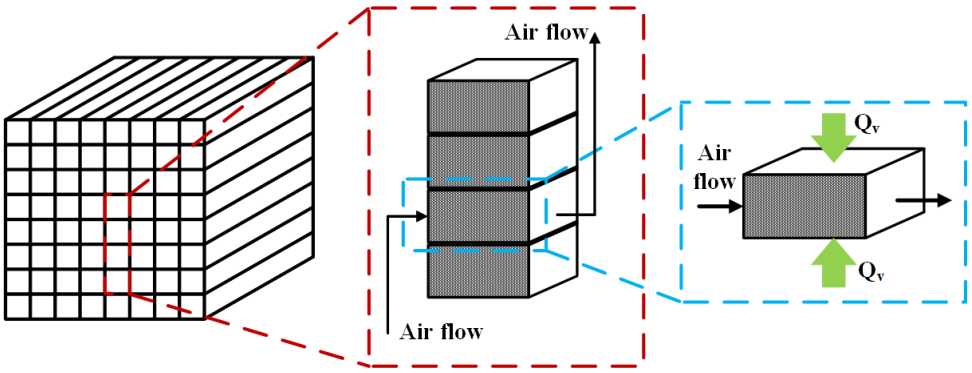

Figure 90 Modular TCS reactor concept during sorption.

The reactor module is further subdivided into a series of control volumes or nodes. For each node *i*, the evolution of the state of charge of the reactor, the hydration level of the TCM and the reaction equilibrium conditions are accounted for by:

- a water mass balance in **equation (78)**, where the difference in humidity of the air flow between the outlet and inlet of the air flow is equal to the flow of water vapour between the TCM and the air flow due to the chemisorption reaction.

$$\frac{d\alpha^i}{dt}\kappa\frac{M_{H2o}}{M_s}\frac{m_s}{n} = 0.62198Q_m\left(\frac{p_v^{i-1}}{101325-p_v^{i-1}} - \frac{p_v^i}{101325-p_v^i}\right) \quad (78)$$

- a kinetics equation in **equation (79)**, which determines the rate of the reaction based on the solid-state kinetic reaction equation which is discussed in more detail in previous chapters.

$$\frac{d\alpha^i}{dt} = k_{cin} f(\alpha^i)(1 - \frac{p_{eq}^i}{p_v^i}) \quad (79)$$

- the salt-water equilibrium described by the Clausius-Clapeyron expression in **equation (80)** which clearly indicates the bivariant equilibrium of the equation which is a function of the local temperature and water vapour pressure.

$$p_{eq} = 101325 e^{\frac{-\Delta H}{RTs} + \frac{\Delta S}{R}} \quad (80)$$

Two different energy balances can be written depending on the heating mode of the TCS reactor, indirect ohmic heating or direct volumetric heating. In the case of indirect ohmic heating, the variation in thermal energy in the bulk of the TCM is equal to difference in thermal energy entering and leaving the reactor module due to the air flow, and the thermal energy absorbed / released by the chemisorption reaction (**equation (81)**).

$$\frac{dT_s^i}{dt}(m_s Cp_s + m_m Cp_m) = \frac{d\alpha^i}{dt} \Delta Hr \frac{\kappa m_s}{n M_{H2O}} + Q_m Cp_f \left(T_s^{i-1} - T_s^i\right) \quad (81)$$

The different modes of direct volumetric heating (radiofrequency, microwaves, etc..) can all be considered as similar for modelling purposes. A volumetric heating power, Q_v^i, is generated at each node of the reactor module. The amount of generated volumetric heating power depends on the selected heating mode. The energy balance for all forms of direct volumetric heating can be seen in **equation (82)**.

$$\frac{dT_s^i}{dt}(m_s Cp_s + m_m Cp_m) = \frac{d\alpha^i}{dt} \Delta Hr \frac{\kappa m_s}{n M_{H2O}} + Q_m Cp_f \left(T_s^{i-1} - T_s^i\right) + Q_v^i \quad (82)$$

The modelling results of both indirect and direct heating are presented in the following sections.

3.2 Indirect ohmic heating

Before integrating the TCS/P2H into a domestic system, the process is simulated using a constant power supply. The results for the simulation of the conventionally heated TCS/P2H process are presented first of all. Electrical energy converted from solar by the PV is in turn converted to heat by a resistive heating element such as an air duct heater, as in this reference [228]. A generalised design for the conversion of electrical energy into thermal energy via the resistive heating element acting as an air heater is shown in **Figure 91**.

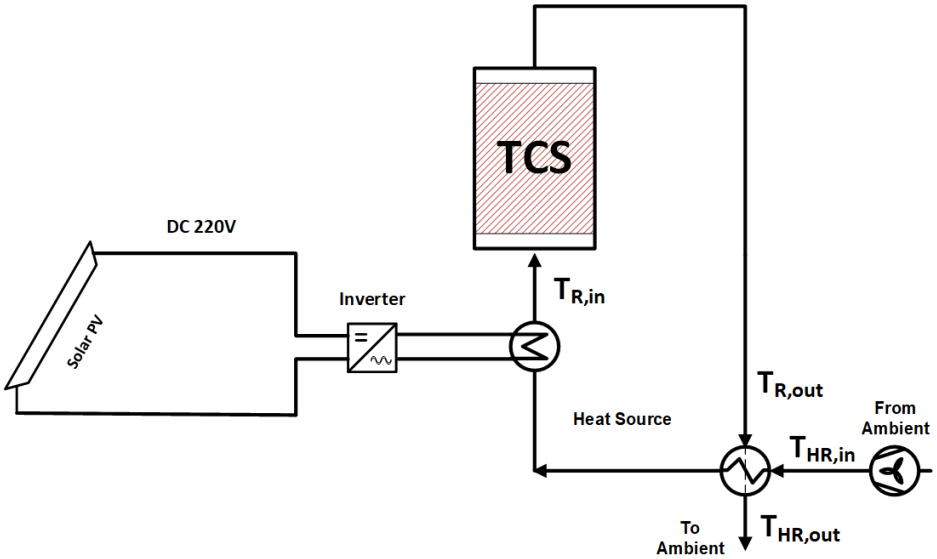

Figure 91 Electrical circuit and flow chart for indirect ohmic heating driven TCS desorption with heat recovery.

Heat recovery is performed by pre-heating the air flow, upstream of the heating element. The model of the heat exchanger is the same as used for heat recovery in the process in **Chapter IV**. Thermal energy is transferred from the heating element to the air flow with a η_{heater} =100% efficiency. The relationship between the heating power, air mass flow rate and heat capacity, and the temperature increment ΔT, is shown in **equation (83)**. Air heat capacity is assumed to be constant in the range 0°C – 150°C.

$$P_{thermal} = Q_m Cp_{air} \Delta T \quad (83)$$

In the following simulation, the inlet air flow, extracted from the ambient at 30°, is assumed to be heated at a constant power 1700W until full desorption**.** The main parameters for the simulation are shown in **Table 38**. The TCS reactor is assumed to be packed with a 60 wt.-% K_2CO_3 vermiculite salt-in-matrix composite, with a volume of 0.05 m^3 which will later be assumed as the volume of individual modules. With this size the TCS contains 40.1 kg of salt and 26.7 kg of vermiculite matrix. For the simulation the TCS reactor is considered as divided along its central axis into 100 nodes.

In **Figure 92**, **Figure 93** and **Figure 94** the resulting temperature, humidity, advancement, and equilibrium vapour pressure profiles inside the TCS reactor during the desorption reaction can be seen. The resulting reactor-level behaviour is similar to conventionally heated TCS reactor with air heated via solar thermal, mainly characterised by the presence of a reaction front. Salt located closest to the inlet dehydrated first.

Table 38 Main parameters for conventionally heated desorption simulation during basic dehydration step at constant heating power 1.8kW.

Reactive Material			Reactor		
Salt	K_2CO_3		AR	2	[-]
ΔH	63635	J/mol	m_s	81.6	kg
ΔS	157	J/mol/K	m_m	54.4	kg
ρ	2430	kg/m^3	V_{Module}	0.102	m^3
Cp	828	J/kg/K	L	0.803	m
M	0.1652	kg/mol	D	0.201	m
Host Material			**Other**		
Matrix	vermiculite		T_{amb}	30	°C
Cp_m	960	J/kg/K	P_{in}	200	Pa
ρ_m	800	kg/m^3	P_{heater}	1700	W
salt content	60%	[-]	k_{cin}	5.10^{-4}	s^{-1}
			t	24	hours
Air Flow			N	100	
Cp_f	1004	J/kg/K			
ρ_f	1.2	kg/m^3			
Q_m	0.06	kg/s			

The temperature (**Figure 92**) of the material inside the reactor, subjected to the high inlet temperature of the heated air flow, increases to the equilibrium temperature corresponding to the local humidity induced by water desorption. The temperature remains stable at this temperature until the node is fully dehydrated, followed by a rapid increase to inlet air temperature. Thermal energy carried by the air flow passes through the dehydrated material and begins dehydrating the following reactor node. During the charging of a conventionally heated reactor, a ~20K temperature gradient along the reactor can be observed. The magnitude of the temperature gradient is equal to the difference between the reaction equilibrium temperature (60°C) and the inlet temperature (at 80°C for most of the reaction, see **Figure 95**).

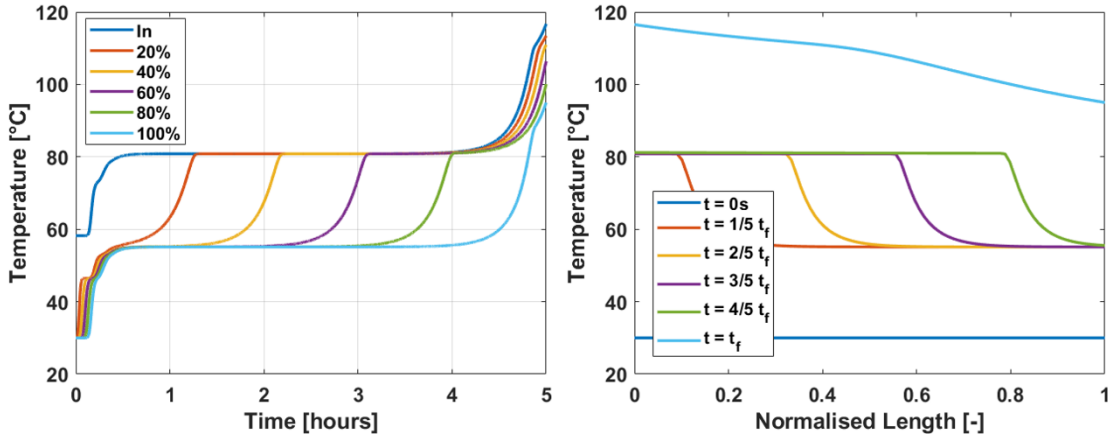

Figure 92 (left) dynamic temperature profiles in TCS reactor at inlet, outlet, and various nodes and (right) temperature profiles along the TCS reactor at different stages of the reaction, dehydration driven by ohmic heating.

At the inlet of the reactor, the humidity of the air flow is very low to induce a large equilibrium vapour pressure which favours reaction kinetics (**Figure 93**). As air travels through the reactor, providing thermal energy to the hydrated salts and triggering the desorption reaction, water vapour is released by the salt. This water is recovered and transported out of the reactor by the air flow. Once the material inside the TCS has fully dehydrated, the air flow inside that reactor node maintains a constant low humidity as no more water is extracted from the TCM.

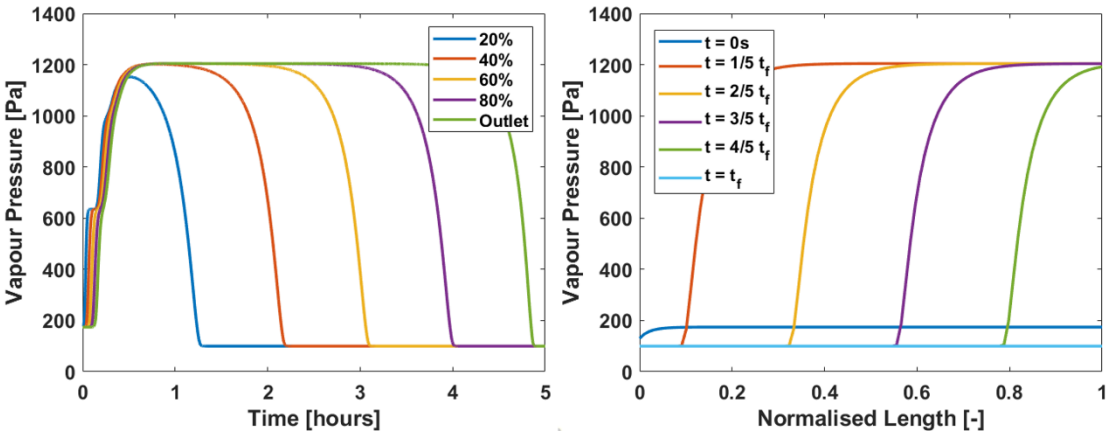

Figure 93 (left) dynamic humidity profiles in TCS reactor at inlet, outlet and various nodes and (right) humidity profiles along the TCS reactor at different stages of the reaction.

The global reaction advancement of the reaction is calculated from the local reaction advancements at each reactor node (**equation (84)**):

$$\alpha_g(t) = \frac{1 - \frac{1}{N}\sum_i (1 - \kappa\alpha^i(t)\frac{M_{H2O}}{M_{salt}})}{\kappa\frac{M_{H2O}}{M_{salt}}} \quad (84)$$

Local and global reaction advancements are shown in **Figure 94**. With 1700W thermal power delivered and heat recovery implemented, full desorption of the reactor (40.1 kg of reactive K_2CO_3) in this configuration is achieved in 5 hours.

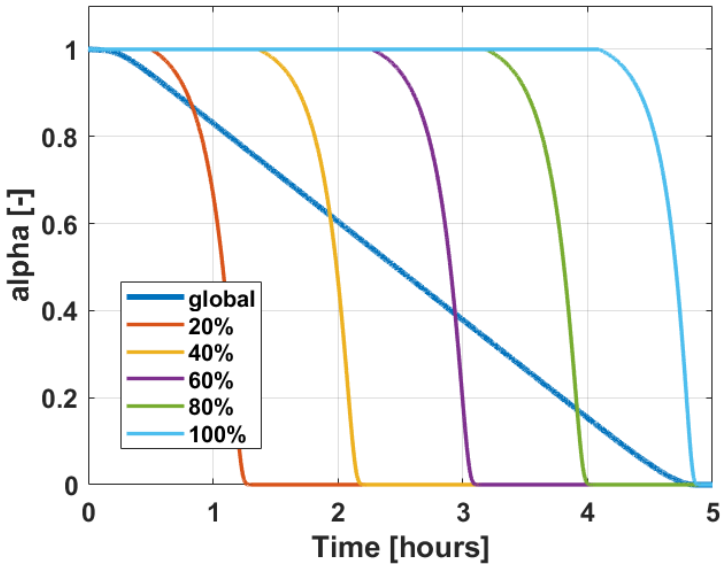

Figure 94 Global and local reaction advancement profiles.

The process-level thermal efficiency for desorption is equal to the energy effectively used to advance the dehydration reaction of the salt, divided by the input thermal energy, and can be calculated with **equation (85)**:

$$\eta_{TCS,des} = \frac{E_{des}}{E_{in}} \quad (85)$$

The total amount of energy used for desorption and therefore stored into the TCS is calculated theoretically with **equation (86)**:

$$E_{des} = \int_0^{t_f} \Delta H\kappa\frac{m_s}{M_s}\alpha dt = \Delta H\kappa\frac{m_s}{M_s} \quad (86)$$

The total amount of thermal energy absorbed by the reactor can calculated according to **equation (87)**:

$$E_{in} = \int_0^{t_f} P dt \tag{87}$$

Which leads in this case scenario to a calculated process-level thermal efficiency of 78.68%. The contribution of the heat recovery can be appreciated in **Figure 95** through the temperature of the air flow at the outlet of the reactor ($T_{R,out}$), and observing the temperature of the air at process outlet ($T_{HR,out}$).

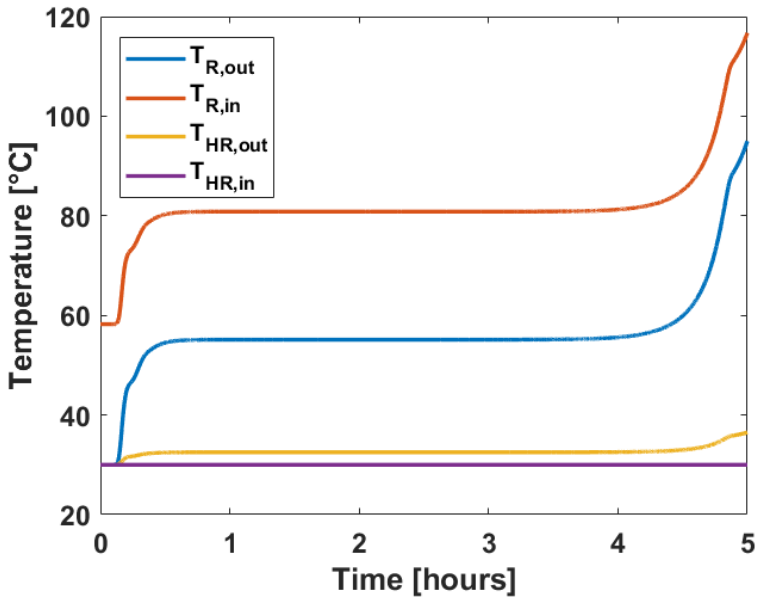

Figure 95 Process temperatures demonstrating the effectiveness of heat recovery during the 1700 W indirect heating powered desorption.

A full process efficiency for indirect ohmic heating (conventional heating CH) may be calculated with **equation (88)** by assuming that the power inverter converts DC to AC power with 92% efficiency, and that the resistance heater converts electrical AC power to thermal power with an efficiency η_{ohm}= 100% .

$$\eta_{P2H/TCS-CH} = \eta_{inv}\eta_{ohm}\frac{E_{des}}{E_{in}} = \eta_{inv}\eta_{ohm}\eta_{TCS,des} \tag{88}$$

This calculation results in complete conversion of incident solar energy to thermochemically stored energy efficiency of 72.39%.

3.3 Direct volumetric heating

Using the modified energy balance in **equation (82)**, the TCS/P2H system with volumetric heating driven desorption was modelled, and the simulation results are presented in the following section.

The layout of the volumetrically-heated reactor is shown in **Figure 86**. As discussed in previous sections, the volumetric heating could be carried out with an electrical power source driving a 2.45 GHz microwave generator to carry out microwave heating of the TCS, an induction heater operating at a frequency in the range 100 kHz to 10 MHz. In any case, the procedure here is to consider a generic volumetric heating source which is assumed to be technically sound, whether it is based on MW-heating, RF-heating, or some alternative solution such as ohmic heating within the reactor. In the case of MW or RF, the main limitation of this model is its ability to evaluate the magnitude the electromagnetic field inside the reactive zone which drives the heating process.

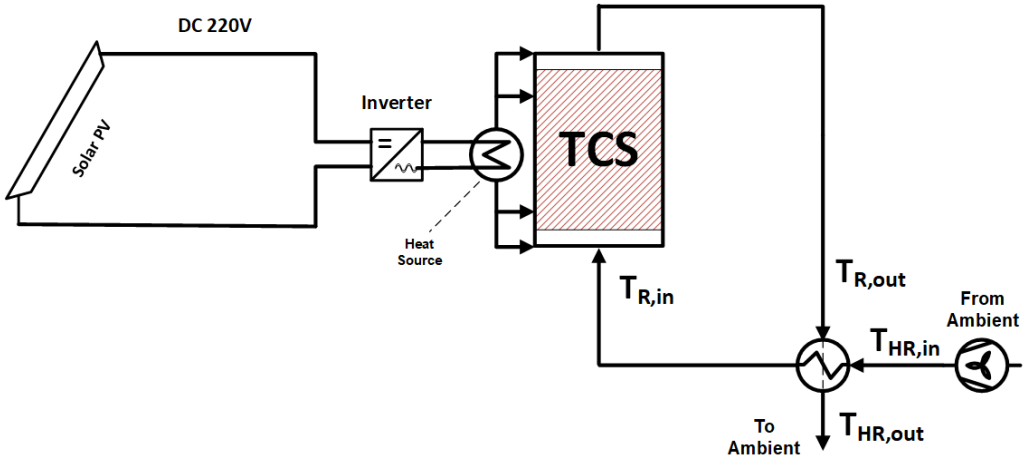

Figure 96 Electrical circuit and flow chart for 1700 W volumetric heating driven TCS desorption with heat recovery.

While the magnitude of the dissipated energy between RF and MW varies due to the different frequency of the EM waves and the difference in heating mechanisms, in both cases the heating effect is a volumetric heating generated simultaneously throughout the reactor volume due to the generation and then dissipation of electromagnetic energy into thermal energy. Volumetric power dissipated as heat into the material is typically quantified with **equation (89)**. The equation is derived from Maxwell's equations and relies on the assumption that the electric field is uniform inside the reactor and material [229–234], with a derivation of the equation being found in [235].

$$Q_v = 2\pi f \varepsilon_0 \varepsilon_r |E|^2 \tag{89}$$

Where f is the frequency of the electromagnetic field, ε_0 the permittivity of free space, ε_r the dielectric loss coefficient of the material (the TCM or water) and E the electrical field intensity. Since the frequency f is constant for any given heating strategy, ε_0 is a universal constant and ε_r depends on the TCS, the determination of the delivered volumetric power hinges on the estimation of the intensity of the electric field $|E|$.

However, the estimation of $|E|$ would theoretically require derivation in time and space of Maxwell's equations which is outside the scope of this study. Furthermore, the presence of solids interacting

with the electric field further complicates the evaluation of the distribution of the electric field intensity inside the reactor. It will therefore be assumed that the volumetric thermal power developed inside the TCS reactor, P_{VH}, will be proportional to the EM energy generated by the magnetrons, weighted by an EM to thermal energy conversion efficiency, η_{MW}.

$$P_{AC}\eta_{VH} = P_{VH} \tag{90}$$

The volumetric heating power depends on the total volume of TCM in the reactor and the total power dissipated inside the reactor, as shown in **equation (91)**.

$$P_{VH} = Q_v V_{TCM} \tag{91}$$

With the assumption of a uniform electric field, the average electric field intensity needed to develop this volumetric heating power can be estimated. Using the expression in **equation** (92), the average electric field intensity in the TCM can be estimated as:

$$|E| = \sqrt{\frac{P_{AC}\eta_{VH}}{2\pi f \varepsilon_0 \varepsilon_r V_{TCM}}} \tag{92}$$

Table 39 Volumetric heating operating parameters.

Symbol	Value	Unit	Description
f_{MW}	2450	MHz	MW frequency
f_{RF}	100 – 10,000	kHz	RF frequency
ε_o	$8.8542.10^{-12}$	$m^{-3}kg^{-1}s^4A^2$	Permittivity of free space
ε_r	1	[-]	Dielectric loss coefficient of the TCM

The following assumptions were made for the simulation of volumetric heating driven desorption, for both MW and RF cases:

- Thermal equilibrium between solid and gas phases.
- Uniformity of the electric field inside the reactor, and the TCM inside the reactor is entirely subjected to the electromagnetic field.
- The dielectric loss coefficient remains constant with variation in hydration level and temperature if microwaves are assumed as the heating method.
- The presence of ferromagnetic particles assumed to be dispersed in the TCM does not reduce the salt weight content in the salt-in-matrix composite in the case of RF heating.
- Heat losses to the reactor walls are neglected.
- No mass transfer limitations in the pure salt or composite SIM.

An unheated air flow (temperature 30°C, mass flow rate Q_m = 0.06 kg/s) is passed through the reactor in order to remove the gaseous water desorbed from the material. Differently from the conventional and ohmic heated reactors, where thermal energy is provided at one end of the reactor, thermal energy

is dissipated volumetrically from the induced electromagnetic field in the entirety of the reactor. A total microwave heating power of 1.7 kW is assumed inside the TCS reactor. With the previously discussed uniform electric field distribution assumption, the average electric field intensity can be estimated with **equation (92)** as 350 V/m in the case of microwave heating, which is within the order of magnitude of electric field intensities found in typical 2450 MHz microwave ovens [236,237]**.** Identical operating parameters to the conventionally heated desorption step were assumed (**Table 38**). The simultaneous heating of the TCM at all points of the reactor may be appreciated through the temporal and spatial temperature profiles shown in **Figure 97**.

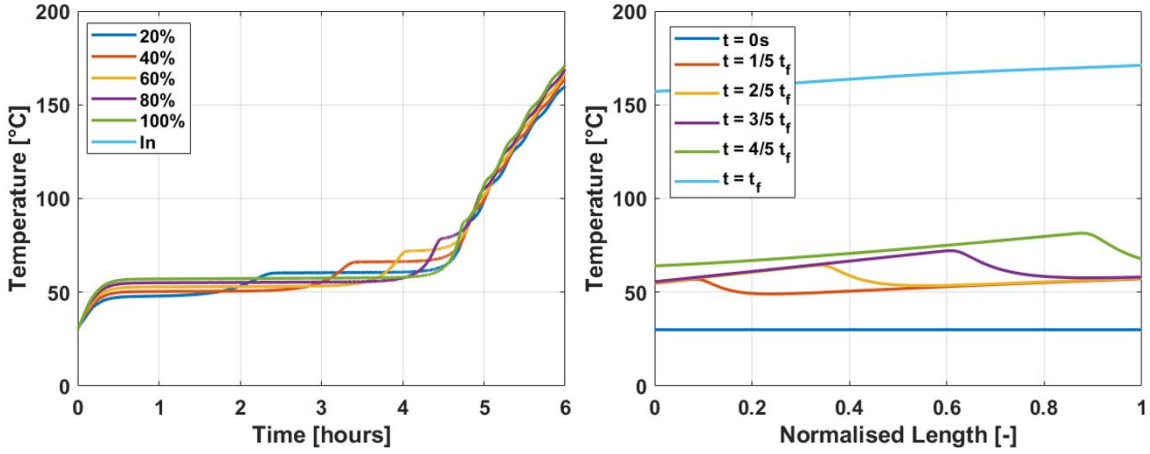

Figure 97 (left) dynamic temperature profiles in TCS reactor at inlet, outlet, and various nodes and (right) temperature profiles along the TCS reactor at different stages of the reaction, dehydration driven by MW heating.

The absence of a reaction front and the presence of an increasing temperature gradient along the reactor at any given time may be attributed to two phenomena:

- At any given node of the reactor, excess thermal energy not dissipated within the solid is exchanged with the cooler air flow and carried over to the next node of the reactor. Thus, the thermal energy at a given node *i+1* will exceed the thermal energy at node *i*.
- Humidity is desorbed during the reaction and transported further along the reactor. The accumulation of water in the air flow leads to a higher desorption equilibrium temperature further along the reactor. The increase in humidity may be appreciated through **Figure 98**.

Such temperature gradients along the reactor length are observable in the literature for other microwave-assisted desorption systems with additional air flow for humidity removal. Temperature measurements carried out at different points along the TCS reactor's central axis show this temperature increase, such as in the experimental desorption of zeolite by Ito et al. [203,234], and during the microwave-assisted TSA desorption process by Meloni et al. [204].

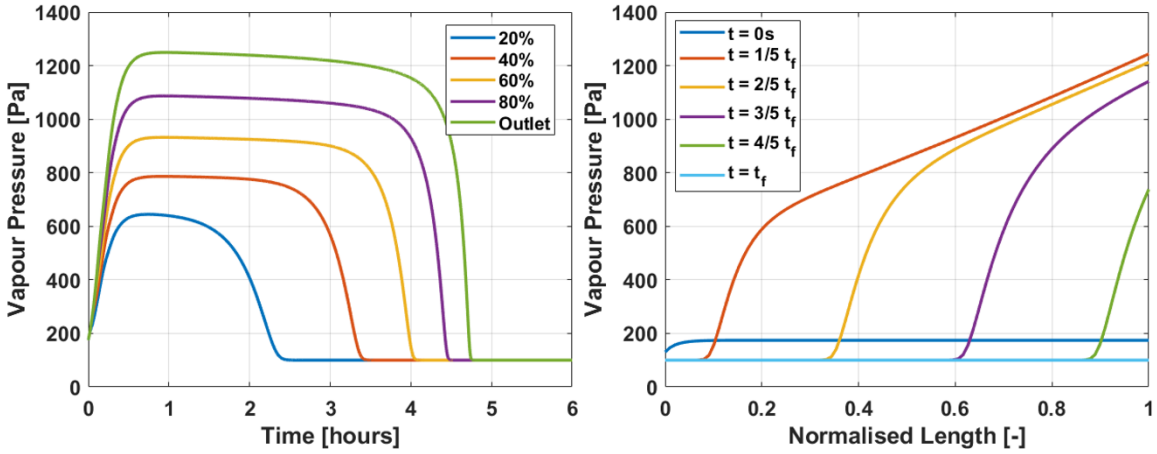

Figure 98 (left) dynamic humidity profiles in TCS reactor at inlet, outlet, and various nodes and (right) humidity profiles along the TCS reactor at different stages of the reaction.

Resulting from the increasing temperature gradient along the reactor, the shifted equilibrium conditions and the distributed heat generation along the entire reaction zone, the dehydration of TCM at nodes further from the air inlet takes place simultaneously to the nodes closer to the inlet. This behaviour is verified by the local reaction advancement profiles in **Figure 99** towards the beginning of the reaction which showcases the difference in desorption dynamics when thermal energy is provided volumetrically throughout the reactor rather than at the inlet of the reactor such as for conventional indirect ohmic heating. However as heat is recovered during the desorption process and returned to the inlet, the TCM towards the inlet dehydrates faster. Thus the behaviour observed in **Figure 99** is a combination of the volumetric heating taking place all over the TCS, and heat being recovered and transported to the reactor inlet.

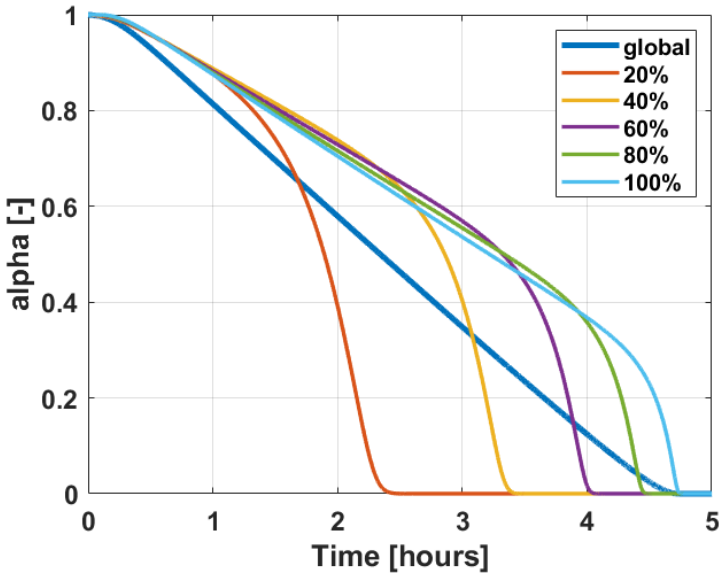

Figure 99 Global and local reaction advancement profiles, dehydration driven by MW heating.

Figure 100 shows the various temperatures at different locations of the process. A key difference to the conventionally heated reactor is the smaller temperature difference between reactor inlet and outlet air flows. The contribution of the heat recovery can also be appreciated here with the very low temperature at the process outlet $T_{HR,out}$.

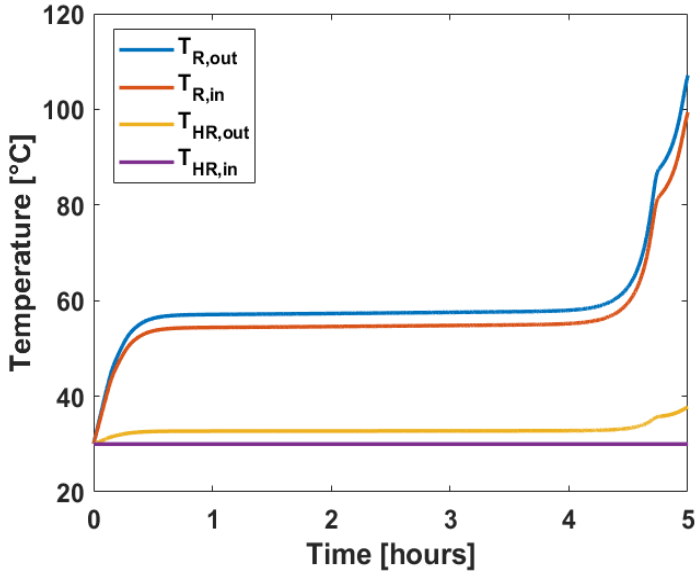

Figure 100 Process temperatures demonstrating the effectiveness of heat recovery during the 1700 W volumetric heating powered desorption.

The air entering the reactor in this scenario is at ambient temperature. The difference in the total energy provided by microwave dissipation and thermal energy exiting the reactor is equal to the energy absorbed by the endothermic reaction and sensible heat used to increase TCM temperature to equilibrium. The energy balance is shown in **equation (93)**.

$$E_{in} - E_{out} = E_{des} + E_{sens} \tag{93}$$

As for the conventionally heated system, the process-level thermal efficiency for volumetric heating desorption is equal to the energy effectively used to advance the dehydration reaction of the salt, divided by the input thermal energy, and can be calculated with **equation (94)**:

$$\eta_{TCS,des} = \frac{E_{des}}{E_{in}} \tag{94}$$

The desorption energy is as for the conventionally heated reactor, calculated in **equation (85)**. In this scenario E_{in} is the energy provided to the inlet air stream and the total microwave energy provided volumetrically to the reactor (**equation (95)**).

$$E_{in} = \int_0^{t_f} Q_m Cp_f (T_{in} - T_{amb}) dt + \int_0^{t_f} P_{MW} dt \tag{95}$$

In the present case scenario, no energy is provided to the inlet air flow ($T_{in} = T_{amb}$). The energy absorbed by the desorption reaction E_{des} and thermal efficiency at the reactor level during volumetric heating are calculated with the same formula as for conventional heating. A process level thermal desorption efficiency of 80.77% is achieved, with full desorption occurring after 4.7 hours. Accounting for solar inverter losses, the final efficiency is 74.31%. The slightly increased efficiency compared to conventional heating is due to the shorter desorption time which ties in with a lower amount of electrical energy needed to dehydrate the same amount of TCM. This increased efficiency and lower desorption can be found across a range of heating powers according to the model (**Figure 101**).

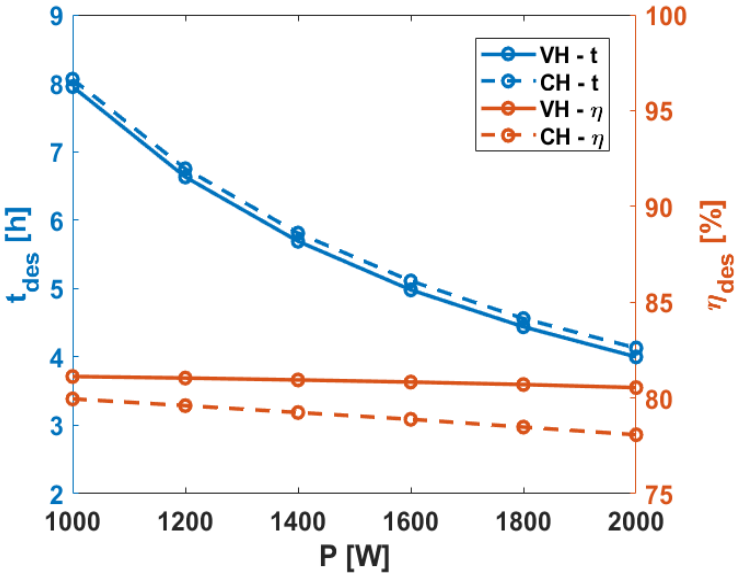

Figure 101 Comparison of volumetric and conventional heating in terms of desorption time and desorption efficiency, effect of heating power.

4 System Integration

Strategies for electrically heating TCS reactors were discussed in the previous sections. It was found that electrical heating divides into *indirect conventional heating* and *direct volumetric heating*. The aim of **Section 4** is to evaluate the performance of a coupled TCS/P2H/PV system with indirect conventional heating when integrated in a dwelling equipped with solar PV as the electrical energy source. The purpose of this system is to attempt to maximise the solar fraction of a dwelling equipped with solar PV, thus reducing reliance on the grid, while decarbonising and electrifying space heating energy sources in dwellings. As was discussed in the introduction of the chapter, the decision to combine TCS with PV through P2H also hinges on the increased temperature levels which are achievable with power to heat. The energy storage potential of inorganic salts and composites can be maximised by the ability to fully desorb them. The overall performance was found to be sensitive to the sizing strategy for the TCS; results are shown for two selected TCS sizing strategies. First unconstrained sizing, then TCS constrained to a maximum of $10m^3$.

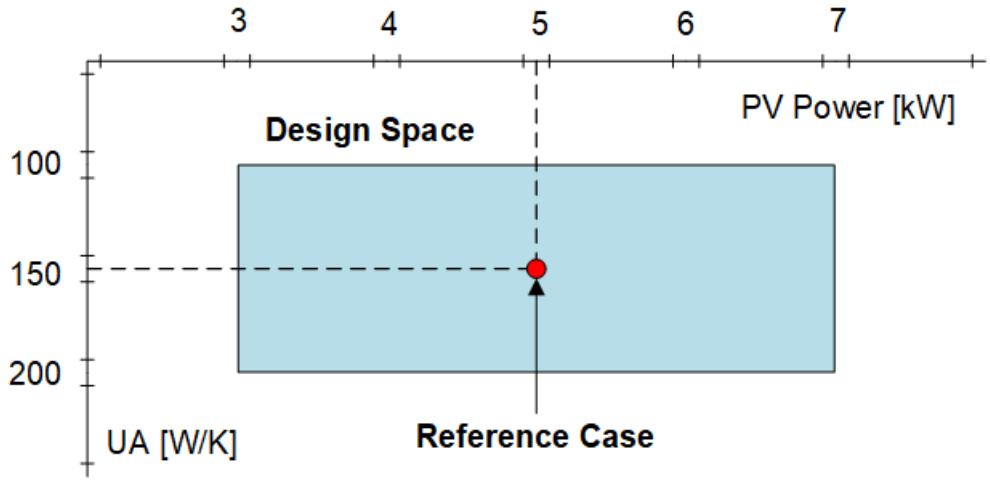

Figure 102 TCS/P2H/PV system design space. To consider a broad range of potential space heating systems in PV equipped dwellings the system was evaluated for PV ranging 3 kW to 7 kW and dwellings with overall heat loss coefficients from 100 W/K to 200 W/K.

Section 4 is structured as follows: an overview of the physical layout and operation strategy of the system (heat source, heat sink and interaction with storage) will be followed by the technical performance of a reference case. This latter step was achieved by operating the TCS over a year to evaluate its contribution to increasing the share of renewable energy in the fulfilment of the building's energy demand and the overall economic feasibility. Departing from the reference scenario, the integrated system was simulated using a range of values for solar photovoltaic system power rating (3 kW to 7 kW) representative of typical domestic solar PV systems, and a range of UA heat loss coefficients (100 W/K, 150 W/K and 200 W/K). From here on, these ranges of solar PV power ratings and building heat loss coefficients represent the ***Design Space*** within which the techno-economic performance of the TCS/P2H/PV system is evaluated (**Figure 102**). Any reference to ***Design Space*** refers to these two ranges of parameters which strongly affect performance. The technical performance of the system in the design space is evaluated with the same operation strategy for the two distinct sizing strategies. The section is then concluded with the economic performance of the system in both cases.

4.1 System description

The main parameters which are varied and constitute the design space are the PV power rating capacity (P_{pv}), and the building heat loss coefficient (UA). The space heating system and demand of the building, energy generated by the PV system and the physical integration of the TCS are discussed. The overall layout of the system is schematically presented in **Figure 103**.

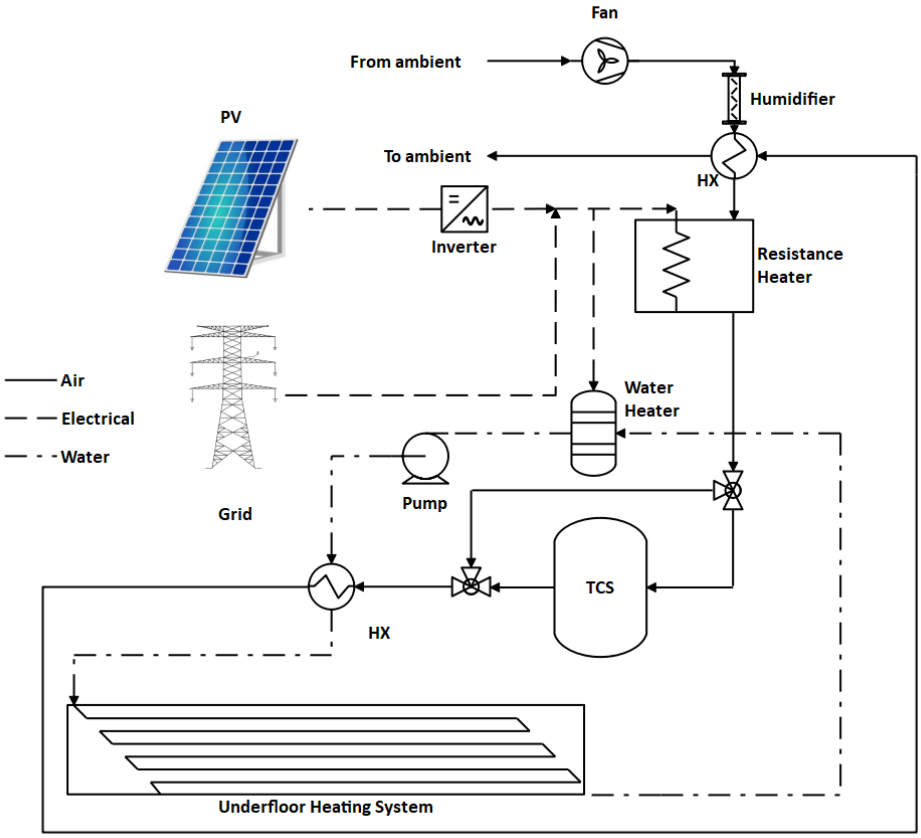

Figure 103 TCS/P2H/PV system using indirect ohmic heating integrated into a dwelling equipped with solar PV and underfloor heating system. System is composed of three circuits: electrical circuit for solar power generation, air circuit which contains the electrical heater and the TCS process, and water circuit for the underfloor heating system. In the analysis, the power rating of the PV system is varied from 3 kW to 7 kW, and the heat loss coefficient of the dwelling between 100 W/K and 200 W/K. These two parameters constitute the design space of the TCS/P2H/PV system. Heat exchanger HX assumed effectiveness of 85%.

Reference building

The aim of the proposed system is to increase the share of solar PV energy in the space heating of the dwelling. Representative dwellings were found in a survey of the UK housing stock featuring solar PV systems [238]. The survey indicates that detached and semi-detached houses are both the most frequently found type of dwelling in the UK and are also the types of dwelling most likely to feature a solar PV system. Thus the selected building is a semi-detached house which is assumed to be in Birmingham, UK.

Space heating demand and system

The space heating demand depends on location, the specific activities of the occupants, and the thermal characteristics of the building. It is the product of the overall building heat loss coefficient UA and the difference between outdoor temperature T_{amb} and a baseline temperature T_{Base} at which the dwelling indoor space should be maintained through heating (**equation (96)**). Rather than conceive an architecture for the dwelling, the overall heat loss coefficient was used as the representative parameter of the heat sink.

$$Q_{space\ heating} = \overline{UA}(T_{Base} - T_{amb}) \tag{96}$$

Typical building overall heat loss coefficients in the UK are shown in **Table 40**, based on a survey of the UK building stock [239,240]. For the case study, the overall heat loss coefficient of the dwelling was varied between 100 W/K and 200 W/K, and a minimum baseline temperature T_{Base} of 20°C. From ambient temperature profiles in Birmingham in 2015, the overall space heating demand for a building with heat loss UA = 150 W/K is shown in **Figure 104**.

Table 40 Heat loss coefficients for typical UK dwellings.

Dwelling Type	Usable floor space	Mean UA
[-]	m^2	W/K
End Terrace	86	140.18
Mid Terrace	81	132.03
Semi-Detached	93	151.59
Detached	152	247.76
Bungalow	77	125.51
Flat	60	97.80

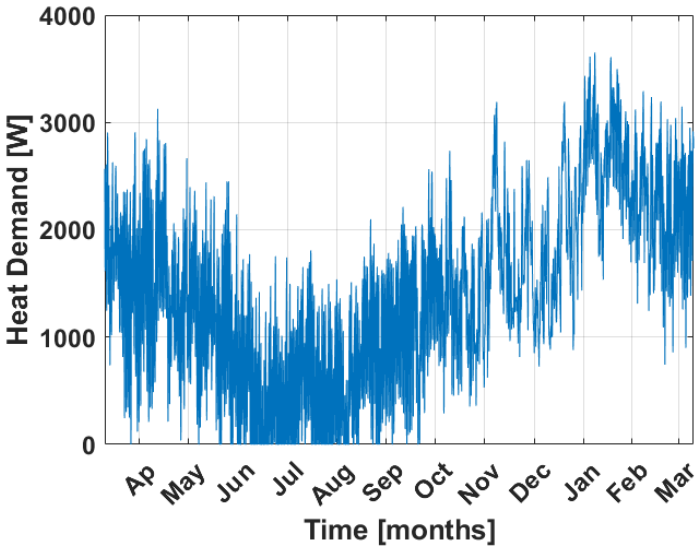

Figure 104 Space heating demand for the reference dwelling with overall heat loss coefficient UA = 150 W/K and baseline temperature of 20°C. Ambient temperature data from Renewables.ninja.

Dwelling space is heated by a hydronic underfloor space heating system (UFH). This heating method is preferred to the other common hydronic heating systems such as radiator heating due to the lower required temperatures to ensure the minimum space heating temperature requirements. Temperature inside the piping for UFH should be in the range 40°C to 55°C to achieve a room temperature of 20°C to 30°C. These temperatures depend on various factors such as the type of floor building method and material, the arrangement of the underfloor piping and water flow rate. **Table 41** shows the key characteristics of the underfloor system to achieve the selected indoor baseline temperature of 20°C. For this system heat needs to be delivered at a minimum of 40°C.

Table 41 Main characteristics for the underfloor heating system.

UFH characteristics		
Floor Area	100	m^2
Length of loop	120	m
Loop coverage	20	m^2
Number of loops	5	[-]
Total pipe length	600	m
Flow rate at the manifold	15	L/min
Temperature Requirement	40	°C
Temperature Difference	10	°C

Solar resources availability

The roof of the dwelling is assumed to be covered with a solar PV system with PV power rating varying between 3 kW and 7 kW which is representative of domestic photovoltaics. An hourly electrical energy profile generated solar PV system in the year 2015 in the centre of Birmingham was obtained through renewables.ninja [5,181], which allows for the generation of solar power and temperature profiles at any global location. The data was calculated for a 1 kW system, which is then factored by the PV power rating to obtain the electrical power generation profile for the range of investigated PV systems. The generated PV power P_{PV} for a 5 kW system is shown in **Figure 105**.

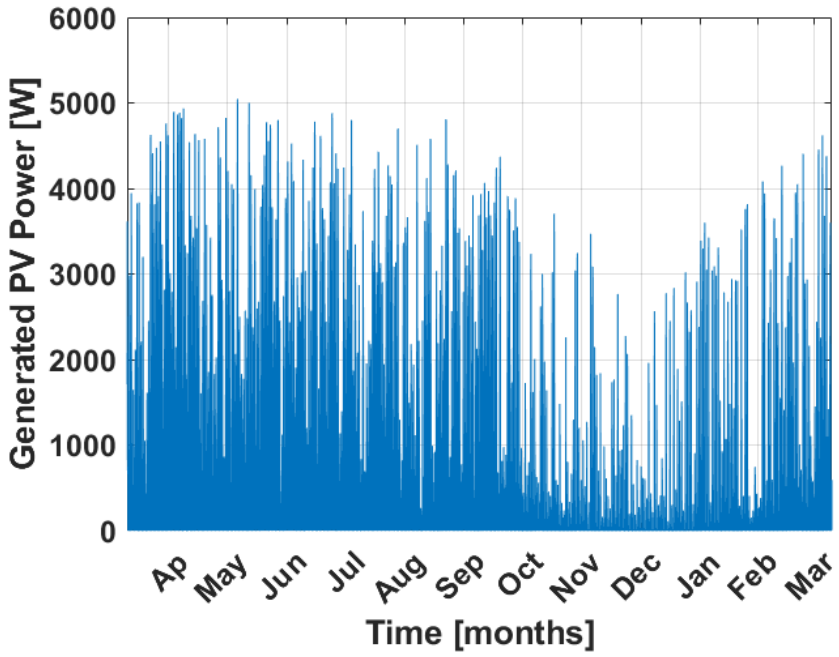

Figure 105 Available generated power by 5 kWp solar PV system in Birmingham in 2015. Solar PV data taken from Renewables.ninja [5,181]**.**

Interaction with the TCS

The monthly heat demand and generated solar energy profiles for the dwelling can be visualised in **Figure 106** averaged out for each month. During summer, available PV power exceeds space heating demand, whereas during the rest of the year heat demand exceeds available PV power. This mismatch justifies the presence of a long-term energy storage system since heat is required to be stored for several months.

$$\Delta Q = Q_{PV} - Q_{space\ heating} \tag{97}$$

Let E_{PV} be the energy delivered at power Q_{PV}, $E_{space\ heating}$ the energy required to heat the dwelling at power $Q_{space\ heating}$ and ΔE the difference between the two. Heat released from the TCS as hot air and exchanged with the closed water circuit of the UFH is the means by which thermal energy is

transferred from the TCS to the load. Heat that contributes to the generation of hot water at the UFH operating temperature (40°C) is considered delivered to the load. The means by which thermal energy is transferred from the UFH to the dwelling living space is not considered in this study.

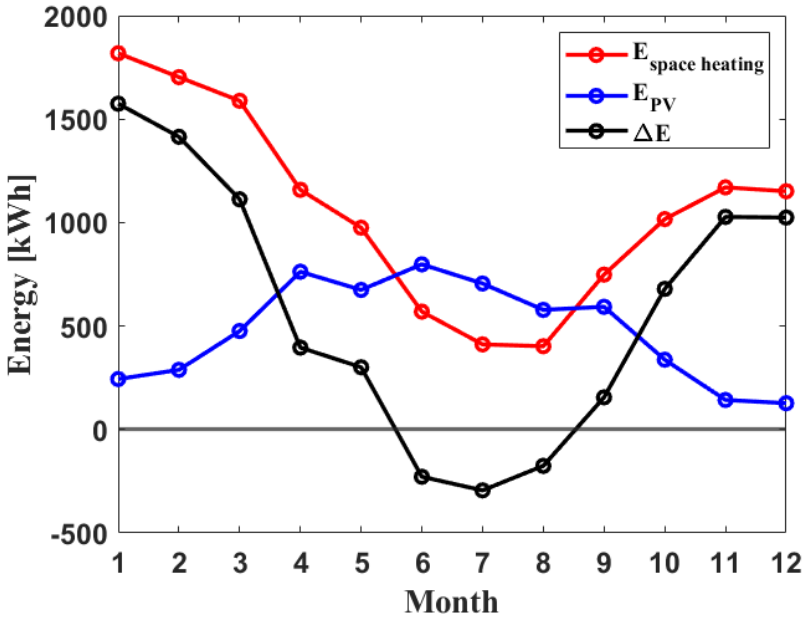

Figure 106 Monthly heat demand, available solar PV energy and difference, averaged for each month, with UA = 150 W/K and P_{pv} = 5 kW.

Reference case description

As was discussed in the description of the model in **Section 3**, the TCS is subdivided into modular reactors in order to minimise the volume of salt during the chemical reaction. Modules are designed to be cylinders with a volume of 0.05 m^3. Cylinders are preferred to cubic / rectangular shapes as edges cause unreacted zones and larger pressure drops. During charge (respectively discharge) thermal energy is transported (respectively removed) to a new module when the previous module is fully charged (respectively discharged). It is assumed that the piping and instrumentation of the reactor enables this transfer. The modules contain a K_2CO_3/vermiculite composite chosen as the TCM. Characteristics of this TCM and of module geometry are shown in **Table 42**.

Table 42 Characteristics of the TCS modules and TCM.

Parameter	Value
Material	Salt/Matrix Composite
Salt	K_2CO_3
Matrix	Vermiculite
Salt wt.%	60%
ɟ m	800 kg/m^3
Cp_m	960 J/kg/K
Module Volume	0.05 m^3
Module Aspect Ratio	1

The reactor is initially assumed to have an infinite number of modules. The finite number of modules is determined after the simulation by evaluating the maximum state of charge of the TCS during the simulation. The TCS is operated according to the strategy shown schematically in **Figure 107**. As for the idealised case, the decision to charge, discharge, or keep the storage idle, is predicated on the difference ΔQ between the available solar PV power and the instantaneous space heating demand at each hour. The TCS storage is assumed to be empty (fully hydrated) at the beginning of the simulation.

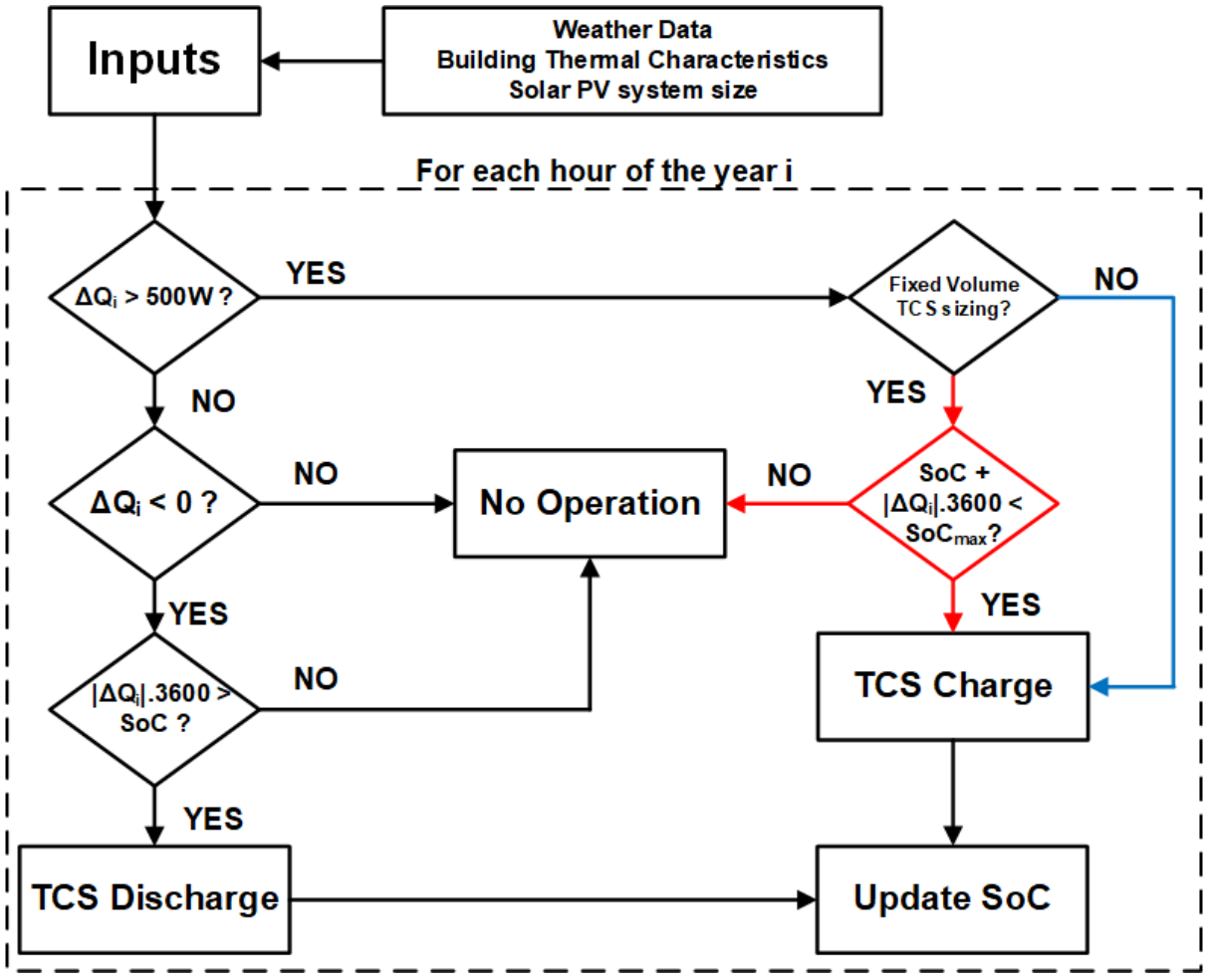

Figure 107 Operational strategy for the TCS. ΔQ_i is the power at the solar PV at hour i, SoC the current state of charge, and SoC_{max} the maximum state of charge if a fixed volume TCS sizing strategy is used (red lines in the logic diagram, with the blue line showing the path for an unconstrained TCS volume sizing strategy).

A positive ΔQ (solar PV power exceeds space heating demand) leads to dehydration if the available power is high enough (over 500 W). Dehydration is carried out at a fixed design temperature (see **Table 43**). Since the power level of the excess PV energy varies every hour, fixed temperature is achieved by controlling for the mass flow rate Q_m. A negative ΔQ (space heating demand exceeds solar PV power) leads to hydration if the current state of charge allows it. During hydration / heat

discharge, when matching space heating demand, air mass flow rate Q_m is kept constant at a chosen design value, while the humidity of the air flow is controlled based on the demand. It is assumed that the humidifier enables a range of vapour pressure spanning 100 Pa to 2000 Pa. At a fixed mass flow rate, increasing the inlet humidity leads to an increase in the power output. The humidity of the inlet is limited by the deliquescence of the salt (2329 Pa for K_2CO_3 at 20°C).

Table 43 Main parameters for the simulation of the reference case.

Parameter	Definition	Value	Unit
	Heat Source		
UA	Overall heat loss coefficient	150	W/K
q_{inv}	Efficiency of the power inverter	0.92	-
q_{P2H}	Efficiency of the P2H component	1	-
Size factor	PV system size	5	kW
T_{base}	Baseline indoor temperature	20	°C
	TCS		
kcin	Reaction rate constant	0.0005	s^{-1}
ə	Stoichiometric Coefficient	1.5	mol/mol
$P_{dehydration}$	Air humidity during charge	500	Pa
$T_{dehydration}$	Air temperature during charge	90	°C
$Q_{m,dehydration}$	Air mass flow rate during charge	Variable	-
$P_{hydration}$	Air humidity during discharge	Variable	Pa
$T_{hydration}$	Air temperature during discharge	20	°C
$Q_{m,hydration}$	Air mass flow rate during discharge	0.06	kg/s
N	Reactor module node number	50	-
	Heat Sink		
Ů	HX efficiency	0.85	-
$T_{w,in}$	Water to be heated temperature	20	°C
$T_{air,out}$	HX outlet air temperature	25	°C

4.2 Technical Performance

Reference case

Reference case simulation results are shown for an unconstrained TCS with a 5 kW PV system and overall heat loss coefficient of UA = 150 W/K, with parameters in **Table 43**. As for the TCS system shown in **Chapter IV**, evaporative humidification induces an air temperature reduction that is taken into account using a Mollier diagram. The interaction of the TCS with the dwelling's space heating system is presented for a week's operation during summer (**Figure 108**), and for week's operation during winter (**Figure 109**). With the chosen control logic, based on the difference ΔQ between generated PV and space heating load, excess PV energy tends to be stored during daytime, whereas heat is released during the night (**Figure 108 top)**. However, during the summer week, the excess daytime PV generated energy charged into the TCS tends to exceed heat discharged from the storage

the next night. The overall state of charge SoC thus gradually increases over the week from ~0.4 to ~0.6, while also displaying daily oscillations due to the night/day energy discrepancy (**Figure 108 bottom**).

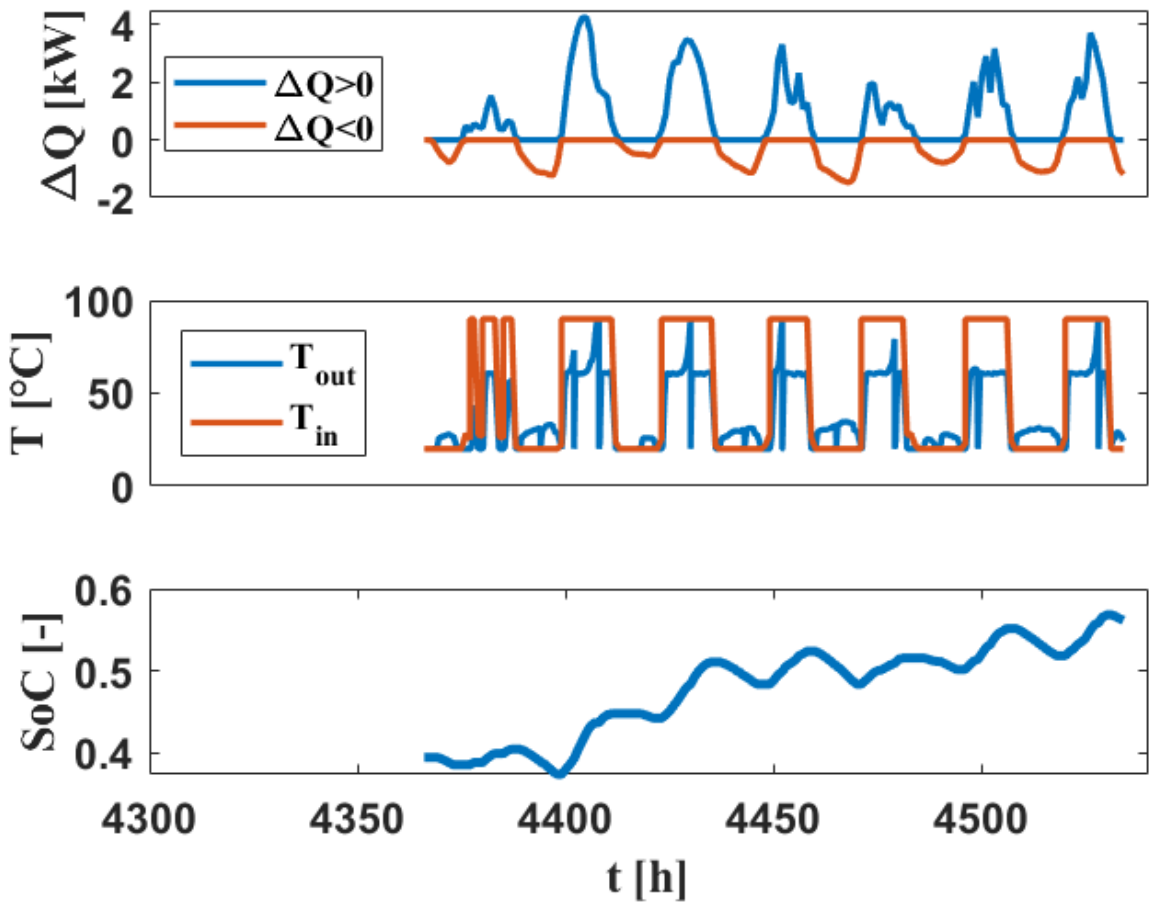

Figure 108 Weekly operation of the dwelling integrated TCS for a summer week dominated by heat charge / dehydration. (Top) Difference in available PV power and space heating demand which drives the TCS operation (when ΔQ > 0, excess PV is converted to heat and stored, and when ΔQ < 0 heat is discharged from the TCS to the dwelling heating system), (middle) temperature profile at inlet and outlet of the TCS reactor, and (bottom) overall state of charge of the TCS.

Figure 108 middle shows the inlet and outlet temperatures of the process. Air is heated to 90°C by the P2H component as a response to the availability of excess PV power for charge. Air mass flow rate Q_m is controlled during this step to maintain a constant 90°C charge temperature with variable power availability. Hot air flows into a hydrated empty storage module. During one of such stages, the outlet temperature of the reactor is approximately ~60°C, which is the equilibrium temperature of dehydration at the inlet dehydration humidity (500 Pa), until increasing up to the inlet temperature which indicates that the reactor module is fully charged. A sharp drop back to the ambient temperature before increasing again to the equilibrium shows that the air flow has been redirected to the next uncharged reactor module.

In the winter week (**Figure 109**), the total amount of energy released from the storage exceeds the loaded amount of thermal energy, which results in a gradual decrease of the overall state of charge during the week. As for the summer week, the SoC displays daily oscillations. By observing the evolution of the SoC for both summer and winter weeks, the dual intermittency of solar energy availability/demand is visible: intermittency at the daily scale, which results in short operation times and turnover between charge and discharge cycles leading to visible oscillations in the SoC, and intermittency at the seasonal scale which drives the long-term trend of the SoC (gradual increase or decrease).

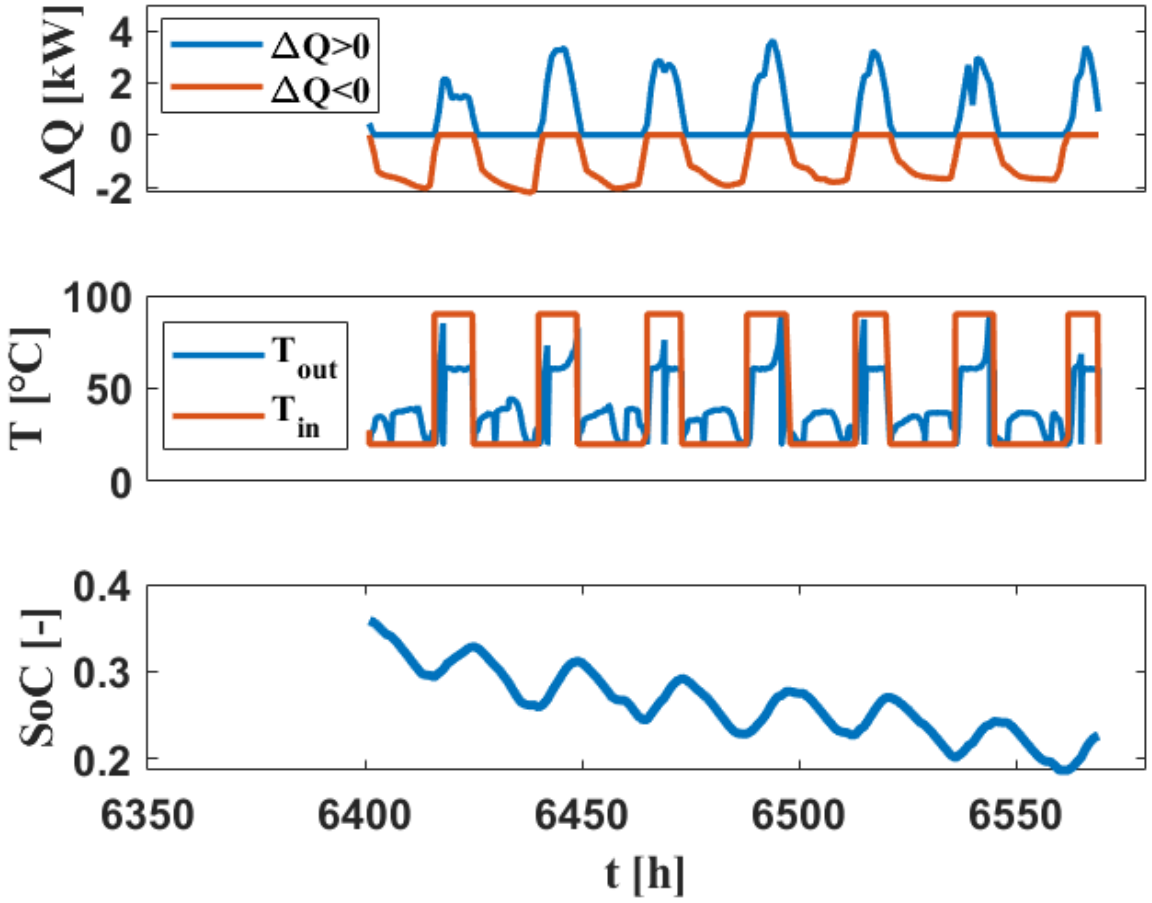

Figure 109 Weekly operation of the dwelling integrated TCS for a winter week dominated by heat discharge / hydration.

During hydration / heat discharge, air is provided at ambient temperature and controlled humidity to trigger the exothermic hydration reaction. A variable temperature rise can be observed at the outlet of the TCS which signals heat being removed from the reactor and directed to the air-to-water heat exchanger to heat up water in the UFH circuit. A challenge during the hydration step is predicting the power output of the reactor for a given flow rate and humidity. Releasing air above the acceptable threshold of 40°C while also delivering over the course of the hour the correct amount of energy requires suitable control. In this simulation the focus was on meeting the space heating demand by

varying the inlet humidity at a fixed flow rate. As a result, the space heating demand was generally met, however a suboptimal amount of heat is released below the threshold of 40°C, which is a limitation of this work.

While **Figure 108** and **Figure 109** covered the system behaviour over week-long time spans, in **Figure 110** the year-long performance can be appreciated. The complete state of charge profile over the year is shown in **Figure 110a**. In the first ~2000 hours of the year, building heat demand consistently exceeds available PV power, so that most of the generated PV energy is used immediately to heat up water in the UFH loop. During this period the TCS is largely unsolicited. As the year progresses and average solar irradiance and ambient temperature increases, more incidences occur of solar PV electricity exceeding building space heating demand, and excess PV energy is converted to heat and stored in the TCS. Stored energy is still used to supply space heating, but not at a high enough rate for the TCS to be fully discharged. As a result, the SoC can be seen to increase until reaching its maximum around ~4600 hours. This maximum corresponds to the maximum relative SoC = 1. Beyond ~4600 hours, ambient temperatures and solar irradiance gradually decrease. The TCS is discharged at a higher rate than it is charged, and the state of charge gradually decreases until reaching 0 at around 6400 hours. Beyond that, for the rest of the year, the storage is unsolicited. The start and end states of charge are similar, in such a way that a year's operation is sufficient to characterise the system behaviour which can be extended to multiple years (assuming non-significant changes in weather and irradiance between two different years).

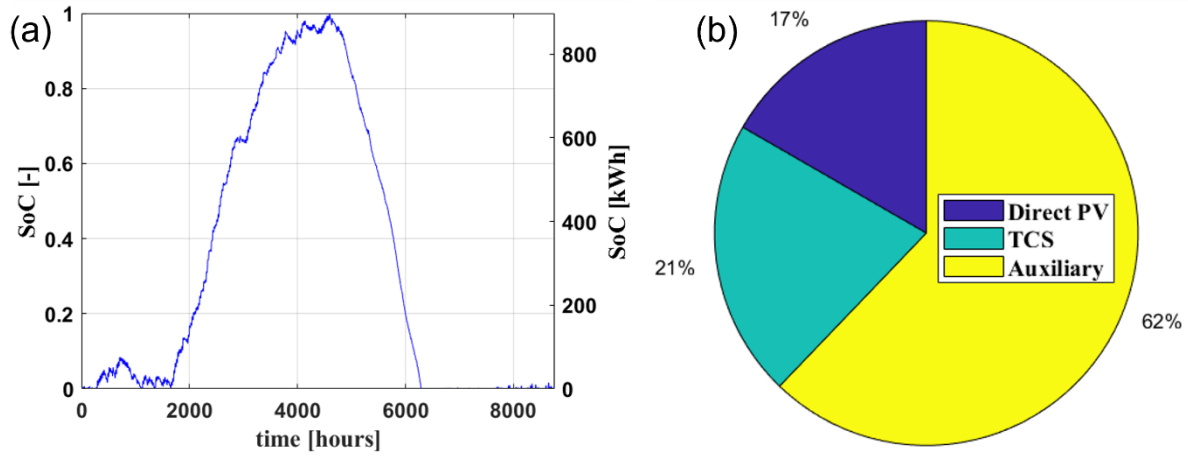

Figure 110 Absolute and relative state of charge of the TCS during year-round simulation in the reference case scenario.

The maximum unconstrained capacity of the storage is 897.6 kWh. With the 60 wt.% K_2CO_3 / vermiculite composite as the TCM, and assuming an overall porosity of the composite material of 0.5, this energy storage capacity results in a volume of ~14 m^3, i.e., an effective energy storage density of ~64 kWh/m^3 (0.23 GJ/m^3). This value is in line with typical TCS system scale energy densities. At material scale energy storage densities in the range 200 – 500 kWh/m^3 are typically reported, which are generally over estimated since an inert matrix generally needs to be included. Furthermore, energy

storage density is in fact a property of operating conditions, and not the material itself, and will depend on charge and discharge temperatures and humidities. At reactor scale, a drop below ~200 kWh/m^3 occurs due to bulk porosity and lower efficiency in reactors compared to milligram scale experiments caused by the larger mass of material. A final energy density drop is expected between reactor and system scales since only heat released above the minimum temperature threshold is counted. As a reference point, the U.S. department of Energy aims for system-level energy storage densities above 80 kWh/m^3 [241]. Increasing the energy storage density of the TCS/P2H/PV system could be achieved at any of the discussed scales: at material scale, by choosing a higher enthalpy salt, increasing the salt fraction in the composite, or using an active matrix, at the reactor scale by decreasing the bulk density of the material, optimising the operating conditions such as humidity during discharge, and at system scale by optimising the control to ensure a higher fraction of the delivered heat is at sufficient power for the application.

The contribution of each energy source (direct PV, heat discharge from TCS, and auxiliary heaters) is shown in **Figure 110b**. In this reference case, 17% of the space heating demand is covered by direct PV usage converted via P2H, and the TCS increases PV consumption in the building space heating demand from 17% by a further 21% up to 38%, i.e. a 123% increase. This fraction of utilised PV power accounts for the various energy losses which occur at the various stages of the heat storage cycle, and particularly during the charging step. These different charge phase energy losses are summarised in **Table 44**. The fraction of heat stored as sensible energy is worth noticing: 0.42 MWh i.e., 16% of the absorbed heat or 13% of the total input is actually stored sensibly rather than as chemically bound energy, which is lost in long term seasonal storage.

Table 44 Overall charging / dehydration phase energy balance.

Dehydration Energy Balance				
Total Excess PV energy			3.15	MWh
	Energy at system outlet		0.43	MWh
	Energy not used for discharge		0.12	MWh
	Energy removed from air stream		2.60	MWh
		Desorption energy	2.18	MWh
		Sensible Energy	0.42	MWh
Charge Efficiency	Desorption energy / Total Excess PV energy		69.41	%

In this reference case, 3.15 MWh thermal energy generated from the conversion of the excess PV electricity through the P2H element is transported into the TCS reactor. 3.8% of that energy is available below 500 W and therefore not used for dehydration, 82.54% of that energy is found at the exit of the reactor, and 2.18 MWh is effectively stored through sorption into the reactor, while 0.42MWh is stored in the reactor as sensible heat, leading to an overall charging efficiency over the year of 69.41%. During the discharge phase, energy is ‘lost’ if delivered below the temperature requirements of the space heating system, in this case the underfloor heating. In this reference case scenario, with a required temperature of 40°C, 1.03 MWh of the 1.39 MWh discharged meet this requirement i.e., 74% of the discharged energy.

Direct solar PV usage in the Design Space

The impact of electricity generated by the solar PV and of the space heating demand on the interaction between TCS/P2H/PV system and building is analysed. With the selected operational strategy, part of the generated PV energy can be converted to heat and directly used for space heating. This occurs when there is a demand for space heating (due to low ambient temperatures) and enough solar irradiation to generate electricity. Over the design space, depending on the ratio between the total PV generated energy and building heat losses, direct usage accounts for 10% to 22% of the space heating demand (**Figure 111**). Increasing the power rating or decreasing building heat losses shows diminishing returns in terms of direct solar usage, as the additional excess energy will tend to be available when heat demand is low or already sufficiently covered by solar PV converted into heat.

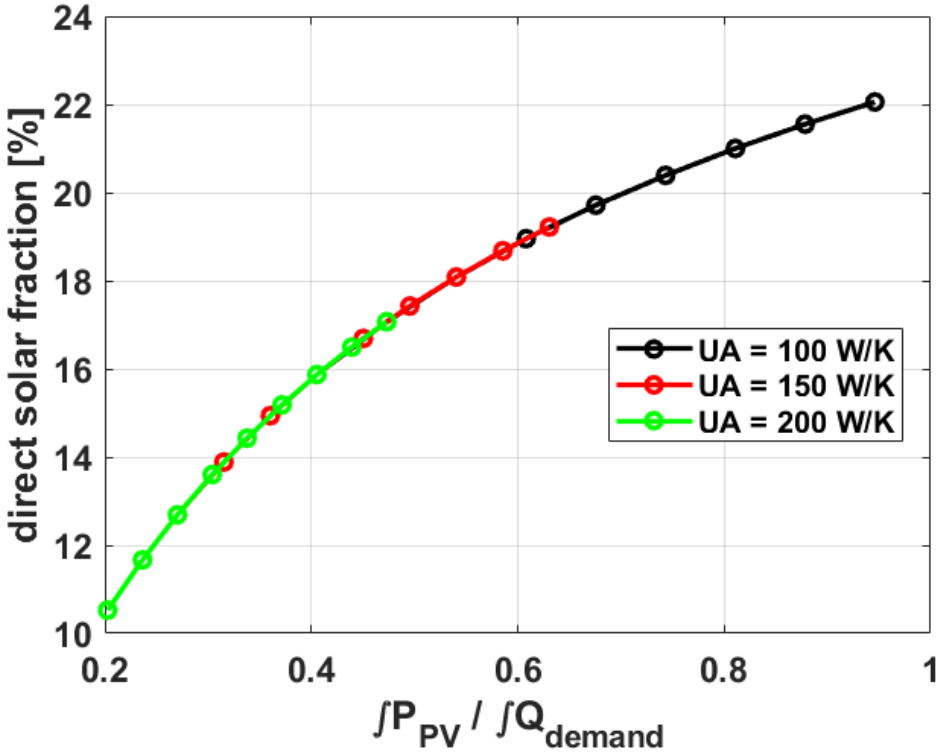

Figure 111 Impact of the ratio of solar PV energy to heat loss on the direct solar fraction. The achievable direct solar fraction is independent of the TCS sizing strategy.

Unconstrained TCS volume

Simulations were carried out with the unconstrained TCS sizing method in the system's design space. The schematic representation of this sizing method in relation to the TCS state of charge is shown in **Figure 112**.

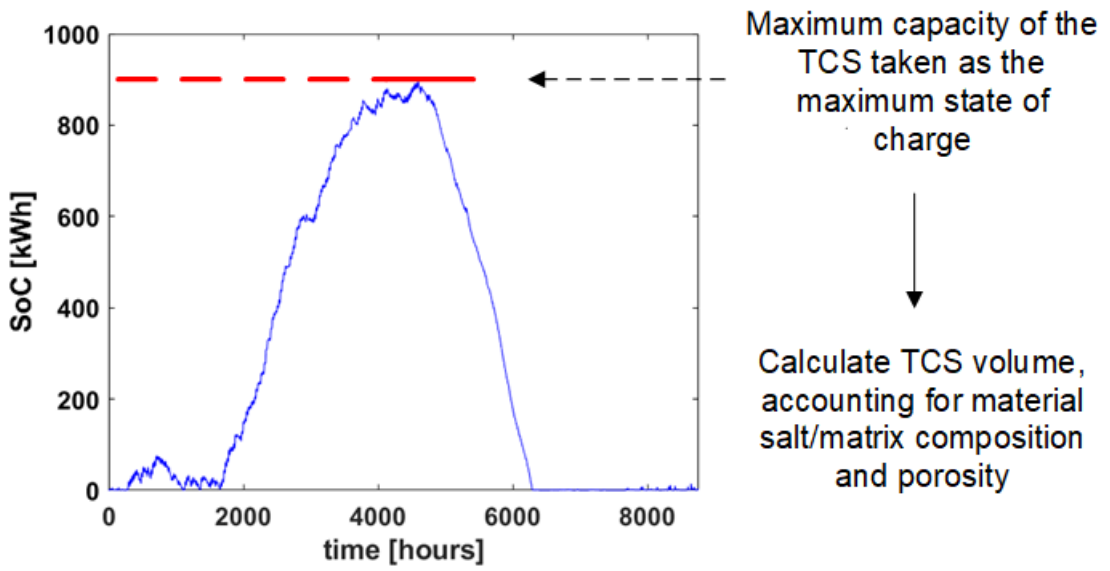

Figure 112 Unconstrained TCS sizing concept: during the simulation (5 kW solar PV and UA = 150 W/K), the TCS is considered to have infinite capacity. After the simulation, the maximum state of charge is used as the capacity of the TCS, which in turn determines the TCS volume.

With this thermochemical material (K_2CO_3 + vermiculite composite) and an assumed bulk porosity of 50%, TCS volumes are obtained in the range 0 m^3 to 20 m^3, i.e. TCS energy storage capacities up to 2800 kWh (**Figure 113**). With the unconstrained TCS sizing method, the volumes tend to increase with either higher PV powers or higher dwelling heat losses.

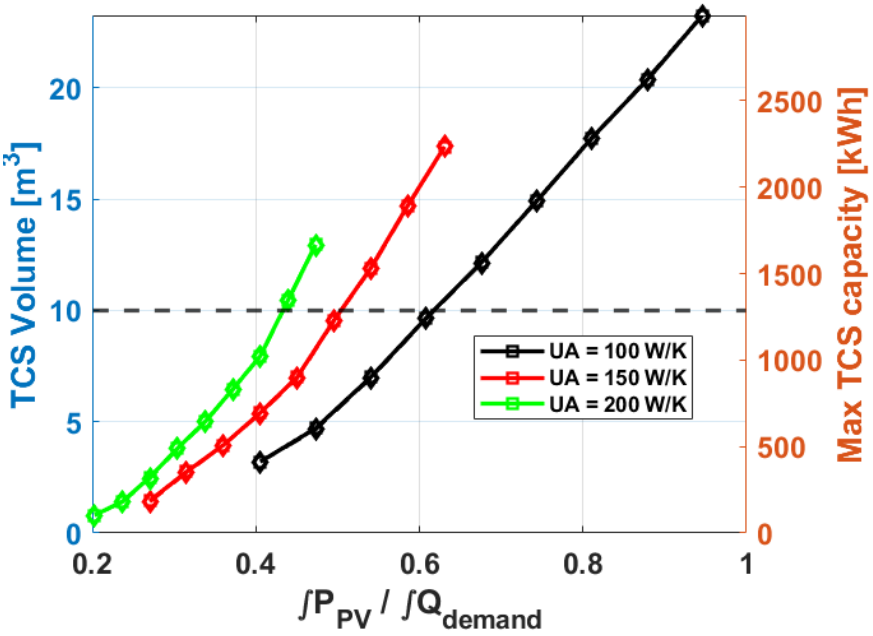

Figure 113 Impact of the ratio of solar PV energy to heat loss on the TCS final volume and heat storage capacity, with unconstrained TCS sizing method. The dotted line represents the typical maximum value of 10m^3 recommended for residential TCS.

However, while the peak maximum energy capacity that could be stored with this sizing method increases with the ratio of PV energy to building energy losses, the actual fraction of space heating covered by heat released from TCS levels out. This trend can be seen in **Figure 114a**. For UA – 100 W/K (lowest heat loss in the design space), the contribution of the TCS caps at a PV power of 5.5 kW for a TCS solar fraction between ~ 35% and 40%. If larger PV systems (beyond 7 kW) had been included, this same plateau would also be observed for the higher heat losses. These results highlight the maximum energy storage capacity beyond which TCS will not further contribute, as the additional energy capacity will not be used at often as the rest of the storage. For the UA = 100 W/K maximum total solar fractions around 60% were achieved in the design space. As will be seen in the economic analysis, these marginal gains do not justify the increase in capital cost from the larger PV system and TCS. To avoid this issue, the TCS/P2H/PV system performance was simulated with a TCS volume limited to 10 m^3 which, in the author's view, is a reasonable size storage for dwellings. The TCS could be buried in a garden or placed in the basement of a large enough dwelling.

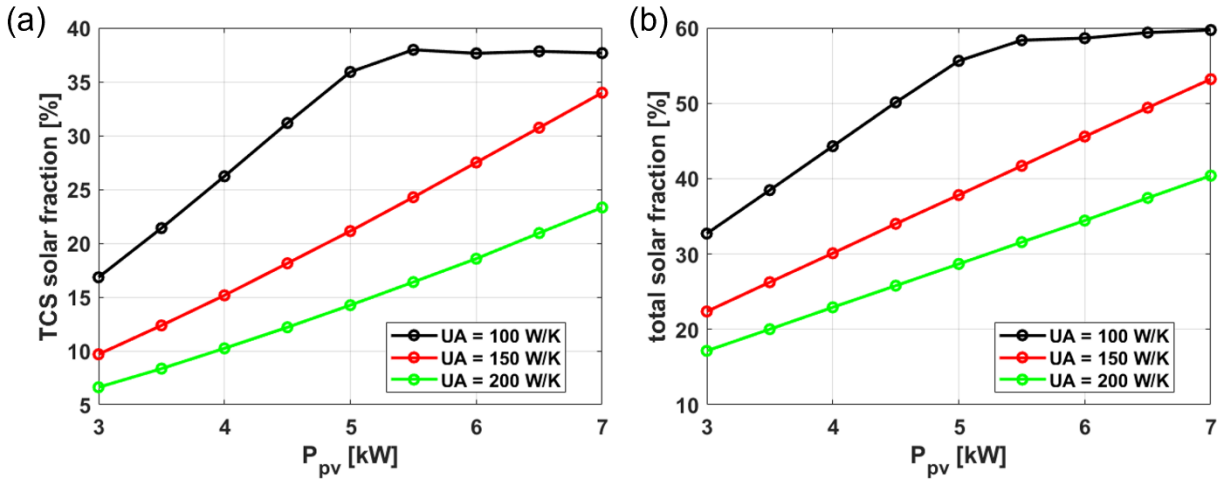

Figure 114 Impact of the ratio of solar PV energy to heat loss on the (a) TCS solar fraction (fraction of total heat demand covered by heat discharged from the TCS) and (b) total solar fraction, with unconstrained TCS volume sizing strategy.

Fixed TCS volume (10 m^3)

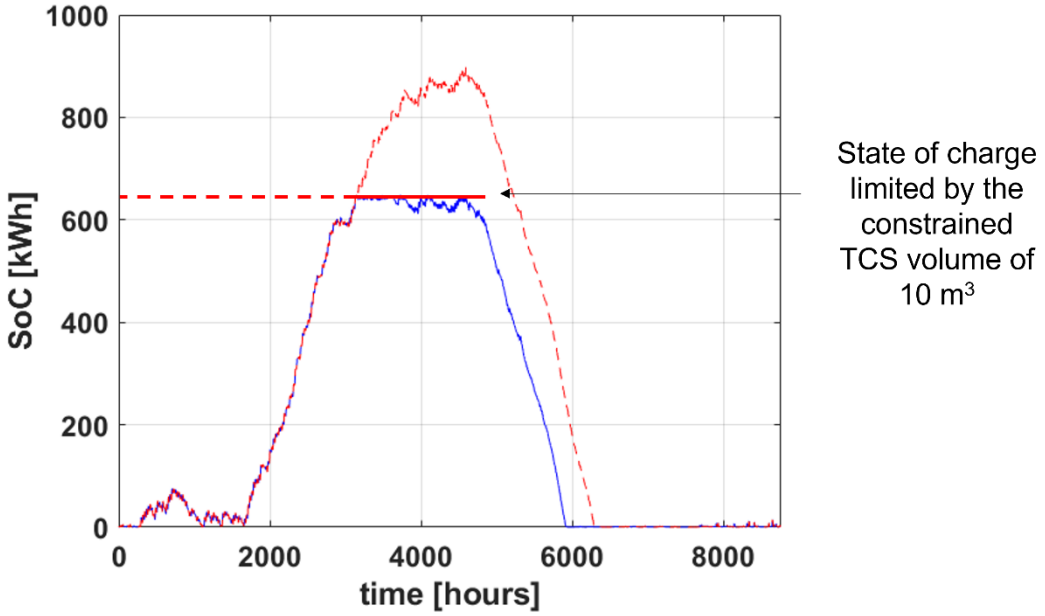

Figure 115 Fixed TCS sizing concept: during the simulation (5 kW solar PV and UA = 150 W/K), the TCS is considered to have a 10m^3. The unconstrained state of charge in the reference is shown for comparison (red curve).

From a technical performance aspect, constraining the TCS volume to 10m^3 within the same design space lowers total solar fraction of the space heating demand compared to an unconstrained method, due to the lower total amount of energy stored and delivered throughout the year (**Figure 115**). While a maximum total solar fraction of 60% was achieved with the unconstrained TCS, the same systems achieve ~30% TCS solar fraction and ~50% total solar fraction with fixed TCS volume (**Figure 116**). From these results, the main question to address is how the limited volume induced change to the total stored/released energy affect the economics of the system, which is explored in the next section.

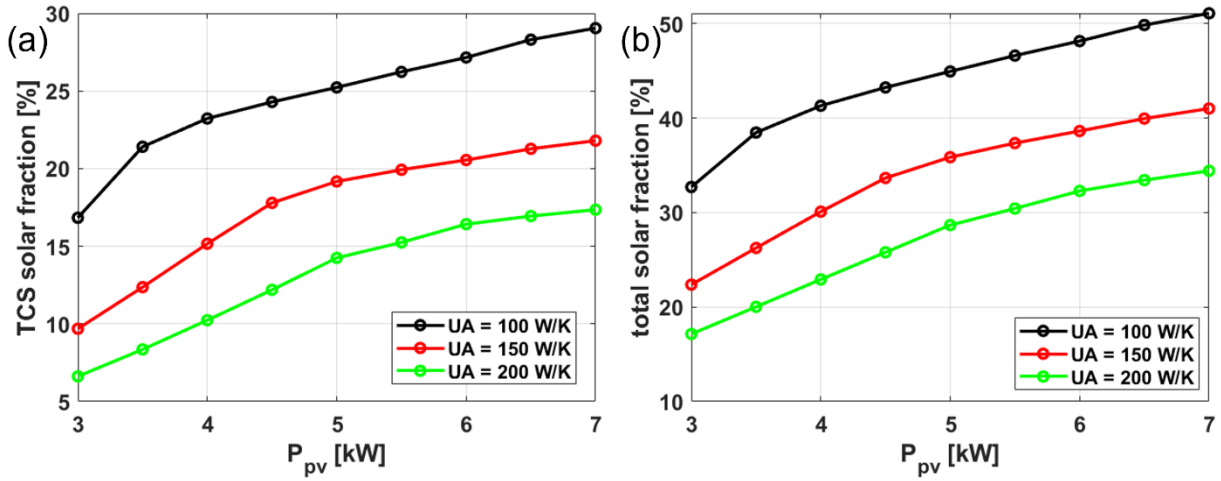

Figure 116 Impact of the ratio of solar PV energy to heat loss on (a) the TCS solar fraction and (b) the total solar fraction, with fixed TCS volume (10m^3) sizing strategy.

4.3 Economic performance

LCOE methodology and initial costs estimation

In the economic analysis the cost and return of integrating the solar photovoltaic system, P2H and TCS along with the auxiliary components are considered. The hydronic heating system, including water boiler and underfloor heating are assumed to be already present. The elements of the system that are included in the analysis are shown schematically in **Figure 117**.

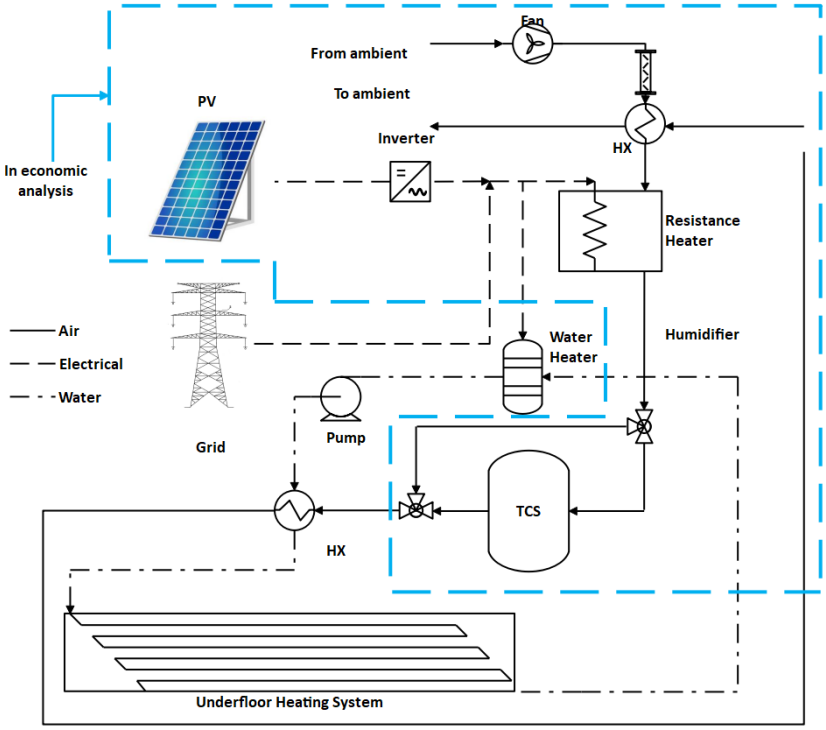

Figure 117 Boundaries of the economic analysis: components within the dashed blue shape are included in the analysis.

An estimation of the economic viability of the proposed TCS/P2H/PV system was carried out using the levelized cost of energy (LCOE, see **equation (98)**) method. With LCOE one can evaluate the actual cost of generating energy / electricity, and compare with other systems irrespectively of their size, capital costs and lifetime. LCOE implies that the cost and output of the electricity generation system (PV system) are included in the analysis along with the costs and outputs of the entire system which is the PV system combined with the TCS storage. Levelized cost of energy is to be distinguished from levelized cost of storage (LCOS) which only accounts for the storage and heat delivered from the storage. In this case (LCOE) the cost and energy output of the PV system are included in the analysis.

$$LCOE = \frac{NPV\ cost}{NPV\ output} = \frac{I + \sum_{t=1}^{n} \frac{O\&M}{(1+r)^t}}{\sum_{t=1}^{n} \frac{E_t}{(1+r)^t}} \quad (98)$$

Where I is the initial capital expenditure, $O\&M$ the yearly operation and maintenance costs of the system (which were assumed to be 3.5% of the initial investment, and no growth of these costs was assumed), E_t the amount of generated energy per year (in the case of LCOE this includes electrical energy generated directly by the PV system and converted to heat, and heat discharged from the storage), t the year number after the initial year, n the system's estimated lifespan (30 years), and r

the discount factor (5%). There are no fuel costs (the fuel in this system is renewable solar energy converted to electricity by the solar PV).

The initial capital expenditure I calculation includes the costs of the reactor C_{TCS} (casing, material, piping, secondary components and installation), the fan C_{Fan}, the solar PV system C_{Inv}, the power inverter, and the power-to-heat component C_{P2H} (**equation (99))**.

$$I = C_{Fan} + C_{PV} + C_{P2H} + C_{TCS} \tag{99}$$

Fans, PV systems and heaters are common process units for which estimating capital costs is relatively simple. The cost of the fan C_{Fan} was estimated by regressing fan and air blower values for various power ratings. Photovoltaic system costs C_{PV} were assumed to include cost of the solar panels, solar power inverter, additional components, and installation. C_{PV} determined using estimates of solar PV costs by official statistics from the UK government [242]. Using the average value for the year 2020/2021, solar PV for installations between 4 kW and 10 kW costs 1960 €/kW. Cost of the power-to-heat component C_{P2H} was estimated by obtaining costs for in line air duct heaters at various power ratings from an air duct equipment supplier [243]. The regression is shown in **equation (100)**.

$$C_{P2H} = 140.535 + 0.0698 * P_{P2H} \tag{100}$$

One of the main challenges in the economic analysis is the estimation of TCS investment costs C_{TCS}. TCS is an immature technology, and the lack of data limits estimation of overall capital cost of TCS systems. An economic climate was assumed for TCS installation related to its capacity cost, $C_{TCS-kWh}$ [€/kWh], which encompasses all of the costs relating to the reactive material, reactor construction/installation, instrumentation, and piping helps translate the energy storage capacity of the TCS E_{TCS} [kWh] into its capital cost. Thus the initial investment for the TCS is calculated with a linear function of the TCS capacity E_{TCS} and TCS capacity cost $C_{TCS-kWh}$.

$$C_{TCS} = E_{TCS} C_{TCS-kWh} \tag{101}$$

In the following sections, the cost of TCS installation was assumed to be $C_{TCS-kWh}$= 20 €/kWh. However at the end of the chapter the impact of this TCS capacity cost on LCOE of the system will be analysed.

Economics of the system with unconstrained TCS sizing

The economic performance is first shown for the TCS/P2H/PV system for which the TCS volume was unconstrained, i.e. the charging capacity is initially assumed to be unlimited, and the TCS is sized to match the maximum state of charge during the simulation (the different TCS volumes in the design space can be recalled in **Figure 113**). With a linear scaling of the costs of PV and TCS, the NPV of the costs scales linearly with the PV rating in the range of 30,000 to 40,000 € (**Figure 118a**). On the

other hand, the net present value of the energy outputs of the system plateaus out after a threshold value for PV power, since the TCS can only increase the contribution of solar energy to space heating to a certain extent. This extent depends on the ratio of generated energy by the PV system with the heat losses from the building envelope (**Figure 118b**).

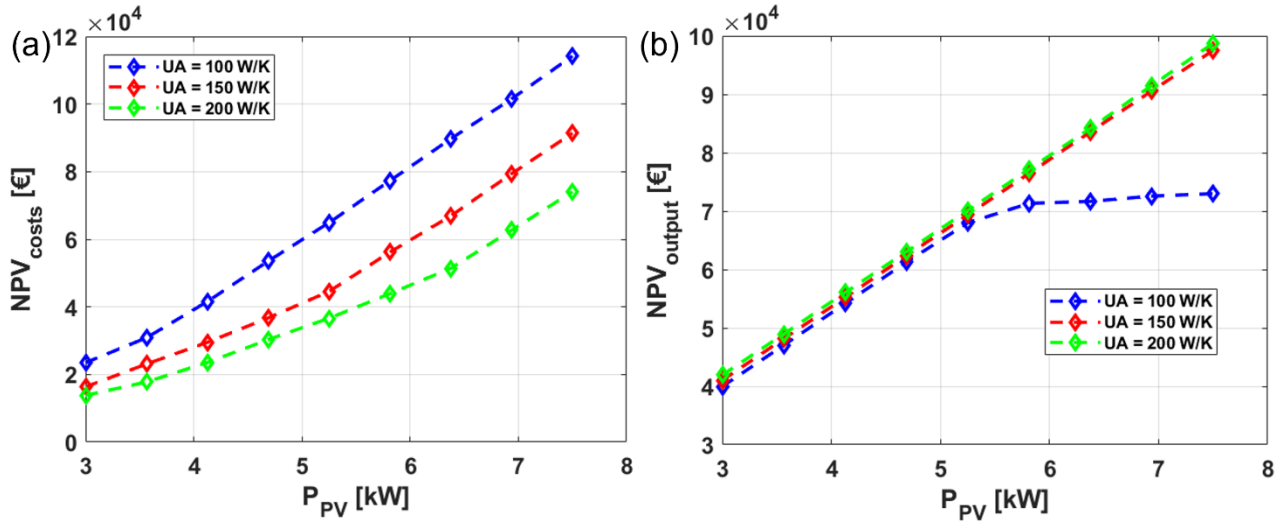

Figure 118 Effect of PV power rating and building heat loss coefficient on (a) net present value of the system costs and (b) net present value of outputs, with unconstrained TCS sizing.

Increasing the PV power rating logically results in increased capital costs for the PV system, for the TCS and consequently for the whole system. On the other hand, beyond a certain threshold the contribution of solar heat to space heating demand no longer increases. Thus, the ratio of NPV of costs to NPV of system energy output increases, which results in an increasing LCOE for the entire system (**Figure 119**). With the unconstrained sizing method, the total capital costs of the TCS are found to outweigh the economic benefits of the contribution of the system. With such a method it would cost money to the user to produce electrical energy with this system. These results highlight the necessity to select a specific volume for the TCS which will likely be optimal for a specific dwelling, with its overall heat loss coefficient, and solar PV system size.

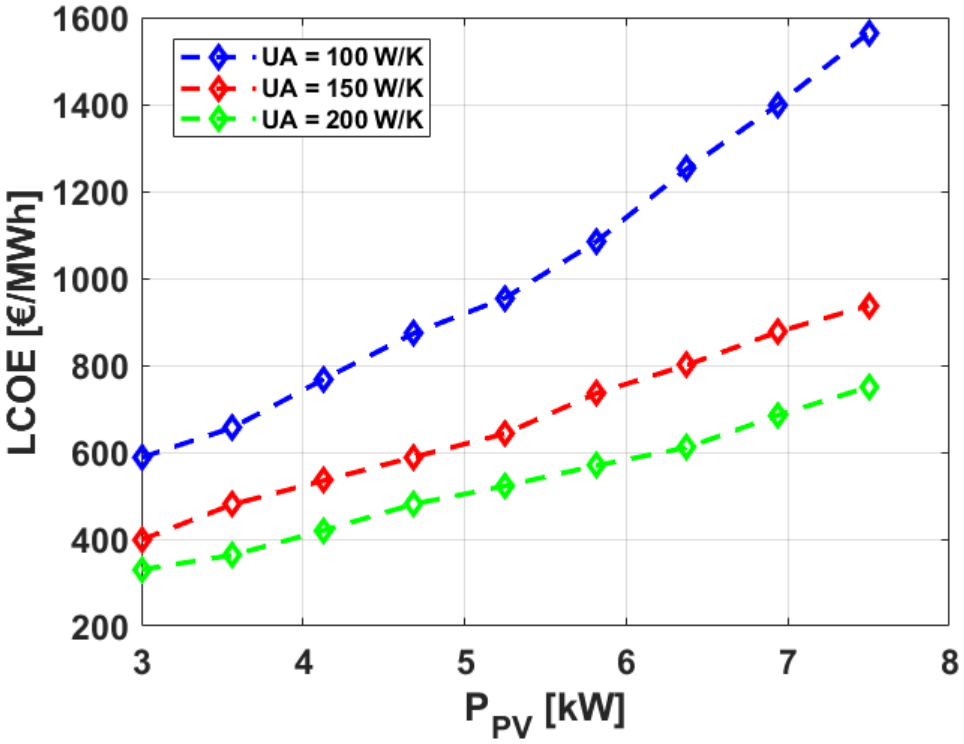

Figure 119 LCOE of the TCS/P2H/PV system as a function of PV power rating and building heat loss, with unconstrained TCS sizing.

System economics with TCS volume constrained to 10m^3

By leaving the TCS volume unconstrained, the costs of a TCS installation with increased PV power rating due to larger amounts of energy to be stored leads to an economically ineffective system. By constraining the TCS volume, one can identify a system in the design space where the total gains from the energy stored compared to the total capital cost are optimal.

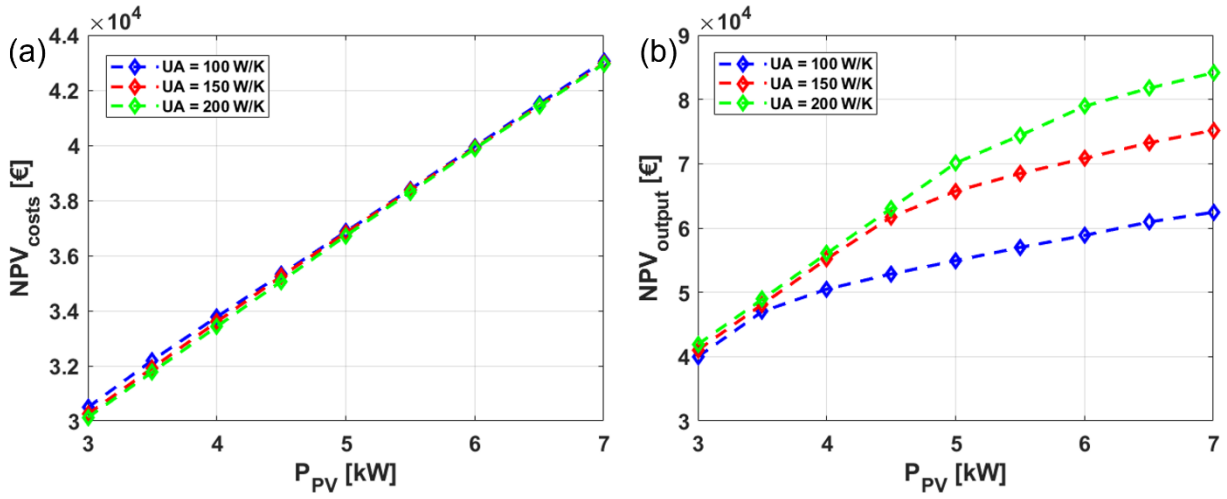

Figure 120 Effect of PV power rating and building heat loss coefficient on net present value of the system costs, with constrained TCS sizing to 10 m^3.

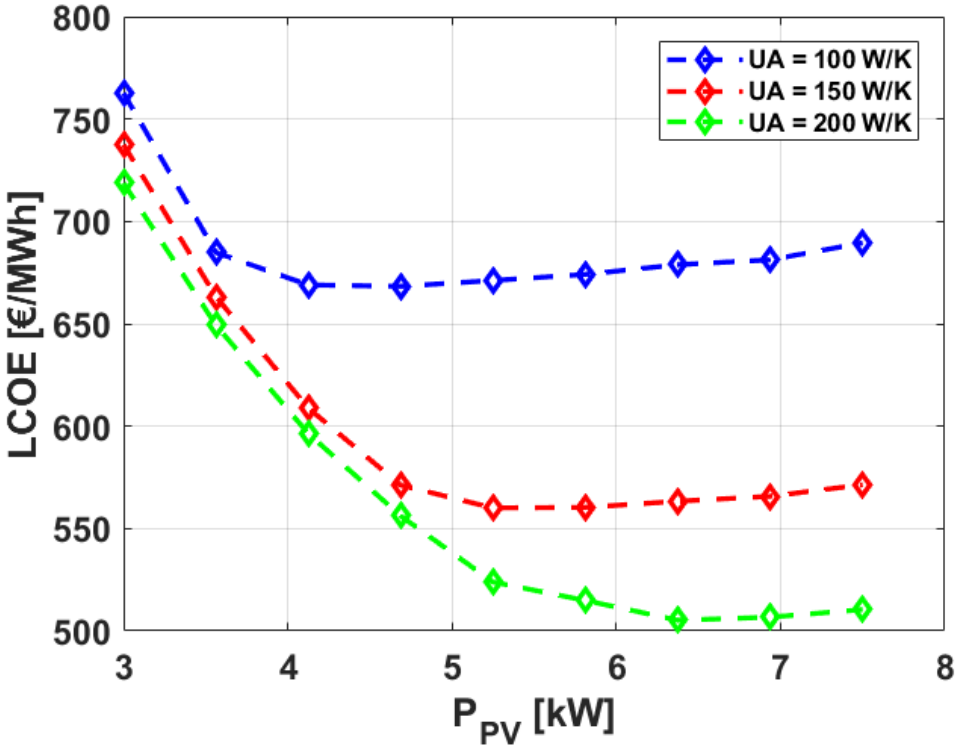

Figure 121 LCOE of the TCS/P2H/PV system as a function of PV power rating and building heat loss, with TCS sizing constrained to 10m^3. TCS capacity costs at 20 €/kWh. Colored dots on the P_{pv} axis show the optimal PV power rating for each dwelling to maximize TCS economic viability.

Combining a fixed volume TCS with solar PV/P2H means that below a specific value of PV power the TCS isn't used to its full capability, which is reflected in the LCOE of the system (**Figure 121**). With increasing PV power, a larger amount of electrical energy is produced in excess of the instantaneous space heating which can be stored in the TCS and used later. However, the fixed TCS volume also means that there is a threshold PV power value beyond which the TCS cannot further store any more energy, even with increased generation capabilities. The increasing PV size leads to increasing PV costs without further increasing the amount of space heating demand covered by the TCS (direct PV usage also flattens out). LCOE increases as a result. **Figure 121** clearly shows that for a specific dwelling (i.e. heat loss coefficient) there is an optimal PV rating that maximises the 10m^3 TCS usage with the lowest PV cost, and therefore minimises LCOE. At UA = 100 W/K the optimal PV power is between 4 kW and 4.5 kW for an LCOE ~670 €/MWh, whereas for UA = 200 W/K this optimal PV power is ~6.5 kW for which an LCOE of 500 €/MWh is achieved.

The magnitude of the LCOE calculated and presented in the results so far is dependent on the economic climate for the capital costs of TCS. Up until now, a specific capacity cost for TCS of 20 €/kWh was assumed. The effect of the TCS costs on the LCOE of the fixed volume TCS/P2H/PV system is shown in **Figure 122**. Decreasing the TCS costs leads the LCOE to converge towards a minimum value of around ~240 €/MWh which represents the NPV of system costs without the TCS (or with an extremely cheap TCS).

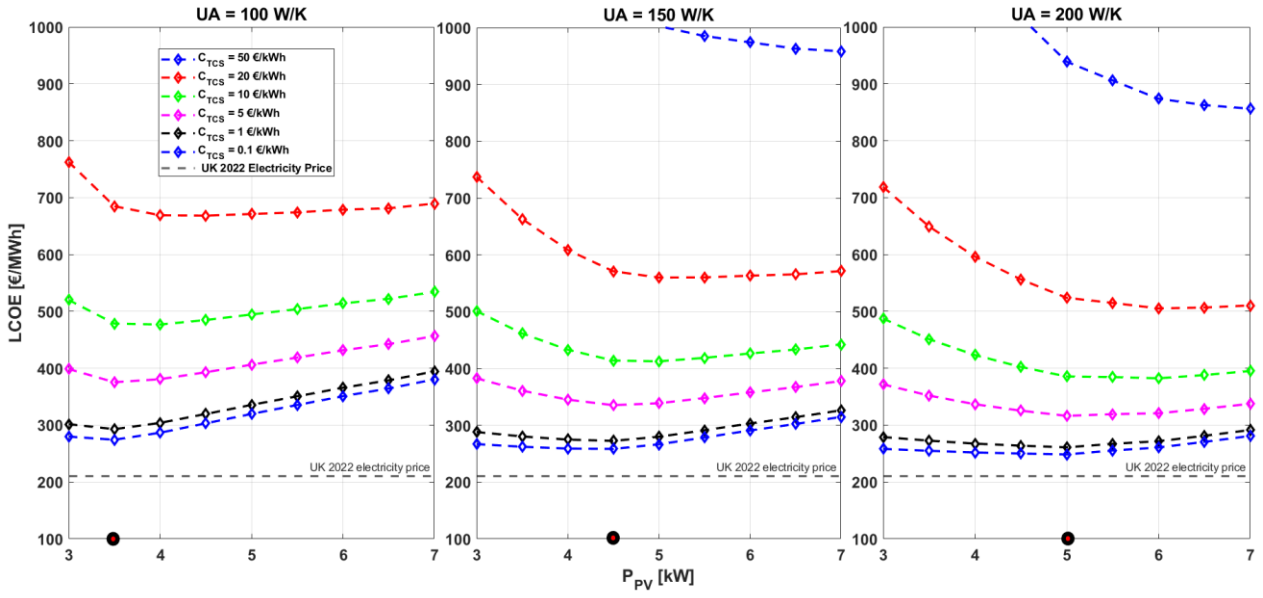

Figure 122 LCOE of the TCS/P2H/PV system for the investigated range of PV system power ratings and building heat loss coefficient, under various economic scenarios for TCS costs.

According to the results, with TCS costs below ~10 €/kWh the system would be expected to produce energy at a cost below 500 €/MWh, regardless of UA and PV power rating. With TCS costs below 1 €/kWh the cost of energy would be similar to current electricity prices in the UK [ref], with the added

advantage of being from a decarbonised energy source i.e. minimal CO2 emissions and increased independence from the grid. As a reference point, the U.S. department of energy aims for system-level TCS to cost below 15 $/kWh = 14.24 €/kWh [241].

The analysis has shown that a 10m^3 TCS seasonally storing heat converted through some power-to-heat from PV-generated electricity, with residential space heating as the end use, has the potential to be economically viable. With a careful balance between TCS size, PV rating and dwelling heat loss the presence of the TCS could more than double the solar fraction of the space heating demand; in the case of a 5 kW PV system with a heat loss coefficient 150 W/K, the solar fraction was increased from 17% (direct PV usage) to 38%. 62% of the space heating demand would still have to be provided by auxiliary sources (purchasing electricity from the grid). However TCS and power-to-heat clearly open the possibility to meaningfully increase the contribution of solar PV in domestic space heating systems. This potential is further increased with the prospect of volumetrically heated reactors through alternative P2H methods.

The main condition for economic viability according to this analysis are the specific costs of TCS which should be below ~20 €/MWh to achieve LCOE below 400 €/MWh. At TCS costs below 5 €/MWh, energy production costs would be around 300 €/MWh, slightly above current UK electricity prices, but with the added advantage of being free of CO_2 emissions and independent from the grid.

5 Conclusions

In this chapter, the viability of coupling conventional thermochemical energy storage with electrically heated chemical reactors was evaluated as an option to increase the penetration of renewable power generation and potentially circumvent the typical limitations of TCS when coupled with solar thermal. First, an overview of the available methods to electrically heat reactors was presented. This overview consisted in a presentation of the physical phenomena, a review of the existing reactor designs and prototypes for ohmic reactors (*conventional indirectly heated reactors*) and microwave / radiofrequency heated reactors (*volumetric directly heated reactors*), and a demonstration with the evidence from the literature that inorganic salt desorption can be carried out with such methods. A modelling strategy for both types of electrically heated reactors was developed, highlighting the effect of either indirect or direct heating on reactor performance. Finally, the techno-economic potential of integrating TCS in residential applications via a coupling with power-to-heat and residential solar photovoltaics was assessed.

- Electrified chemical reactors are either *indirectly conventionally heated*, where electrical energy is converted to thermal energy by means of a fluid passing through an ohmic resistance heater, or *directly volumetrically heated*, with heat generated directly in the reactor via electromagnetic conversion. *Direct volumetric heating* can be further subdivided into microwave heating or radiofrequency heating. Inorganic salts and SIMs can be desorbed with either of these volumetric heating methods. Microwave driven reactors were found in the literature in the 1 kW to 6 kW heating power range; their reactive volumes are limited due to

the low penetration depth of microwaves. However this limitation opens the door to moving bed reactors which transport the solid material to and from the reactive area and can process large amounts of material despite the low reactor volume. Radiofrequency heating can theoretically allow for larger reaction zones due to the deeper penetration of radiofrequency waves compared to microwaves, however from a technological standpoint these reactors are still only available at very small scale.

- Models for TCS desorption were presented through either *indirect conventional heating* or *direct volumetric heating*. The behaviour of the former reaction is similar to conventional TCS with thermal energy added to the fluid flow upstream of the reactor, whereas the latter departed from this conventional behaviour. *Direct volumetric heating* was characterised by an initial lack of reaction front since all sections of the reactor are heated simultaneously. Heat is also provided conventionally by recovering the unused heat at the exit of the reactor and returning it to the reactor inlet, which led to a reaction front in the latter stages of the reaction.

- An electrically driven TCS with *indirect conventional heating* was integrated in a domestic space heating system with solar PV, to form a so-called TCS/P2H/PV system. With a $10m^3$ TCS, the system achieved approximately 40% to 60% PV self-consumption, more than doubling PV self-consumption without the storage, and energy storage densities around 60 – 80 kWh/m^3. This energy storage density could be improved by increasing the fraction of salt in the composite material, or by using a higher enthalpy salt such as $MgSO_4$. With the LCOE method, the cost of producing electricity with these systems was calculated in the range of 400 €/MWh to 600 €/MWh depending on the size of the PV system and heat demand of the dwelling. The analysis showed potential viability of such systems which was strongly dependent on the capital cost for TCS installation, which should ideally be reduced to less than 5 €/kWh.

Chapter VI. Conclusions

1 Summary and contributions

The overarching aim of this thesis was to develop the current understanding of the multiscale dynamic behaviour of low-temperature TCS with composite materials, during both steps of the heat storage cycle, and how overall system performance could be affected. Key research questions were formulated in **Chapter I**, and the following subsection presents how the contributions of this thesis address these research questions.

- Q1: What are typical materials used for low-temperature TCS? What kinetic models exist to capture their dynamic reaction behaviour at material and reactor scale?

A comprehensive review of the current candidate inorganic salts for TCS and existing kinetic studies of these inorganic salts' hydration and dehydration was carried out and presented in **Chapter II**. An analysis of the available literature revealed the lack of fundamental knowledge surrounding:
(a) the physical mechanisms controlling the hydration behaviour of inorganic salts,
(b) the influence of the so-called host matrix on these physical mechanisms,
(c) the best solid-state kinetic models for predicting the hydration behaviour of TCMs. Most studies involving hydration kinetics of inorganic salts take an order-based approach in modelling reaction kinetics.
These knowledge gaps in the TCS literature motivated the work presented in **Chapter III** and **Chapter IV**.

- Q2: What is the impact of salt impregnation on the kinetic behaviour during salt hydration? How is the choice of kinetic model affected by the impregnation of the salt to a host matrix?

Chapter III presented the kinetic study of the hydration of four promising TCMs through the framework of solid-state kinetic analysis: potassium carbonate K_2CO_3, magnesium chloride $MgCl_2$ and composites formulated through their integration into a vermiculite matrix. Thermogravimetric experiments were carried out in a Dynamic Vapour Sorption apparatus. The hydration behaviour was investigated through a hybrid experimental / numerical methodology constructed and presented in this work. Analysis of the raw thermogravimetric data and numerical fitting of relevant solid-state kinetic models to that data were coupled to evaluate the rate-limiting process of these hydration reactions, and the accuracy and validity of solid-state kinetic models in predicting the experimental behaviour was assessed.

The hydration of K_2CO_3 was found to be severely hindered by an apparent diffusion barrier at the sample level. The existence of a diffusion barrier was uncovered from the analysis of the raw gravimetric data and by observing that the final amount of hydrated material scaled with the volume of the salt sample and a simple geometrical analysis of the conical sample holder of the DVS.

However, impregnation of K_2CO_3 into vermiculite led to a significant increase in the hydration reaction rate, which was found to be controlled, according to the model-fitting results, by nucleation at 25°C and by phase-boundary control at 40°C. Despite the relatively low energy storage density of potassium carbonate, the results indicated that integration of K_2CO_3 to a host matrix is essential for performance. The hydration of $MgCl_2$ did not appear to be purely hindered by any intra-particle level mechanism, but rather by a combination of bulk and particle diffusion, and complete hydration was achieved. This reaction was found to be best modelled by first-order models and solid-state models of the diffusion class. Integration into a vermiculite, however, at a 50% mass ratio led to 5 to 10 times higher reaction rates, and numerical results of model fitting indicate that the hydration is controlled by intra-particle phenomena, highlighting the clear shift in control mechanism induced by matrix integration.

For both salts, integration into the host matrix alleviates the impact of bulk (interparticle) physical phenomena as a controlling mechanism; water vapour transport between TCM particles is significantly improved and shifts the overall reaction control to the particle scale, leading to faster reaction times, and consequently improved power output. The kinetic modelling of $MgCl_2$ hydration was not significantly affected by matrix inclusion: for both salt and composite, diffusion D3 and D4, and geometrical contraction model R3 accurately predicted hydration behaviour. A notable change is the lower precision of F1 in modelling the composite behaviour. Thus the often favoured F1 first-order model was found to be more suited to the pure salt than the composite in the case of $MgCl_2$. The hydration of K_2CO_3 departs from conventional behaviour due to the presence of a diffusion barrier; as a result none of the selected kinetic models accurately reflect its behaviour. On the other hand, the hydration of K_2CO_3 in vermiculite was well modelled by nucleation and growth models A3 and A4 at 25°C, and by R2, R3 and F1 at 40°C which reflect the analysed rate limiting processes. Overall, standard solid-state kinetic models are well-suited to both pure salt (provided the reaction is not hindered by a diffusional barrier) and vermiculite-based composites hydration. The precision of specifically F1 was found to be both dependent on the material and the hydration conditions.

- Q3: What impact does the selected thermochemical material (TCM) and the reaction kinetics have on the performance of a sorption-based low-temperature TCS process?

In order to evaluate the impact of the reaction kinetics and TCM selection on the performance of TCS processes, a simple dynamic quasi-1D TCS reactor model was developed where the thermophysical properties, reaction kinetics and matrix properties are accounted for. This work was carried out in **Chapter IV**. The reactor model was validated and found to be accurate for TCM amounts ~10^1-10^2 kg. The reactor model was coupled to process unit models, and the TCS process was assumed to be integrated into a dwelling equipped with solar thermal collectors as the heat source. Techno-economic performance of the TCS process was evaluated through key performance indicators.

It was found that in various European locations, open hydration without forced humidification led to low temperature rises (ΔT below 25K) of the transport medium, air, which in turn led to poor values of key performance indicators. The best performing TCS processes were those using K_2CO_3 or $MgCl_2$

based composites, which showed sufficient techno-economic performance with temperature lifts above 20K in low humidity conditions. These two materials' performances can be explained by (a) low equilibrium pressure compared to most of the investigated inorganic salts and (b) their specific capacity costs below 1.5 €/kWh. Strontium bromide showed good technical performance with an 18 K temperature lift at 1200 Pa and energy storage density ~118 kWh/m^3, which was however offset by a high material cost (SCC = ~9.8 €/kWh) and impaired the economic potential of $SrBr_2$-based TCS processes. $MgSO_4$ based processes showed high energy storage density (> 250 kWh/m^3), however a temperature lift of ~12K was the lowest among the investigated materials.

Investigation of the effect of kinetic model and kinetic rate constant showed that increasing the kinetic rate constant results in an increase in volumetric power output and average temperature lift up to a certain point (approximately ~10^{-3} s^{-1} in the simulated scenario). Increasing the rate constant from 10^{-4} s^{-1} to 5.10^{-4} s^{-1} (two values typically found in the literature which are almost interchangeable) led to increasing volumetric power density by over 100%. Varying the selected kinetic model, from a selection of models determined experimentally using solid-state kinetic methodology, resulted in increases from 30% to 70% in volumetric power density and impacted the predicted useful energy storage density by up to ~5%. Thus, the work presented in this chapter highlighted the impact of material selection on the predicted discharge performance of a TCS system, and how clear identification of hydration reaction models and kinetic rate constants is essential to measure the viability of these systems.

- Q4: Can domestic solar photovoltaics or other electricity generation technologies be feasibly coupled to a low-temperature TCS system? Is combining solar photovoltaics and power-to-heat technologies with TCS technically and economically viable?

In **Chapter V** the technical and economic potential of coupling solar photovoltaics with low-temperature TCS with electrical energy conversion to thermal energy through power-to-heat technologies was investigated. The fundamentals behind power-to-heat methods, and potential applications in chemical reactors, were reviewed with the perspective of storing excess electrical energy with TCS. Study of the literature revealed that microwave-driven or radiofrequency-driven desorption (i.e. heat charge) in both physical and chemical sorbents is possible, and show higher reaction rates and lower temperatures than conventional heating. The penetration depth of microwaves could prove to be the main technical hurdle. Conveyor belt or circular moving bed reactors could be a solution to carry out volumetrically heated TCS.

TCS reactors with conventional heating of the inlet air flow and volumetric heating of the reactive bed were modelled. It was assumed that volumetric heating can be carried out on 10^1 10^2 kg amount of TCM. As expected, the conventionally heated reactor behaved similarly to solar thermal driven TCS. The volumetric heating, however, displayed unconventional profiles due to the combination of simultaneous heating and air flow carrying excess heat along the reactor. Temperatures were found to increase along the reactor, and the usual reaction front in conventional TCS was not observed here, with the level of reaction advancement of different segments of the TCS not proportional to their

distance from the inlet. In both cases, implementing heat recovery by preheating the inlet air flow during dehydration is imperative, as a non-negligible amount of the input heat can be retrieved as the reactor outlet. Dehydration efficiencies approximately ~75%-80% were achieved for conventionally heated reactors, and above 80% for volumetrically heated reactors.

Having evaluated the potential and practicalities of electrically heated sorption reactors, the TCS process model developed in **Chapter IV** was adapted to simulate a dwelling equipped with solar PV and underfloor heating and a P2H/TCS system. The techno-economic viability of such a system was investigated. The conventionally heated reactor and TCS process was integrated into a domestic space heating system to run a year-round simulation. With a TCS storage with volume fixed at $10m^3$, depending on the PV system power rating and heat loss of the dwelling, total solar fractions in the range 40% to 60% were achieved, with the TCS over doubling the solar fraction of the PV system without storage. This solar fraction only counted heat delivered above the minimum threshold temperature of 40°C for underfloor space heating, and also accounted for unused PV-generated energy due to insufficient power, to make sure these results are as conservative and non-optimistic as possible. The economics of the system were found to be highly dependent on the initial capital cost for TCS installation. For three dwellings with overall heat loss coefficients 100 W/K, 150W/K and 200 W/K, the optimal PV system to combine with a $10m^3$ TCS storage was 3.5 kW, 5.5 kW and 6.5 kW respectively, which with TCS installation costs below 20 €/kWh led to LCOEs between 400 €/MWh and 500 €/MWh. With TCS costs below 5 €/kWh, the LCOE could be below 400 €/MWh according to the model. Thus TCS, and specifically TCS with PV and power-to-heat, has the possibility to be economically feasible for residential applications, on the condition that capital costs for TCS are sufficiently low.

2 Recommendations

Analysis of the literature highlighted gaps in the knowledge surrounding TCS. Work carried out in this thesis attempted to address some of these areas where information is lacking. Some of the raised questions were answered, while others remain. The main approach was through the scope of reaction kinetics which are required knowledge for the time-dependent analysis of TCS. In particular, the work in this thesis helps bridge the gap between knowledge of the reaction behaviour at material scale, the intermediate process scale, and our understanding of system scale TCS. From the work carried out, the following recommendations are suggested for researchers in the field of salt-based low temperature TCS:

- The reaction kinetics of several inorganic salts should be investigated since many are still unknown. Comparison of the reaction kinetics between salts can then be carried out and the best materials can be discriminated on the basis of dynamic reaction performance. A similar issue exists for salt-in-matrix composites. More complex supporting matrixes are currently being developed (foams, metal-organic frameworks, encapsulation), yet the impact of impregnating even the simpler matrices with salt is largely unknown (the impact of

vermiculite was investigated in this thesis). Thus the rate at which kinetics of composites are analysed needs to increase to match the rate of new material development.

- The impact of material-scale kinetics on reactor and process performance was found to be non-trivial. Future research simulation should carry out an uncertainty analysis on the effect of kinetic rate and kinetic model on predicted performance. In these works the choice of kinetic model should be better justified, and predicated as much as possible on existing kinetic studies, particularly for relatively novel materials.

- The system techno-economics of TCS with power-to-heat were investigated, however many assumptions had to be made for the operational strategy of the TCS. One challenge that emerged was the discharge of the TCS to match specific heat demand power requirements. Future works on TCS should consider the operation strategy in relation to the heat sources / sinks of the considered application. Control strategies should be developed, in particular surrounding the power output of TCS during discharge through the humidity/mass flow rate of the air flow used to hydrate the TCM.

- The technical and economic performances evaluated in **chapters IV** and **V** should be better compared to equivalent studies with different types of seasonal thermal energy storage for dwellings. A clear framework for the evaluation of long term energy storage with solar should be formulated, to enable the fair and pragmatic comparison of different technologies and/or system configurations.

References

[1] Krinner G, Germany F, Shongwe M, Africa S, France SB, Uk BBBB, et al. Long-term climate change: Projections, commitments and irreversibility. Clim Chang 2013 Phys Sci Basis Work Gr I Contrib to Fifth Assess Rep Intergov Panel Clim Chang 2013;9781107057:1029–136. https://doi.org/10.1017/CBO9781107415324.024.

[2] European Commission. State of the Energy Union 2021 – Contributing to the European Green Deal and the Union's recovery 2021:31.

[3] European Commission. EU Energy in figures. 2021. https://doi.org/10.2833/87498.

[4] Kato Y, Nomura T. Thermal and Thermochemical Storage. Issues Environ Sci Technol 2019;2019-Janua:210–27. https://doi.org/10.1039/9781788015530-00210.

[5] Pfenninger S, Staffell I. Long-term patterns of European PV output using 30 years of validated hourly reanalysis and satellite data. Energy 2016;114:1251–65. https://doi.org/10.1016/j.energy.2016.08.060.

[6] IEA. Energy Technology Perspectives 2020. Energy Technol Perspect 2020 2020. https://doi.org/10.1787/ab43a9a5-en.

[7] Ease/Eera. European Energy Storage Technology Development Roadmap - 2017 Update. 2017 2017:128.

[8] Eaborn C. Compendium of chemical Terminology: IUPAC Recommendations. vol. 356. 1988. https://doi.org/10.1016/0022-328x(88)83113-9.

[9] Ruthven DM. Principles of adsorption and adsorption processes. vol. 4. 1985. https://doi.org/10.1016/0167-6989(85)90037-6.

[10] N'Tsoukpoe KE, Liu H, Le Pierrès N, Luo L. A review on long-term sorption solar energy storage. Renew Sustain Energy Rev 2009;13:2385–96. https://doi.org/10.1016/j.rser.2009.05.008.

[11] Koohi-Fayegh S, Rosen MA. A review of energy storage types, applications and recent developments. J Energy Storage 2020;27:101047. https://doi.org/10.1016/j.est.2019.101047.

[12] Desai F, Prasad S, Muthukumar P, Mustafizur M. Thermochemical energy storage system for cooling and process heating applications : A review. Energy Convers Manag 2021;229:113617. https://doi.org/10.1016/j.enconman.2020.113617.

[13] Scapino L, Zondag HA, Van Bael J, Diriken J, Rindt CCM. Sorption heat storage for long-term low-temperature applications: A review on the advancements at material and prototype scale. Appl Energy 2017;190:920–48. https://doi.org/10.1016/j.apenergy.2016.12.148.

[14] Rindt CCM, Gaastra-Nedea S V. Modeling thermochemical reactions in thermal energy storage systems. Woodhead Publishing Limited; 2014. https://doi.org/10.1533/9781782420965.3.375.

[15] Scapino L, Zondag HA, Van Bael J, Diriken J, Rindt CCM. Energy density and storage capacity cost comparison of conceptual solid and liquid sorption seasonal heat storage systems for low-temperature space heating. Renew Sustain Energy Rev 2017;76:1314–31. https://doi.org/10.1016/j.rser.2017.03.101.

[16] Mamani V, Gutierrez A, Ushak S. Development of low-cost inorganic salt hydrate as a thermochemical energy storage material. Sol Energy Mater Sol Cells 2018;176:346–56. https://doi.org/10.1016/j.solmat.2017.10.021.

[17] Okhrimenko L, Favergeon L, Johannes K, Kuznik F, Pijolat M. Thermodynamic study of MgSO4 – H2O system dehydration at low pressure in view of heat storage. Thermochim Acta 2017;656:135–43. https://doi.org/10.1016/j.tca.2017.08.015.

[18] Glasser L, Jenkins HDB. The thermodynamic solvate difference rule: Solvation parameters

and their use in interpretation of the role of bound solvent in condensed-phase solvates. Inorg Chem 2007;46:9768–78. https://doi.org/10.1021/ic701105p.
[19] Donkers P, Sögütoglu LC, Huinink H, Fischer H, Adan OCG. A review of salt hydrates for seasonal heat storage in domestic applications. Appl Energy 2017;199:45–68. https://doi.org/10.1016/j.apenergy.2017.04.080.
[20] Stengler J, Bürger I, Linder M. Thermodynamic and kinetic investigations of the SrBr2 hydration and dehydration reactions for thermochemical energy storage and heat transformation. Appl Energy 2020;277:115432. https://doi.org/10.1016/j.apenergy.2020.115432.
[21] Esaki T, Kobayashi N. Reaction Rate Characteristics of SrBr2 Hydration System for Chemical Heat Pump Cooling Mode. J Mater Sci Chem Eng 2016;04:106–15. https://doi.org/10.4236/msce.2016.42012.
[22] Shizume K, Hatada N, Yasui S, Uda T. Multi-step hydration/dehydration mechanisms of rhombohedral Y2(SO4)3: A candidate material for low-temperature thermochemical heat storage. RSC Adv 2020;10:15604–13. https://doi.org/10.1039/d0ra02566f.
[23] Richter M, Habermann EM, Siebecke E, Linder M. A systematic screening of salt hydrates as materials for a thermochemical heat transformer. Thermochim Acta 2018;659:136–50. https://doi.org/10.1016/j.tca.2017.06.011.
[24] Steiger M, Linnow K, Juling H, Brüggerhoff S, Kirchner D. Hydration of MgSO4·H2O and Generation of Stress in Porous Materials. Growth Cryst Des 2008:2–9.
[25] Sögütoglu LC, Steiger M, Houben J, Biemans D, Fischer H, Donkers P, et al. Understanding the Hydration Process of Salts: The Impact of a Nucleation Barrier. Cryst Growth Des 2019;19:2279–88. https://doi.org/10.1021/acs.cgd.8b01908.
[26] N'Tsoukpoe KE, Schmidt T, Rammelberg HU, Watts BA, Ruck WKL. A systematic multi-step screening of numerous salt hydrates for low temperature thermochemical energy storage. Appl Energy 2014;124:1–16. https://doi.org/10.1016/j.apenergy.2014.02.053.
[27] Aristov YI. New family of solid sorbents for adsorptive cooling: Material scientist approach. J Eng Thermophys 2007;16:63–72. https://doi.org/10.1134/S1810232807020026.
[28] Sögütoglu LC, Donkers P, Fischer H, Huinink H, Adan OCG. In-depth investigation of thermochemical performance in a heat battery: Cyclic analysis of K2CO3, MgCl2and Na2S. Appl Energy 2018;215:159–73. https://doi.org/10.1016/j.apenergy.2018.01.083.
[29] Beving MAJM, Frijns AJH, Rindt CCM, Smeulders DMJ. Effect of cycle-induced crack formation on the hydration behaviour of K2CO3 particles: experiments and modelling. Thermochim Acta 2020;692:178752. https://doi.org/10.1016/j.tca.2020.178752.
[30] Ferchaud CJ. Experimental study of salt hydrates for thermochemical seasonal heat storage. Thesis 2016.
[31] Linnow K, Niermann M, Bonatz D, Posern K, Steiger M. Experimental studies of the mechanism and kinetics of hydration reactions. Energy Procedia 2014;48:394–404. https://doi.org/10.1016/j.egypro.2014.02.046.
[32] European Commission. Study on the Eu's list of critical raw materials - Critical raw materials factsheets. 2020. https://doi.org/10.2873/11619.
[33] Zhao YJ, Wang RZ, Zhang YN, Yu N. Development of SrBr2composite sorbents for a sorption thermal energy storage system to store low-temperature heat. Energy 2016;115:129–39. https://doi.org/10.1016/j.energy.2016.09.013.
[34] Voort van de IM. Characterization of a thermochemical storage material. Master's Thesis 2007:58.
[35] Shkatulov A, Joosten R, Fischer H, Huinink H. Core–Shell Encapsulation of Salt Hydrates into Mesoporous Silica Shells for Thermochemical Energy Storage. ACS Appl Energy Mater

2020;3:6860–9. https://doi.org/10.1021/acsaem.0c00971.
[36] Posern K, Kaps C. Calorimetric studies of thermochemical heat storage materials based on mixtures of MgSO4 and MgCl2. Thermochim Acta 2010;502:73–6. https://doi.org/10.1016/j.tca.2010.02.009.
[37] Druske MM, Fopah-Lele A, Korhammer K, Rammelberg HU, Wegscheider N, Ruck WKL, et al. Developed materials for thermal energy storage: Synthesis and characterization. Energy Procedia 2014;61:96–9. https://doi.org/10.1016/j.egypro.2014.11.915.
[38] Gaeini M, Rouws AL, Salari JWO, Zondag HA, Rindt CCM. Characterization of microencapsulated and impregnated porous host materials based on calcium chloride for thermochemical energy storage. Appl Energy 2018;212:1165–77. https://doi.org/10.1016/j.apenergy.2017.12.131.
[39] Gordeeva LG, Aristov YI. Composites "salt inside porous matrix" for adsorption heat transformation: A current state-of-the-art and new trends. Int J Low-Carbon Technol 2012;7:288–302. https://doi.org/10.1093/ijlct/cts050.
[40] Dawoud B, Aristov YI. Experimental study on the kinetics of water vapor sorption on selective water sorbents, silica gel and alumina under typical operating conditions of sorption heat pumps. Int J Heat Mass Transf 2003;46:273–81. https://doi.org/10.1016/S0017-9310(02)00288-0.
[41] Zhu D, Wu H, Wang S. Experimental study on composite silica gel supported CaCl2 sorbent for low grade heat storage. Int J Therm Sci 2006;45:804–13. https://doi.org/10.1016/j.ijthermalsci.2005.10.009.
[42] Palomba V, Frazzica A. Recent advancements in sorption technology for solar thermal energy storage applications. Sol Energy 2018:1–37. https://doi.org/10.1016/j.solener.2018.06.102.
[43] Grekova AD, Gordeeva LG, Aristov YI. Composite "LiCl/vermiculite" as advanced water sorbent for thermal energy storage. Appl Therm Eng 2017;124:1401–8. https://doi.org/10.1016/j.applthermaleng.2017.06.122.
[44] Zhao H, Huang T, Liu T, Lei M, Zhang M. Synthesis of MgCl 2 /vermiculite and its water vapor adsorption-desorption performance. Int J Energy Res 2021:1–15. https://doi.org/10.1002/er.7188.
[45] Brancato V, Gordeeva LG, Sapienza A, Palomba V, Vasta S, Grekova AD, et al. Experimental characterization of the LiCl/vermiculite composite for sorption heat storage applications. Int J Refrig 2019;105:92–100. https://doi.org/10.1016/j.ijrefrig.2018.08.006.
[46] Zhang Y, Wang R, Li T, Zhao Y. Thermochemical characterizations of novel vermiculite-LiCl composite sorbents for low-temperature heat storage. Energies 2016;9. https://doi.org/10.3390/en9100854.
[47] Shkatulov A, Houben J, Huinink H. Stabilization of K2CO3 in expanded vermiculite for thermochemical energy storage. Renew Energy 2019:1–10. https://doi.org/10.1016/j.renene.2019.11.119.
[48] Zhang YN, Wang RZ, Zhao YJ, Li TX, Riffat S, Wajid NM. Development and thermochemical characterizations of vermiculite/SrBr2composite sorbents for low-temperature heat storage. Energy 2016;115:120–8. https://doi.org/10.1016/j.energy.2016.08.108.
[49] Aristov YI, Restuccia G, Tokarev MM, Buerger HD, Freni A. Selective water sorbents for multiple applications. 11. CaCl2 confined to expanded vermiculite. React Kinet Catal Lett 2000;71:377–84. https://doi.org/10.1023/A:1010351815698.
[50] Cammarata A, Verda V, Sciacovelli A, Ding Y. Hybrid strontium bromide-natural graphite composites for low to medium temperature thermochemical energy storage: Formulation, fabrication and performance investigation. Energy Convers Manag 2018;166:233–40. https://doi.org/10.1016/j.enconman.2018.04.031.

[51] Ousaleh HA, Sair S, Zaki A, Younes A, Faik A, El Bouari A. Advanced experimental investigation of double hydrated salts and their composite for improved cycling stability and metal compatibility for long-term heat storage technologies. Renew Energy 2020;162:447–57. https://doi.org/10.1016/j.renene.2020.08.085.
[52] van Ravensteijn BGP, Donkers P, Ruliaman RC, Eversdijk J, Fischer HR, Huinink H, et al. Encapsulation of Salt Hydrates by Polymer Coatings for Low-Temperature Heat Storage Applications. ACS Appl Polym Mater 2021. https://doi.org/10.1021/acsapm.0c01186.
[53] Mazur N, Salviati S, Huinink H, Fina A, Carosio F. Impact of polymeric stabilisers on the reaction kinetics of SrBr2. Sol Energy Mater Sol Cells 2022;238:111648. https://doi.org/10.1016/j.solmat.2022.111648.
[54] Calabrese L, Brancato V, Palomba V, Frazzica A, Cabeza LF. Innovative composite sorbent for thermal energy storage based on a SrBr 2 · 6H 2 O fi lled silicone composite foam. J Energy Storage 2019;26:100954. https://doi.org/10.1016/j.est.2019.100954.
[55] Zhang Y, Miao Q, Jia X, Jin Y, Li Z, Tan L, et al. Diatomite-based magnesium sulfate composites for thermochemical energy storage: Preparation and performance investigation. Sol Energy 2021;224:907–15. https://doi.org/10.1016/j.solener.2021.05.054.
[56] Yilmaz B, Yüksel B, Orhan G, Aydin D, Utlu Z. Synthesis and characterization of salt-impregnated anodic aluminum oxide composites for low-grade heat storage. Int J Miner Metall Mater 2020;27:112–8. https://doi.org/10.1007/s12613-019-1890-x.
[57] Tabard L, Prud'Homme E, Garnier V, Gremillard L. Hierarchical salt-ceramic composites for efficient thermochemical energy storage. Appl Mater Today 2020;20. https://doi.org/10.1016/j.apmt.2020.100658.
[58] Ait Ousaleh H, Sair S, Mansouri S, Abboud Y, Faik A, El Bouari A. New hybrid graphene/inorganic salt composites for thermochemical energy storage: Synthesis, cyclability investigation and heat exchanger metal corrosion protection performance. Sol Energy Mater Sol Cells 2020;215:110601. https://doi.org/10.1016/j.solmat.2020.110601.
[59] Zhang YN, Wang RZ, Li TX. Thermochemical characterizations of high-stable activated alumina/LiCl composites with multistage sorption process for thermal storage. Energy 2018;156:240–9. https://doi.org/10.1016/j.energy.2018.05.047.
[60] Hongois S, Kuznik F, Stevens P, Roux JJ. Development and characterisation of a new MgSO4-zeolite composite for long-term thermal energy storage. Sol Energy Mater Sol Cells 2011;95:1831–7. https://doi.org/10.1016/j.solmat.2011.01.050.
[61] Courbon E, D'Ans P, Permyakova A, Skrylnyk O, Steunou N, Degrez M, et al. A new composite sorbent based on SrBr2and silica gel for solar energy storage application with high energy storage density and stability. Appl Energy 2017;190:1184–94. https://doi.org/10.1016/j.apenergy.2017.01.041.
[62] Courbon E, D'Ans P, Skrylnyk O, Frère M. New prominent lithium bromide-based composites for thermal energy storage. J Energy Storage 2020;32:101699. https://doi.org/10.1016/j.est.2020.101699.
[63] Jabbari-Hichri A, Bennici S, Auroux A. Enhancing the heat storage density of silica–alumina by addition of hygroscopic salts (CaCl2, Ba(OH)2, and LiNO3). Sol Energy Mater Sol Cells 2015;140:351–60. https://doi.org/10.1016/j.solmat.2015.04.032.
[64] Sun Y, Spieß A, Jansen C, Nuhnen A, Gökpinar S, Wiedey R, et al. Tunable LiCl@UiO-66 composites for water sorption-based heat transformation applications. J Mater Chem A 2020;8:13364–75. https://doi.org/10.1039/d0ta03442h.
[65] Lou L, Xu M, Huai X, Huang C, Liu Z. Composite MWCNT/ MIL-101 (Cr)/CaCl2 as High-Capacity Water Adsorbent for Long-Term Thermal Energy Storage. Front Mater 2021;8:1–18. https://doi.org/10.3389/fmats.2021.653933.

[66] Liu H, Nagano K, Togawa J. A composite material made of mesoporous siliceous shale impregnated with lithium chloride for an open sorption thermal energy storage system. Sol Energy 2015;111:186–200. https://doi.org/10.1016/j.solener.2014.10.044.
[67] Christoph Lehmann. Towards the numerical modelling of salt/zeolite composites for thermochemical energy storage. 2018.
[68] Casey SP, Aydin D, Elvins J, Riffat S. Salt impregnated desiccant matrices for 'open' thermochemical energy conversion and storage – Improving energy density utilisation through hygrodynamic & thermodynamic reactor design. Energy Convers Manag 2017;142:426–40. https://doi.org/10.1016/j.enconman.2017.03.066.
[69] Casey SP, Elvins J, Riffat S, Robinson A. Salt impregnated desiccant matrices for "open" thermochemical energy storage - Selection, synthesis and characterisation of candidate materials. Energy Build 2014;84:412–25. https://doi.org/10.1016/j.enbuild.2014.08.028.
[70] Casey SP, Aydin D, Riffat S, Elvins J. Salt impregnated desiccant matrices for "open" thermochemical energy storage - Hygrothermal cyclic behaviour and energetic analysis by physical experimentation. Energy Build 2015;92:128–39. https://doi.org/10.1016/j.enbuild.2015.01.048.
[71] Cortés FB, Chejne F, Carrasco-Marín F, Pérez-Cadenas AF, Moreno-Castilla C. Water sorption on silica- and zeolite-supported hygroscopic salts for cooling system applications. Energy Convers Manag 2012;53:219–23. https://doi.org/10.1016/j.enconman.2011.09.001.
[72] Chan KC, Chao CYH, Sze-To GN, Hui KS. Performance predictions for a new zeolite 13X/CaCl2composite adsorbent for adsorption cooling systems. Int J Heat Mass Transf 2012;55:3214–24. https://doi.org/10.1016/j.ijheatmasstransfer.2012.02.054.
[73] Whiting GT, Grondin D, Stosic D, Bennici S, Auroux A. Zeolite-MgCl2composites as potential long-term heat storage materials: Influence of zeolite properties on heats of water sorption. Sol Energy Mater Sol Cells 2014;128:289–95. https://doi.org/10.1016/j.solmat.2014.05.016.
[74] Rehman AU, Iqbal M, Guan ZH, Shah MZ, Afzal W, Rasheed S, et al. Inorganic salt hydrates and zeolites composites studies for thermochemical heat storage. Zeitschrift Fur Phys Chemie 2021. https://doi.org/10.1515/zpch-2021-3012.
[75] Nonnen T, Preißler H, Kött S, Beckert S, Gläser R. Salt inclusion and deliquescence in salt/zeolite X composites for thermochemical heat storage. Microporous Mesoporous Mater 2020;303. https://doi.org/10.1016/j.micromeso.2020.110239.
[76] Xu JX, Li TX, Chao JW, Yan TS, Wang RZ. High energy-density multi-form thermochemical energy storage based on multi-step sorption processes. Energy 2019;185. https://doi.org/10.1016/j.energy.2019.07.076.
[77] Wang Q, Xie Y, Ding B, Yu G, Ye F, Xu C. Structure and hydration state characterizations of MgSO4-zeolite 13x composite materials for long-term thermochemical heat storage. Sol Energy Mater Sol Cells 2019;200:110047. https://doi.org/10.1016/j.solmat.2019.110047.
[78] Nonnen T, Preißler H, Kött S, Beckert S, Gläser R. Salt inclusion and deliquescence in salt/zeolite X composites for thermochemical heat storage. Microporous Mesoporous Mater 2020;303. https://doi.org/10.1016/j.micromeso.2020.110239.
[79] Whiting GT, Grondin D, Bennici S, Auroux A. Heats of water sorption studies on zeolite-MgSO4composites as potential thermochemical heat storage materials. Sol Energy Mater Sol Cells 2013;112:112–9. https://doi.org/10.1016/j.solmat.2013.01.020.
[80] Cindrella L, Dyer A. Ion-exchanged and salt hydrates-encapsulated zeolites for solar refrigeration. Sol Energy Mater Sol Cells 2009;93:161–6. https://doi.org/10.1016/j.solmat.2008.09.057.
[81] Silvester L, Touloumet Q, Kamaruddin A, Chassagneux F, Postole G, Auroux A, et al.

Influence of Silica Functionalization on Water Sorption and Thermochemical Heat Storage of Mesoporous SBA-15/CaCl 2 Composites. ACS Appl Energy Mater 2021;4:5944–56. https://doi.org/10.1021/acsaem.1c00786.
[82] Vyazovkin S, Burnham AK, Criado JM, Pérez-Maqueda LA, Popescu C, Sbirrazzuoli N. ICTAC Kinetics Committee recommendations for performing kinetic computations on thermal analysis data. Thermochim Acta 2011;520:1–19. https://doi.org/10.1016/j.tca.2011.03.034.
[83] Farcot L, Michel B, Le N, Papillon P. Numerical investigations of a continuous thermochemical heat storage reactor. J Energy Storage 2016;20:109–19. https://doi.org/10.1016/j.est.2018.08.020.
[84] Khawam A, Flanagan DR. Solid-state kinetic models: Basics and mathematical fundamentals. J Phys Chem B 2006;110:17315–28. https://doi.org/10.1021/jp062746a.
[85] El D. Hamad S. An experimental study of the salt hydrate MgSO4.7H2O. Thermochim Acta 1975;13:409–18.
[86] Galwey AK, Koga N, Tanaka H. A kinetic and microscopic investigation of the thermal dehydration of lithium sulphate monohydrate. J Chem Soc Faraday Trans 1990;86:531–7. https://doi.org/10.1039/FT9908600531.
[87] Gaponov YA, Kidyarov BI, Kirdyashkina NA, Lyakhov NZ, Okhotnikov V. Comparative Study of Single-Crystal Dehydration of LiCOOH.H2O and LiSO4.H2O. J Therm Anal 1988;33:547–51.
[88] Lan S, Zondag HA, Van Steenhoven A, Rindt CCM. Kinetic study of the dehydration reaction of lithium sulfate monohydrate crystals using microscopy and modeling. Thermochim Acta 2015;621:44–55. https://doi.org/10.1016/j.tca.2015.10.005.
[89] L'Vov B V. Mechanism of thermal dehydration of Li2SO4.H2O. Thermochim Acta 1998;315:145–57.
[90] Modestov AN, Poplaukhin P V., Lyakhov NZ. Dehydration kinetics of lithium sulfate monohydrate single crystals. J Therm Anal Calorim 2001;65:121–30. https://doi.org/10.1023/A:1011576502046.
[91] Okhotnikov V, Yakobson B, Lyakhov N. Kinetics of Thermal Dehydration of Li2SO4.H2O. React Kinet Catal Lett 1983;23:125–30.
[92] Tanaka H, Koga N. Self-Cooling Effect on the Kinetics of Ninisothermal Dehydration of Lithium Sulfate Monohydrate. J Therm Anal 1990;36:2601–10.
[93] Levitskij EA, Aristov YI, Tokarev MM, Parmon VN. "Chemical Heat Accumulators": A new approach to accumulating low potential heat. Sol Energy Mater Sol Cells 1996;44:219–35. https://doi.org/10.1016/0927-0248(96)00010-4.
[94] Tokarev MM, Aristov YI. Selective water sorbents for multiple applications, 4. CaCl2confined in silica gel pores: Sorption/desorption kinetics. React Kinet Catal Lett 1997;62:143–50. https://doi.org/10.1007/BF02475725.
[95] Huang Q, Lu G, Wang J, Yu J-G. Mechanism and Kinetics of Thermal Decomposition of MgCl2 × 6H2O. Metall Mater Trans B 2010;41:1059–66. https://doi.org/10.1007/s11663-010-9390-4.
[96] Stanish MA, Perlmutter DD. Kinetics and transport effects in the dehydration of crystalline potassium carbonate hydrate. AIChE J 1983;29:806–12. https://doi.org/10.1002/aic.690290515.
[97] Stanish MA, Perlmutter DD. Kinetics of hydration-dehydration reactions considered as solid transformations. AIChE J 1984;30:557–63. https://doi.org/10.1002/aic.690300405.
[98] Gaeini M, Shaik SA, Rindt CCM. Characterization of potassium carbonate salt hydrate for thermochemical energy storage in buildings. Energy Build 2019;196:178–93. https://doi.org/10.1016/j.enbuild.2019.05.029.

[99] Aristov YI, Glaznev IS, Freni A, Restuccia G. Kinetics of water sorption on SWS-1L (calcium chloride confined to mesoporous silica gel): Influence of grain size and temperature. Chem Eng Sci 2006;61:1453–8. https://doi.org/10.1016/j.ces.2005.08.033.
[100] Chen H jun, Cui Q, Tang Y, Chen X jun, Yao H qing. Attapulgite based LiCl composite adsorbents for cooling and air conditioning applications. Appl Therm Eng 2008;28:2187–93. https://doi.org/10.1016/j.applthermaleng.2007.12.015.
[101] Jabbari-Hichri A, Bennici S, Auroux A. CaCl2-containing composites as thermochemical heat storage materials. Sol Energy Mater Sol Cells 2017;172:177–85. https://doi.org/10.1016/j.solmat.2017.07.037.
[102] Lehmann C, Kolditz O, Nagel T. Modelling sorption equilibria and kinetics in numerical simulations of dynamic sorption experiments in packed beds of salt/zeolite composites for thermochemical energy storage. Int J Heat Mass Transf 2019;128:1102–13. https://doi.org/10.1016/j.ijheatmasstransfer.2018.09.042.
[103] Doyle, C. D. Kinetic analysis of thermogravimetric data. J Appl Polym Sci 1961;5:285–92. https://doi.org/10.1016/0040-6031(83)80350-5.
[104] Coats and Redfern. Kinetic parameters from Thermogravimetric Data. Nature 1964;201:68–9.
[105] Kärger J, Ruthven DM, Theodorou DN. Diffusion in Nanoporous Materials. 2012. https://doi.org/10.1002/9783527651276.
[106] Nagel T, Shao H, Roßkopf C, Linder M, Wörner A, Kolditz O. The influence of gas – solid reaction kinetics in models of thermochemical heat storage under monotonic and cyclic loading. Appl Energy 2014;136:289–302. https://doi.org/10.1016/j.apenergy.2014.08.104.
[107] Fumey B, Weber R, Baldini L. Sorption based long-term thermal energy storage – Process classification and analysis of performance limitations: A review. Renew Sustain Energy Rev 2019;111:57–74. https://doi.org/10.1016/j.rser.2019.05.006.
[108] Michel B, Neveu P, Mazet N. Comparison of closed and open thermochemical processes, for long-term thermal energy storage applications. Energy 2014;72:702–16. https://doi.org/10.1016/j.energy.2014.05.097.
[109] Michel B, Mazet N, Neveu P. Experimental investigation of an open thermochemical process operating with a hydrate salt for thermal storage of solar energy: Local reactive bed evolution. Appl Energy 2016;180:234–44. https://doi.org/10.1016/j.apenergy.2016.07.108.
[110] Skrylnyk O, Courbon E, Heymans N, Frère M. Combined solar thermochemical solid/gas energy storage process for domestic thermal applications: Analysis of global performance. Appl Sci 2019;9. https://doi.org/10.3390/app9091946.
[111] Wyttenbach J, Bougard J, Descy G, Skrylnyk O, Courbon E, Frère M, et al. Performances and modelling of a circular moving bed thermochemical reactor for seasonal storage. Appl Energy 2018;230:803–15. https://doi.org/10.1016/j.apenergy.2018.09.008.
[112] Scapino L. Sorption thermal energy storage for smart grids - A system-scale analysis. Thesis 2019:255.
[113] Fumey B, Baldini L. Static Temperature Guideline for Comparative Testing of Sorption Heat Storage Systems for Building Application. Energies 2021:1–15.
[114] Zondag HA, Kikkert B, Smeding S, Boer R de, Bakker M. Prototype thermochemical heat storage with open reactor system. Appl Energy 2013;109:360–5. https://doi.org/10.1016/j.apenergy.2013.01.082.
[115] Farcot L, Le Pierrès N, Fourmigué JF. Experimental investigation of a moving-bed heat storage thermochemical reactor with SrBr2/H2O couple. J Energy Storage 2019;26:101009. https://doi.org/10.1016/j.est.2019.101009.
[116] N'Tsoukpoe KE, Kuznik F. A reality check on long-term thermochemical heat storage for household applications. Renew Sustain Energy Rev 2021;139.

https://doi.org/10.1016/j.rser.2020.110683.
[117] Liu H, Wang W, Zhang Y. Performance gap between thermochemical energy storage systems based on salt hydrates and materials. J Clean Prod 2021;313:127908. https://doi.org/10.1016/j.jclepro.2021.127908.
[118] Xu C, Yu Z, Xie Y, Ren Y, Ye F, Ju X. Study of the hydration behavior of zeolite-MgSO 4 composites for long-term heat storage. Appl Therm Eng 2018;129:250–9. https://doi.org/10.1016/j.applthermaleng.2017.10.031.
[119] Zondag HA, van Essen VM, Bleijendaal LPJ, Kikkert B, Bakker M. Application of MgCl2·6H2O for thermochemical seasonal solar heat storage. 5th IRES Conf 2011:22–4.
[120] Aydin D, Casey SP, Chen X, Riffat S. Novel "open-sorption pipe" reactor for solar thermal energy storage. Energy Convers Manag 2016;121:321–34. https://doi.org/10.1016/j.enconman.2016.05.045.
[121] Walsh S, Reynolds J, Abbas B, Woods R, Searle J, Jewell E, et al. Assessing the Dynamic Performance of Thermochemical Storage Materials. Energies 2020.
[122] Skrylnyk O, Courbon E, Heymans N, Frère M, Bougard J, Descy G. Energy Performances of Open Sorption Reactor with Ultra-Low Grade Heat Upgrading for Thermochemical Energy Storage Applications. Energy Procedia 2017;135:304–16. https://doi.org/10.1016/j.egypro.2017.09.522.
[123] Zhang YN, Wang RZ, Li TX. Experimental investigation on an open sorption thermal storage system for space heating. Energy 2017;141:2421–33. https://doi.org/10.1016/j.energy.2017.12.003.
[124] Bertsch, F., Mette, B., Asenbeck, S., Kerskes, H., & Müller-Steinhagen H. Low temperature chemical heat storage–an investigation of hydration reactions. Effstock Conf Stock 2009:1–8.
[125] Sutton RJ, Jewell E, Elvins J, Searle JR, Jones P. Characterising the discharge cycle of CaCl 2 and LiNO 3 hydrated salts within a vermiculite composite scaffold for thermochemical storage. Energy Build 2018;162:109–20. https://doi.org/10.1016/j.enbuild.2017.11.068.
[126] Mette B, Kerskes H, Drück H. Process and Reactor Design for Thermo-Chemical Energy Stores. Proc ISES Sol World Congr 2011 2011:1–12. https://doi.org/10.18086/swc.2011.29.18.
[127] Fopah-Lele A, Kuznik F, Osterland T, Ruck WKL. Thermal synthesis of a thermochemical heat storage with heat exchanger optimization. Appl Therm Eng 2016;101:669–77. https://doi.org/10.1016/j.applthermaleng.2015.12.103.
[128] Balasubramanian G, Ghommem M, Hajj MR, Wong WP, Tomlin JA, Puri IK. Modeling of thermochemical energy storage by salt hydrates. Int J Heat Mass Transf 2010;53:5700–6. https://doi.org/10.1016/j.ijheatmasstransfer.2010.08.012.
[129] Ghommem M, Balasubramanian G, Hajj MR, Wong WP, Tomlin JA, Puri IK. Release of stored thermochemical energy from dehydrated salts. Int J Heat Mass Transf 2011;54:4856–63. https://doi.org/10.1016/j.ijheatmasstransfer.2011.06.041.
[130] Omar A-A, Abdessattar A, Mehdi G. Modeling and assessment of a thermochemical energy storage using salt hydrates. Arch Thermodyn 2012;33:23–40. https://doi.org/10.1002/er.
[131] Kharbanda JS, Yadav SK, Soni V, Kumar A. Modeling of heat transfer and fluid flow in epsom salt (MgSO4•7H2O) dissociation for thermochemical energy storage. J Energy Storage 2020;31:101712. https://doi.org/10.1016/j.est.2020.101712.
[132] Lebrun M, Spinner B. Models of heat and mass transfers in solid-gas reactors used as chemical heat pumps. Chem Eng Sci 1990;45:1743–53. https://doi.org/10.1016/0009-2509(90)87052-T.
[133] Xu C, Xie Y, Liao Z, Ren Y, Ye F. Numerical study on the desorption process of a thermochemical reactor filled with MgCl2·6H2O for seasonal heat storage. Appl Therm Eng

2019;146:785–94. https://doi.org/10.1016/j.applthermaleng.2018.10.019.
[134] Mazet N, Amouroux M, Spinner B. Analysis and experimental study of the transformation of a non-isothermal solid/gas reacting medium. Chem Eng Commun 1991;99:155–74. https://doi.org/10.1080/00986449108911585.
[135] Longuet B, Gillard P. Experimental investigation on the heterogeneous kinetic process of the low thermal decomposition of ammonium perchlorate particles. Propellants, Explos Pyrotech 2009;34:59–71. https://doi.org/10.1002/prep.200700203.
[136] Fopah-Lele A, Kuznik F, Rammelberg HU, Schmidt T, Ruck WKL. Modeling Approach of Thermal Decomposition of Salt-Hydrates for Heat Storage Systems. Vol 1 Heat Transf Energy Syst Thermophys Prop Theory Fundam Res Heat Transf 2013:V001T01A010. https://doi.org/10.1115/HT2013-17022.
[137] Michel B. Procédé thermochimique pour le stockage intersaisonnier de l ' énergie solaire : modélisation multi-échelles et expérimentation d ' un prototype sous air humide. Thesis 2012:259.
[138] Li W, Guo H, Zeng M, Wang Q. Performance of SrBr2·6H2O based seasonal thermochemical heat storage in a novel multilayered sieve reactor. Energy Convers Manag 2019;198:111843. https://doi.org/10.1016/j.enconman.2019.111843.
[139] Gaeini M. Thermochemical seasonal heat storage for the built environment. Thesis 2017.
[140] Scapino L, Zondag HA, Diriken J, Rindt CCM, Van Bael J, Sciacovelli A. Modeling the performance of a sorption thermal energy storage reactor using artificial neural networks. Appl Energy 2019;253:113525. https://doi.org/10.1016/j.apenergy.2019.113525.
[141] Mukherjee A, Majumdar R, Saha SK, Kumar L. Assessment of open thermochemical energy storage system performance for low temperature heating applications. Appl Therm Eng 2019;156:453–70. https://doi.org/10.1016/j.applthermaleng.2019.04.096.
[142] Jiang L, Lin YC, Liu W, Ma ZW, Wang RQ, Zhang XJ, et al. Thermophysical characterization of magnesium chloride and its application in open sorption thermal energy storage system. Sol Energy Mater Sol Cells 2021. https://doi.org/10.1016/j.solmat.2021.111528.
[143] Stanish MA, Perlmutter DD. Rate processes in cycling a reversible gas-solid reaction. AIChE J 1983;30:56–62. https://doi.org/10.1002/aic.690300110.
[144] Beving MAJM, Frijns AJH, Rindt CCM, Smeulders DMJ. Characterization and modelling of K2CO3 cycles for thermochemical energy storage applications. Proc Eurotherm Semin 112 2019:1–10.
[145] Stanish MA, Perlmutter DD. Salt hydrates as absorbents in heat pump cycles. Sol Energy 1981;26:333–9. https://doi.org/10.1016/0038-092X(81)90179-1.
[146] Aristov YI, Restuccia G, Cacciola G, Parmon VN. A family of new working materials for solid sorption air conditioning systems. Appl Therm Eng 2002;22:191–204. https://doi.org/10.1016/S1359-4311(01)00072-2.
[147] Surface Measurement Systems 2019. https://www.surfacemeasurementsystems.com/solutions/dynamic_vapor_sorption/ (accessed December 16, 2019).
[148] Rammelberg HU, Schmidt T, Ruck WKL. Hydration and dehydration of salt hydrates and hydroxides for thermal energy storage - Kinetics and energy release. Energy Procedia 2012;30:362–9. https://doi.org/10.1016/j.egypro.2012.11.043.
[149] Huang Q, Lu G, Wang J, Yu J-G. Thermal decomposition mechanisms of MgCl2·6H2O and MgCl2·H2O. J Anal Appl Pyrolysis 2011;91:159–64. https://doi.org/10.1016/j.jaap.2011.02.005.
[150] Sugimoto K, Dinnebier RE, Hanson JC. Structures of three dehydration products of bischofite from in situ synchrotron powder diffraction data (MgCl2·nH2O; n = 1, 2, 4). Acta Crystallogr

Sect B Struct Sci 2007;63:235–42. https://doi.org/10.1107/S0108768107002558.
[151] Surface Measurement Systems L. DVS Advantage Operation Manual 2009:192.
[152] Albas-Martin C. An investigation of K2CO3 impregnated vermiculite composites : formulation and reaction process kinetic analysis. 2019.
[153] Fopah-Lele A, Kuznik F, Opel O, Ruck WKL. Performance analysis of a thermochemical based heat storage as an addition to cogeneration systems. Energy Convers Manag 2015;106:1327–44. https://doi.org/10.1016/j.enconman.2015.10.068.
[154] Janna WS. Engineering Heat Transfer. 3rd editio. 2009.
[155] Kenisarin M, Mahkamov K. Salt hydrates as latent heat storage materials:Thermophysical properties and costs. Sol Energy Mater Sol Cells 2016;145:255–86. https://doi.org/10.1016/j.solmat.2015.10.029.
[156] Kleiner F, Posern K, Osburg A. Thermal conductivity of selected salt hydrates for thermochemical solar heat storage applications measured by the light flash method. Appl Therm Eng 2017;113:1189–93. https://doi.org/10.1016/j.applthermaleng.2016.11.125.
[157] Fopah-Lele A, Tamba JG. A review on the use of SrBr2·6H2O as a potential material for low temperature energy storage systems and building applications. Sol Energy Mater Sol Cells 2017;164:175–87. https://doi.org/10.1016/j.solmat.2017.02.018.
[158] Fopah-Lele A. A Thermochemical Heat Storage System for Households: Thermal Transfers Coupled to Chemical Reaction Investigations. Thesis 2015.
[159] Richter M, Bouché M, Linder M. Heat transformation based on CaCl 2 /H 2 O – Part A: Closed operation principle. Appl Therm Eng 2016;102:615–21. https://doi.org/10.1016/j.applthermaleng.2016.03.076.
[160] Sutton RJ, Jewell E, Searle J, Elvins J. Discharge performance of blended salt in matrix materials for low enthalpy thermochemical storage. Appl Therm Eng 2018;145:483–93. https://doi.org/10.1016/j.applthermaleng.2018.09.052.
[161] Mauer LJ, Taylor LS. Water-Solids Interactions: Deliquescence. Annu Rev Food Sci Technol 2010;1:41–63. https://doi.org/10.1146/annurev.food.080708.100915.
[162] Fopah-Lele A, Kuznik F, Rammelberg HU, Schmidt T, Ruck WKL. Thermal decomposition kinetic of salt hydrates for heat storage systems. Appl Energy 2015;154:447–58. https://doi.org/10.1016/j.apenergy.2015.02.011.
[163] Peterson VK, Neumann DA, Livingston RA. Hydration of tricalcium and dicalcium silicate mixtures studied using quasielastic neutron scattering. J Phys Chem B 2005;109:14449–53. https://doi.org/10.1021/jp052147o.
[164] Vyazovkin S, Chrissafis K, Di Lorenzo ML, Koga N, Pijolat M, Roduit B, et al. ICTAC Kinetics Committee recommendations for collecting experimental thermal analysis data for kinetic computations. Thermochim Acta 2014;590:1–23. https://doi.org/10.1016/j.tca.2014.05.036.
[165] Eurostat. Final energy consumption in the residential sector by end use, Eu-27, 2019 2021. https://ec.europa.eu/eurostat/statistics-explained/index.php?title=Energy_consumption_in_households#Energy_consumption_in_households_by_type_of_end-use (accessed October 27, 2021).
[166] Palomba V, Frazzica A. Comparative analysis of thermal energy storage technologies through the definition of suitable key performance indicators. Energy Build 2019;185:88–102. https://doi.org/S0378778818330354.
[167] Cabeza LF, Galindo E, Prieto C, Barreneche C, Inés Fernández A. Key performance indicators in thermal energy storage: Survey and assessment. Renew Energy 2015;83:820–7. https://doi.org/10.1016/j.renene.2015.05.019.
[168] Duffie JA, Beckman WA. Solar Engineering of Thermal Processes. 2013.

[169] Kuznik F, Johannes K, Obrecht C, David D. A review on recent developments in physisorption thermal energy storage for building applications. Renew Sustain Energy Rev 2018;94:576–86. https://doi.org/10.1016/j.rser.2018.06.038.
[170] Weber R, Asenbeck S, Kerskes H, Drück H. SolSpaces - Testing and Performance Analysis of a Segmented Sorption Store for Solar Thermal Space Heating. Energy Procedia 2016;91:250–8. https://doi.org/10.1016/j.egypro.2016.06.214.
[171] Michel B, Mazet N, Neveu P. Experimental investigation of an innovative thermochemical process operating with a hydrate salt and moist air for thermal storage of solar energy: Global performance. Appl Energy 2014;129:177–86. https://doi.org/10.1016/j.apenergy.2014.04.073.
[172] Mahon D, Henshall P, Claudio G, Eames PC. Feasibility study of MgSO4 + zeolite based composite thermochemical energy stores charged by vacuum flat plate solar thermal collectors for seasonal thermal energy storage. Renew Energy 2020;145:1799–807. https://doi.org/10.1016/j.renene.2019.05.135.
[173] Van Beek T, Rindt CCM, Zondag HA. Performance analysis of an atmospheric packed bed thermo-chemical heat storage system. Proc 12th Int Conf Energy Storage 2012:1–9.
[174] Trausel F, De Jong AJ, Cuypers R. A review on the properties of salt hydrates for thermochemical storage. Energy Procedia 2014;48:447–52. https://doi.org/10.1016/j.egypro.2014.02.053.
[175] Ovchinnikov P, Borodiņecs A, Strelets K. Utilization potential of low temperature hydronic space heating systems: A comparative review. Build Environ 2017;112:88–98. https://doi.org/10.1016/j.buildenv.2016.11.029.
[176] Wagman DD, Evans WH, Parker VB, Schumm RH, Halow I, Bailey SM, et al. The NBS tables of chemical thermodynamic properties - selected values for inorganic and C-1 and C-2 organic-substances in si units. vol. 11. 1982.
[177] Corporation OC. Calcium chloride - A Guide to Physical Properties. Chem Mark Report 2002;262:18.
[178] N'Tsoukpoe KE, Rammelberg HU, Lele AF, Korhammer K, Watts BA, Schmidt T, et al. A review on the use of calcium chloride in applied thermal engineering. Appl Therm Eng 2015;75:513–31. https://doi.org/10.1016/j.applthermaleng.2014.09.047.
[179] Gondre D. Numerical modeling and analysis of heat and mass transfers in an adsorption heat storage tank : Influences of material properties , operating conditions and system design on storage performances. Thesis 2016.
[180] Enerconcept. Lubi Solar Air Heater 2023. https://www.enerconcept.com/en/solar-air-heating-products/lubi/ (accessed January 18, 2023).
[181] Staffell I, Pfenninger S. Using bias-corrected reanalysis to simulate current and future wind power output. Energy 2016;114:1224–39. https://doi.org/10.1016/j.energy.2016.08.068.
[182] Bergman TL, Lavine AS, Incropera FP, DeWitt DP. Fundamentals of heat and mass transfer, 2011. vol. 13. Sixth Edit. 2015.
[183] Kays WM, London AL. Compact heat exchangers. Third Edition. 1984.
[184] Mukherjee A, Majumdar R, Saha SK, Subramaniam C, Kumar L. Performance evaluation of an open thermochemical energy storage system integrated with flat plate solar collector. Appl Therm Eng 2020;173:115218. https://doi.org/10.1016/j.applthermaleng.2020.115218.
[185] Mauran S, Lahmidi H, Goetz V. Solar heating and cooling by a thermochemical process. First experiments of a prototype storing 60 kW h by a solid/gas reaction. Sol Energy 2008;82:623–36. https://doi.org/10.1016/j.solener.2008.01.002.
[186] Romani J, Gasia J, Cabeza LF. Definitions of technical parameters for thermal energy storage (TES) 2018.
[187] Toshiba Air Conditioning - Air to air heat exchangers 20123. https://www.toshiba-

aircon.co.uk/product/air-air-heat-exchangers/ (accessed March 21, 2023).
[188] Rehman AU, Shah MZ, Ali A, Zhao T, Shah R, Ullah I, et al. Thermochemical heat storage ability of ZnSO 4 · 7H 2 O as potential long-term heat storage material. Int J Energy Res 2020:1–9. https://doi.org/10.1002/er.6077.
[189] Chen B, Johannes K, Ratel L, Horgnies M, Morin V, Kuznik F. Investigation on ettringite as a low-cost high-density thermochemical heat storage material: Thermodynamics and kinetics. Sol Energy Mater Sol Cells 2020:110877. https://doi.org/10.1016/j.solmat.2020.110877.
[190] Rathgeber C, Lävemann E, Hauer A. Economic top-down evaluation of the costs of energy storages-A simple economic truth in two equations. J Energy Storage 2015;2:43–6. https://doi.org/10.1016/j.est.2015.06.001.
[191] Moran MJ, Shapiro HN, Boettner DD, Bailey MB. Fundamentals of Engineering Thermodynamics. 2018. https://doi.org/10.4324/9781315119717.
[192] Kärger J, Ruthven DM. Diffusion in nanoporous materials: Fundamental principles, insights and challenges. New J Chem 2016;40:4027–48. https://doi.org/10.1039/c5nj02836a.
[193] Aarts J, de Jong S, Cotti M, Donkers P, Fischer H, Adan O, et al. Diffusion limited hydration kinetics of millimeter sized salt hydrate particles for thermochemical heat storage. J Energy Storage 2021:103554. https://doi.org/10.1016/j.est.2021.103554.
[194] Okhrimenko L, Favergeon L, Johannes K, Kuznik F. New kinetic model of the dehydration reaction of magnesium sulfate hexahydrate: Application for heat storage. Thermochim Acta 2020;687:178569. https://doi.org/10.1016/j.tca.2020.178569.
[195] Lin J, Zhao Q, Huang H, Mao H, Liu Y, Xiao Y. Applications of low-temperature thermochemical energy storage systems for salt hydrates based on material classification: A review. Sol Energy 2021;214:149–78. https://doi.org/10.1016/j.solener.2020.11.055.
[196] Mertens K. Photovoltaics: Fundamentals, Technology and Practice. 2014. https://doi.org/10.1201/9781315374192.
[197] Solarstore E. 'https://www.europe-solarstore.com/solar-inverters/sma/sunny-boy.html n.d.
[198] Schüwer D, Schneider C. Electrification of industrial process heat: Long-term applications, potentials and impacts. Eceee Ind Summer Study Proc 2018;2018-June:411–22.
[199] Galema SA. Microwave chemistry. Chem Soc Rev 1997;26:233. https://doi.org/10.1039/cs9972600233.
[200] Kitchen HJ, Vallance SR, Kennedy JL, Tapia-Ruiz N, Carassiti L, Harrison A, et al. Modern microwave methods in solid-state inorganic materials chemistry: From fundamentals to manufacturing. Chem Rev 2014;114:1170–206. https://doi.org/10.1021/cr4002353.
[201] Anwar J, Shafique U, Waheed-uz-Zaman, Rehman R, Salman M, Dar A, et al. Microwave chemistry: Effect of ions on dielectric heating in microwave ovens. Arab J Chem 2015;8:100–4. https://doi.org/10.1016/j.arabjc.2011.01.014.
[202] Kubota M, Hanada T, Yabe S, Kuchar D, Matsuda H. Water desorption behavior of desiccant rotor under microwave irradiation. Appl Therm Eng 2011;31:1482–6. https://doi.org/10.1016/j.applthermaleng.2011.01.027.
[203] Seiya Ito, Hongyu Huang, Fujio Watanabe, Masanobu Hasatani, Jun Li NK. A Theoretical Study of Heat and Mass Transfer in Water Vapor Desorption using Both Microwaves and Hot Air. Int J Eng Res Technol 2015;4:732–8.
[204] Meloni E, Martino M, Pullumbi P, Brandani F, Palma V. Intensification of TSA processes using a microwave-assisted regeneration step. Chem Eng Process - Process Intensif 2021;160:108291. https://doi.org/10.1016/j.cep.2020.108291.
[205] Demir H. Experimental study on a novel microwave-assisted adsorption heat pump. Energy Econ 2014;45:35–43. https://doi.org/10.1016/j.ijrefrig.2014.05.001.
[206] Zheng Y, Meyer G, Lanagan M, Agrawal D, Cheng J. A study of water sorption effects on the

microwave dielectric properties of calcium chloride/silica gel composites. Mater Lett 2013;95:157–9. https://doi.org/10.1016/j.matlet.2012.12.112.
[207] Burton EF, Turnbull LG. Dielectric constants of solids at high frequencies and the influence of water of crystallization on dielectric constant. Proc R Soc London Ser A - Math Phys Sci 1937;158:182–98. https://doi.org/10.1098/rspa.1937.0013.
[208] Young KF, Frederikse HPR. Compilation of the Static Dielectric Constant of Inorganic Solids. J Phys Chem Ref Data 1973;2:313–410. https://doi.org/10.1063/1.3253121.
[209] Pizzetti M, Petricci E. Heterogeneous Catalysis Under Microwave Heating. La Chim L'Industria 2012;4:78–80.
[210] Tang P, Hu G, Gao Y, Li W, Yao S, Liu Z, et al. The microwave adsorption behavior and microwave-assisted heteroatoms doping of graphene-based nano-carbon materials. Sci Rep 2014;4:1–7. https://doi.org/10.1038/srep05901.
[211] Kabalka GW, Pagni RM, Wang L, Namboodiri V, Hair CM. Microwave-assisted, solventless suzuki coupling reactions on palladium-doped alumina. Green Chem 2000;2:120–2. https://doi.org/10.1039/b001191f.
[212] Díaz-Ortiz, Prieto P, de la Hoz A. A Critical Overview on the Effect of Microwave Irradiation in Organic Synthesis. Chem Rec 2019;19:85–97. https://doi.org/10.1002/tcr.201800059.
[213] Rao KJ, B. V. MG, Ramakrishnan. PA. Synthesis of Inorganic Solids Using Microwaves. Che Mater 1999;11:882–95.
[214] Bilecka I, Niederberger M. Microwave chemistry for inorganic nanomaterials synthesis. Nanoscale 2010;2:1358–74. https://doi.org/10.1039/b9nr00377k.
[215] Esveld E, Chemat F, Van Haveren J. Pilot scale continuous microwave dry-media reactor Part 1: Design and modeling. Chem Eng Technol 2000;23:279–83. https://doi.org/10.1002/(SICI)1521-4125(200003)23:3<279::AID-CEAT279>3.0.CO;2-P.
[216] Nüchter M, Ondruschka B, Bonrath W, Gum A. Microwave assisted synthesis – a critical technology overview. Green Chem 2004;6:128–41. https://doi.org/10.1039/b310502d.
[217] Haneishi N, Tsubaki S, Abe E, Maitani MM, Suzuki E ichi, Fujii S, et al. Enhancement of Fixed-bed Flow Reactions under Microwave Irradiation by Local Heating at the Vicinal Contact Points of Catalyst Particles. Sci Rep 2019;9:1–12. https://doi.org/10.1038/s41598-018-35988-y.
[218] Buttress AJ, Hargreaves G, Ilchev A, Monti T, Sklavounou A, Katrib J, et al. Design and optimisation of a microwave reactor for kilo-scale polymer synthesis. Chem Eng Sci X 2019;2:100022. https://doi.org/10.1016/j.cesx.2019.100022.
[219] Chemat F, Cravotto G. Microwave-assisted Extraction for Bioactive Compounds: Theory and Practice. 2013. https://doi.org/10.1007/978-1-4614-4830-3_1.
[220] Demir H. Development of microwave assisted zeolite-water adsorption heat pump. Int J Refrig 2013;36:2289–96. https://doi.org/10.1016/j.ijrefrig.2013.07.005.
[221] Rudnev V, Loveless D, Cook RL. Handbook of Induction Heating, Second Edition. 2018.
[222] Zadražil A, Štěpánek F. Remote control of desorption by radiofrequency heating: Single pellet experiments. Chem Eng Sci 2013;101:382–9. https://doi.org/10.1016/j.ces.2013.06.012.
[223] SaltX Technology AB. WO 2019/234082 A1 - System and method for transferring energy, 2019.
[224] MORTENSEN PM. WO2017036794A1: Induction heating of endothermic reactions, 2017.
[225] Chatterjee S, Degirmenci V, Aiouache F, Rebrov E V. Design of a radio frequency heated isothermal micro-trickle bed reactor. Chem Eng J 2014;243:225–33. https://doi.org/10.1016/j.cej.2013.12.059.
[226] Fernández J, Sotenko M, Derevschikov V, Lysikov A, Rebrov E V. A radiofrequency heated reactor system for post-combustion carbon capture. Chem Eng Process Process Intensif

2016;108:17–26. https://doi.org/10.1016/j.cep.2016.07.004.
[227] Fernández J, Chatterjee S, Degirmenci V, Rebrov E V. Scale-up of an RF heated micro trickle bed reactor to a kg/day production scale. Green Process Synth 2015;4:343–53. https://doi.org/10.1515/gps-2015-0035.
[228] AirTrack. AirTrack Vent Axia Heaters n.d.
[229] Ratanadecho P, Aoki K, Akahori M. Influence of irradiation time, particle sizes, and initial moisture content during microwave drying of multi-layered capillary porous materials. J Heat Transfer 2002;124:151–61. https://doi.org/10.1115/1.1423951.
[230] Perry WL, Datye AK, Prinja AK, Brown LF, Katz JD. Microwave heating of endothermic catalytic reactions: Reforming of methanol. AIChE J 2002;48:820–31. https://doi.org/10.1002/aic.690480416.
[231] Fabio G, G. BG, L. M. Microwave Heating of Porous Media. J Heat Transfer 1987;109:522–5.
[232] Gadkari S, Fidalgo B, Gu S. Numerical analysis of microwave assisted thermocatalytic decomposition of methane. Int J Hydrogen Energy 2017;42:4061–8. https://doi.org/10.1016/j.ijhydene.2016.09.126.
[233] Gediz Ilis G, Demir H. Influence of bed thickness and particle size on performance of microwave regenerated adsorption heat pump. Int J Heat Mass Transf 2018;123:16–24. https://doi.org/10.1016/j.ijheatmasstransfer.2018.02.063.
[234] Ito S, Huang H, Watanabe F, Yuan H, Hasatani M, Kobayashi N. Heat Transfer during Microwave-Assisted Desorption of Water Vapor from Zeolite Packed Bed. Dry Technol 2012;30:1707–13. https://doi.org/10.1080/07373937.2012.714825.
[235] Metaxas AC, Meredith RJ. Industrial Microwave Heating. vol. 24. 1983. https://doi.org/10.1080/08327823.1989.11688082.
[236] Gaikwad SV, Gaikwad AN. RF and microwave low power dielectric heating using parallel plate applicator to control insect pests on tomato plant. Prog Electromagn Res M 2016;49:81–9. https://doi.org/10.2528/PIERM16051806.
[237] Hong YK, Stanley R, Tang J, Bui L, Ghandi A. Effect of electric field distribution on the heating uniformity of a model ready-to-eat meal in microwave-assisted thermal sterilization using the FDTD method. Foods 2021;10. https://doi.org/10.3390/foods10020311.
[238] Department of Enegy and Climate Change. Energy Usage in Households with Solar PV Installations 2014:85–92.
[239] Johnston D, Wingfield J, Miles-Shenton D. Measuring the fabric performance of UK dwellings. Assoc Res Constr Manag ARCOM 2010 - Proc 26th Annu Conf 2010:1371–80.
[240] Bell M, Stafford A, Gorse C. Building Confidence – A working paper 2012:29.
[241] Energy USD of. Thermal Energy Storage Technologies Subprogram Area 2022. https://www.energy.gov/eere/buildings/thermal-energy-storage.
[242] Department of Energy & Climate Change. Official Statistics: Solar photovoltaic (PV) cost data. 2021.
[243] Ducting-Express. Inline Duct Heaters n.d. https://www.ducting-express.co.uk/category/ducting-fittings/inline-duct-heaters.
[244] de Boer R, Smeding S, Zondag HA, Krol G. Development of a prototype system for seasonal solar heat storage using an open sorption process. Eurotherm Semin 2014:1–9.

Appendices

Appendix I: Full thermophysical data of the considered salt/water reactions

Step by step reaction	Khi	Delta H [J/mol]	Delta S [J/mol/K]	Lower Hydrate Rho [kg/m3]	Cp [J/mol/K]		M [g/mol]
SrBr2 + H2O = SrBr2. H2O	1	-717600.0	135.1	4216.0	79.5		247.4
SrBr2.H2O + 5H2O = SrBr2.6H2O	5	-1031400.0	180.0	2396.0	120.9	455.5	265.4
MgSO4 + H2O = MgSO4.H2O	1	-1284900.0	91.6	2660.0	96.5	801.6	120.4
MgSO4.H2O + 5H2O = MgSO4.6H2O	5	-1602100.0	126.4	2570.0	144.9	1047.0	138.4
MgSO4.6H2O + H2O = MgSO4.7H2O	1	-3087000.0	348.1	1750.0	348.1	1524.4	228.4
CaCl2 + H2O = CaCl2.H2O	1	-795800.0	104.0	2160.0	72.6	654.1	111.0
CaCl2.H2O + H2O = CaCl2.2H2O	1	-1109200.0		2240.0	108.3	840.0	129.0
CaCl2.2H2O + 2H2O = CaCl2.4H2O	2	-1402900.0	206.2	1850.0	172.0	1170.0	147.0
CaCl2.4H2O + 2H2O = CaCl2.6H2O	2	-2009600.0	271.9	1830.0	245.2	1340.0	183.0
MgCl2 + H2O = MgCl2.H2O	1	-640905.0	89.6	2320.0	71.4	749.7	95.2
MgCl2.H2O + H2O = MgCl2.2H2O	1	-966630.0	137.2		115.3	1018.2	113.2
MgCl2.2H2O + 2H2O = MgCl2.4H2O	2	-1279720.0	179.9	1860.0	159.2	1213.3	131.2
MgCl2.4H2O + 2H2O = MgCl2.6H2O	2	-1898990.0	264.0	1290.0	241.4	1443.8	167.2
K2CO3 + 1.5H2O = K2CO3.1.5H2O	1.5	-1151020.0	155.5	2430.0	114.4	828.0	138.2
BaCl2 + H2O = BaCl2. H2O	1	-858600.0	123.7	3856.0	75.1	360.9	208.2
BaCl2.H2O+H2O = BaCl2.2H2O	1	-1160600.0	166.9	3476.5	117.9		226.2
CaSO4 + 0.5H2O = CaSO4.0.5H2O	0.5	-1425240.0	108.4	2960.0	100.2	736.1	136.1
CaSO4.0.5H2O + 1.5H2O = CaSO4.2H2O	1.5	-1576740.0	130.5		119.4	822.7	145.1
CuCl2 + 2H2O = CuCl2.2H2O	2	-220100.0	108.1	3386.0	71.9	534.6	134.5
LiCl + H2O = LiCl. H2O	1	-468610.0	59.3	2068.0	243	5731.9	42.4
LiCl.H2O + H2O = LiCl.2H2O	1	-712580.0	102.8	1760.0	494.1		60.4
LiCl.2H2O + H2O = LiCl.3H2O	1	-1012650.0	139.2	1760.0			78.4
Li2SO4 + H2O = Li2SO4.H2O	1	-1424221.0	115.1	2221.0	117.6	1069.4	109.9
ZnSO4 + H2O = ZnSO4. H2O	1	-982800	110.5	3540.0	117.04		161.5
ZnSO4.H2O + 5H2O = ZnSO4.6H2O	5	-1304490	138.5		145.046		179.5
ZnSO4.6H2O + H2O = ZnSO4.7H2O	1	-2777490	363.3	2072	337.744		269.5

Step by step reaction	Khi	Delta H [J/mol]	Delta S [J/mol/K]	Upper hydrate Rho [kg/m3]	Upper hydrate Cp [J/mol/K]		M [g/mol]
SrBr2 + H2O = SrBr2. H2O	1	-1031400.0	180.0	2396.0	120.9	455.5	265.4
SrBr2.H2O + 5H2O = SrBr2.6H2O	5	-2531300.0	406.0	2386.0	343.5	966.4	355.4
MgSO4 + H2O = MgSO4.H2O	1	-1602100.0	126.4	2570.0	144.9	1047.0	138.4
MgSO4.H2O + 5H2O = MgSO4.6H2O	5	-3087000.0	348.1	1750.0	348.1	1524.4	228.4
MgSO4.6H2O + H2O = MgSO4.7H2O	1	-3388710.0	372.0	1680.0	380.9	1546.0	246.4
CaCl2 + H2O = CaCl2.H2O	1	-1109200.0		2240.0	108.3	840.0	129.0
CaCl2.H2O + H2O = CaCl2.2H2O	1	-1402900.0	206.2	1850.0	172.0	1170.0	147.0
CaCl2.2H2O + 2H2O = CaCl2.4H2O	2	-2009600.0	271.9	1830.0	245.2	1340.0	183.0
CaCl2.4H2O + 2H2O = CaCl2.6H2O	2	-2607900.0	341.7	1710.0	328.5	1500.0	219.0
MgCl2 + H2O = MgCl2.H2O	1	-966630.0	137.2	2320.0	115.3	1018.2	113.2
MgCl2.H2O + H2O = MgCl2.2H2O	1	-1279720.0	179.9	1860.0	159.2	1213.3	131.2
MgCl2.2H2O + 2H2O = MgCl2.4H2O	2	-1898990.0	264.0	1290.0	241.4	1443.8	167.2
MgCl2.4H2O + 2H2O = MgCl2.6H2O	2	-2499020.0	366.1	1569.0	315.1	1550.4	203.2
K2CO3 + 1.5H2O = K2CO3.1.5H2O	1.5	-1609200.0	203.3	2430.0			165.2
BaCl2 + H2O = BaCl2. H2O	1	-1160600.0	166.9	3476.5	117.9		226.2
BaCl2.H2O+H2O = BaCl2.2H2O	1	-1460100.0	202.9	3097.0	162.0	663.1	244.2
CaSO4 + 0.5H2O = CaSO4.0.5H2O	0.5	-1576740.0	130.5		119.4	822.7	145.1
CaSO4.0.5H2O + 1.5H2O = CaSO4.2H2O	1.5	-2022630.0	194.1	2320.0	186.0	1080.6	172.1
CuCl2 + 2H2O = CuCl2.2H2O	2	-821300.0	167.0	2510.0			170.5
LiCl + H2O = LiCl. H2O	1	-712580.0	102.8	1760.0	494.1		60.4
LiCl.H2O + H2O = LiCl.2H2O	1	-1012650.0	139.2	1760.0			78.4
LiCl.2H2O + H2O = LiCl.3H2O	1	-1311300.0	188.3	1760.0			96.4
Li2SO4 + H2O = Li2SO4.H2O	1	-1715520.0	163.6	2060.0	151.1	1180.9	127.9
ZnSO4 + H2O = ZnSO4. H2O	1	-1304490	138.5		145.046		179.5
ZnSO4.H2O + 5H2O = ZnSO4.6H2O	5	-2777490	363.3	2072	337.744		269.5
ZnSO4.6H2O + H2O = ZnSO4.7H2O	1	-3077750	388.7		418.836		287.5

Step by step reaction	Khi	Delta H [J/mol]	Delta S [J/mol/K]	Complete reaction step [J/mol]	Ed tot [GJ/m3]
SrBr2 + H2O = SrBr2. H2O	1	71982.0	143.9	71982.0	0.6
SrBr2.H2O + 5H2O = SrBr2.6H2O	5	58162.0	143.6	290810.0	2.0
MgSO4 + H2O = MgSO4.H2O	1	75382.0	154.0	75382.0	1.4
MgSO4.H2O + 5H2O = MgSO4.6H2O	5	55162.0	144.5	275810.0	2.1
MgSO4.6H2O + H2O = MgSO4.7H2O	1	59892.0	164.9	59892.0	0.4
CaCl2 + H2O = CaCl2.H2O	1	71582.0	292.8	71582.0	1.2
CaCl2.H2O + H2O = CaCl2.2H2O	1	51882.0	-17.4	51882.0	0.7
CaCl2.2H2O + 2H2O = CaCl2.4H2O	2	61532.0	156.0	123064.0	1.2
CaCl2.4H2O + 2H2O = CaCl2.6H2O	2	57332.0	153.9	114664.0	0.9
MgCl2 + H2O = MgCl2.H2O	1	83907.0	141.2	83907.0	1.7
MgCl2.H2O + H2O = MgCl2.2H2O	1	71272.0	146.1	71272.0	1.0
MgCl2.2H2O + 2H2O = MgCl2.4H2O	2	67817.0	146.8	135634.0	1.0
MgCl2.4H2O + 2H2O = MgCl2.6H2O	2	58197.0	137.8	116394.0	0.9
K2CO3 + 1.5H2O = K2CO3.1.5H2O	1.5	63635.3	157.0	95453.0	1.4
BaCl2 + H2O = BaCl2. H2O	1	60182.0	145.6	60182.0	0.9
BaCl2.H2O+H2O = BaCl2.2H2O	1	57682.0	152.8	57682.0	0.7
CaSO4 + 0.5H2O = CaSO4.0.5H2O	0.5	61182.0	144.6	30591.0	0.0
CaSO4.0.5H2O + 1.5H2O = CaSO4.2H2O	1.5	55442.0	146.4	83163.0	1.1
CuCl2 + 2H2O = CuCl2.2H2O	2	58782.0	159.4	117564.0	1.7
LiCl + H2O = LiCl. H2O	1	2152.0	145.3	2152.0	0.1
LiCl.H2O + H2O = LiCl.2H2O	1	58252.0	152.5	58252.0	1.3
LiCl.2H2O + H2O = LiCl.3H2O	1	56832.0	139.7	56832.0	1.0
Li2SO4 + H2O = Li2SO4.H2O	1	49481.0	140.3	49481.0	0.8
ZnSO4 + H2O = ZnSO4. H2O	1	79872.0	160.8	79872.0	0.0
ZnSO4.H2O + 5H2O = ZnSO4.6H2O	5	52782.0	143.9	263910.0	2.0
ZnSO4.6H2O + H2O = ZnSO4.7H2O	1	58442.0	163.4	58442.0	0.0

GESTIS Substance Database
NBS
Wikipedia
Donkers review
OXY - A guide to physical properties of CaCl2
Calculated Value
Unknown / Estimated
Rubino, de Boer, 2012
van de Voort TUE Thesis
N'Tsoukpoe, 2015 Review on CaCl2
Monnin, 2002, Thermodynamics of LiCl + H2O
Trausel, 2014 Review
Zhao, Wang et al. 2016, Development of SrBr2
Perry's Handbook of Chemical Engineering

Appendix II: Fan utilisation in the TCS/P2H/PV system

A major cause of electrical energy usage is the air fan which drives both steps of the TCS cycle. Fan and air blower energy consumption is understood in the TCS literature to have an impact on the performance of open TCS systems [15]. Reactor module geometry and air flow rate need to be carefully selected so that TCS thermal energy delivery is not eclipsed by the process electrical consumption. Fan power consumption depends on the pressure drop through a reactor module and the delivered volumetric flow rate and is calculated with **equation (102)**.

$$P_{fan} = (\frac{1}{\eta_{fan}}) Q_v \Delta P_{drop} \quad (102)$$

Where η_{fan}could be approximately 0.5 depending on the fan model. The pressure drop in a porous bed can be calculated with Ergun's **equation (103)**

$$\frac{\Delta P_{drop}}{L} = \frac{150\mu_{air}(1-\varepsilon)^2}{\varepsilon^3 Dp^2} v_{air} + \frac{1.75\rho_{air}(1-\varepsilon)}{\varepsilon^3 Dp} {v_{air}}^2 \quad (103)$$

Where L is the length of a reactor module, μ_{air} is the air dynamic viscosity (assumed constant at 20.10^{-6} Pa/s), ε is the bulk porosity of the TCM, Dp is the average TCM particle diameter (assumed to be 1 mm [15]), ρ_{air} the air density (assumed constant at 1.2 kg/m3 for the temperature range ~15°C to 80°C in the considered system) and v_{air} air flow velocity which depends on the mass flow rate and the diameter of the reactor module.

$$v_{air} = Q_v \Delta P_{drop} \quad (104)$$

Pressure drop ultimately depends on the properties of the porous material, the air flow rate, and the geometry of the reactive bed. As discussed earlier, 0.05 m^3 individual cylindrical modules with aspect ratios of AR = Diameter / Length = 1 were considered. Cylindrical shape avoids corners on the reactor which can lead to reactive 'dead zones' (areas where humid/dry air does not access the dehydrated/hydrated TCM). Based on this selected design volume, aspect ratio and shape, the derived geometrical characteristics of the entire TCS reactor and the individual modules are shown in **Table 45**.

Table 45 TCS reactor and individual module geometric characteristics.

Reactor Module Geometry		
Total Volume	2.25	m^3
Number of modules	27	[-]
Module Volume	0.05	m^3
Module Aspect Ratio	1	[-]
Module Radius	0.1996	m
Module Length	0.3993	m

Due to the choice of control of the air flow, the mass flow rate of air:

- is set to 0.06 kg/s during heat discharge with variable humidity. Using **equation (104)** results in a fan power of 86 W.
- varies with the inlet power during heat charge to keep a constant design dehydration temperature. A histogram of the variation in mass flow rate throughout the year during dehydration steps is shown in **Figure 123**. Fan power varies accordingly between 0W and 86W.

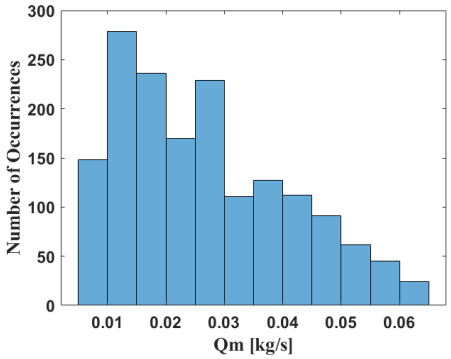

Figure 123 Frequency of occurrences of different mass flow rates during heat charge / dehydration. Each occurrence represents one hour of operation of the air fan.

For the reference case scenario, the total electrical used by the fan is ~182.9 kWh which, considering the total delivered useful energy of 1426 kWh, equates to 12.86% of the delivered thermal energy. De Boer et al. [244] estimated that the fan should ideally consume less than 5% of the thermal energy delivered by the TCS for overall viability. Lowering the energy consumption of the fan compared to the TCS could be achieved by either lowering the operating flow rate, or by lowering the pressure drop in the TCS modules by reducing the length of the reactor and/or increasing the bulk porosity of the TCM. This sensitivity is shown in **Figure 124**.

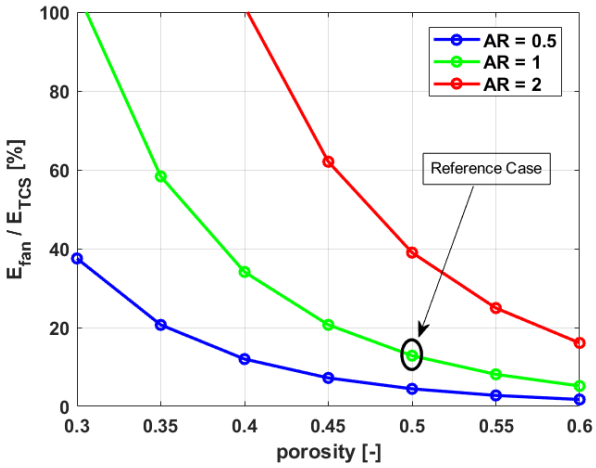

Figure 124 Ratio of total fan energy consumption over energy delivered by the TCS sensitivity to TCM porosity.

Appendix III: Idealised scenario for the TCS/P2H/PV system

Prior to carrying out the dynamic simulations of the TCS/P2H/PV system using the TCS reactor model, a preliminary analysis of the case study in an ideal scenario is carried out. Using the hourly space heating demand and generated PV power profile, an ideal case scenario is simulated using a basic control algorithm. The purpose is to visualise the ideal case where all energy is transferred to and from the storage with 100% efficiency and showcase an ideal scenario which represents the performance limit of the TCS within the space heating system. The analysis is carried out with the following assumptions:

- Any excess PV power ($\Delta Q > 0$) is stored at 100% in the TCS.
- Any excess space heating demand ($\Delta Q < 0$) is covered by the TCS with 100% efficiency if the current state of charge (SoC) allows for it.
- If the current SoC is lower than the heat demand, the TCS is fully discharged, and the uncovered difference is provided by the auxiliary.
- Any other unmatched heat demand is provided by the auxiliary.
- The storage is assumed to be initially fully discharged (i.e., completely hydrated).
- Once the storage profile is drawn, the maximum SoC is taken as the final size of the thermochemical storage.

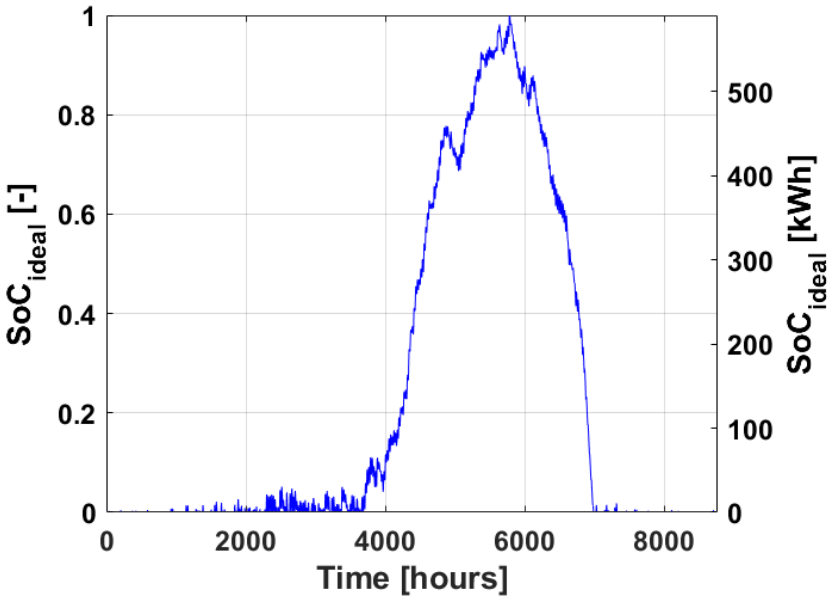

Figure 125 State-of-charge of the TCS based on the instantaneous space heating demand and solar PV generation in the ideal case scenario. The maximum state of charge is 605 kWh.

The evolution of the state of charge of the TCS in such a scenario can be visualised in **Figure 125**. In the first ~2000 hours, the building heat demand is generally higher than the available PV power. During this period, most of the generated PV energy is directly sent to the UFH. As the year progresses (solar irradiance and ambient temperatures increase), generated solar PV tends to exceed building space heating demand. In this period, excess PV energy is converted to heat and stored in TCS. SoC increases until reaching a maximum of 605.6 kWh at the 5778th hour of the year i.e., 28th of July 18h00. This maximum corresponds to the maximum relative state of charge SoC = 1. After this date, ambient temperatures and solar irradiance gradually decrease. The TCS is discharged at a higher rate than it is charged, and the overall SoC gradually decreases until reaching 0 at the 6980th hour (2nd of October 08h00). After that very little energy stored in the TCS, and SoC remains close to 0.

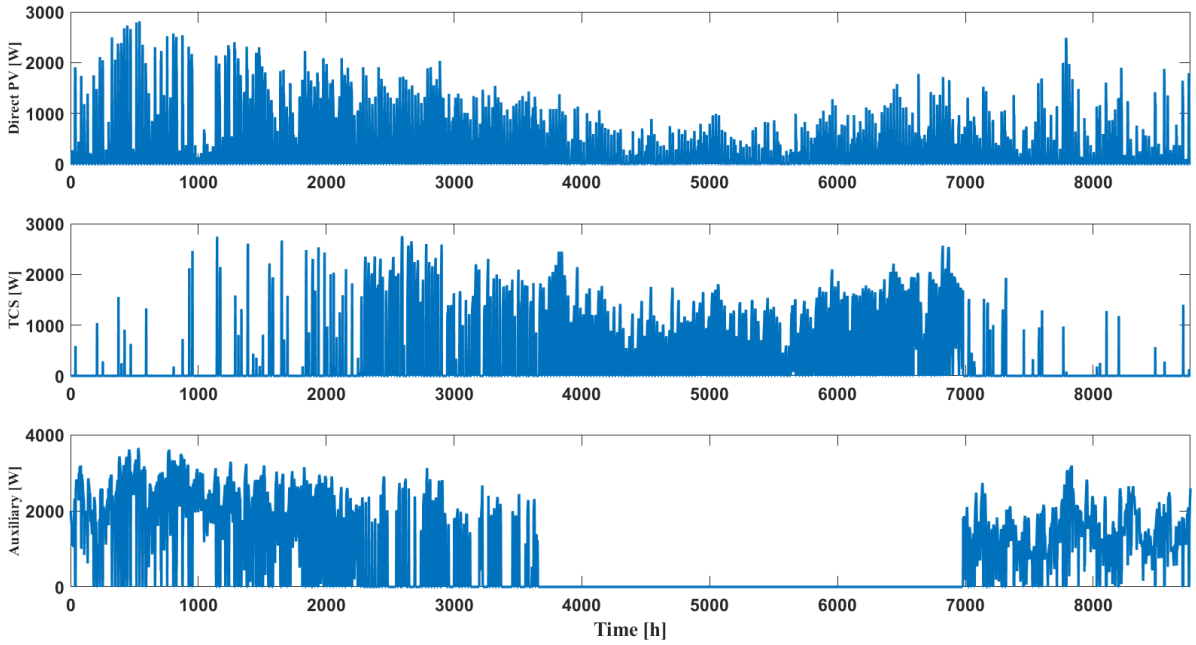

Figure 126 Power delivered by direct PV, TCS and auxiliary heating system to cover space heating demand in the ideal case scenario.

The contribution of the TCS can be appreciated with the distribution of heat of heating power delivered by the different sources (direct PV, TCS discharge and auxiliary) in **Figure 126**. During winter, up to 4 kW of heating power may be required from the auxiliary as heat demand is very high from the low ambient temperature and solar irradiance and the resulting generated PV power is low. However, between ~4000 hours and ~7000 hours (roughly May through October), direct PV and stored thermochemical energy should be enough to completely satisfy space heating demand. In this ideal case scenario, auxiliary heating accounts for 59% of the space heating demand, direct PV for 17%, while heat discharged from the TCS delivers 24% of the space heating demand, effectively increasing the solar fraction by 24% from 17% to 41% (see **Figure 127**).

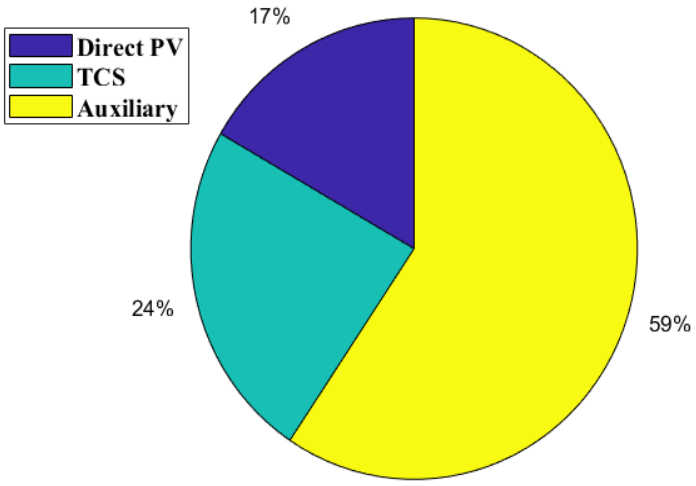

Figure 127 Final contribution of each energy source (PV, TCS, auxiliary) to the overall space heating demand in the ideal case scenario.

The maximum potential of the TCS to increase the solar fraction in space heating load depends on the two system determining parameters, overall heat transfer coefficient UA and solar PV system power rating. **Figure 128** shows the contribution of direct PV, TCS and auxiliary heating in dwellings with UA values varying from 100 to 200 W/K, solar PV systems from 3 kW to 7 kW. These values are typical and representative of the entire building stock in the UK in terms of heat loss, and most domestic PV systems can be found within this range of power ratings. Solar fraction (direct PV usage + TCS heat release) can be seen to vary from just below 20% in the case of a high heat loss building (UA = 200 W/K) with a small PV system (3 kW), to above 70% for a low heat loss building (100 W/K) with a large PV system (7 kW).

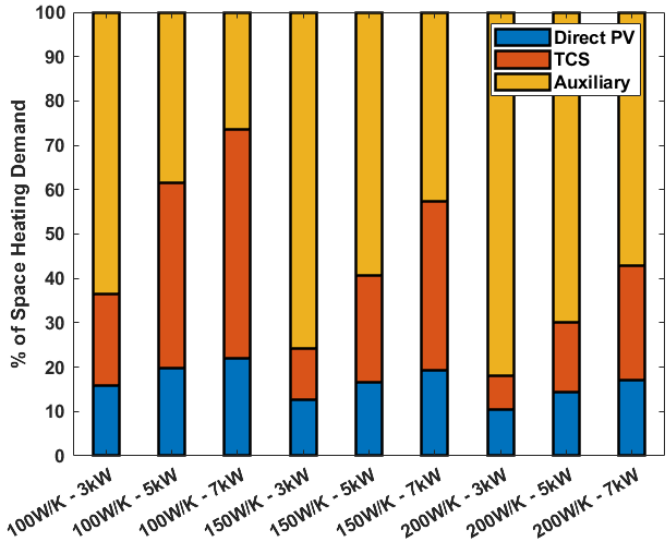

Figure 128 Variation of the final contribution of each energy source (PV, TCS, auxiliary) with power rating of the PV system and overall heat loss coefficient UA, in the ideal case scenario.

The previous section presented the ideal potential of the TCS/P2H/PV system for the given reference scenario. The actual overall performance is likely to be lower due to:

- Losses incurred from the conversion of electrical to thermal energy.
- The efficiency of dehydration / charge of the generated thermal energy.
- The efficiency of the hydration / release of the stored heat to the heating system.
- Heat released during discharge below the minimum temperature for the UFH loop.
- Excess solar PV energy below a sufficient power to desorb the thermochemical material.
- The efficiency of the heat exchange between the hot air exiting the reactor during discharge and the water flow of the UFH circuit.

The following section presents the evaluation of the performance of the TCS/P2H/PV system, using a similar control logic to the idealised case scenario, while accounting for the dynamic effects of the thermochemical energy storage cycle using the indirect conventionally heated TCS/P2H model.

Appendix IV: Program Listings (main Matlab codes for **chapters III** to **V**)

Chapter III

```
clearvars
close all
clc
tic
summary=ones(11,3);
load('C:\Users\Robin Fisher\Documents\MATLAB\Kinetics\DVS\Curve Fittings\DVS_DATA_MP.mat')

c=2;

min_alpha= 0.01;
max_alpha = 0.95;

if c==1
data = MP_25C_1630mg;
else
data = MP_40C_1539mg;
end

index = min_alpha<data(:,3);
index2 = max_alpha>data(:,3);
data_x = data(index&index2,:);
time=data_x(:,1);
alpha=data_x(:,3);

time_init = time;
alpha_init = alpha;

all_alpha = ones(size(alpha,1),11);

for model=1:11

B0 = 10^-3;
options=optimoptions('lsqcurvefit','Algorithm','levenberg-marquardt');
opts = odeset('RelTol',1e-4,'AbsTol',1e-4);

k=lsqcurvefit(@(B,time) Kinetic_Models(B,time,model,min_alpha,[]),B0,time,alpha,[],[],options);

alphaan=Kinetic_Models(k,time,model,min_alpha,[]);

   if model == 1
      alpha_A2 = alphaan;
      all_alpha(:, model) = alphaan;
   elseif model == 2
      alpha_A3 = alphaan;
      all_alpha(:, model) = alphaan;
   elseif model == 3
      alpha_A4 = alphaan;
      all_alpha(:, model) = alphaan;
   elseif model == 4
      alpha_R2 = alphaan;
      all_alpha(:, model) = alphaan;
```

```
    elseif model == 5
      alpha_R3 = alphaan;
      all_alpha(:, model) = alphaan;
    elseif model == 6
      alpha_D1 = alphaan;
      all_alpha(:, model) = alphaan;
    elseif model == 7
      alpha_D2 = alphaan;
      all_alpha(:, model) = alphaan;
    elseif model == 8
     alpha_D3 = alphaan;
     all_alpha(:, model) = alphaan;
    elseif model == 9
     alpha_D4 = alphaan;
     all_alpha(:, model) = alphaan;
    elseif model == 10
     alpha_F1 = alphaan;
     all_alpha(:, model) = alphaan;
    elseif model == 11
     alpha_VC = alphaan;
     all_alpha(:,model)=alphaan;
    end

det_coef_num = sum((alpha - alphaan).^2) ;
det_coef_den = sum((alpha - mean(alpha)).^2);
r2 = 1 - det_coef_num / det_coef_den ;

AICc    = size(alphaan,1)*log(det_coef_num/size(alphaan,1))+2;

summary(model,1) = k    ;
summary(model,2) = r2   ;
summary(model,3) = AICc ;

x = real(alpha);
y = real(alphaan);
z = x.*y;
N = size(alpha,1);
r_pearson = (N*sum(z)-sum(x)*sum(y)) / sqrt ( (N*sum(x.*x)-sum(x)^2) * (N*sum(y.*y)-sum(y)^2) );
R2 = r_pearson^2;
summary(model,4) = R2 ;

end

file = 'C:\Users\Robin Fisher\Documents\MATLAB\Kinetics\DVS\Curve Fittings\MP.xlsx';

writematrix(summary,  file,'Sheet',c, 'Range', 'C3')
writematrix(time,     file,'Sheet',c, 'Range', 'g4')
writematrix(alpha,    file,'Sheet',c, 'Range', 'h4')
writematrix(all_alpha,file,'Sheet',c, 'Range', 'i4')

function alpha=Hydration(k,t,model,alpha0,opts)
% code for differential equations describing hydration process:
% dalpha/dt=Aexp(-Ea/R/T)*(1-alpha)*(1-peq/p)
%   with:
%       Variables:  alpha
%       Parameters: k = B
```

```
%alpha0=0.02;

z=1.37;
[~,Sv]=ode45(@DifEq,t,alpha0,opts);

function dalpha=DifEq(~,alpha)
 if     model==1 %A2
 dalpha=  k*2*(1-alpha)*(-log(1-alpha))^(1/2);

 elseif model==2 %A3
 dalpha = k*3*(1-alpha)*(-log(1-alpha))^(2/3);

 elseif model==3 %A4
 dalpha = k*4*(1-alpha)*(-log(1-alpha))^(3/4);

 elseif model==4 %R2
 dalpha = k*2*(1-alpha)^(1/2);

 elseif model==5 %R3
 dalpha = k*3*(1-alpha)^(2/3);

 elseif model==6 %D1
 dalpha = k*(1/(2*alpha));

 elseif model==7 %D2
 dalpha = k*(-1/(log(1-alpha)));

 elseif model==8 %D3
 dalpha = k*(3*(1-alpha)^(2/3)/(2*(1-(1-alpha)^(1/3))));

 elseif model==9 %D4
 dalpha = k*(3/(2*((1-alpha)^(-1/3)-1)));

 elseif model==10 %F1
 dalpha =(k*(1-alpha));

 elseif model==11 %Vc
 dalpha = k*1.5*(1/(z-1))*(((1+(z-1)*alpha)^(1/3))*((1-alpha)^(1/3))/((1-alpha)^(1/3)-1+(z-1)*alpha)^(1/3));
end
end

alpha=Sv;

end
```

Chapter IV

```
clear
clearvars
clc
close all
tic

%============================study type==================================
study_location  = 0;
```

```
study_material  = 0;

%==============================Heat Demand=================================
Heat_Demand_Year = 10*10^9;              % [J] Total heat demand over 212 days
Days = 212;                              % [days with heat demand]
Heat_Demand_Day  = Heat_Demand_Year / Days; % [J] Total heat demand over 1 day

%============================parameters====================================
%solid properties
%choice of material %1:SrBr2 %2:MgSO4 %3:CaCl2 %4:MgCl2 %5:K2CO3 %6:BaCl2 %7:CaSO4 %8:CuCl2 %9:LiCl %10:LiSO4
load('C:\Users\rfish\OneDrive\Documents\MATLAB\Reactor_Model\CORRECTED 0.5D Thermal Reactor v4\salt_properties.mat')
load('C:\Users\rfish\OneDrive\Documents\MATLAB\Reactor_Model\CORRECTED 0.5D Thermal Reactor v4\T_out_FPC_CORRECTED')

hydration     = 2 ; %1 or 2
location      = 0 ; % 0 to 6
material      = 1 ;

n             = 1 ;
kinetic_model = 1 ;
n_mat         = 1 ;
max_models    = 2 ;
max_param = max_models;

Cp_f       = 1004;       % [J/kg/K] Air heat capacity
rho_f      = 1.2;        % [kg/m3] Air density
mu_f       = 20*10^-6;   % [Pa.s] Air dynamic viscosity
M_h2o      = 18*10^-3;   % [kg/mol] Water molar mass
R          = 8.314;      % [J/mol/K] Perfect gas constant
Qm         = 0.0671;
Qhtf       = 0.0671;
Cp_htf     = Cp_f;       % [J/kg/K] HTF (HeX) heat capacity
comp       = 0.6;        % [-]  m[salt]/(m[salt]+m[matrix])
Cp_matrix  = 960;        % [J/kg/K] Matrix heat capacity
rho_matrix = 800;        % [kg/m3] Matrix density
porosity   = 0.5;        % [-] material porosity
Dp         = 1*10^-3;    % [m] solid particle average diameter
% k_cin     = 10^-4 ;    % [1/s] kinetic coefficient
t0         = 0;
N          = 50; %number of reactor subdivisions
AR         = 4;  %reactor aspect ratio (L/D)
V_max      = 1;
thickness_steel  = 2*10^-3; %m
density_steel    = 8000; %kg/m3
price_steel      = 2.7; %€/kg
price_electricity=210/3600*10^-6 ; %€/J from European 2020 data

%heat exchanger
Qm_hot   = Qm;
Qm_cold  = Qm;
Cp_hot   = Cp_f;
Cp_cold  = Cp_htf;
C_hot    = Qm_hot*Cp_hot;
C_cold   = Qm_cold*Cp_cold ;
C_min    = min(C_hot,C_cold);
C_max    = max(C_hot,C_cold);
```

```
C_r     = C_min/C_max;
U = 35; % W/m2/K
A = 35; % m2

k_cin  = 5*10^-4;
k=1;

while(k < 2)
%     if k == 1
%         k_cin = 10^-4;
%     elseif k == 2
%         k_cin = 5*10^-4;
%     elseif k == 3
%         k_cin = 2.5*10^-3;
%     elseif k == 4
%         k_cin = 10^-2;
%     elseif k == 5
%         k_cin = 5*10^-2;
%     end

%sorption material properties
khi          = salt_properties(material,1 )       ; % [mol h2o/mol salt] stoechiometric coefficient
rho_salt     = salt_properties(material,2 )       ; % [kg/m3] unhydrated solid heat capacity
Cp_salt      = salt_properties(material,3 )       ; % [J/kg/K] salt heat capacity
M_salt       = salt_properties(material,4 )*10^-3 ; % [kg/mol]
dH           = salt_properties(material,8 )       ; % [J/mol h2o] reaction enthalpy [molar to water]
dS           = salt_properties(material,9 )       ; % [J/mol h2o/K] reaction entropy
Ed           = salt_properties(material,10)       ; % [GJ/m3] Theoretical energy density
price_salt   = salt_properties(material,11) ; % [euros/kg]

dHm        = dH*khi/M_salt;          % [J/kg salt] Reaction enthalpy [specific to salt]
m_salt     = Heat_Demand_Day / dHm;   % [kg] Theoretical mass of salt to match demand
m_matrix   = m_salt*(1-comp)/comp;    % [kg] mass of matrix material
V_salt     = m_salt / rho_salt ;              % [m3] volume occupied by salt
V_matrix   = m_matrix / rho_matrix;           % [m3] volume occupied by matrix
V_reactor = (V_salt + V_matrix)/(1-porosity) ;  % [m3] volume occupied by material
D_reactor = (4*V_reactor/pi/AR)^(1/3);        % [m] reactor diameter
L_reactor = D_reactor*AR;                     % [m] reactor length
R_reactor = D_reactor/2;                      % [m] reactor radius
surface_reactor = 2*pi*(R_reactor)*L_reactor;   % [m2]
volume_steel = surface_reactor * thickness_steel;%[m3]
weight_reactor = volume_steel*density_steel;

Ea = 46.220*10^3 ;    % [J/mol] activation energy
Af = 1.0838/60*10^6 ; % [1/s] frequency factor

if hydration == 1
   t_final    = 2*24*3600;
   eta_hx  = 0.85;
   eta_hru = 0.85;
   a=1;
   b=0;
   Tamb = 19+273.15;     % [K] ambient temperature
   T_in = Tamb;          % [K] inlet air temperature
   p_in = 1500;
   w_in = 0.62198 / (101325/p_in-1);    % [kg_h2o/kg_air] Inlet absolute humidity
```

```
    Ts_o     = Tamb;              % [K] initial reactor temperature
    w_o      = 0.0001;            % [kg_h2o/kg_air] initial humidity surrounding reactor material
    alpha_o = 0.01;               % [-] initial state of reaction advancement
    Xs_o     = alpha_o*khi*M_h2o/M_salt; % [kg_h2o/kg_salt] initial material water loading
elseif hydration == 2
    eta_hx  = 0.01;
    eta_hru = 0.01;
    t_final    = 24*3600;

     if location==1
     FPC_coefs = coefs_Birmingham;      % [Pa] Inlet water vapour pressure
     elseif location==2
     FPC_coefs = coefs_Eindhoven;
     elseif location==3
     FPC_coefs = coefs_Lyon;
     elseif location==4
     FPC_coefs = coefs_Stuttgart;
     elseif location==5
     FPC_coefs = coefs_Helsinki;
     elseif location==6
     FPC_coefs = coefs_Barcelona;
     elseif location==0
     FPC_coefs = coefs_Birmingham;
     end

     a=0;
     b=1;
     Tamb = 25 + 273.15;
     T_in = 100+273.15;            % [K] inlet air temperature
     p_in = 0.01 * 101.325;        % [Pa] inlet air water vapour pressure
     w_in = 0.62198 / (101325/p_in-1); % [kg_h2o/kg_air] Inlet absolute humidity
     alpha_o = 1;
     Ts_o     = 25+273.15;       % [K] initial reactor temperature
     w_o      = 0.005;           % [kg_h2o/kg_air] initial humidity surrounding reactor material
     Xs_o     = khi*M_h2o/M_salt; % [kg_h2o/kg_salt] initial material water loading
end

peq_o = 101325*exp(-dH/Ts_o/R+dS/R);
pv_o    = w_o*101325/(0.622+w_o); % [Pa] inlet air water vapour pressure

k=1;

%============================equations system=====================================
n_eqs=4;
syms Ts(t)    [N 1]
syms alpha(t) [N 1]
syms peq(t)   [N 1]
syms pv(t)    [N 1]
syms Thx(t)
syms Tr(t)

Ts    = formula(Ts);
alpha = formula(alpha);
peq   = formula(peq);
pv    = formula(pv);
eqns = sym('eqn',[1 N*n_eqs+2]);
```

```
for i = 1:N
      if i==1
  eqns((i-1)*n_eqs+1)          =          diff(Ts(i),1)*(m_salt*Cp_salt+m_matrix*Cp_matrix)/N          ==          Qm*Cp_f*(Tr(t)-
Ts(i))+diff(alpha(i),1)*dH*m_salt/N*khi/M_salt;

         if kinetic_model == 1
  eqns((i-1)*n_eqs+2) = diff(alpha(i),1)       == k_cin*((f_kinetics(alpha(i),kinetic_model))^a)*(alpha(i))^b*(1-peq(i)/pv(i));
         elseif kinetic_model == 2
  eqns((i-1)*n_eqs+2)  =  diff(alpha(i),1)            ==  Af*exp(-Ea/R/Ts(i))*((f_kinetics(alpha(i),kinetic_model))^a)*(alpha(i))^b*(1-
peq(i)/pv(i));
         end

  eqns((i-1)*n_eqs+3) = diff(alpha(i),1)*khi*M_h2o/M_salt*m_salt/N       == (0.62198*p_in/(101325-p_in)-0.62198*pv(i)/(101325-
pv(i)))*Qm;
  eqns((i-1)*n_eqs+4) = peq(i)                                  == (101325*exp(-dH/Ts(i)/R+dS/R));
      else
  eqns((i-1)*n_eqs+1)          =          diff(Ts(i),1)*(m_salt*Cp_salt+m_matrix*Cp_matrix)/N          ==          Qm*Cp_f*(Ts(i-1)-
Ts(i))+diff(alpha(i),1)*dH*m_salt/N*khi/M_salt;
  eqns((i-1)*n_eqs+2) = diff(alpha(i),1)                                  == k_cin*((f_kinetics(alpha(i),kinetic_model))^a)*(alpha(i))^b*(1-
peq(i)/pv(i));
  eqns((i-1)*n_eqs+3)   =   diff(alpha(i),1)*khi*M_h2o/M_salt*m_salt/N                  ==   (0.62198*pv(i-1)/(101325-pv(i-1))-
0.62198*pv(i)/(101325-pv(i)))*Qm;
  eqns((i-1)*n_eqs+4) = peq(i)                                  == (101325*exp(-dH/Ts(i)/R+dS/R));
      end
end

if hydration == 1
  eqns(N*n_eqs+1)=          Thx(t)    ==    Ts(N)    -    ((Ts(N)    -    Tamb).*C_min).*(1    -    exp((1/C_r)*    ((U*A/C_min)^0.22)*(exp(-
C_r*((U*A/C_min)^0.78))-1)))/C_hot ;
  eqns(N*n_eqs+2)=    Tr(t)  == T_in + eta_hru*(Thx(t)-T_in);
else
  eqns(N*n_eqs+1)    = Thx(t) == Ts(N) - (Ts(N) - Tamb)*eta_hx*min(Qm*Cp_f,Qhtf*Cp_htf)/(Qm*Cp_f);
  eqns(N*n_eqs+2)    = Tr(t)  == T_inlet(t,FPC_coefs) + eta_hru*(Thx(t)-T_inlet(t,FPC_coefs));
end

%============================solving section=====================================
vars = sym([1 N*n_eqs+2]);
   for j = 1:N
      vars((j-1)*n_eqs+1) = Ts(j);
      vars((j-1)*n_eqs+2) = alpha(j);
      vars((j-1)*n_eqs+3) = peq(j);
      vars((j-1)*n_eqs+4) = pv(j);
   end
      vars(N*n_eqs+1) = Thx(t);
      vars(N*n_eqs+2) = Tr(t);

[M,F] = massMatrixForm(eqns,vars);
M = odeFunction(M,vars);
F = odeFunction(F,vars);
F = @(t,Y) F(t,Y);

y0 = zeros(N*n_eqs+2, 1);
   for j = 1:N
      y0((j-1)*n_eqs+1) = Ts_o;
      y0((j-1)*n_eqs+2) = alpha_o;
```

```
        y0((j-1)*n_eqs+3) = peq_o;
        y0((j-1)*n_eqs+4) = pv_o;
    end
        y0(N*n_eqs+1) = Tamb;
        y0(N*n_eqs+2) = Tamb;

yp0 = zeros(N*n_eqs+2, 1);
opt    = odeset('mass',M,'InitialSlope',yp0,'RelTol',5.421011e-6,'AbsTol',5.421011e-6);

    y_sol = ode15s(F, [t0, t_final], y0, opt);

%==================extracting solution vectors & post-processing================================
t_sol{k}  = y_sol.x';
yy_sol{k} = y_sol.y';

k=k+1;
end

path = 'C:\Users\rfish\OneDrive\Documents\MATLAB\Reactor_Model\CORRECTED 0.5D Thermal Reactor v4\Chapter 4 - Section 4 Basic Cycle\Basic Cycle\Dehydration_Vars_Out.mat';
Dehydration_Vars_Out = [t_sol; yy_sol];
save(path, 'Dehydration_Vars_Out');

save('Dehydration_Params_Out','N', 'khi', 'M_h2o', 'M_salt', 'comp', 'Tamb', 'C_min', 'C_r', 'U', 'A', 'C_cold', 'eta_hru', 'material', 'V_reactor', 'dH', 'dS', 'R',...
    'Qm', 'Cp_htf', 'T_in', 'm_salt', 'w_in', 'Ts_o', 'pv_o','Qhtf','p_in','rho_f','Cp_f','porosity','R_reactor','mu_f','Dp','L_reactor','weight_reactor',...
    'price_salt','Heat_Demand_Year','max_param','N')
toc
```

Chapter V

```
clear
clc
close all
tic
clearvars

load salt_properties.mat'
load solar_PV_data.mat

%1:SrBr2 %2:MgSO4 %3:CaCl2 %4:MgCl2 %5:K2CO3 %6:BaCl2 %7:CaSO4 %8:CuCl2 %9:LiCl %10:LiSO4
material        = 5;
N               = 50;
comp            = 0.6;        % [-]   m[salt]/(m[salt]+m[matrix])
k_cin           = 5*10^-4;    % [1/s] kinetic rate constant
Tamb            = 20 + 273.15; % [C]
Qm              = 0.06;       % [kg/s]
p_in_dehydration = 500;         % [Pa]
p_in_hydration   = 600;        % [Pa]
T_dh_design     = 90 + 273.15; % [C]
i_min           = 1;
i_max           = 8760;

Size_factor     = 5;    % [kW]  Size of PV setup
```

```
UA_Loss          = 150;   % [W/K] Building heat loss coefficient
Baseline_temp    = 20 ;   % [C]   Baseline temperature for thermal comfort
eff_inv          = 0.92;  % [-]   Inverter efficiency
eff_resistance   = 1;     % [-]   Resistance efficiency
lifetime         = 30;    %[yrs] System project lifetime, for economics calculation

Cp_f       = 1004;       % [J/kg/K] Air heat capacity
rho_f      = 1.2;        % [kg/m3]  Air density
Cp_matrix  = 960;        % [J/kg/K] Matrix heat capacity
rho_matrix = 800;        % [kg/m3]  Matrix density
R          = 8.314;      % [J/mol/K] Universal Gas Constant
M_h2o      = 18*10^-3;   % [kg/mol]
porosity   = 0.6;        % [-]

eff_hx       = 0.85;              % [-]
rho_water    = 1000;              % [kg/m3]
Qv_UFH       = 1 * 10^-3 / 60;    % [m3/s]
Qm_UFH       = Qv_UFH * rho_water; % [kg/s]
T_air_out    = 25 + 273.15;       % [K]
T_water_cold = 20 + 273.15;       % [K]
Cp_water     = 4180;              % [J/kg/K]

khi         = salt_properties(material,1 )      ; % [mol h2o/mol salt] stoechiometric coefficient
rho_salt_dh = salt_properties(material,2 )      ; % [kg/m3] density
Cp_salt_dh  = salt_properties(material,3 )      ; % [J/kg/K] salt heat capacity
M_salt_dh   = salt_properties(material,4 )*10^-3 ; % [kg/mol]
rho_salt_h  = salt_properties(material,5 )      ; % [kg/m3] density
Cp_salt_h   = salt_properties(material,6 )      ; % [J/kg/K] salt heat capacity
M_salt_h    = salt_properties(material,7 )*10^-3 ; % [kg/mol]
dH          = salt_properties(material,8 )      ; % [J/mol h2o] reaction enthalpy [molar to water]
dS          = salt_properties(material,9 )      ; % [J/mol h2o/K] reaction entro
price_salt  = salt_properties(material,11) ;      % [euros/kg]
dHm         = dH*khi/M_salt_h;                    % [J/kg salt] Reaction enthalpy [specific to salt]

price_steel       = 2.7;             % [€/kg]
price_electricity = 210/3600*10^-6 ; % [€/J] from European 2020 data
Cost_Heat         = 0.20184;         % [€/kWh]
price_matrix      = 0.14 ;           % [€/kg]
thickness_steel   = 2*10^-3;         % [m]
density_steel     = 8000;            % [kg/m3]
mu_f              = 20*10^-6;        % [Pa.s] Air dynamic viscosity
Dp                = 1*10^-3;         % [m]

V_TCM_module    = 0.05; % [m3]
m_salt_module   = V_TCM_module*(rho_salt_h*rho_matrix*comp)/(comp*rho_matrix+(1-comp)*rho_salt_h);
m_matrix_module = m_salt_module*(1-comp)/comp;    % [kg] mass of matrix material
V_salt_module   = m_salt_module / rho_salt_h;
E_module_capacity = dHm * m_salt_module;
V_matrix_module = m_matrix_module / rho_matrix;
m_salt_module_h = m_salt_module * (1 + khi/M_salt_dh*M_h2o);

P_Heat_Demand    = max((Baseline_temp - T_amb) * UA_Loss,0); % [W]
E_Demand_total   = sum(P_Heat_Demand)*3600;                  % [J]
P_PV             = P_PV * Size_factor * 1000;                % [W]
P_P2H            = P_PV * eff_inv * eff_resistance;          % [W]
delta            = P_P2H - P_Heat_Demand;                    % [W]
```

```
P_res           = (max(delta,0));                       % [W]
P_Excess_Demand  = (min(delta,0));                      % [W]
E_Excess_PV      = sum(P_res)*3600;                     % [J] Energy not directly used for heating
E_Excess_Demand  = sum(abs(P_Excess_Demand))*3600;      % [J]
P_Direct_Heating = min(P_Heat_Demand, P_P2H);           % [W]
E_Direct_Heating = sum(P_Direct_Heating)*3600;          % [J] Energy instantly directly used for heating

State_of_Charge_hourly = ones(1, i_max - i_min + 1)';
Aux_Usage_hourly       = ones(1, i_max - i_min + 1)';
P_TCS                  = ones(1, i_max - i_min + 1)';
module_count           = ones(i_max-i_min+1,1);
nt                     = ones(i_max-i_min+1,1);
idx_cycle              = cell(i_max-i_min+1,1);
alpha_global_hour      = cell(i_max-i_min+1,1);
tout_hour              = cell(i_max-i_min+1,1);
T_in_hour              = cell(i_max-i_min+1,1);
yout_hour              = cell(i_max-i_min+1,1);
idx_cycle_hour         = zeros(i_max - i_min+1, 1);
idx_vect               = zeros(i_max - i_min+1, 2);
module_change          = zeros(i_max - i_min+1, 1);
P_TCS_notoperated      = zeros(i_max - i_min+1, 1);
E_released             = zeros(i_max - i_min+1, 1);
E_removed              = zeros(i_max - i_min+1, 1);
E_chem                 = zeros(i_max - i_min+1, 1);
E_sens                 = zeros(i_max - i_min+1, N);
E_sens_total           = zeros(i_max - i_min+1, 1);
E_stored               = zeros(i_max - i_min+1, 1);
E_SoC                  = zeros(i_max - i_min+1, 1);
E_SoC_discharge        = zeros(i_max - i_min+1, 1);
E_in_ideal             = zeros(i_max - i_min+1, 1);
E_out                  = zeros(i_max - i_min+1, 1);
Qm_all                 = zeros(i_max - i_min+1, 1);
p_in_h                 = zeros(i_max - i_min+1, 1);
OM_cost                = zeros(lifetime, 1);
Fuel_cost              = zeros(lifetime, 1);
discount_factor        = zeros(lifetime, 1);
PVC                    = zeros(lifetime, 1);
PVC_Output             = zeros(lifetime, 1);
time_hour              = linspace(1,8760, 8760)';
time_seconds           = linspace(1,8760*3600, 8760)';

T_in_initial         = Tamb + P_res ./ Qm ./ Cp_f;
T_in_initial         = T_in_initial(i_min:i_max);
T_eq_initial         = dH / (dS - R*log(p_in_dehydration / 101325)) ;
P_res_interval       = P_res(i_min:i_max);
T_in_initial_interval = T_in_initial(i_min:i_max);

delta                = P_Excess_Demand + P_res;
alpha_o_h            = 0;
alpha_o_dh           = 1;
E_SoCi               = 0;
E_SoC(1)             = E_SoCi ;
h                    = 0;
E_removed_max        = 0 ;
E_released_max       = 0 ;
Initial_State_of_Charge = E_SoCi; %[J]
```

```
%% ------------------------ Ideal Discharging / Charging Cycle -----------

for i = i_min:i_max
   h=h+1;
      if h == 1
         if delta(i) < 0
            if Initial_State_of_Charge < abs(3600 * delta(i))
               State_of_Charge_hourly(i) = 0;
               Aux_Usage_hourly(i) = abs(3600 * delta(i));
               E_released_max = E_released_max + abs(3600 * delta(i));
               P_TCS(i) = abs(State_of_Charge_hourly(i));
            else
               State_of_Charge_hourly(i) = Initial_State_of_Charge + 3600 * delta(i);
               Aux_Usage_hourly(i) = abs(3600 * delta(i)) - Initial_State_of_Charge;
               E_released_max = E_released_max + abs(3600 * delta(i));
               P_TCS(i) = abs(delta(i));
            end
         elseif delta(i) >= 0
               State_of_Charge_hourly(i) = Initial_State_of_Charge + 3600 * delta(i);
               Aux_Usage_hourly(i) = 0;
               E_removed_max = E_removed_max + 3600 * delta(i);
               P_TCS(i) = 0;
         end
      else
         if delta(i) < 0
            if State_of_Charge_hourly(i-1) < abs(3600 * delta(i))
               State_of_Charge_hourly(i) = 0;
               Aux_Usage_hourly(i) = abs(3600 * delta(i)) - State_of_Charge_hourly(i-1);
               E_released_max = E_released_max + State_of_Charge_hourly(i-1);
               P_TCS(i) = abs(State_of_Charge_hourly(i));
            else
               State_of_Charge_hourly(i) = State_of_Charge_hourly(i-1) + 3600 * delta(i);
               Aux_Usage_hourly(i) = 0;
               E_released_max = E_released_max + abs(3600 * delta(i));
               P_TCS(i) = abs(delta(i));
            end
         elseif delta(i) >= 0
               State_of_Charge_hourly(i) = State_of_Charge_hourly(i-1) + 3600 * delta(i);
               Aux_Usage_hourly(i) = 0;
               E_removed_max = E_removed_max + 3600 * delta(i);
               P_TCS(i) = 0;
         end
      end
end
SoC_max_ideal = max(State_of_Charge_hourly);
Module_num_ideal = round( SoC_max_ideal /  E_module_capacity  );
E_TCS_ideal = sum (P_TCS)*3600;

%% ---------------------- Dynamic TCS Operation -----------------------------
n_eqs = 3;
M = zeros(3*N);
y_o = [alpha_o_dh; Tamb; 101325*exp(-dH/Tamb/R+dS/R)];
y0     = ones(n_eqs*N,1)';

for j = 1:N
```

```
    y0((j-1)*n_eqs+1) = y_o(1);
    y0((j-1)*n_eqs+2) = y_o(2);
    y0((j-1)*n_eqs+3) = y_o(3);

    M(n_eqs*(j-1)+1,n_eqs*(j-1)+1) = 1;
    M(n_eqs*(j-1)+2,n_eqs*(j-1)+2) = 1;
    M(n_eqs*(j-1)+3,n_eqs*(j-1)+3) = 0;
end

abs_tol_vect = ones(1,3*N).*10^-6;
options  = odeset('Mass',M,'MassSingular','yes','RelTol',1e-6,'AbsTol',abs_tol_vect);
tout  = 0;
yout  = y0;
h=0;

for i = i_min:i_max

    h = h+1;
    module_change(h) = 0;
    if h ~= 1
        E_SoC(h) = E_SoC(h-1);
    end

    %--------------------------------Dehydration--------------------------
    if delta(i) > 500 % --> dehydration
        if h == 1  %if dehydration during 1st hour if the year
            tout = (i-1)*3600;
            for q = 1:N
                y0((q-1)*n_eqs +1) = alpha_o_dh;
                y0((q-1)*n_eqs +2) = Tamb;
                y0((q-1)*n_eqs +3) = 101325*exp(-dH/Tamb/R+dS/R);
            end
            yout  = y0;
        elseif idx_cycle_hour(h-1) == 2 %if dehydration when dehydration occured in the previous hour
            if module_change(h-1) == 1 && module_direction == 0
              module_change(h) = 0;
                for q = 1:N
                    y0((q-1)*n_eqs +1) = alpha_o_dh;
                    y0((q-1)*n_eqs +2) = Tamb;
                    y0((q-1)*n_eqs +3) = 101325*exp(-dH/Tamb/R+dS/R);
                end
            else
                for q = 1:N
                    y0((q-1)*n_eqs +1) = yout(end,(q-1)*n_eqs +1);
                    y0((q-1)*n_eqs +2) = yout(end,(q-1)*n_eqs +2);
                    y0((q-1)*n_eqs +3) = yout(end,(q-1)*n_eqs +3);
                end
            end

        else %if dehydration when hydration or nothing occured in the previous hour
            for q = 1:N
                y0((q-1)*n_eqs +1) = yout(end,(q-1)*n_eqs +1);
                y0((q-1)*n_eqs +2) = Tamb;
                y0((q-1)*n_eqs +3) = 101325*exp(-dH/Tamb/R+dS/R);
            end
        end
```

```
    Qm_dehydration = delta(i)  /Cp_f / (T_dh_design - Tamb);
    Qm_all(h)  = Qm_dehydration;

    [t_sol,y_sol]                                                                                                    =
ode23t(@(t_sol,y_sol)TCS_dehydration_UFH(t_sol,y_sol,dH,dS,k_cin,Qm_dehydration,Cp_f,m_salt_module,Cp_salt_h,m_matrix_
module,Cp_matrix,khi,M_salt_h,p_in_dehydration,N,T_dh_design),[(i-1)*3600 i*3600],y0,options);

    nt(h) = length(t_sol);
    tout  = [tout; t_sol(2:nt(h))];
    yout  = [yout; y_sol(2:nt(h),:)];
    idx_cycle_hour(h) = 2;

    if h == 1
       tout_hour{h} = t_sol(1:nt(h));
       yout_hour{h} = y_sol(1:nt(h),:);
       idx_cycle{h} = ones(nt(h),1)'.*2;
       T_in_hour{h} = ones(nt(h),1).*T_dh_design;
       E_in_ideal(h) = 3600 * abs(delta(i));

       for d=1:N
          E_sens(h,d) = (Cp_matrix*m_matrix_module+Cp_salt_dh*m_salt_module)/N*sum(diff(y_sol(:,(d-1)*n_eqs+2)));
       end
          E_sens_total(h) = sum(E_sens(h,:));

       E_removed(h) = Cp_f * Qm_dehydration * trapz(t_sol(1:nt(h)), T_in_hour{h}' - y_sol(1:end,(N-1)*n_eqs+2));
       E_stored(h) = E_removed(h) -  E_sens_total(h);

       E_out(h) = Cp_f * Qm_dehydration * trapz(t_sol(2:nt(h)), y_sol(1:end,(N-1)*n_eqs+2) - Tamb);

       E_SoC(h) = E_SoCi + E_removed(h);
       E_SoC_discharge(h) = E_SoCi;
       nt(h) = length(t_sol);
    else
       tout_hour{h} = t_sol(2:nt(h));
       yout_hour{h} = y_sol(2:nt(h),:);
       idx_cycle{h} = ones(nt(h)-1,1)'.*2;
       T_in_hour{h} = ones(nt(h)-1,1).*T_dh_design;
       E_in_ideal(h) = 3600 * abs(delta(i));

       for d=1:N
          E_sens(h,d) = (Cp_matrix*m_matrix_module+Cp_salt_dh*m_salt_module)/N*sum(diff(y_sol(2:end,(d-1)*n_eqs+2)));
       end
          E_sens_total(h) = sum(E_sens(h,:));

       E_removed(h)  = Cp_f * Qm_dehydration * trapz(t_sol(2:nt(h)), T_in_hour{h} - y_sol(2:end,(N-1)*n_eqs+2));
       E_stored(h) = E_removed(h) -  E_sens_total(h);

       E_out(h) = Cp_f * Qm_dehydration * trapz(t_sol(2:nt(h)), y_sol(2:end,(N-1)*n_eqs+2) - Tamb);

       clear alpha_global
       alpha = zeros(nt(h)-1,N);
       for r = 1:N
          alpha(:,r) = y_sol(2:end,(r-1)*n_eqs+1) ;
       end
       alpha_global = sum(alpha,2)./N;
```

```
        alpha_global_hour{h} = alpha_global;

        if(nt(h)>1)
            E_chem(h) = abs(alpha_global(end) - alpha_global(1))*dH*khi/M_salt_h*m_salt_module_h ;
        else
            E_chem(h) = 0;
        end

        E_SoC(h) = E_SoC(h-1) + E_removed(h);
        E_SoC_discharge(h) = E_SoC_discharge(h-1);
        nt(h) = length(t_sol)-1;
    end

    if y_sol(end,3*(N-1)+1)<0.01 && y_sol(end,3*(1-1)+1)<0.01 %check if first and final nodes of module is fully charged
        module_change(h) = 1;
        module_direction = 0; % direction = 0 => fully dehydrated module
    end

%---------------------------------Hydration----------------------------
elseif delta(i) < -500 && abs(delta(i)*3600) <= E_SoC(h) %%if energy demand > excess solar PV energy --> hydration
    if  h == 1 % if hydration during the 1st hour of the year
        tout = (i-1)*3600;
        for q = 1:N
            y0((q-1)*n_eqs +1) = alpha_o_h;
            y0((q-1)*n_eqs +2) = Tamb;
            y0((q-1)*n_eqs +3) = 101325*exp(-dH/Tamb/R+dS/R);
        end
        yout  = y0;
    elseif idx_cycle_hour(h-1) == 1 % if hydration when hydration occured in the previous hour
        if module_change(h-1) == 1 && module_direction == 1
            module_count(h) = module_count(h-1)-1;
            module_change(h) = 0;
            for q = 1:N
                y0((q-1)*n_eqs +1) = alpha_o_h;
                y0((q-1)*n_eqs +2) = Tamb;
                y0((q-1)*n_eqs +3) = 101325*exp(-dH/Tamb/R+dS/R);
            end
        else
            for q = 1:N
                y0((q-1)*n_eqs +1) = yout(end,(q-1)*n_eqs +1);
                y0((q-1)*n_eqs +2) = yout(end,(q-1)*n_eqs +2);
                y0((q-1)*n_eqs +3) = yout(end,(q-1)*n_eqs +3);
            end
        end
    elseif idx_cycle_hour(h-1) == 2 || idx_cycle_hour(h-1) == 0 % if hydration when dehydration or nothing occured in the previous
hour
        for q = 1:N
            y0((q-1)*n_eqs +1) = yout(end,(q-1)*n_eqs +1);
            y0((q-1)*n_eqs +2) = Tamb;
            y0((q-1)*n_eqs +3) = 101325*exp(-dH/Tamb/R+dS/R);
        end
    end

    if (abs(delta(i))>0) && (abs(delta(i))<=100)
        p_in_hydration = 80;
    elseif (abs(delta(i))>100) && (abs(delta(i))<=200)
```

```
      p_in_hydration = 100;
    elseif (abs(delta(i))>200) && (abs(delta(i))<=300)
      p_in_hydration = 250;
    elseif (abs(delta(i))>300) && (abs(delta(i))<=400)
      p_in_hydration = 300;
    elseif (abs(delta(i))>400) && (abs(delta(i))<=500)
      p_in_hydration = 350;
    elseif (abs(delta(i))>500) && (abs(delta(i))<=600)
      p_in_hydration = 400;
    elseif (abs(delta(i))>600) && (abs(delta(i))<=700)
      p_in_hydration = 450;
    elseif (abs(delta(i))>700) && (abs(delta(i))<=800)
      p_in_hydration = 500;
    elseif (abs(delta(i))>800) && (abs(delta(i))<=900)
      p_in_hydration = 550;
    elseif (abs(delta(i))>900) && (abs(delta(i))<=1000)
      p_in_hydration = 600;
    elseif (abs(delta(i))>1000) && (abs(delta(i))<=1100)
      p_in_hydration = 650;
    elseif (abs(delta(i))>1100) && (abs(delta(i))<=1200)
      p_in_hydration = 700;
    elseif (abs(delta(i))>1200) && (abs(delta(i))<=1300)
      p_in_hydration = 800;
    elseif (abs(delta(i))>1300) && (abs(delta(i))<=1400)
      p_in_hydration = 850;
    elseif (abs(delta(i))>1400) && (abs(delta(i))<=1500)
      p_in_hydration = 900;
    elseif (abs(delta(i))>1500) && (abs(delta(i))<=1600)
      p_in_hydration = 950;
    elseif (abs(delta(i))>1600) && (abs(delta(i))<=1700)
      p_in_hydration = 1050;
    elseif (abs(delta(i))>1700) && (abs(delta(i))<=1800)
      p_in_hydration = 1100;
    elseif (abs(delta(i))>1800) && (abs(delta(i))<=1900)
      p_in_hydration = 1150;
    elseif (abs(delta(i))>1900) && (abs(delta(i))<=2000)
      p_in_hydration = 1200;
    elseif (abs(delta(i))>2000)
      p_in_hydration = 1600;
    end

    for q = 1:N
      if (yout(end,(q-1)*n_eqs +1)>1)
        yout(end,(q-1)*n_eqs +1) = 1;
        y0((q-1)*n_eqs +1) = yout(end,(q-1)*n_eqs +1);
      end
    end

    p_in_h(h) = p_in_hydration;
    Qm_all(h) = Qm;

    [t_sol,y_sol] =
ode23t(@(t_sol,y_sol)TCS_hydration_UFH(t_sol,y_sol,dH,dS,k_cin,Qm,Cp_f,m_salt_module,Cp_salt_dh,m_matrix_module,Cp_m
atrix,khi,M_salt_dh,p_in_hydration,N,Tamb),[(i-1)*3600 (i)*3600],y0,options);

    nt(h) = length(t_sol);
```

```
    tout = [tout; t_sol(2:nt(h))];
    yout = [yout; y_sol(2:nt(h),:)];
    idx_cycle_hour(h) = 1;

    if h == 1
        tout_hour{h} = t_sol(1:nt(h));
        yout_hour{h} = y_sol(1:nt(h),:);
        T_in_hour{h} = ones(nt(h),1).*T_in_initial(i);
        idx_cycle{h} = ones(nt(h),1)'.*1;

        E_released(h)      = Qm * Cp_f * trapz(t_sol(1:nt(h)),y_sol(1:end,(N-1)*n_eqs+2) - Tamb);
        E_SoC(h)           = E_SoCi - E_released(h);
        E_SoC_discharge(h) = E_SoCi - E_released(h);

        idx_vect(h,1) = 1;
        idx_vect(h,2) = nt(h);

        nt(h) = length(t_sol);

    else
        tout_hour{h} = t_sol(2:nt(h));
        yout_hour{h} = y_sol(2:nt(h),:);
        T_in_hour{h} = ones(nt(h)-1,1).*T_in_initial(i);
        idx_cycle{h} = ones(nt(h)-1,1)'.*1;

        E_released(h)      = Qm * Cp_f * trapz(t_sol(2:nt(h)),y_sol(2:end,(N-1)*n_eqs+2) - T_in_hour{h});
        E_SoC(h)           = E_SoC(h-1)          - E_released(h);
        E_SoC_discharge(h) = E_SoC_discharge(h-1)- E_released(h);

        nt(h) = length(t_sol)-1;
    end

    if y_sol(end,3*(N-1)+1)>0.99 && y_sol(end,3*(1-1)+1)>0.99 %check if final node of module is fully discharged
        module_change(h) = 1;
        module_direction = 1; % direction = 1 => fully hydrated module
    end
else %if heat demand perfectly matches available solar PV --> no TCS operation
    idx_cycle_hour(h) = 0;
    Qm_all(h) = 0;
    P_TCS_notoperated(h) = delta(h);

    if h == 1   %if its the first hour of the year
        tout = [(i-1)*3600;i*3600];
        yout = [y0;y0];
        tout_hour{h} = [tout;i*3600];
        yout_hour{h} = yout;
        T_in_hour{h} = [T_in_initial(i);T_in_initial(i)];
        idx_cycle{h} = [0, 0];
        E_SoC(h) = E_SoCi;
        E_SoC_discharge(h) = E_SoCi;

        idx_vect(h,1) = 1;
        idx_vect(h,2) = 1;

        nt(h) = 2;
    else        %any other hour of the year
```

```
            for q = 1:N
                yout_hour{h}((q-1)*n_eqs +1) = yout(end,(q-1)*n_eqs +1);
                yout_hour{h}((q-1)*n_eqs +2) = Tamb;
                yout_hour{h}((q-1)*n_eqs +3) = 101325*exp(-dH/Tamb/R+dS/R);
            end

            tout = [tout;i*3600];
            yout = [yout;yout_hour{h}(end,:)];
            tout_hour{h} = i*3600;
            T_in_hour{h} = T_in_initial(i);
            idx_cycle{h} = 0;
            E_SoC(h) =  E_SoC(h-1);
            E_SoC_discharge(h) = E_SoC_discharge(h-1);

            nt(h) =  1;
        end
    end
end

%% ------------------------ Post Process ----------------------------------

idx_cycle_all   = cat(2,idx_cycle{1:end})';
T_in_all        = cat(1,T_in_hour{1:end});

eff_dehydration = E_removed ./ E_in_ideal ;
eff_dehydration2 = E_stored ./ E_in_ideal ;

eff_dehydration(isnan(eff_dehydration)) = 0;
t_sol = tout;
y_sol = yout;

E_in_dh = P_res.*3600;
E_in_dh(E_in_dh<500*3600) =0;

dh_balance = E_in_dh - E_sens_total - E_chem - E_out;

clear alpha_f T_sf pvf peq
for k=1:N
    alpha_f(:,k) = yout(:,(k-1)*n_eqs+1);
    T_sf(:,k)    = yout(:,(k-1)*n_eqs+2);
    pvf(:,k)     = yout(:,(k-1)*n_eqs+3);
    peq(:,k)     = 101325*exp(-dH./T_sf(:,k) /R+dS/R);
end
T_out = T_sf(:,end);
T_out_Useful = zeros(size(idx_cycle_all,1),1);
Temp_limit = 20+273.15;

for x = 1:size(idx_cycle_all,1)
    if idx_cycle_all(x) == 1 && T_out(x)>= Temp_limit
        T_out_Useful(x) = T_out(x);
    else
        T_out_Useful(x) = Tamb;
    end
end
```

```
T_UFH = eff_hx * Cp_f * Qm .* (T_out_Useful - T_air_out) / (Qm_UFH*Cp_water) + T_water_cold;

P_SoC_discharge     = E_released ./ 3600;
E_TCS_real          = sum(E_released);
E_delivered_fromTCS = trapz(tout, T_out_Useful - Tamb)*Cp_f*Qm;

E_delivered_fromTCS_all = trapz(tout, T_out - Tamb)*Cp_f*Qm;
E_delivered_fromTCS_useful = trapz(tout, T_out_Useful - Tamb)*Cp_f*Qm;

E_generated_ideal         = E_TCS_ideal ;
P_aux = Aux_Usage_hourly ./ 3600;
P_TCS_notoperated_dh = max(P_TCS_notoperated,0);

E_PV_notoperated_cumu = cumsum(P_TCS_notoperated_dh.*3600);
E_out_cumu            = cumsum(E_out);
E_sens_cumu           = cumsum(E_sens_total);
E_removed_cumu        = cumsum(E_removed);
E_chem_cumu           = cumsum(E_chem);

Module_count_real = ceil(E_SoC ./ E_module_capacity);
Module_num_real = max(Module_count_real);
Volume_TCS_real = Module_num_real * V_TCM_module;

%% ---------- Economics ----------

AR              = 1;
R_reactor       = (V_TCM_module / (2*pi*AR))^(1/3);
L_reactor       = 2*R_reactor * AR;
surface_reactor   = 2*pi*(R_reactor)*L_reactor;   % [m2]
volume_steel      = surface_reactor * thickness_steel;%[m3]
weight_reactor    = volume_steel*density_steel;
m_salt          = m_salt_module   * Module_num_real;
m_matrix          = m_matrix_module * Module_num_real;
V_TCM             = V_TCM_module    * Module_num_real * (1/porosity);

Qv_all          = Qm_all/rho_f;
velocity_f      = Qv_all ./ (pi*(R_reactor)^2);                    % [m/s]
Ergun_losses    = 150.*mu_f.*velocity_f.*((1-porosity).^2)./(porosity.^3)./(Dp.^2)...
   +1.75.*rho_f.*(velocity_f.^2).*(1-porosity)./(porosity.^3)./(Dp);          % [Pa/m]
Pressure_Losses   = Ergun_losses.*L_reactor;
P_fan           = Ergun_losses.*L_reactor.*Qv_all;                 % [W]
E_fan           = sum(P_fan .* 3600);                              % [J]

price_steel     = 2.7;          % [€/kg]
price_electricity = 210/3600*10^-6 ; % [€/J] from European 2020 data
price_PV_kW     = 1960;
price_Heat      = 0.20184;      % [€/kWh]

cost_fanpower     = price_electricity * E_fan;

Annual_Heat_Savings = E_delivered_fromTCS * price_Heat ;

price_salt          = 1.35; % [€/kg]
price_matrix_volume  =  80 ; % [€/m3]
matrix_bulk_density  = 100 ; % [kg/m3]
price_matrix        = price_matrix_volume / matrix_bulk_density; % [€/jg]
```

```
manufacturing_factor = 0.1 ; % asssume the cost of fabricating the composite is equal to XX%
                           % of the raw materials cos
C_p2h     = 140.535 + 0.0698 * 1000 * Size_factor ;        % [€]
C_casing  = price_steel * weight_reactor * Module_num_real;
C_tcm     = (m_salt * price_salt + m_matrix * price_matrix)*(1+manufacturing_factor); % [€]
C_piping  = 1000;     % [€]
C_fab     = 2000;    % [€]
C_fan     = 500;     % [€], representative cost of 180W, 180m3/h, 600 Pa duct air blower.              % [€/kW]
C_PV      = price_PV_kW * Size_factor;   % [€]

Init_Investment = C_tcm + C_fab + C_piping + C_casing + C_fan + C_PV + C_p2h; % [€]
SPT_ideal = Init_Investment / Annual_Heat_Savings; % [yrs]

OM            = 0.035 * Init_Investment;
OM_growth     = 0;
fuel          = 0;
discount_rate = 0.05;
Entry_Value   = Init_Investment;

OM_cost=ones(lifetime,1);Fuel_cost=ones(lifetime,1);
discount_factor=ones(lifetime,1);PVC=ones(lifetime,1);

for n = 1:round(lifetime)
   if n == 1
      OM_cost(n) = 0;
      Fuel_cost(n) = cost_fanpower;
   elseif n == 2
      OM_cost(n) = OM + fuel;
      Fuel_cost(n) = cost_fanpower;
   else
      OM_cost(n) = OM_cost(n-1) * (1+OM_growth);
      Fuel_cost(n) = cost_fanpower;
   end
   discount_factor(n) = 1 / (1 + discount_rate)^n ;

   PVC(n) = (OM_cost(n) + Fuel_cost(n))*discount_factor(n);
end
NPV = Entry_Value+sum(PVC);

for n = 1:round(lifetime)
   if n == 1
      PVC_Output(n) = 0;
   else
      PVC_Output(n) = ((E_delivered_fromTCS +  E_Direct_Heating)/ (3.6*10^6))*discount_factor(n);
   end
end
NPV_Output = sum(PVC_Output);
LCOE_syst = NPV / NPV_Output * 1000; % [€/MWh]



function dydt = TCS_hydration_UFH(t,y,dH,dS,k_cin,Qm,Cp_f,m_s,Cp_s,m_mat,Cp_mat,khi,M_s,Pin,N,T_in)

R=8.314;
M_h2o = 18*10^-3;
p_eq = @(dH, dS, T) 101325*exp(-dH/R./T+dS/R);
```

```
   for i=1:N
   if i == 1
      dzdt = [ k_cin*(1-y((i-1)*3+1))*(1-p_eq(dH, dS, y((i-1)*3+2))/y((i-1)*3+3));
      Qm*Cp_f*(T_in - y((i-1)*3+2))/((m_s*Cp_s+m_mat*Cp_mat)/N) + k_cin*(1-y((i-1)*3+1))*(1-p_eq(dH, dS, y((i-1)*3+2))/y((i-1)*3+3))*dH*(m_s/N)*khi/M_s/((m_s*Cp_s+m_mat*Cp_mat)/N);
      (0.62198*Pin/(101325-Pin)) - 0.62198*y((i-1)*3+3)/(101325-y((i-1)*3+3)) - k_cin*(1-y((i-1)*3+1))*(1-p_eq(dH, dS, y((i-1)*3+2))/y((i-1)*3+3))*khi*M_h2o/M_s*(m_s/N)/Qm];
      dydt = dzdt;
   else
      dzdt = [ k_cin*(1-y((i-1)*3+1))*(1-p_eq(dH, dS, y((i-1)*3+2))/y((i-1)*3+3));
      Qm*Cp_f*(y((i-2)*3+2) - y((i-1)*3+2))/((m_s*Cp_s+m_mat*Cp_mat)/N) + k_cin*(1-y((i-1)*3+1))*(1-p_eq(dH, dS, y((i-1)*3+2))/y((i-1)*3+3))*dH*(m_s/N)*khi/M_s/((m_s*Cp_s+m_mat*Cp_mat)/N);
      (0.62198*y((i-2)*3+3)/(101325-y((i-2)*3+3))) - 0.62198*y((i-1)*3+3)/(101325-y((i-1)*3+3)) - k_cin*(1-y((i-1)*3+1))*(1-p_eq(dH, dS, y((i-1)*3+2))/y((i-1)*3+3))*khi*M_h2o/M_s*(m_s/N)/Qm];
      dydt = [dydt; dzdt];
   end
   end
end
```

List of Publications

Journal publications

Fisher R, Ding Y, Sciacovelli A. Hydration kinetics of K_2CO_3, $MgCl_2$ and vermiculite-based composites in view of low-temperature thermochemical energy storage. J Energy Storage 2021;38:102561. doi:10.1016/j.est.2021.102561.

Conference proceedings

Fisher R, Ding Y, Sciacovelli A., Salts/matrix composites for thermochemical energy storage – Analysis of the couplings between sorption kinetics and performance of packed bed reactors, ECOS 2019 proceedings.

Fisher R, Ding Y, Sciacovelli A. Kinetic Modelling of Thermochemical Reactions for Long-Term Storage of Waste Heat, Sustainable Places 2021 proceedings.

Fisher R, Vecchi A, Palomba V, Frazzica A, Sciacovelli A. Techno-economic analysis of coupling thermochemical energy storage with power-to heat for increased utilisation of solar PV in residential space heating systems, SDEWES 2021 proceedings.

Fisher R, Palomba V, Frazzica A, Sciacovelli A. Thermochemical energy storage coupled with solar PV for increased renewable electricity generation: interplay between thermophysical behaviour and techno-economic performance. ECOS 2022 proceedings.